Image Simulation Framework for Digital Mammography Systems

Mary Yip

Submitted for the Degree of
Doctor of Philosophy
from the
University of Surrey



Centre for Vision, Speech and Signal Processing
School of Electronics and Physical Sciences
University of Surrey
Guildford, Surrey GU2 7XH, U.K.

June 2010

© Mary Yip 2010

Summary

A wide range of technology is available in commercial digital mammography; these vary greatly in physical performance measures such as Modulation Transfer Function (MTF) and Noise Power Spectrum (NPS). However, the relationship between a digital mamography system's physical performance and its impact on the clinician's ability to detect and characterise cancer from its images is unclear. Use of clinical trials to compare digital mammography technology would be expensive and time-consuming. Simulation of images acquired on such digital mammography systems provides a powerful way to compare and optimise technology. The aim of this work has been to develop and validate an image simulation framework to generate images as if acquired from specific digital mammography systems.

Signal and noise transfer properties of various systems were characterised using detector response, MTF and NPS measurements. Straight-edge and flat-field images were synthesized to validate the image simulation framework with experimentally acquired images. Excellent agreement was seen between synthetically generated and corresponding experimentally acquired images. Theory was developed to investigate the resampling effects upon measured MTF using the image simulation framework. The image simulation framework was further extended to generate CDMAM phantom images. The CDMAM phantom provides a method to quantify the detectability of details imaged on a mammography system based on an observer's ability to detect discs of varying contrast and diameter. Simulation of the CDMAM phantom image based on MTF and NPS alone was seen to be insufficient to create physically accurate CDMAM phantom images. Non-uniformity effects such as heel-effect, local pixel variance, geometric magnification and scatter effects were modelled to improve the image simulation framework.

Reducing the radiation dose to the patient whilst preserving sufficient information in the resultant mammogram to diagnose cancer is a very important issue. Lower exposure levels can be used in digital mammography systems compared with screen-film. However, there is ambiguity as to the optimal exposure level as well as the effects upon the characterisation and detection of cancer lesions from such images. A multiple noise source model was developed taking into account the major sources of noise: electronic, quantum and structural, thus increasing the exposure range at which the system noise can be accurately simulated. Comparison of 'dose reduced' experimentally acquired flat-field, CDMAM phantom and mastectomy images with corresponding lower dose experimentally acquired images showed excellent results. This marks the first study to have simulated such images for direct comparison in dose-reduction.

Key words: digital mammography, CDMAM phantom, image simulation, dose reduction, CDMAM scoring, MTF, NPS, mastectomy samples

Email: m.yip@surrey.ac.uk
WWW: http://www.eps.surrey.ac.uk/

Acknowledgements

This work has been undertaken with the support of Professor Kenneth Young, Professor David Dance, Dr. Jennifer Oduko, Alistair Mackenzie and Dr. Ozcan Gundogdu from the National Coordinating Centre for the Physics of Mammography at the Royal Surrey County Hospital. I would like to thank National Coordinating Centre for the Physics of Mammography and Leuven Radiology Department, Belgium, for sharing their images with me for this study. Without which, this work would not have been possible.

I would like to thank the members of the Medical Imaging Group, past and present, for their support in knowledge as well as part of the PhD process. I would like to acknowledge the help of Walter Chukwu and Evangelos Kottis for their help in developing the Quantitative Assessment Software (QAS) used in this work.

I would like to give a special thanks to my supervisors Dr. Kevin Wells and Dr. Emma Lewis for their patience and guidance throughout this process.

Finally, a personal thanks to my ever-patient partner Michael Braidley who has always encouraged me to take the chances and find my limits.

Contents

1 Introduction **1**

1.1 Screening for Breast Cancer 3

1.1.1 The UK National Health Service's Breast Screening Programme 3

1.1.2 Requirements of Breast Imaging 3

1.1.3 Moving to Digital Technology 4

1.2 Motivation and Aims 5

1.3 Thesis structure 6

1.4 Achievements and Major Contributions 8

2 Review of Mammography **9**

2.1 X-ray Mammography 9

2.1.1 Production of X-rays 10

2.1.2 X-ray Spectrum 12

2.1.3 X-ray Photon Interactions in Mammography 14

2.1.4 Anti-Scatter Grid 15

2.2 Detector Technology 16

2.2.1 Computed Radiography (CR) 16

2.2.2 Flat Panel Detectors 18

2.3 Summary 19

3 Image Quality Analysis **21**

3.1 Detector Response Measurement 22

3.2 Modulation Transfer Function 25

3.2.1 Measuring the MTF 26

3.2.2 The effects of undersampling 29

3.2.3 Comparison of experimental detector MTFs 30
3.3 Noise Power Spectrum (NPS) 31
3.3.1 Measuring the NPS for a digital system 32
3.3.2 Measuring the NPS clinically 36
3.3.3 NPS as a function of dose 37
3.4 Subjective Image Quality Analysis 38
3.4.1 The CDMAM test phantom 39
3.4.2 Signal Detection Theory 43
3.5 Summary 46

4 Developing the Image Simulation Chain 47
4.1 Literature review 47
4.1.1 Starting from an ideal image 48
4.1.2 Modifying a clinical image 49
4.2 Detector response 51
4.3 MTF Blurring and Resampling of the Images 52
4.3.1 Developing the blurring and resampling simulation chain 53
4.3.2 MTF 53
4.3.3 Resampling 57
4.3.4 Finding the minimum sampling ratio 57
4.3.5 Validation methodology 58
4.3.6 Validation Results 59
4.4 Intrinsic Sampling MTF 61
4.4.1 Resolution modification of idealised images 61
4.4.2 Clinical Image Synthesis 62
4.4.3 Validation results 64
4.5 MTF analysis 67
4.6 Noise Simulation 69
4.6.1 NPS filter 70
4.6.2 Dose simulation 72
4.6.3 Validation methodology 74
4.7 Validation Results 75
4.7.1 Noise 75
4.8 Discussion and Conclusions 80

5 CDMAM Synthesis and Contrast Detail Analysis 83

5.1 Methodology . . . 84

5.1.1 Modelling the CDMAM Phantom . . . 85

5.1.2 Creating the discs . . . 86

5.1.3 Inserting the Discs . . . 91

5.2 Evaluation methodology . . . 93

5.2.1 CDCOM software . . . 94

5.2.2 Quantitative Assessment System (QAS) . . . 96

5.3 Preliminary Results . . . 98

5.3.1 Contrast-detail Curves . . . 99

5.3.2 Contrast and Noise Measurements . . . 105

5.4 Limitations and Subsequent Requirements . . . 110

6 Non-Uniformity Considerations 117

6.1 Spatial Intensity Variation . . . 117

6.1.1 Causes of the Spatial Intensity Variation . . . 118

6.1.2 Modelling the spatial intensity variation: a literature review . . . 120

6.1.3 Modelling the Residual Heel-effect . . . 123

6.1.4 Spatial intensity variation for the three systems . . . 125

6.2 Pixel Intensity Variance across the Detector . . . 127

6.2.1 Consequences of Pixel Intensity Variance . . . 127

6.2.2 Introducing the effects of the Pixel Intensity Variance . . . 129

6.3 Magnification through Geometric Setup . . . 130

6.3.1 Combining the non-uniformity effects . . . 133

6.4 Scatter Modelling . . . 143

6.4.1 Principles of Scatter . . . 143

6.4.2 Prior work . . . 144

6.4.3 The Scatter Model . . . 144

6.4.4 Scatter-to-Primary Ratio Map . . . 145

6.4.5 Sensitivity of Disc Contrast Calculations to Experimental Set Up Parameters . . . 147

6.5 Contrast and Noise measurements from the synthetic CDMAM images . 151

6.6 Discussion and Conclusions . . . 151

7 Application of the Image Simulation Framework to Clinical Images 159

7.1 Multiple noise source model 160

7.1.1 Methodology 161

7.2 Validation 162

7.3 Modifying Experimental Images 163

7.3.1 Reducing the dose 163

7.3.2 Flat-field validations 165

7.3.3 Contrast-detail Measurements of dose reduced images 166

7.4 Clinical Mastectomy Images 168

7.4.1 Materials 168

7.4.2 Flat-field Validations 168

7.4.3 Analysis of modified clinical images 168

7.4.4 Qualitative Comparisons 170

7.4.5 Quantitative Comparisons 173

7.5 Discussion and Conclusions 176

8 Conclusions and Further Work 179

8.1 Further Work 181

A Anatomy and Pathology of the breast 183

A.1 The Breast 183

A.2 Breast Cancer 183

A.2.1 Lobular Carcinoma in situ (LCIS) 184

A.2.2 Ductal Carcinoma in situ (DCIS) 184

A.2.3 Invasive Lobular Carcinoma (ILC) 185

A.2.4 Invasive Ductal Carcinoma (IDC) 185

B Individual contrast-detail curves 187

B.1 Hologic Selenia system - amorphous selenium technology 188

B.1.1 Uniform images 188

B.1.2 Heel effect mask 189

B.1.3 Variance Map 190

B.1.4 Heel effect and Variance Map 191

B.1.5 Geometric blurring 192
B.1.6 Non-uniformity effects 193
B.1.7 Comparison of scatter models 194
B.2 GE Essential system - Caesium Iodide - amorphous silicon flat panel technology 195
B.2.1 Uniform images 195
B.2.2 Heel effect mask 196
B.2.3 Variance Map 197
B.2.4 Heel effect and Variance Map 198
B.2.5 Geometric blurring 199
B.2.6 Non-uniformity effects 200
B.2.7 Comparison of scatter models 201
B.3 Agfa CR system - caesium bromide needle crystal imaging plate technology 202
B.3.1 Uniform images 202
B.3.2 Heel effect mask 203
B.3.3 Variance Map 204
B.3.4 Heel effect and Variance Map 205
B.3.5 Geometric Blurring 206
B.3.6 Non-uniformity effects 207
B.3.7 Comparison of scatter models 208

C Sensitivity of Disc Contrast calculations **209**

Bibliography **211**

List of Figures

1.1 Incidence and mortality of different types of cancer in women worldwide in 2002[1]. 2

1.2 Incidence and mortality of different types of cancer in women in the UK between 1971 to 2005. Taken from National Statistics[2]. 2

1.3 An example of a mass in a screen film mammogram. [3]. 4

1.4 (a) An example of microcalcifications in a digital mammogram with Hologic image processing applied. (b) is a magnified region of microcalcifications from (a). Courtesy of St. George's Hospital. 5

2.1 Schematic of a typical mammography system. 10

2.2 Components of an X-ray tube. 10

2.3 An example of an X-ray spectrum. The bremsstrahlung spectrum represents a range of energies, the maximum of which, E_o, is determined by the tube voltage times the electron charge. Filtering removes the low energy photons. The dotted line represents the effect of increasing E_o. 11

2.4 X-ray linear attentuation coefficients of fat, fibroglandular tissue and ductal carcinoma for different energies. From Johns and Yaffe[4] 12

2.5 Spectra for typical target materials used in mammography [5]. 13

2.6 Spectra for Molybdenum/Rhodium target/filter material, with the K-edge of Rhodium marked. 14

2.7 (a) Photoelectric effect (b) Rayleigh scattering (c) Compton scattering. 15

2.8 A detector element, typically will be made up of active and inactive regions due to electronics. Fill factor, ideally 100%, is found using the ratio of the squared pixel aperture to the squared del pitch. 16

2.9 Simultaneous dual side reading of a CR plate. Courtesy of Fuji Medical Systems[6]. 17

2.10 An example of how light may be scattered in powdered phosphor compared to needle crystalline phosphor. The columnar structure guides the light such that the point spread function is sharper than with powedered phosphor. 18

2.11 Concept of a flat-panel detector, with reference to the indirect CsI detector. 19

2.12 Schematic of the selenium flat panel. Although there are inactive regions as in the indirect detectors, the electric field draws all the charge released to the active regions giving a higher effective fill-factor. 20

3.1 X-ray images of the (a) TORMAM, (b) TORMAX and (c) CDMAM. . 23

3.2 Geometric setup for MTF measurement. 27

3.3 The MTF calculated by each of the algorithms assessed by Samei et al[7] for the noise free simulated edge image (Image 7) and the simulated edge image with noise (Image 8). Algorithms A - F are published algorithms by a range of authors as outlined in the text. Taken from Samei et al[7] 29

3.4 A range of MTFs acquired by Rivetti et al[8]. IMS refers to an a-Se system, GE is a CsI scintillator system, Fuji is a CR system taken in the scan and subscan directions. The scan direction is defined as the direction of the laser as it reads from left to right across the image. The subscan direction is perpendicular to this and is the direction of the plate as it moves along the reader. 30

3.5 MTF of powdered phosphor CR detector compared with needle imaging plate CR. The two systems are both from Agfa as measured from experimentally acquired images. Images were acquired as part of a study of Agfa NIP and MM3 systems found in a report by NHSBSP[9] 31

3.6 The low frequency drop (LFD) present in the MTF due to scattering material[10] in the set up 32

3.7 A comparison of the effects of background trend removal techniques on NPS estimation, using a synthesized data set from Williams et al[11]. The NPS is presented with no background trend applied to the synthetic data (diamonds), with background trend added but no removal technique applied (squares), with a 2D second order polynomial fit to the data (triangles), and a low-pass filtered version of the data (crosses). 36

3.8 (a) Region obtained from a uniform image, acquired with an anti-scatter grid in place. (b) The 2D NNPS for region shown in (a). (c) The same region obtained from a uniform image, acquired without an anti-scatter grid in place. (d) The 2D NNPS for the region shown in (c). Figure is from Marshall's publication[12] 37

3.9 A photograph image of a CDMAM test object phantom. Multiple X-ray exposures of this test object is made for assessment of the digital mammography system at various X-ray settings. 38

3.10 Two contrast-detail curves for the average of two human observers and CDCOM, plotting threshold gold thickness against disc diameter for the same set of CDMAM images. Results were derived from a previous study[13] 41

3.11 The effects of MTF upon the contrast-detail curve. A *superior* MTF would cause the gradient of the contrast-detail curve to become shallow. However, a *poorer* MTF would cause the gradient of the contrast-detail curve to increase. The contrast-detail curve was derived from images acquired in a study as part of the NHSBSP technical report[14]. 42

3.12 Contrast detail curves for the same system using different doses. Contrast detail curves were derived from images acquired in a study as part of the NHSBSP technical report[15] 42

3.13 Schematic diagram showing the overlap between decision variable histograms of case images with truly positive and truly negative populations. Variation of the threshold value will change both sensitivity and specificity. Applying a lower threshold value results in the fraction of true positives (TPF) will be higher but the false negative fraction (FNF) will decrease (higher sensitivity) . A lower threshold value will reduce the fraction of true negatives (TNF) and increase the false positive fraction (FPF) (lower specificity). 45

4.1 Detector response of the three systems used in this study. Note that the Hologic Selenia system has an offset shown in (a). (b) shows the detector response for the GE Essential system.(c) and (d) show the detector response for the Agfa CR system before and after the images were linearised as in Equation 4.4. 52

4.2 Flow chart illustrating the process to simulate resolution properties of digital mammography system images. An idealised image is created (as described below) and filtered with the MTF filter in the frequency domain. The MTF filter described here is derived from the detector presampled MTF. The inverse Fourier transform of this resultant image is resampled to the pixel size representing the digital mammography system to be modelled. 53

4.3 Experimental presampled MTF in horizontal and vertical directions for digital mammography systems modelled. 54

4.4 Examples of the Gaussian curve (red) fitted to the measured MTF data (blue o), extrapolated to show the model tapers to zero. 56

4.5 Neighbourhood averaging of pixels in $I_B(x, y)$ into $I_{B,R}(x, y)$ 57

4.6 The experimentally measured MTF (blue curve) plotted against presampled MTFs measured from synthetic edge images. The synthetic edge resampled at 5:1 ratio is shown in red and the synthetic edge resampled at 10:1 is shown in green. 58

4.7 Presampled MTF measured from a sharp edge image of $10\mu m$ pixel size. The data falls to zero at the Nyquist frequency for the subpixel sampling of $1\mu m$. 59

4.8 MTF profiles derived from synthetically derived edge images compared with the experimentally acquired counterparts. 60

4.9 The modelled intrinsic MTF (blue curve) was used to filter a $7a$ pixel edge image and the resultant measured presampled MTF (green data points) was compared with the theoretical presampled MTF (red curve). 64

4.10 The measured presampled MTF was used to filter an edge image sampled at $5a$. The theoretical MTF for system B is shown in red. Different sinc functions were applied to the presampled MTF for filtering the $5a$ edge image, denoted in brackets. 65

4.11 Presampled MTFs acquired from an edge image from the Hologic Selenia system (green) and GE Essential system (red). The edge image from the Hologic Selnia system was filtered and resampled to appear as if acquired on the GE Essential system and the presampled MTF measured (blue). 66

4.12 The effects of resampling before or after the filtering stage in an image simulation chain for a clinical edge image. 66

4.13 Effects of the sinc function on the presampled MTF. (a) is the presampled input MTF, (b) is the 2D sinc function corresponding to the original sampling of the presampled MTF, (c) is the resultant MTF filter after division of the input MTF by the sinc function. A clearer idea of the effects is shown in the profile in (d) for the Hologic system.(e) reiterates this point with an example for the GE Essential system. 68

4.14 An example of the synthetic MTF derived from a Hann windowed MTF filter (blue points) compared with that derived from a Gaussian modelled MTF filter (red points). Both MTFs have been compared with the experimentally acquired MTF to be modelled (solid green curve). 69

4.15 Flow chart to depicting the process to simulate the noise properties of digital mammography images. 70

4.16 (a) Sample ROIs defined within the uniform PMMA image for NNPS measurement. (b) Profile across the ROI before and after correction for the residual heel effect. 71

4.17 (a)2D NNPS illustrating the spikes in the x and y axis and 45°. (b) shows the NNPS in the x, y and 45° axes (blue, red and green respectively). . 72

4.18 Measuring the mean-variance relationship. 73

4.19 Radial NNPS of experimental (solid lines) compared to simulated (points) images for six doses for the Hologic Selenia. 76

4.20 The radial NNPS for the GE Essential system. Solid curves show the radial NNPS of experimentally acquired images, circular points show the radial NNPS of the synthetic images. Doses correspond to those detailed in Table 4.4. 77

4.21 Comparison of radial NNPS from experimental (blue, green and orange curve) and simulated (red circles) images for the Agfa CR system. The doses (from top down) are 16.8, 50.2, 102.7, 204 and 504 μGy. 79

4.22 Radial NNPS of images simulated at 44.8μGy from different doses. The experimental NNPS is shown in the bold solid curve for comparison. . . 79

5.1 Set up for the acquisition of a CDMAM image 85

5.2 The CDMAM phantom binary template created from thresholding an X-ray image of the test phantom. 86

5.3 ROIs used for measuring the pixel value within the discs and local background. 87

5.4 Comparison of the measured (solid blue curve) contrast-thickness relationship with the analytical model (dashed red curve) for the same beam quality (32kVp, Mo/Rh). The red error bars indicate the 10% error associated with the analytical model, whereas the dark blue error bars give the standard mean error for the measured data. 89

5.5 Illustration of the distances used to locate each disc, from central to central disc and from central to eccentric disc. Each pixel was equivalent to 70μm. 91

5.6 The image simulation framework to synthesise an image with the resolution and noise properties of a user-defined digital mammography system. $I_{B,R}$ is the blurred, resampled image whilst $I_{N,S}$ is the scaled, noise image. 93

5.7 Contrast detail curves resulting from one set of images scored by (a) CDCOM scoring unaltered compared with human observers, (b) CDCOM scoring fitted to predict human scoring implementing Young et al's[16, 17] methodology compared to the same human observer scoring results from (a). 95

5.8 (a) Illustrates the intersections of the grid within the CDMAM image. (b) Calculation of the corner disc coordinates in relation to the central discs from adjacent cells. The distance between the central disc (large red circle) and the eccentric disc (small red circle) is approximately one third of the distance between the central discs of adjacent cells. 98

5.9 Example of the search area construction (a) Original cell in CDMAM phantom (b) Diagrammatic of a CDMAM cell. Border shows cell eroded to 85% of the cell area, to avoid grid lines. Placement of five search areas within the cell is shown with dark squares. 99

5.10 Comparison of 0.25m diameter disc in an experimentally acquired and synthetic CDMAM images. Images on the left show the experimentally acquired and image on the right show the synthetic. (a) and (b) show the disc for the Hologic Selenia system for 3.37mGy MGD. (c) and (d) show the disc for the GE Essential system for 4.16mGy MGD. (e) and (f) show the disc for the Agfa CR system for 3.35mGy. 100

5.11 Comparison of the contrast-detail curves for experimental (a) and synthetic (b) images for the Hologic Selenia system. Error bars denote two standard errors of mean. 101

5.12 (a)Direct comparison of the contrast-detail curves for experimental (solid) and synthetic (dashed) images for the Hologic Selenia system at each dose. (b) R_{d_i} for each dose. Error bars denote two standard errors of mean. 102

5.13 Comparison of the contrast-detail curves for experimental (a) and synthetic (b) images for the GE Essential system. Error bars denote two standard errors of mean. 103

5.14 (a)Direct comparison of the contrast-detail curves for experimental (solid curves) and synthetic (dashed curves) images for the GE Essential system at each dose.(b) R_{d_i} for each dose. Error bars denote two standard errors of mean. 104

5.15 Comparison of the contrast-detail curves for experimental (a) and synthetic (b) images for the Agfa CR system. Error bars denote two standard errors of mean. 106

5.16 (a)Direct comparison of the contrast-detail curves for experimental(solid curves) and synthetic (dashed curves) images for the Agfa CR system at each dose. (b) R_{d_i} for all doses. Error bars denote two standard errors of mean. 107

5.17 Red cells denote the cells that were used for CNR measurements 108

5.18 (a) CDF measured from experimentally acquired and synthetically generated images for the Hologic Selenia system.(b) CNR measured from experimentally acquired and synthetically generated images for the Hologic Selenia system. Solid curves show lines of best fit for experimentally acquired images and dashed curves represent the lines of best fit for synthetically generated images. Error bars denote two standard error means 109

5.19 (a) Contrast measurements for all doses, from synthetic and experimentally acquired images, for the Hologic Selenia system. Error bars show two standard errors of mean. (b) Standard deviation measurements local to discs measured in (a), from synthetic and experimentally acquired images (dashed and solid lines respectively). 110

5.20 (a) CDF measured from experimentally acquired and synthetically generated images for the GE Essential system.(b) CNR measured from experimentally acquired and synthetically generated images for the GE Essential system. Solid curves show the lines of best fit for experimentally acquired images and dashed curves represent the lines of best fit for synthetically generated images. Error bars denote two standard error means 111

5.21 (a) Contrast measurements for all doses, from synthetic and experimentally acquired images, for the GE Essential system. (b) Standard deviation measurements local to discs measured in (a), from synthetic and experimentally acquired images (dashed and solid lines respectively). . . 112

5.22 (a) CDF measured from experimentally acquired and synthetically generated images for the Agfa CR system.(b) CNR measured from experimentally acquired and synthetically generated images for the Agfa CR system. Solid curves show the lines of best fit for experimentally acquired images and dashed curves represent the lines of best fit for synthetically generated images. Error bars denote two standard error means 113

5.23 (a) Contrast measurements for all doses, from synthetic and experimentally acquired images, for the Agfa CR system. (b) Standard deviation measurements local to discs measured in (a), from synthetic and experimentally acquired images (dashed and solid lines respectively). Error bars denote two standard error means. 114

6.1 Schematic of the contributing factors to spatial intensity variation in mammography. The differing path lengths a to a' leads to an inhomogenous intensity beam exiting the X-ray tube, this phenomena is known as the heel-effect. Path obliquity is demonstrated by the differing path lengths within the object, t compared to t' would lead to greater attenuation at the point under t'.SID is the source-to-imager distance. Image taken from [18]. 118

6.2 An example of the heel-effect upon the contrast of a set of identical discs on a uniform background. (a) shows the X-ray image and (b) shows the 3D plot of the same image[19]. The sharp artefact in the right hand side of the image is a pointer. 119

6.3 (a)The results of a simulation of a 4cm slab of PMMA with 28kVp spectrum. The curves show the individual effects of the inverse-square law, path obliquity with and without the compression paddle and all effects including the heel-effect. All curves were shifted to provide the same signal intensity at the chest wall. (b) Experimental profile results of a 4cm slab of PMMA with 28kVp spectrum. The profiles are shown with and without correction with mean and standard deviations [18]. . . 121

6.4 (a)Flat field image presented as a surface with its histogram and profile along the anode-cathode axis (solid line) and perpendicular to this axis (dotted line). (b) Averaged profile (dotted line) and the fitted model (solid line) of the flat field image. The subimage presents the fitted model as the white grid overlaid on the rendered surface of the flat field image. (c) Surface, histogram and profile of the corrected flat field image. (d) same as (a) for the hand image. (e) same as (b) for the hand image. (f) same as (c) for the corrected hand image. Image taken from [20]. . . 122

6.5 Profile taken of the heel effect masks derived using median filter kernels of size 150x150, 200x200 and 300x300 pixels.(a) shows the profile across the image. (b) shows a cropped region of (a) for clarification on the rippling effect. 125

6.6 (a) An experimentally acquired CDMAM image for the Hologic Selenia system. (b) A simulated CDMAM image with heel effect mask applied for the same system. The yellow lines show the location of the profiles taken for comparison in (c). There are sharp spikes in the profiles relate to the grid lines in the CDMAM phantom image. Polynomial fits to the experimental and simulated data are shown in red and green for clarity. 126

6.7 Normalised heel-effect masks implemented for each system. The smudge in the corner of (a) is an artefact from implementation of the median filter upon a high pixel intensity value object in the corner of the CDMAM phantom image. This does not affect the analysis of the CDMAM phantom image. There is a blur in the heel effect mask for (a) due to the presence of a high pixel intensity object in the corner of the original CDMAM image (an image identifier). It was possible to acquire the CDMAM images for GE and Agfa systems without the identifier present. 127

6.8 A 2D representation of the variance in a uniform image from a CsI scintillator detector. High variance is represented by white pixels whilst the low variance is shown in black. The chest wall of this image is at the bottom. 128

6.9 An example of disc details simulated with differing CNR levels. 129

6.10 (a)The surface plot (black) modelled on the variance image (blue points) created from the GE Essential system. (b-d) shows profiles from the chest wall to the nipple side of the variance image at three profiles along the perpendicular direction of the image. The red curve is the 2D polynomial fit to the variance image (blue). 131

6.11 Detailed flow chart of the noise creation framework with alterations to include the variance map. The variance map is applied before the noise image is scaled to the mean-variance relationship to account for the relative change in variance across the detector. 132

6.12 (a)MTF_{geo} for differing focal spot sizes and magnification of 1.08. (b) MTF_{geo} for different magnifications and focal spot size of 0.3mm. 133

6.13 The image simulation framework with all non-uniformity considerations included. New additions to the image simulatio framework are shown in light blue. 134

6.14 (a)Comparison of contrast detail curves for experimental and synthetic CDMAM images with heel-effect mask, variance map and geometric magnification applied for the Hologic Selenia system. (b) gives the ratio of the contrast-detail curves shown in (a). Error bars denote the standard deviation of the data. 136

6.15 (a)Comparison of contrast detail curves for experimental and synthetic CDMAM images with heel-effect mask, variance map and geometric magnification applied for the GE Essential system. (b) gives the ratio of the contrast-detail curves shown in (a). Error bars give the standard deviation of the data. 137

6.16 (a)Comparison of contrast detail curves for experimental and synthetic CDMAM images with heel-effect mask, variance map and geometric magnification applied for the Agfa CR system. (b) gives the ratio of the contrast-detail curves shown in (a). Error bars denote the standard deviation of the data. 138

6.17 (a) Experimentally acquired and (b) synthetically generated CDMAM phantom images for the Hologic Selenia system at the highest dose for 28kVp MoRh beam quality. 140

6.18 (a) Experimentally acquired and (b) synthetically generated CDMAM phantom images for the GE Essential system at the highest dose for 28kVp MoRh beam quality. 141

6.19 (a) Experimentally acquired and (b) synthetically generated CDMAM phantom images for the Agfa CR system at the highest dose for 28kVp MoRh beam quality. 142

6.20 Surface plots of S/P for the three systems modelled (a) Hologic Selenia (b) GE Essential and (c) Agfa CR. The orientation is such that the chest wall to anode is from the left to rightof each plot. 146

6.21 (a)Contrast-detail curves for experimental CDMAM images and synthetic CDMAM images with all non-uniformity considerations applied with the scatter model included for the Hologic Selenia system. (b) Ratio of contrast-detail curves found in (a). Error bars denote 2 standard error means. 148

6.22 (a)Contrast-detail curves for experimental CDMAM images and synthetic CDMAM images with all non-uniformity considerations applied with the scatter model included for the GE Essential system. (b) Ratio of contrast-detail curves found in (a).Error bars denote 2 standard error means. 149

6.23 (a)Contrast-detail curves for experimental CDMAM images and synthetic CDMAM images with all non-uniformity considerations applied with the scatter model included for the Agfa CR system. (b) Ratio of contrast-detail curves found in (a).Error bars denote 2 standard error means. 150

6.24 (a) Standard deviation measured in the local background to the discs for experimentally acquired (solid) and sythetically generated (dashed) images of the Hologic Selenia system. (b) Resulting CNR calculated with new standard deviation measured in (a). Data from experimentally acquired images is shown in solid curves and synthetically generated images is shown in dashed curves. Error bars denote two standard errors of mean. 153

6.25 (a) Standard deviation measured in the local background to the discs for experimentally acquired (solid) and sythetically generated (dashed) images of the GE Essential system. (b) Resulting CNR calculated with new standard deviation measured in (a). Data from experimentally acquired images is shown in solid curves and synthetically generated images is shown in dashed curves. Error bars denote two standard errors of mean. 154

6.26 (a) Standard deviation measured in the local background to the discs for experimentally acquired (solid) and sythetically generated (dashed) images of the GE Essential system. (b) Resulting CNR calculated with new standard deviation measured in (a). Data from experimentally acquired images is shown in solid curves and synthetically generated images is shown in dashed curves. Error bars denote two standard errors of mean. 155

6.27 CDF measured from experimentally acquired and synthetically generated images for the Hologic Selenia system. Error bars denote two standard error means 156

6.28 CDF measured from experimentally acquired and synthetically generated images for the GE Essential system.Error bars denote two standard error means. 157

6.29 CDF measured from experimentally acquired and synthetically generated images for the Agfa CR system. Error bars denote two standard error means 158

7.1 Radial NNPS of experimentally acquired flat-field images (blue) overlaid on synthetically derived flat-field images (red). 162

7.2 (a)Contrast-detail curves for the Holgic system. Dashed lines denote the contrast detail curves for the synthetic images whilst the solid lines denote the experimentally acquired counterparts. Error bars represent two standard error means.(b) Ratio of experimental to synthetic contrast-detail curves shown in (a) 164

7.3 Radial profiles of the NNPS of experimentally acquired flat images at five doses are shown in solid blue lines. The highest dose was used to simulate the synthetic lower dose images. The NNPS for the synthetic images are shown in dashed red lines. 166

7.4 (a)Contrast detail curves obtained from experimentally acquired CDMAM images at different doses (solid curves) and the simulated reduced dose CDMAM images (dashed curves) for the Hologic Selenia system. Four doses (0.34, 0.80, 1.48, 2.95mGy MGD, from top down) were simulated from the highest dose of 5.91mGy. Error bars denote two standard error means.(b) Ratio of contrast-detail curves shown in (a)(experimental to synthetic CDMAM images). 167

7.5 NNPS profiles for the Siemens Novation. (a) NNPS curves are given for (from top down) 0.2, 0.4, 0.7, 1.0, 1.3 and 4.3mGy MGD for the system setup with 3cm PMMA 25kVp Mo/Rh. (b) NNPS curves for (from top down) 0.1, 0.2, 0.4, 0.8, 1.3, 2.5mGy MGD for the system setup with 5cm PMMA 29kVp W/Rh. Blue solid curves show the NNPS profiles for experimentally acquired images and the red dashed curves show the NNPS profiles for the synthetic images. 169

7.6 (a) and (b) show the same cropped region of a mastectomy acquired at 4.3 and 1.0mGy (MGD), respectively. (c) shows the mastectomy sample synthetically dose reduced from 4.3 to 1.0mGy. (d) shows the profiles taken across (b) and (c) to compare the experimentally acquired low dose image with the simulated low dose image. 170

7.7 (Left)Cropped region of mastectomy image set 1 acquired at 1.4, 0.7 and 0.4mGy MGD. (right) Cropped region of mastectomy image acquired at 2.7mGy synthetically dose reduced to the same dose level as shown on the left. 171

7.8 (Left)Cropped region of mastectomy image set 2 acquired at 0.4, 0.2 and 0.1mGy MGD. (right) Cropped region of mastectomy image acquired at 0.6mGy synthetically dose reduced to the same dose level as shown on the left. 172

7.9 (a) and (b) Cropped region of mastectomy image set 3 acquired at 1.3 and 0.2mGy MGD, respectively. (c) Cropped region of mastectomy image acquired at 1.3mGy synthetically dose reduced to 0.2mGy. Some calcifications have been displaced in this image between the two exposures. 173

7.10 (a – d) Radially averaged noise power spectra of a region in sets 1 – 4, respectively, of mastectomy images acquired at different doses and their synthetic counterparts. The dark purple curve represents the highest dose image from which the other low dose images were degraded. Red dashed curves illustrate the NPS of synthetically degraded images whilst the blue solid curves show the NPS of their experimentally acquired counterparts. 174

7.11 An example of the NPS for mastectomy set 2. NPS for the experimentally acquired mastectomy images is shown in red and blue (0.1 and 0.6mGy, respectively). As the high dose image is scaled to $I_{o,sc}$, the resultant NPS (shown in green) overlaps with the experimentally acquired low dose NPS for the low frequencies. However there is insufficient noise in $I_{o,sc}$ to match the low dose image. When the noise is added, the NPS measured for I_{sim} overlaps the experimental NPS for the higher spatial frequencies also. The ratio across all spatial frequencies for this set up was measured to be 1.04. 175

7.12 An example of the NNPS for mastectomy set 4. NNPS profiles from the experimental images are shown in solid blue and the synthetically dose reduced images are shown in dashed red. 176

A.1 Anatomy of the breast (1) Chest wall, (2) Pectoralis muscles, (3) Lobules (containing milk glands), (4) Nipple surface, (5) Areola, (6) Lactiferous duct, (7) Adipose (fatty) tissue, (8) Skin.[21] 184

A.2 An invasive ductal carcinoma (denoted by the *) in the breast image on the right. There is also associated thickening of the skin (white arrows) shown in this digital mammogram.[22] 185

B.1 Direct comparison of the contrast-detail curves for experimental and synthetic images for the Hologic Selenia system at each dose. Results are from Chapter 5. 188

B.2 (a)Contrast detail curves for all simulated doses with the heel effect mask applied for the Hologic Selenia system. Contrast detail curves for the simulated CDMAM images with the heel effect mask applied are presented overlapping the results for experimental and simulated CDMAM images from chapter 5 (b) - (f). 189

B.3 (a)Contrast detail curves for all simulated doses with the variance map applied for the Hologic Selenia system. Contrast detail curves for the simulated CDMAM images with the variance map applied are presented overlapping the results for experimental and simulated CDMAM images from chapter 5 (b) - (f). 190

B.4 (a)Contrast detail curves for all simulated doses with the variance map and heel effect mask applied for the Hologic Selenia system. Contrast detail curves for the simulated CDMAM images with the variance map applied are presented overlapping the results for experimental and simulated CDMAM images from chapter 5 (b) - (f). 191

B.5 a)Contrast detail curves for all simulated doses with the geometric MTF applied for the Hologic Selenia system. (b) - (f) Contrast-detail curves for the simulated CDMAM images with the non-uniformity effects applied are presented overlapping the results for experimental and simulated CDMAM images (with uniform model from the chapter 5. 192

B.6 a)Contrast detail curves for all simulated doses with the heel-effect mask, variance map and geometric MTF applied for the Hologic Selenia system. (b) - (f) Contrast-detail curves for the simulated CDMAM images with the non-uniformity effects applied are presented overlapping the results for experimental and simulated CDMAM images (with uniform model from the chapter 5. 193

B.7 a)Contrast detail curves for all simulated doses with the heel-effect mask, variance map and geometric MTF applied for the Hologic Selenia system. (b) - (f) Contrast-detail curves for the simulated CDMAM images with the non-uniformity effects applied are presented overlapping the results for experimental and simulated CDMAM images (with the all non-uniformity effects shown in Figure B.6). 194

B.8 Direct comparison of the contrast-detail curves for experimental and synthetic images for the GE Essential system at each dose. 195

B.9 (a)Contrast detail curves for all simulated doses with the heel effect mask applied for the GE Essential system. Contrast detail curves for the simulated CDMAM images with the heel effect mask applied are presented overlapping the results for experimental and simulated CDMAM images from chapter 5 (b) - (f). 196

B.10 (a)Contrast detail curves for all simulated doses with the variance map applied for the GE Essential system. Contrast detail curves for the simulated CDMAM images with the heel effect mask applied are presented overlapping the results for experimental and simulated CDMAM images from chapter 5 (b) - (f). 197

B.11 (a)Contrast detail curves for all simulated doses with the heel effect mask and variance map applied for the GE Essential system. Contrast detail curves for the simulated CDMAM images with the heel effect mask applied are presented overlapping the results for experimental and simulated CDMAM images from chapter 5 (b) - (f). 198

B.12 (a)Contrast detail curves for all simulated doses with the geometric MTF applied for the GE Essential system. (b) - (f) Contrast-detail curves for the simulated CDMAM images with non-uniformity effects applied are presented overlapping the results for experimental and simulated CDMAM images(with the uniform model from Chapter 5. 199

B.13 (a)Contrast detail curves for all simulated doses with the heel effect mask, variance map and geometric MTF applied for the GE Essential system. (b) - (f) Contrast-detail curves for the simulated CDMAM images with non-uniformity effects applied are presented overlapping the results for experimental and simulated CDMAM images(with the uniform model from Chapter 5. 200

B.14 (a)Contrast detail curves for all simulated doses with the heel effect mask, variance map and geometric MTF applied for the GE Essential system. (b) - (f) Contrast-detail curves for the simulated CDMAM images with non-uniformity effects applied are presented overlapping the results for experimental and simulated CDMAM images(with the all non-uniformity effects shown in Figure B.13) 201

B.15 Direct comparison of the contrast-detail curves for experimental and synthetic images for the Agfa Needle-IP system at each dose. 202

B.16 a)Contrast detail curves for all simulated doses with the heel effect mask applied for the Agfa CR system. Contrast detail curves for the simulated CDMAM images with the heel effect mask applied are presented overlapping the results for experimental and simulated CDMAM images from chapter 5 (b) - (d). 203

B.17 (a)Contrast detail curves for all simulated doses with the variance map applied for the Agfa CR system. Contrast detail curves for the simulated CDMAM images with the heel effect mask applied are presented overlapping the results for experimental and simulated CDMAM images from chapter 5 (b) - (d). 204

B.18 (a)Contrast detail curves for all simulated doses with the heel effect and variance map applied for the Agfa CR system. Contrast detail curves for the simulated CDMAM images with the heel effect mask and variance map applied are presented overlapping the results for experimental and simulated CDMAM images from chapter 5 (b) - (d). 205

B.19 (a)Contrast detail curves for all simulated doses with the geometric blurring applied for the Agfa CR system. Contrast detail curves for the simulated CDMAM images with the heel effect mask and variance map applied are presented overlapping the results for experimental and simulated CDMAM images from chapter 5 (b) - (d). 206

B.20 (a)Contrast-detail curves for all simulated doses with the heel-effect mask, variance map and geometric MTF applied for the Agfa CR system. (b) - (d) Contrast-detail curves for the simulated CDMAM images with the non-uniformity effects applied are presented overlapping the results for experimental and simulated CDMAM phantom images (with the uniform model from the chapter 5 207

B.21 (a)Contrast-detail curves for all simulated doses with the heel-effect mask, variance map and geometric MTF and Monte Carlo derived S/P map applied for the Agfa CR system. (b) - (d) Contrast-detail curves for the simulated CDMAM images with the non-uniformity effects applied are presented overlapping the results for experimental and simulated CDMAM phantom images (with the all non-uniformity effects shown in Figure B.20) 208

List of Tables

2.1 X-ray target/filter materials and their characteristic X-ray and K-edge energies. 13

3.1 Parameters for the NPS methods evaluated in the work by Dobbins[23]. Methods A, B, C represent the methods published by different authors. NOL and OL represent non overlapping and overlapping ROIs used. Detrending refers to the polynomial function fitted to remove the low frequency shape across the image. Data rows averaged indicate how many rows on either side of the u or v axis in the 2D NPS were averaged to give the 1D NPS. 35

3.2 Acceptable and achievable levels published in the European protocol.[24]. Acceptable levels indicate the minimum detection levels, whilst achievable levels indicate the upper limits of detection levels. 39

4.1 Description of the digital mammography systems modelled 51

4.2 Relative difference between experimental and simulated MTF curves at respective spatial frequencies for each imaging system for different ranges up to the Nyquist frequency. Brackets denote the v direction in the Agfa system. 61

4.3 Relative noise measured for the experimental and simulated images for the Hologic Selenia System. A set up of 31kVp W/Rh target/filter settings were used with a variety of tube current-time products to achieve different doses. All simulated images were simulated using the same reference dose. 75

4.4 Relative noise measured for the GE Essential System, for the experimental and simulated images. A set up of 29kVp Rh/Rh target/filter settings, using a variety of tube current-time products to achieve different doses. All simulated images were derived from using the same reference dose. 75

4.5 Relative noise measurements for the Agfa System, for the experimental and simulated images. A set up of 29kVp Mo/Rh target/filter settings were used with a variety of tube current-time products to achieve different doses. All simulated images were generated using the same reference dose. 76

4.6 Revised relative noise measurements for the Agfa System, for the experimental and simulated images using the mean-variance relationship developed in Equation 4.35. All simulated images were simulated using the same reference dose. 78

5.1 Relative differences in C_{obs} and C_{fit} of gold discs in the CDMAM phantom for the 29kVp RhRh beam quality compared with C using Equations 5.10 and 5.11. Measured C for each disc thickness is compared with analytically calculated C_p. C_{obs} was derived from Equation 5.9 90

5.2 Settings for the CDMAM images acquired experimentally. 94

5.3 Disc diameter at which CDF(0.5) was found for all systems modelled, for synthetic and experimentally acquired images. Error denotes standard error mean. 108

6.1 Ratios of experimental to synthetic threshold gold thickness $R_{d_{all}}$ averaged across all doses used in each study for the Hologic Selenia system. 134

6.2 Ratios of experimental to synthetic threshold gold thickness $R_{d_{all}}$ averaged across all doses used in each study for the GE Essential system. . . 135

6.3 Ratios of experimental to synthetic threshold gold thickness $R_{d_{all}}$ averaged across all doses used in each study for the Agfa CR system. 135

6.4 Ratios of experimental to synthetic threshold gold thickness $R_{d_{all}}$ averaged across all doses used in each study. 147

7.1 Settings used for acquiring CDMAM phantom images, beam quality was maintained at 31kVp Mo/Rh. Tube current time product and mean glandular dose (for an equivalent 50:50 fatty:glandular 6cm thick breast) are shown for each set of images. 162

7.2 Beam quality, Tube current time product and mean glandular dose settings for each mastectomy sample set. Doses in brackets denote the highest dose image from which the other low dose images were derived. 168

C.1 Ratios of a selection of disc contrasts for 29kVp Rh/Rh GE Essential system before and after different factors such as the receptor efficiency, ε; compression paddle; HVL matching were modeled. Effects of combining all factors have been shown in the last column. 210

Abbreviations and Acronyms

a-Se - amorphous Selenium
AEC - Automated Exposure Control
CNR - Contrast to Noise ratio
CR - Computed Radiography
CsI - Caesium Iodide
DQE - Detected Quantum Efficiency
DM - Digital Mammography
DR - direct radiography
EAKS - Entrance Air Kerma at Surface of detector
ESF - edge spread function
FFT - fast Fourier transform
IFFT - inverse fast Fourier transform
IEC - International Electrotechnical Commission
LSF - Line Spread Function
MGD - mean glandular dose
MTF - Modulation Transfer Function
NHS - National Health Service
NHSBSP - National Health Service Breast Screening Programme
NPS - Noise Power Spectrum
NNPS - Normalised Noise Power Spectrum
NTF - noise transfer function
PMMA - polymethyl methacrylate
PSF - Point Spread Function
QAS - Quantitative Assessment Software
ROC - Reciever Operator Characteristics
ROI - region of interest
SFM - Screen Film Mammography
SNR - Signal to Noise ratio
TFT - Thin Film Transistors

Chapter 1

Introduction

Breast cancer accounted for 10.9% of all cancers worldwide in 2008[25] and is now more prevalent in developed countries than developing countries. In 2002, there were over 80 per 100,000 new cases in developed countries compared with less than 30 per 100,000 new cases for developing countries[1]. Breast cancer is also the most prevalent form of cancer in the UK and in 2007, there were 45,700 new cases diagnosed of which 1% of these were accounted for by men.

Early diagnosis of breast cancer is an important factor in reducing patient mortality, reducing the need for drastic treatment and reducing the risk of developing secondary cancers due to metastasis. Consequently, there is also a greater increase in patient quality of life. Despite the numerous new cases of breast cancer in females worldwide, early diagnosis through breast cancer screening programmes and modern treatment facilities resulted in lower mortality rates in developed countries than in developing countries during 2002 as shown in Figure 1.1.

The effect of this relationship can be demonstrated by Figure 1.2 which illustrates UK breast cancer incidences and the corresponding mortality rates before and after the introduction of the UK National Health Service's Breast Screening Programme (NHSBSP) (vertical dashed line). While mortality rates remain stable, and incidence rates demonstrate a small increase, in the years prior to the introduction of the NHSBSP, Figure 1.2 reveals a sharp rise in incidence rates, coupled with a reduction in mortality rates, after the introduction of the screening programme[2].

Breast cancer screening typically uses the X-ray mammography technique as this is currently the gold standard in screening for breast cancer. While many centres have replaced conventional X-ray imaging facilities with digital technology, few have done so with mammography due to the challenges of cancer detection. The high contrast and resolution required to accurately visualise breast cancer signatures, in addition to high capital cost and uncertainty over the most appropriate technology, has resulted in many hospital opting to retain screen-film technology.

It is one of the last medical imaging modality to 'go digital' and the main reason for this are the challenges faced in screening for breast cancer. These challenges will be discussed within this chapter with regards to the requirements of imaging the breast for effective cancer detection.

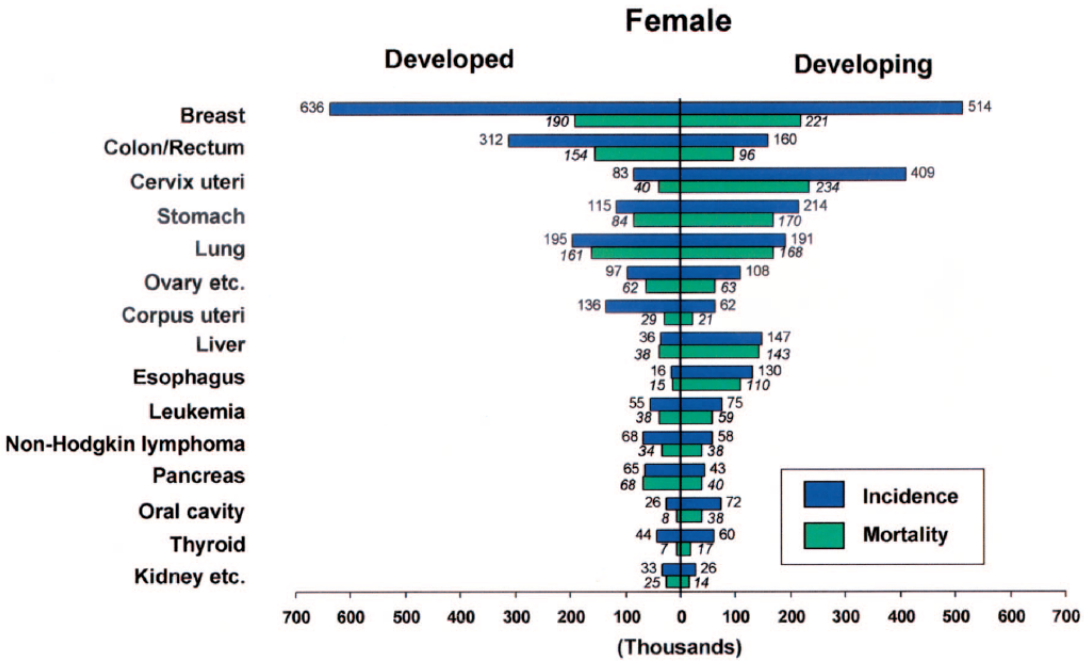


Figure 1.1: Incidence and mortality of different types of cancer in women worldwide in 2002[1].

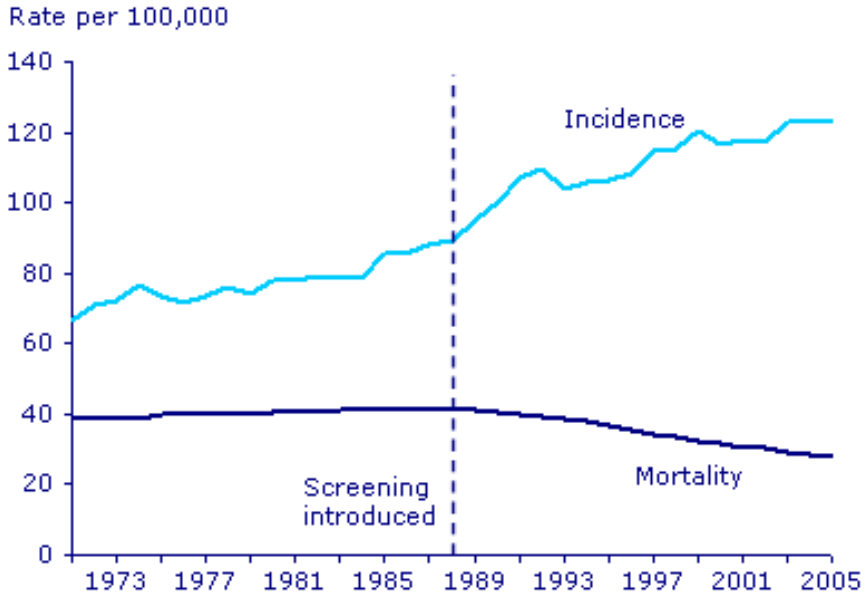


Figure 1.2: Incidence and mortality of different types of cancer in women in the UK between 1971 to 2005. Taken from National Statistics[2].

1.1 Screening for Breast Cancer

1.1.1 The UK National Health Service's Breast Screening Programme

The NHSBSP was established in response to the Forrest report in 1986[26], to reduce the mortality rates of breast cancer. Screening was implemented using the gold standard of traditional film-screen mammography systems in conjunction with clinical or self breast examination. Screening was offered to women between the ages of 50-64 years of age, aiming to detect cancer early in the 'at-risk' age group. Subsequent screenings are offered every three years hence, in contrast to the US protocol of annual screening. This reflects the compromise between cost to the NHS, radiation dose given in a life time to a patient and benefit of early detection of breast cancer. The success of the NHSBSP was initially dampened as the incidence rates were higher than predicted figures. However, predicted figures for the NHSBSP for interval cancers (cancers diagnosed between screening visits of three years) were based on the Swedish Two County Trial. These predicted figures were found to be unrealistically low for the UK, thus the targets were soon revised after 1995[27].

At the turn of the millenium, the NHS Cancer Plan announced plans of increasing the age limit to 70 years of age and employing 2-view mammography at all screenings by 2004. Prior to this, 2-view mammography had only been implemented at the initial screening. This has lead to an estimated 35% reduction in mortality for women with breast cancer who have been screened regularly in England[28].

1.1.2 Requirements of Breast Imaging

In screening, radiologists are tasked to find any signs of cancer from two views of each breast. The systems typically used in NHSBSP are conventional screen-film mammography (SFM) systems. Digital mammography (DM) systems are reserved for symptomatic patients or recalled patients. However, the NHSBSP is now replacing systems with digital technology and currently DM systems account for up to 20% of mammography systems in the screening programme[29]. If there are any suspicious signs of cancerous lesions in the screened images, the patient will be recalled for further tests such as with magnified views on the suspected lesion or biopsy. Figure 1.3 and 1.4 are examples of the two main signs of cancer that radiologists are looking for: masses and microcalcifications.

Masses exhibit similar X-ray attenuation to their local parenchymal tissue, even if the mass distorts the local parenchymal tissue it can be difficult to visualise the lesion and therefore high contrast is needed. For dense breasts, it is more difficult to ascertain the tumour mass from the local parenchymal tissue. With the advent of DM, interpretation of images of dense breasts has become an easier task as the process of acquisition and display have been separated. This allows for separate optimization of the processes to improve this interpretation of the images. However, for contrast between tumourous and healthy tissue, lower doses are necessary. Another requirement of breast imaging is to effectively image the microcalcifications that may be present. Visibility of microcalcifications begin from $100\mu m$ in diameter, thus high resolution is necessary. For

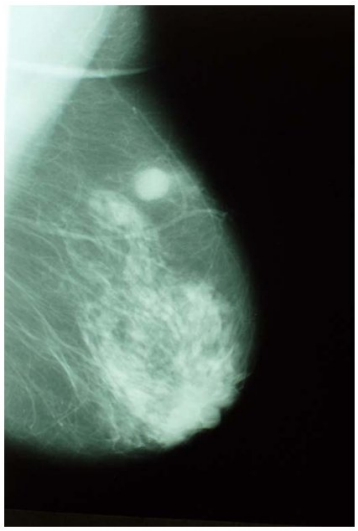


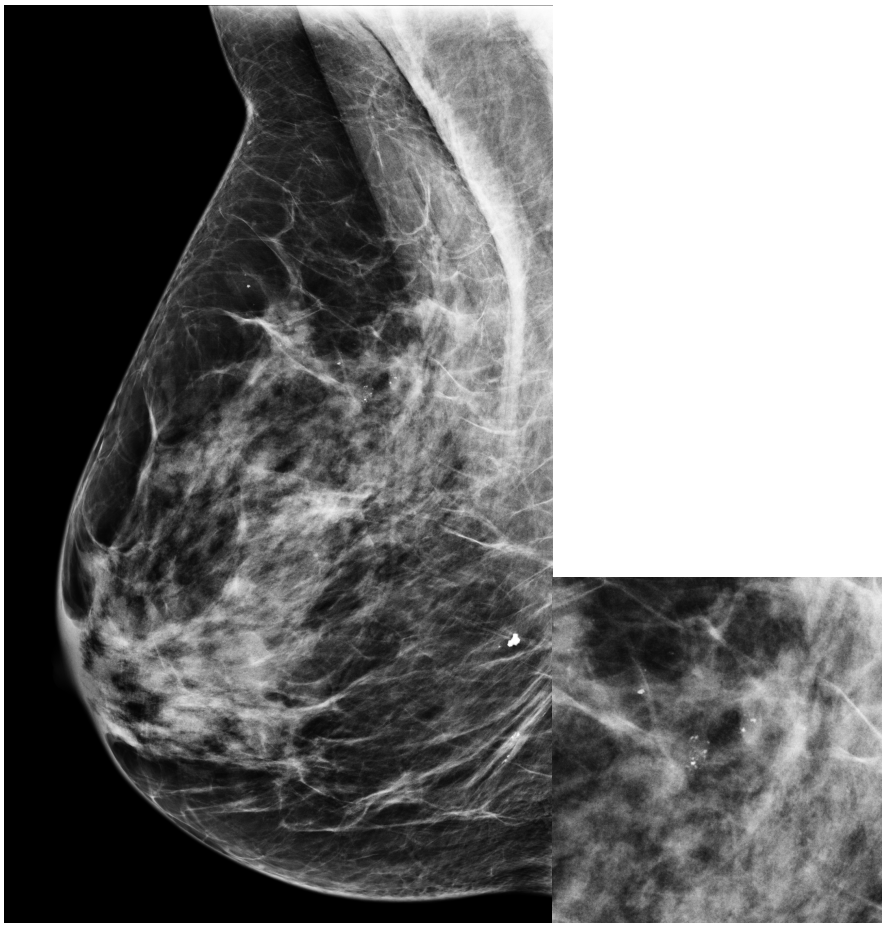
Figure 1.3: An example of a mass in a screen film mammogram. [3].

high resolution, higher doses would be desirable. For this reason, mammography is considered a difficult imaging task. These concepts will be discussed further in Section 2.1.2.

1.1.3 Moving to Digital Technology

Digital technology offers a number of advantages over screen-film technology, such as:

- An infinite number of image copies may be made without degradation to the image quality. With the integration of the Picture Archiving and Communications Systems (PACS), digital images can be conveyed to multiple workstations or even referral centres.
- Storage of patient data is much more efficient. A few months of film images compared to 10 years worth of digital images could be stored in the same space.
- Digital images have wide linear dynamic range. Thus it has been found that digital mammography systems are more effective at imaging thicker, denser breasts. (DMIST clinical trials[30]).
- There are a wide range of digital image processing tools to improve visualisation of mammographic lesions.
- Average dose in DM compared with SFM was found to be 22% less[30].
- Computer Aided Diagnosis software can be implemented to aid radiologists in searching for signs of cancer in images.
- DM yields new opportunities in development of new medical imaging modalities such as contrast-enhanced DM, dual-energy mammography, breast computed tomography (BCT) and and breast tomosynthesis (BT).



(a) (b)

Figure 1.4: (a) An example of microcalcifications in a digital mammogram with Hologic image processing applied. (b) is a magnified region of microcalcifications from (a). Courtesy of St. George's Hospital.

The NHSBSP has been looking to roll out digital mammography technology across the UK. However, as with all new technologies, it is necessary to be able to assess the systems' effectiveness for screening and/or diagnostic imaging.

1.2 Motivation and Aims

Studies comparing the physical performance of DM are numerous. Physical performance can be measured using image quality metrics such as signal-to-noise ratio (SNR), contrast-to-noise ratio (CNR), modulation transfer function (MTF) and noise power spectra (NPS). Image quality metrics such as SNR, CNR, MTF and NPS offer direct comparison of system performances. However, the metrics are measured based on uniform backgrounds and with objects unrealistic to the clinical detection task. A more appropriate performance measure would be with the use of observer based tasks.

To set up a clinical trial to optimise each setting parameter in a DM system would require extensive resources in terms of time and man-power[30]. Alternatively, comparing the efficacy of DM systems in detecting and characterising lesions would need enough lesion-specific images and observers for a statistically powerful study. Approximately 8 cases in a screening population of 1000 may be diagnosed with breast cancer in the NHSBSP[31]. This leads to difficulties in creating a database of sufficient size for a statistically significant study.

To bridge the gap between physical performance measures and image quality metrics that take account of observer performance, simulation methods are becoming powerful tools. Examples of this include generating large data sets[32, 33], focussing optimisation parameters[32, 33] or answering questions that would be difficult to answer with clinical trials such as the effect of resolution and noise on observer performance[34]. Through image simulation, it would possible to compare physical performances of different DM systems by modifying the same image set. It would be otherwise unethical to image the same woman with different DM systems to acquire such data, but simulation methods could provide such means to directly compare the effect of different physical performance characteristics on the same image. To modify such clinical images, it is necessary to understand the image formation process to accurately simulate DM images.

This thesis aims to develop and validate an image simulation framework to simulate DM images that are clinically realistic and physically accurate.

1.3 Thesis structure

In order to compare such technologies in the absence of extensive clincial trials, a method of creating and simulating lesions (masses/ microcalcifications) is needed. These could be inserted into mammograms or computerised breast models. The next stage would be to degrade such images with signal and noise transfer properties of a DM system. The former part of this plan is not within the scope of this work but the reader can find this in [35, 36, 37].

The focus of this thesis is to develop an image simulation tool that can accurately model this degradation of the image. In order to do this, there has been an investigation into the physics of image formation in Chapter 2. This will provide an understanding of the image formation process on the radiographic image that the image simulation framework will need to model.

Analysis of the physical performance of mammography systems is an important aspect of this work which is explored in Chapter 3 extensively with respect to digital systems. Image quality metrics act as descriptors of DM systems and therefore provide an understanding of which metrics are relevant in simulating a radiographic image. However, at present, there is still a need for an image quality metric that has a greater relevance to the clinical environment by describing the performance of DM systems with the inclusion of an observer. This chapter seeks to address image quality metrics, and their relevance, by reviewing current literature while also providing an overview of

commonly used mammography test objects, developed for the purpose of investigating image quality metrics.

As the image quality metrics such as MTF and NPS were found to be effective representations of the physical performance of an imaging system, there has been a number of seminal pieces of work in utilising this image simulation methodology as a non-Monte Carlo image simulation tool. Chapter 4 investigates current image simulation methods. It was found that with image quality metrics, radiographic images could be effectively synthesized without the need for extensive computing resources or specific knowledge of the detector set up. This chapter is split into two parts to assess the simulation of blurring and noise properties for three DM systems. MTF edge images were created to validate the blurring and resampling process of the image simulation chain. Idealised edge images were created and filtered with MTF frequency filters and resampled to specific pixel sizes for the three systems modelled in this study. In addition, the image simulation chain provided a method of validating the effects of image resampling theory. Signal transfer properties of the individual DM systems were used to create flat-field images with the correct exposure and corrupted with the use of NPS descriptors.

The purpose of the image simulation framework will be to provide a means to generate clinically realistic images. Thus the application of signal and noise transfer properties on images of clinical test objects was investigated its effect on detection based tasks. A widely used mammography test object for detection studies is the CDMAM phantom which has a range of gold discs with varying diameter and thickness. Information can be derived from scoring CDMAM phantom images to find the minimum contrast and detail size which can be detected for the system with specific settings. The CDMAM phantom was used for the purpose of validating the image simulation framework in Chapter 5. Creating completely synthetic images has the potential to replace experimentally acquired test object images and provide a way to optimise mammography systems. Preliminary results showed that the synthetic CDMAM phantom images did not exhibit non-uniformity effects present in the experimentally acquired images. Contrast-detail curves were used to assess the CDMAM phantom images further with the use of CDCOM[38] software tool. As CDCOM does not provide information about the discs detected, an automated CDMAM scoring software tool, QAS, was developed in-house for this purpose. With the use of QAS, further investigation into the nature of the CDMAM phantom images showed there were some non-uniformity effects that had not been taken account of in the image simulation framework. Thus non-uniformity effects needed to be modelled in order to create visually realistic and physically accurate DM images which were addressed in Chapter 6.

Four areas of non-uniformity effects were identified to improve the realistic nature of the synthetic CDMAM phantom images: spatial intensity variation, local variance, geometric magnification and scatter. Each non-uniformity consideration was examined individually and combined to develop a more sophisticated simulation framework for CDMAM phantom images.

Clinical test objects have been used to validate the image simulation frame work. However, to provide a meaningful measure of the performance of a DM system with respect to an observer, the study must focus on a more clinically relevant task such as cancer lesion detection and characterisation. Computerised breast models are not currently at

a stage where they may be implemented fully for such studies. The alternative would be to degrade readily available clinical mammograms. It was found in Chapter 4 that the noise simulation model would only be effective for a finite range in which the quantum noise was the dominant source of noise. In Chapter 7 a multiple noise source model was introduced and validated with synthetic flat-field and CDMAM images. This multiple noise source model was developed to degrade clinical images to appear as if acquired at lower doses. This process was applied on experimentally acquired flat-field, CDMAM and mastectomy images and produced excellent synthetic images for direct comparison.

Conclusions will be made in Chapter 8 to summarise findings in this thesis. Further work will also be explored.

1.4 Achievements and Major Contributions

- Chapter 4 presents a methodology to simulate images with the signal and noise transfer properties of three commercial systetms. This work presents the first use of an anisotropic MTF to model the CR system.
- Furthermore, with the development of the image simulation framework, comprehensive theory has been developed to prescribe the correct method of image resampling. This work has been submitted to PMB August.
- Chapters 5 and 6 present a sophisticated and fast method of simulating CDMAM phantom images. Non-uniformity effects such as spatial intensity variation, variance, geometric magnification and scatter were modelled and implemented in such a non-Monte Carlo based image simulation framework for the first time. This work was published in the International Workshop on Digital Mammography 2008 proceedings[39].
- An automated CDMAM scoring software was developed to assess CDMAM phantom images. Valuable information could be obtained about the signal, contrast and noise of discs correctly detected in the CDMAM phantom images. This work was published in the SPIE Medical Imaging proceedings[13].
- A multiple noise source model was developed in chapter 7 to accurately model the level and texture of noise for a given X-ray exposure which can be applied to a wide range of doses, beyond that of the quantum-limited dose range.
- The first study of a dose reduction methodology has been applied on CDMAM and mastectomy images for the purpose of direct comparison. This work will be presented in the International Workshop on Digital Mammography 2010 proceedings [40].

Chapter 2

Review of Mammography

The preceding chapter discussed the motivation for implementing screening for breast cancer. The physics governing the images generated from such mammography systems will also be presented with background information on current digital detector technologies.

2.1 X-ray Mammography

Mammography is a demanding task since it needs to provide sufficient contrast to detect tumour masses which have a similar tissue composition as local breast tissue. In addition, high resolution is needed to identify the presence of microcalcification. Abnormal clusters of microcalcifications are arguably one of the most important indicators of breast cancer, as these are present in 50-70% of malignant tumours of the breast[41]. For this reason, visualisation and differentiation of the shape and distribution of the microcalcification is often seen as key to early detection of breast cancer, which is important in cancer survival. Calcifications vary greatly in morphology, cluster shape and size. Characterisation of these calcifications help diagnose malignancy.

A typical X-ray imaging system is made up of three parts: the X-ray source, the object to be imaged (either breast or test phantom) and the detector. The mammographic unit (Figure 2.1) is designed to allow for easy positioning of the patient's breast from a range of directions. The X-ray tube and breast support plate may be rotated to achieve the desired mammographic projection. An anti-scatter grid is placed between the breast support plate and detector. The detector may be a screen-film cassette or a digital detector and will be discussed further in Section 2.2. During examination, the breast is placed under firm pressure from the plastic compression paddle. An Automatic Exposure Control (AEC) device beneath the detector terminates the exposure once the required signal level is reached in the image.

Production of the X-ray photons, along with their physical interaction within the breast tissue is discussed in Section 2.1.1 to Section 2.1.3. Other design features of the mammography set such as the compression paddle and anti-scatter grid will also be described before a review of the detector technologies.

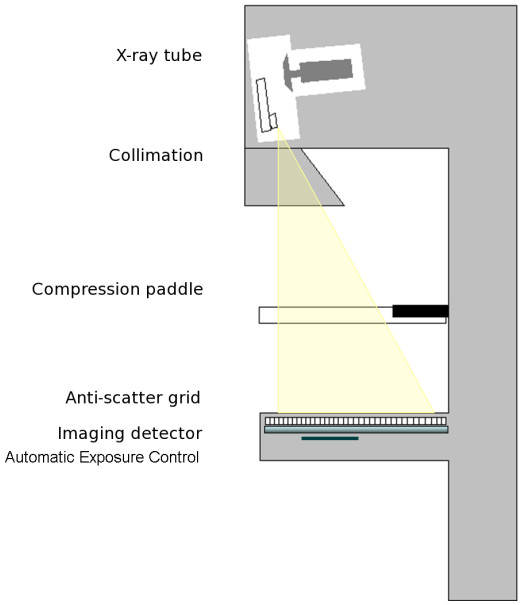


Figure 2.1: Schematic of a typical mammography system.

The compression paddle is used in mammography to reduce the motion blur, patient dose, anatomical structure overlap and scatter whilst improving contrast and visualisation of the breast tissue.

2.1.1 Production of X-rays

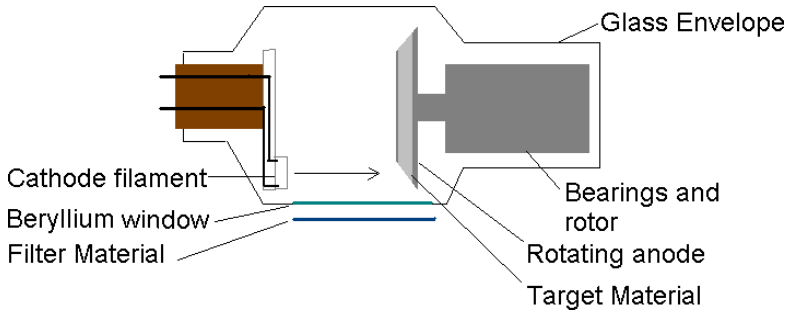


Figure 2.2: Components of an X-ray tube.

The X-ray tube is illustrated in Figure 2.2. As can be seen in Figure 2.1, the X-ray tube is tilted to achieve full field coverage at a given source-to-image distance. In order to obtain high contrast between soft tissue and tumours, the X-ray tube is ordinarily operated at approximately 23-35kVp. During exposure, the cathode filament heats up and electrons are produced. High voltage between the cathode and anode cause the electrons to be accelerated towards the rotating anode. As the electrons strike the anode, energy is lost in one of three processes: (a) Bremmstrahlung, (b) Characteristic X-rays or (c) heat.

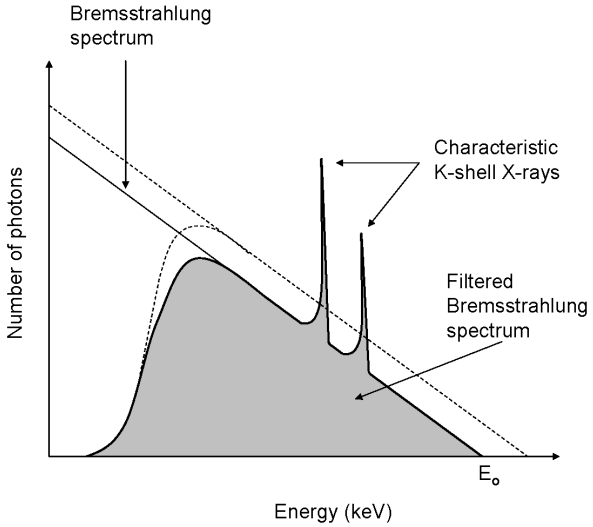


Figure 2.3: An example of an X-ray spectrum. The bremsstrahlung spectrum represents a range of energies, the maximum of which, E_o, is determined by the tube voltage times the electron charge. Filtering removes the low energy photons. The dotted line represents the effect of increasing E_o.

- Bremmstrahlung radiation: This occurs when an accelerated electron is deflected by another charged particle, within the anode in this case. Deflection causes the electron to lose momentum and the energy is released as X-ray radiation. This does not rely on energy states within the anode atom and as such Bremmstrahlung is known to have a continuous energy spectrum. This is highlighted in Figure 2.3.
- Characteristic X-rays: This occurs when the accelerated electron interacts with the inner shell electron of the anode atom nucleus and has an energy that exceeds the binding energy, this causes the inner shell electron to be ejected from its shell. Subsequently, an outer shell electron fills this vacancy and a characteristic X-ray is emitted equal to the difference between the binding energies of the inner and outer shells. This gives the characteristic peaks superimposed on the continuous Bremmstrahlung X-ray spectrum, shown in Figure 2.3.
- Heat: The accelerated electron may strike the outer shell electrons of the anode and thus part of its energy is transferred to the outer shell electron and deposited as heat.

A large amount of the accelerated electron energy is dissipated as heat in the anode; the X-ray tube has an X-ray generation efficiency of only 0.5% at the energies used in mammography. Therefore, cooling of the anode is an important design consideration. One solution is to use a rotating anode to help dissipate this heat. In addition, the anode is tilted over a small angle leading to a larger area of the anode that is hit by electrons. Due to the tilt in the anode, X-rays that are produced will traverse different distances in the anode before it reaches the filter window. This leads to an inhomogenous projected X-ray beam in the anode-cathode direction. This phenomenon is known as the *heel effect*.

2.1.2 X-ray Spectrum

As mentioned earlier, mammography requires very low X-ray energies (compared to other areas of radiology) in order to achieve an acceptable contrast between tumour masses and the surrounding breast tissue. At low energies, the attenuation coefficients for the breast tissues diverge, leading to improved tissue contrast as shown in Figure 2.4. The difference between attenuation coefficients of different breast tissues is thus greatest at the lower photon energies.

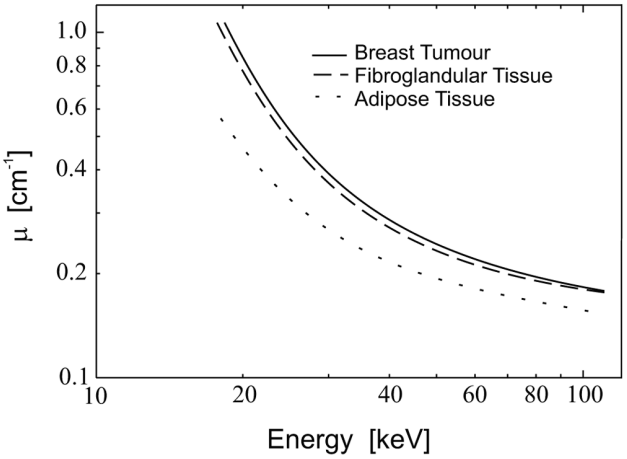


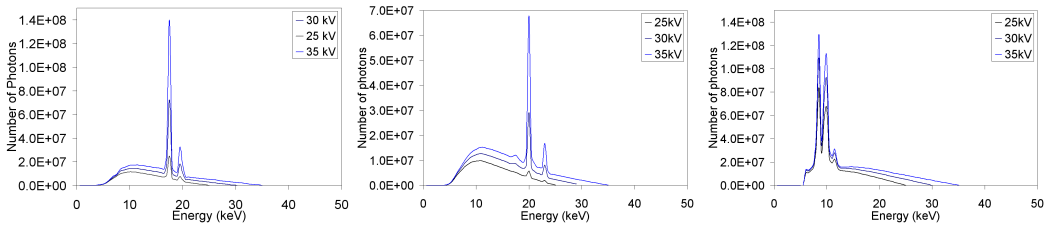
Figure 2.4: X-ray linear attentuation coefficients of fat, fibroglandular tissue and ductal carcinoma for different energies. From Johns and Yaffe[4]

X-ray beam quality is a description of its spectra based on the target/filter material and tube voltage used. Tube voltage controls the energy of the X-ray photons. Peak voltage of the X-ray tube is denoted by 'kVp', which determines the highest energy in the bremmstrahlung spectrum and therefore the quality of the output, as shown in Figure 2.3. Increasing the peak voltage alters the spectrum in two main ways, the maximum energy of the photons increases and the overall intensity of the beam (given by the area under the spectrum, number of photons per unit area) increases also. Increase in energy and number of X-ray photons lead to a greater number of photons passing through the breast tissue to create an image with higher intensity.

Increasing the energy may not be desireable in some cases if the breast is relatively small as the photons may pass straight through without being attenuated. This would reduce the diagnostic usefulness of the image as the image may have lower contrast. Thus, the peak voltage may be increased for patients with denser and thicker breasts to ensure enough X-ray photons are attenuated in the tissue to create an image and are not absorbed in the tissue, dissipating its energy. Entrance dose describes the energy per unit mass (deposited in the tissue) of the incident X-ray beam and is measured in Grays (1Gy=1J/kg).

Molybdenum (Mo), Rhodium (Rh) and Tungsten (W) are typically used in mammography as the target material as their characteristic X-rays are ideal for breast imaging. Their high proton numbers with high melting point make them ideal as target materials in order to cope with the high heat generation associated in X-ray production. For the

same kVp, the X-ray spectrum of Rh are harder than for a Mo target as the energy of characteristic lines is higher for Rh than for Mo. This indicates a higher binding energy and a higher atomic number. Thus, Rh may be used to image thicker and denser breasts. As the proton number of the material increases, the total intensity of photons increases as there is a higher probability of collision between electrons and larger nuclei. In addition, characteristic X-rays will be shifted to higher energies in the spectra. Figure 2.5 illustrates the spectra for different target materials used in mammography.



(a) Molybdenum (b) Rhodium (c) Tungsten

Figure 2.5: Spectra for typical target materials used in mammography [5].

As the X-ray photons leave the tube, these pass through a Beryllium window and an extra filter. The Beryllium window is approximately 1mm in thickness and minimises beam hardening that would otherwise be caused by the glass X-ray tube This allows for a greater control of beam hardening and spectral shaping by the additional filter. Beam hardening removes the lower energy photon, reduces the number of photons that are stopped in the breast tissue, depositing their energy and not contributing to the overall image. The effects on the spectra of this is illustrated in Figure 2.3.

Typically, a mammography unit may have more than one target and/or filter material available to it so that the X-ray spectrum may be varied according to the breast density and size to be imaged. Mammography X-ray spectra are shaped with K-edge filtration. K-edge is the energy level associated with the K-shell of the atom, which leads to a sharp rise in the linear attenuation cofficient. The effect of this is illustrated in Figure 2.6 for a Molybdenum target filtered with Rhodium. The characteristic X-ray emissions are at 17.4keV and 19.6keV, whilst the K-edge of Mo is 20.0keV. This causes the filter to significantly reduce the photon energies above 20.0keV,as the attenuation coefficient rises abruptly at this energy. Table 2.1 shows the energies of the characteristic X-rays for the different materials used in mammography. In the case of W, the lines shown in 2.5c are from the L-shells. Thus the K edge is

Table 2.1: X-ray target/filter materials and their characteristic X-ray and K-edge energies.

Material	K_α (keV)	K_β (keV)	K-edge (keV)
Molybdenum	17.4	19.6	20.0
Rhodium	20.2	22.7	23.3
Tungsten	58.6	67.4	69.4

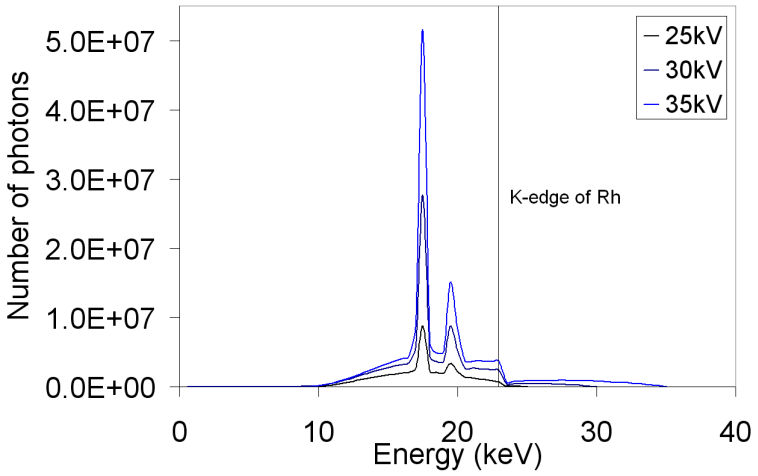


Figure 2.6: Spectra for Molybdenum/Rhodium target/filter material, with the K-edge of Rhodium marked.

2.1.3 X-ray Photon Interactions in Mammography

In the mammographic energy range, there are three main photon interactions: photoelectric effect, coherent and incoherent scattering.

The photoelectric effect occurs when an incident X-ray photon interacts with an electron of an atom. This X-ray photon is completely absorbed and its energy is transferred to the electron, which subsequently escapes the atom. Electron transitions will take place to fill the vacancy left by the electron and a characteristic X-ray is emitted. This is the most dominant interaction at photon energies below 22keV in biological tissue.

Coherent and incoherent scattering refers to whether the energy of the interaction is elastic or inelastic. Coherent scattering will be described first.

Rayleigh scattering is a form of coherent scattering, which involves the scattering of X-rays by atomic electrons. However, in Rayleigh scattering, there is no ionisation as the energy of the scattered X-ray is identical to that of the incident X-ray. The impact of Rayleigh scattering is that the trajectory of the scattered X-ray is different to that of the incident X-ray. Thus, if detected in the imaging plate, this is considered as a scattered photon and is undesirable in terms of contributing to the image creation. Rayleigh scattering is typically a forward-scattering mechanism, especially with increasing energies.

Incoherent scattering is also called Compton scattering, where part of the incident X-ray photon energy is transferred to an outer shell electron of an atom, ejecting the electron from its shell. In addition, a photon is scattered. Compton scattering typically occurs at higher X-ray energies, where the energy of the X-ray photon greatly exceeds that of the binding energy of the atomic electron. Thus, Compton scattering occurs with the outer-shell electrons. In Compton scattering, there is a relationship between fractional energy loss, scattered photon energy E to incident energy E_0, and the scattering angle

θ:

$$\frac{E}{E_0} = \frac{1}{1 + \alpha(1 - cos\theta)} \tag{2.1}$$

where

$$\alpha = \frac{E_0}{m_0 c^2} \tag{2.2}$$

and m_o is the mass of the electron. This implies that the energy of the scattered X-ray photon decreases as the scattering angle increases. Therefore, lower energy photons are more likely to be back-scattered. All the photon interactions are shown in Figure 2.7.

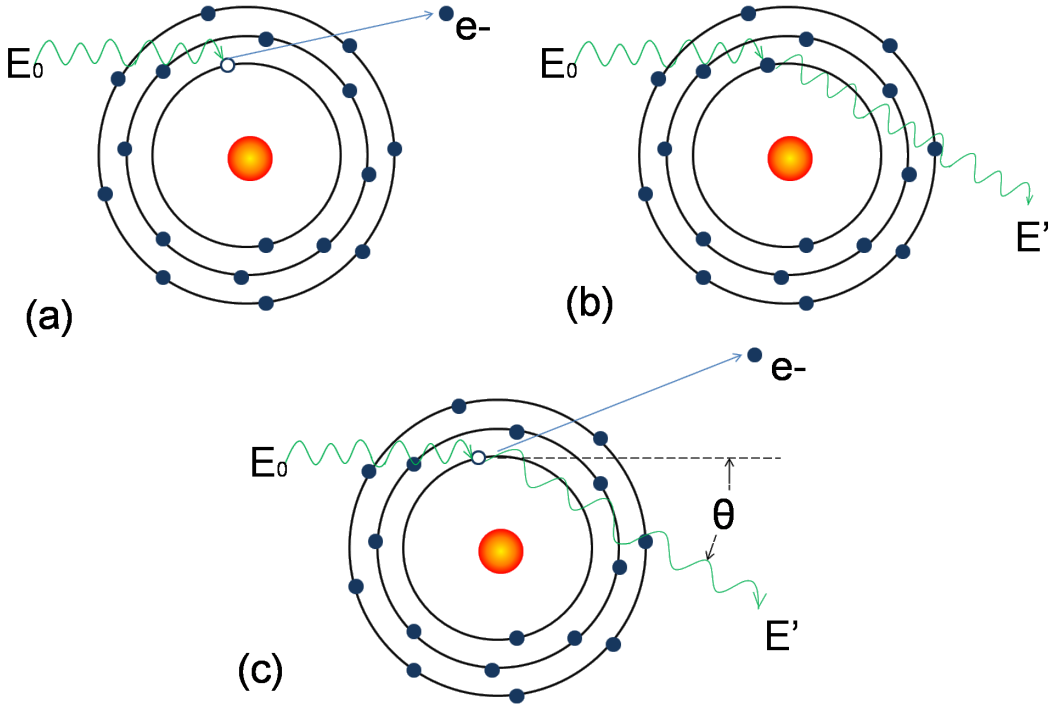


Figure 2.7: (a) Photoelectric effect (b) Rayleigh scattering (c) Compton scattering.

2.1.4 Anti-Scatter Grid

An anti-scatter grid is implemented in mammography as scatter degrades the contrast, signal-to-noise ratio and the dynamic range of the image. Scattered photons arise from secondary interactions in material between the breast and the detector as well as the coherent and incoherent scatter described above. The trajectory of secondary interactions differ from primary X-ray photons and thus are more likely to strike the anti-scatter grid. Different manufacturers may use different grid setups such as linear or cellular (square or hexagonal) structures. The grid is normally oscillated to blur the grid line pattern from the image. Ideally, all primary photons would be transmitted through the grid and all the scattered photons would be absorbed. In reality, 30-45% of the primary photons are attenuated by the anti-scatter grid[42], thus the dose needs to be increased in order to achieve an acceptable image quality. Typically, 80-95% of the scattered photons are absorbed by an anti-scatter grid[42].

2.2 Detector Technology

In recent years, conventional SFM has started to be replaced with DM. At the time of writing, the NHSBSP is still utilising SFM technology. However, DM technology is slowly being rolled out across the nation and is primarily used for symptomatic patients. Due to the large capital cost of DM systems, it is necessary to be confident of the clinical impact of the detector technology in breast screening. The aim of this work is to consider the clinical impact of different DM technologies based on their detector performance. Thus, this review will concentrate on the DM technologies currently available commericially.

Before discussing the different technologies, it is appropriate to explain nomenclature for better understanding of detector performance theory.

Digital detectors are made up of discrete sensing elements (with the exception of CR systems as discussed in the next section) as illustrated in Figure 2.8. The detector elements (del) play a large role in defining the imaging performance of the DM system. The del is, strictly speaking, the pixel aperture, or the 'active region' within a pixel where the photons are detected. Due to spatial requirements of the electronics for each pixel or the septa between pixels, there is also an inactive region. The fill factor describes the ratio of the area of the pixel which is active to that which is inactive.

$$fillfactor = \frac{d^2}{p^2} \tag{2.3}$$

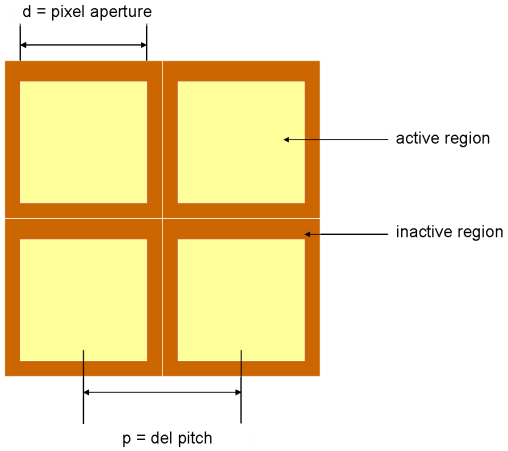


Figure 2.8: A detector element, typically will be made up of active and inactive regions due to electronics. Fill factor, ideally 100%, is found using the ratio of the squared pixel aperture to the squared del pitch.

2.2.1 Computed Radiography (CR)

CR is a form of indirect conversion detector, also known as photostimulable phosphor or storage phosphor systems. Energy from X-ray absorption causes electrons to be

liberated in the phosphor crystal temporarily and are captured and stored in traps within the crystal lattice. The number of filled traps is proportional to the absorbed X-ray signal.

The CR plate is scanned with a red HeNe laser light in a separate reader as shown in Figure 2.9, causing the electrons to be re-excited from their traps. As the electrons return to ground state, energy is emitted in the form of blue light[43]. This process is known as photostimulated luminescence. The amount of blue light emitted and measured by the photomultiplier tube is proportional to the amount of energy absorbed by the phosphor. Spatial coordinates are related to the time at which the laser beam strikes a give location on the CR plate.

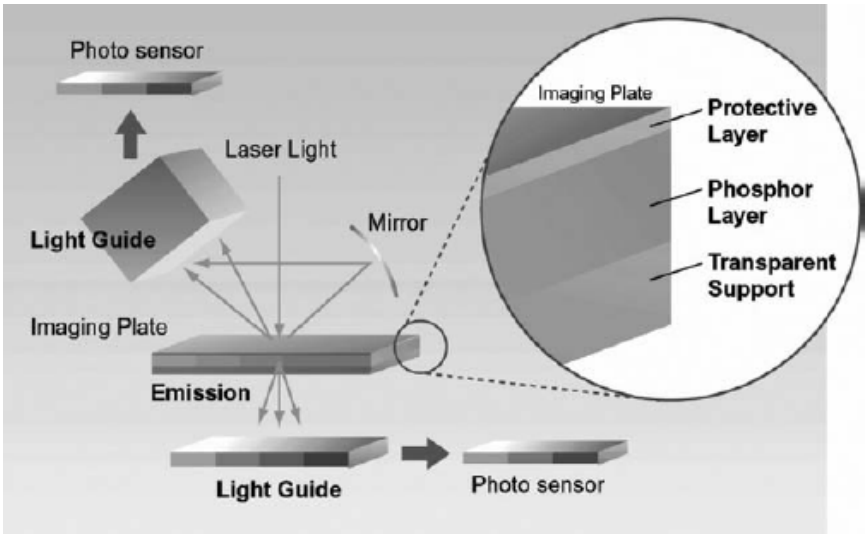


Figure 2.9: Simultaneous dual side reading of a CR plate. Courtesy of Fuji Medical Systems[6].

Spatial resolution in the CR system is determined by the laser beam size (effective del), the phosphor structure, laser penetration and the distance between sample measurements (del pitch). During readout, the laser beam must penetrate into the entire phosphor layer in order to release all the traps. Increasing the layer thickness will increase absorption efficiency of X-ray photons. However, this has an adverse effect, either the power or the dwell time of the laser will need to be increased, which increases the chance of adjacent traps in the phosphor being discharged. Fuji Medical Systems, Konica, Kodak and Agfa Healthcare have been developing CR technology in mammography. A del size of $50\mu m$ as the readout process has been improved with the use of transparent support to enable double-sided readout as shown in Figure 2.9. With a double-sided readout, the thickness of the phosphor is increased in order to absorb the photons, improving the system's efficiency.

CR plates typically use powdered phosphor, which can suffer poor spatial resolution as the light diverges heavily from its point of creation as illustrated in Figure 2.10. More recently, there has been development of needle crystal phosphor technology in mammography which channels the light to reduce lateral spread of light in the phosphor[43].

CR technology is the least expensive in terms of capital cost, as the screen-film cassette in conventional mammography may simply be replaced with a CR plate, which is also reusable.

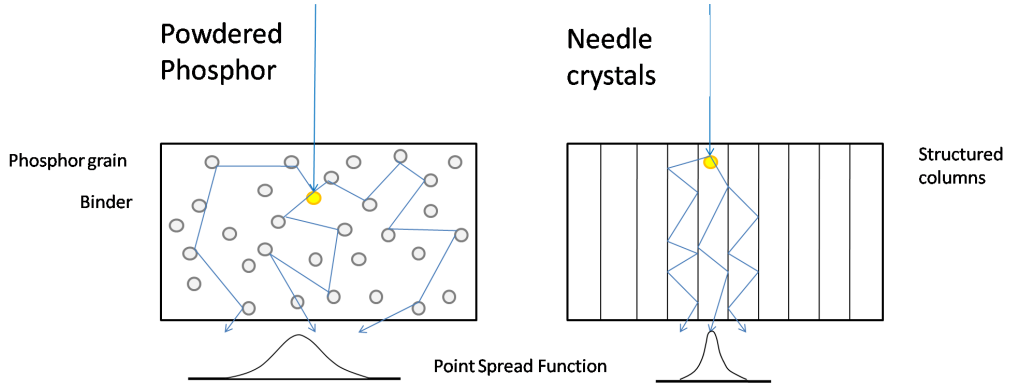


Figure 2.10: An example of how light may be scattered in powdered phosphor compared to needle crystalline phosphor. The columnar structure guides the light such that the point spread function is sharper than with powedered phosphor.

2.2.2 Flat Panel Detectors

An alternative imaging approach utilises an integrated flat panel detector. It is appropriate to describe flat panel detector technology before discussing the indirect and direct detector options. Flat panel detectors use large-area active matrix arrays made of amorphous silicon (a-Si:H) with thin film transistors (TFTs) connected to individual pixel electrodes. One panel consists of two sheets of glass with a uniform layer of liquid crystal, a-Si, in between. One sheet is the active matrix array whilst the other sheet is a uniform electrode layer. There are two main technologies which use flat-panel detectors: scintillator based and solid-state based detectors, also referred to as indirect and direct methods, respectively.

Indirect Detectors

In the indirect method, the amorphous silicon flat-panel is typically covered with Thallium activated Caesium Iodide (CsI(Tl)), the design of which is outlined in Figure 2.11.

As an X-ray photon is absorbed in the phosphor, light is produced. The detector pixel is configured as a photodiode which converts the light produced in the phosphor into charge which is stored in the pixel capacitance. During readout, a thin-film transistor (TFT) switch within each del is activated sequentially in each row by control lines on each column of the detector matrix.

The advantage of CsI phosphor is that it can be grown into columnar crystals, acting as light channels and limiting the light spread as shown in Figure 2.10. This improves the spatial resolution considerably compared to 'settled' phosphor used typically in CR

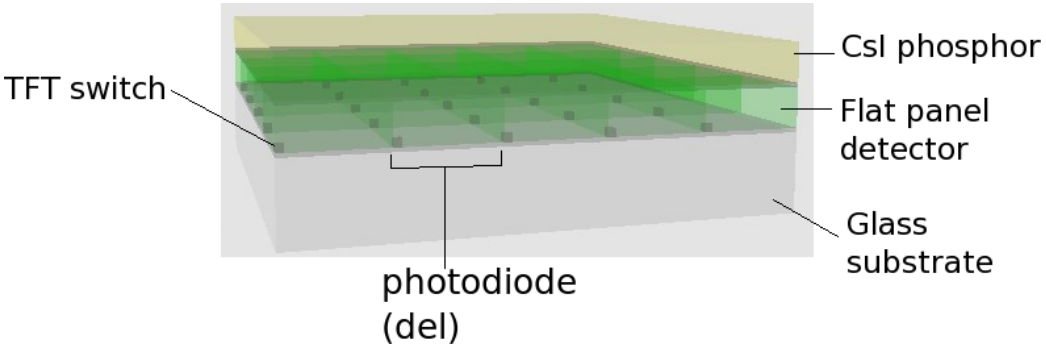


Figure 2.11: Concept of a flat-panel detector, with reference to the indirect CsI detector.

technology. One disadvantage of the indirect method is that each pixel must contain the photodiode, switching device and control and signal lines thus the fill factors is less than 100%. Reducing the del pitch in flat panel detectors increases spatial resolution, however, this will also reduce the fill factor as this increases the inactive area in the del. As such, the current compromise for this is with the use of $100\mu m$ pixel sizes for flat-panel phosphor technology, used by GE healthcare.

Direct Detectors

Direct conversion detectors do not use a phosphor-based X-ray absorber, but instead an amorphous Selenium (a-Se) material is deposited on the flat panel system described above (Figure 2.11). However, the photodiodes are replaced by electrode pads. When the X-ray photon is absorbed in the a-Se, charge is released in the form of an electron-hole pair. Bias electrodes create an electric field, thus the charge signal is collected by the electrode pads on the readout surface.

Unlike the flat panel phosphor system, the spatial resolution of the detector may be increased through reduction in the del size[43]. As shown in Figure 2.12, although there is still part of the readout surface which is inactive, warping of the electric field in the detector causes the charge collected in this area to be shifted laterally so that it falls on the electrode. Therefore, the fill factor can be increased with the effective del.

This technology may be susceptible to 'ghosting' in the image, where there may be a signal lag in the detector after exposure[44]. This can reduce throughput in screening.

2.3 Summary

Requirements for breast imaging have been highlighted along with the advantages of digital mammography in the clinical environment. The physical aspects of the mammography system, focussing on the digital detectors currently available have been discussed. The next chapter will consider the different aspects of assessing the image quality of such detectors, investigating the link between objective and subjective image analysis.

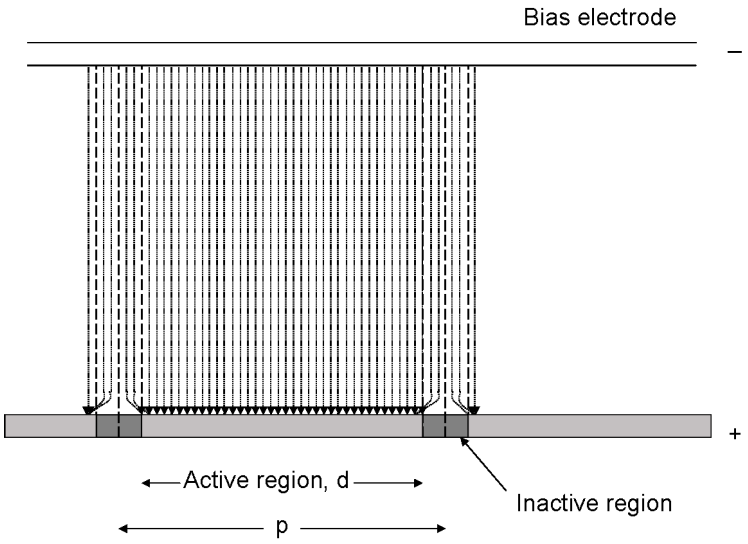


Figure 2.12: Schematic of the selenium flat panel. Although there are inactive regions as in the indirect detectors, the electric field draws all the charge released to the active regions giving a higher effective fill-factor.

There are three dominant technologies available: CR, indirect and direct flat panel detectors. There is also photon counting technology employed in mammography, which is not within the scope of this thesis. The reader may find further information on photon counting technology in [43, 45, 46]. Based on the technologies, it can be seen that there would be a difference in the images generated. However, how they differ and how they affect the observer's ability to make a decision based on the image generated is not clear. The next chapter will review image quality metrics available for characterisation of DM systems.

Chapter 3

Image Quality Analysis

As described in the previous chapter, digital radiography is still an emergent approach in mammography. Currently, DM systems only make up approximately 20% of the NHSBSP screening technology[29]. The technological difference between conventional SFM and DM systems has meant that new acceptance tests for these systems have had to be developed[47].

In broad terms, objective image quality measurements are of key interest to imaging physicists as they give a direct comparison between imaging systems. With the use of test object phantoms, it is possible to compare digital mammography systems based on their physical performance. However, this method of image quality measurement does not currently translate easily to performance in a clinical environment: the methods of image quality measurement often use a uniform background which bear little similarity to clinical tasks which would include anatomical noise hindering the detection process.

When considering the imaging chain, from image acquisition to image display, it is important to include the observer's perceptual response as well. Subjective measurements of image quality use settings and tasks more akin to the clinical environment. Clinical trials are set up to take into account how such imaging systems may be used. However, this is very time-consuming and requires extensive resourcing[30]. In such cases, one can then run the risk that a new, improved imaging system will have been developed in the time that the clinical trial was carried out to assess the commerically available systems. Clinical trials would include the use of Receiver Operator Characteristics (ROC) analysis which assesses the clinical impact of various individual settings in the detection task. Further bridging the gap between objective and subjective image quality testing is the use of test object phantoms CDMAM, TORMAX and TORMAM. Examples of these test objects are shown in Figure 3.1. These test phantoms have been developed for the purpose of measuring the detection capabilities of the imaging system, with consideration of an observer. However, it must be borne in mind that TORMAM and TORMAX are not appropriate for observer performance tasks and as such CDMAM has been made the focus of this work.

The TORMAM (Figure 3.1a) contains circular discs of diminishing contrast with linear structures in one half of the setup. In the second half of the set up, there is simulated breast tissue with clusters of microcalcifications. The TORMAX (Figure 3.1b) includes

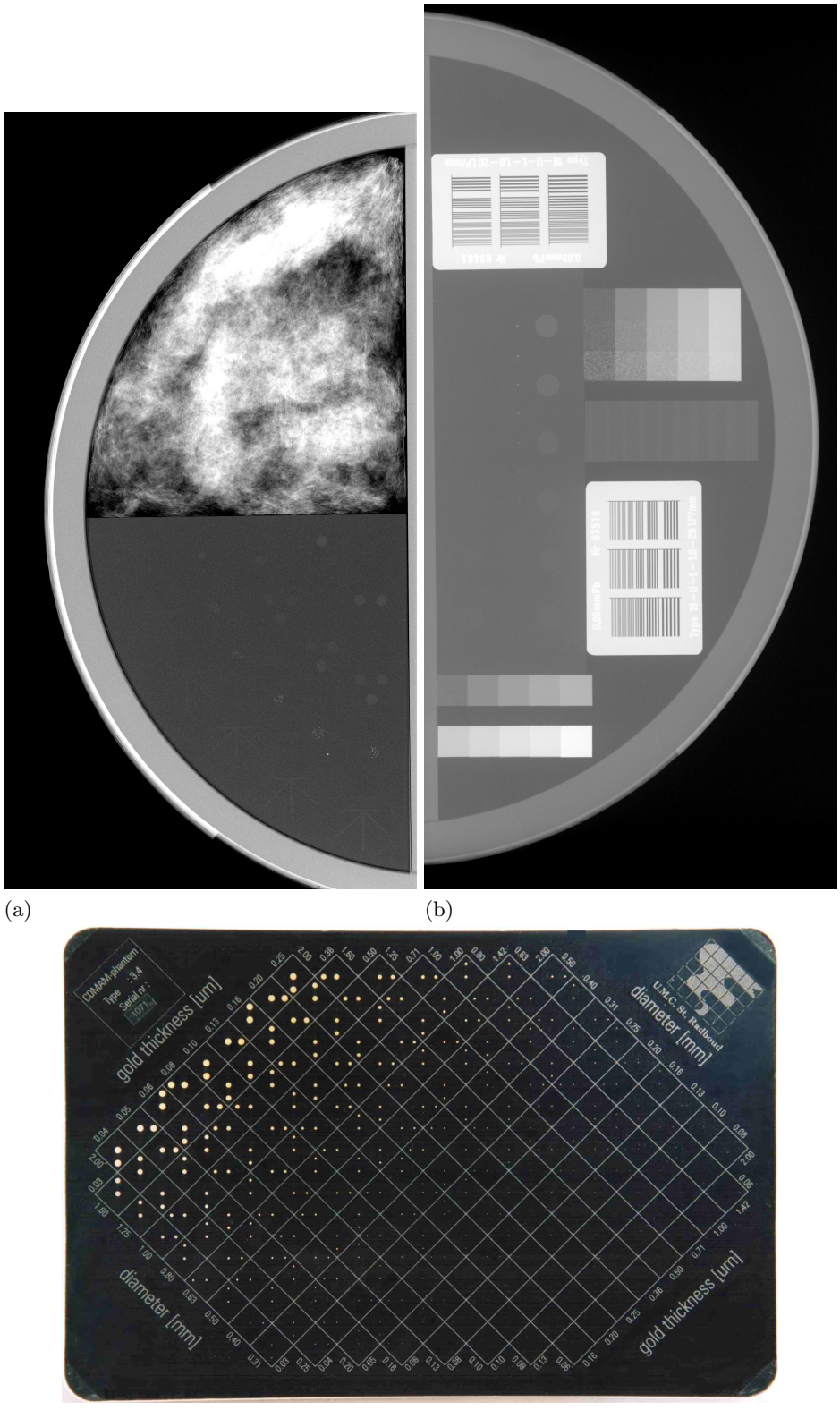
circular objects of differing contrast and line pair grids for measuring resolution. The limitations of these test phantoms are that the detection tasks are either too memorable or bear little resemblance to the clinical detection task. The CDMAM test phantom (Figure 3.1c) is of particular interest in this thesis, as it offers results that are easily quantifiable and comparable for different systems, with the use of human and automated observers. The aim of this thesis is to develop a simulation tool that will ultimately offer a method to generate DM images for the purpose of observer performance studies. The CDMAM phantom consists of gold discs that varying in diameter and thickness. Detection of such discs show similarity to the clinical task of detecting microcalcifications in a mammogram. In addition, scoring the images of the CDMAM phantom offers a method to quantify such an observer-based detection task. Thus the CDMAM phantom will provide a useful validation method for the image simulation tool. The use of the CDMAM phantom will be discussed in the last section of this chapter.

The previous chapter discussed the physics of mammography and the resulting effects upon images that are obtained from different DM technologies. From these images it is possible to assess and characterise the performance of the system. As digital technology is relatively new to the field of mammography, the definitive method in which to characterise digital mammography detectors is still changing[47]. IEC protocols have been set up for the purpose of standardising methods of measuring image quality metrics such as MTF, NPS and DQE (digital quantum efficiency)[48, 49]. However, these protocols are liable to change as research develops in this area.

Accurate objective analysis is crucial in order to characterise the detector and be able to simulate accurate and realistic images for the system. In addition, it will be with the use of the aforementioned image quality metrics that the simulated images will be validated initially. Thus, this thesis has endeavoured to comply with IEC protocol in measurements of the image quality metrics. This chapter will discuss methods of characterising the DM system objectively such as MTF and NPS, starting with the theory and leading to the practicalities of measuring these parameters in the clinical environment. Examples of MTFs and NPS will be presented to consider the interpretation of such metrics. The chapter will finish with the effects of such objective measures on subjective image analysis, with CDMAM scorings presented as a form of subjective measurement.

3.1 Detector Response Measurement

Imaging systems obey linear systems theory. Although some imaging systems may be logarithmic for example, these systems still obey the linear systems theory if the images are linearisable. *Linearity* of an imaging system refers to its detector response curve. This is the relationship between input intensity and output signal in the detector. This influences the range over which acceptable imaging performance is obtained. Typically, during testing, this is one of the most important to be undertaken, with the use of an ionising chamber to measure the dose at the surface of the detector, known as entrance air kerma at the surface of the detector (EAKS). The pixel value intensity



(a) (b)

(c)

Figure 3.1: X-ray images of the (a) TORMAM, (b) TORMAX and (c) CDMAM.

in the resulting image is measured for a range of doses and a graph depicting the pixel value intensity as a function of exposure plotted to define the linear range of the detector. It is important in these measurements - and during all physical performance measurements - that the image processing settings are turned off, such that the image represents the 'raw' pixel value intensities.

Particular DM detectors differ in the way they respond in detecting photons, even if made by the same manufacturer. Different manufacturers apply their own gain factors, although it is possible to linearise the pixel value intensity, P, to find the EAKS, E:

$$P = a.E + b \tag{3.1}$$

Some manufacturers apply a logarithmic response, therefore linearising the pixel value intensities into dose is applied thus:

$$P_{log} = a.ln(E) + b \tag{3.2}$$

Measuring the detector response is not a simple task. Although the digital detector will give the relative intensity of photons that are detected at each point in the detector, due to the way the X-ray tube is designed, as mentioned in section 2.1.1, the exposure across the detector is not uniform. For a standard measurement of the detector response, the exposure and pixel value intensity is typically measured directly under the anode, which is approximately 6cm from the chest wall side of the image. It is within this region that the global spatial measurements are made, such as the mean pixel value intensity, the pixel intensity variance and contrast to noise ratio (CNR).

A graph of variance as a function of pixel value intensity (and thus the exposure to the detector) is expected to be a power relationship. The nature of the recorded number of photon events is a Poisson distribution. Thus, the standard deviation in the image is equal to square root of the number of detected photons[50, 11], N_p, that are detected at the imaging plate (ignoring any other forms of statistical noise), which is proportional to the square root of pixel value intensity, P:

$$\sigma = \sqrt{N_p} = \sqrt{P} \tag{3.3}$$

However, this is only strictly accurate within the range known as the quantum-limited range. This is where the quantum noise source is the dominant source. The other main sources of noise include electronic noise and structural noise.

Electronic noise originates from the electronics needed to read out the charge collected in the flat-panel. This noise source remains constant, regardless of the exposure to the imaging plate. In terms of relative noise (noise measured as a ratio of standard deviation to mean pixel value), electronic noise would be dominant at low doses as quantum noise follows the relationship described in Equation 3.3. CR technologies are expected to have little or no electronic noise in comparison with its integrated detector counterparts.

Structural or fixed pattern noise originates from structures that are either temporally or spatially invariant. Typically, structural noise is a resultant of antiscatter grids that

may not be oscillating fast enough to be undetected in the image. Structural noise becomes more apparent as the exposure increases.

Based on work by Evans et al[51] and Ravaglia et al[52], the total variance in a mammography image, σ_t^2, is the summation of all three noise sources:

$$\sigma_t^2 = \sigma_e^2 + \sigma_q^2 + \sigma_s^2 \tag{3.4}$$

where σ_e,σ_q,σ_s are the standard deviation noise from electronic, quantum and structural sources, respectively. This can be re-written in terms of relative noise, σ_t/P, as in [52]:

$$\frac{\sigma_t^2}{\bar{P}^2} = \frac{\sigma_e^2 + \sigma_q^2 + \sigma_s^2}{G^2.E^2} = \left(\frac{k_e}{E}\right)^2 + \frac{k_q^2}{E} + k_s^2 \tag{3.5}$$

where $\bar{P}$ is the mean pixel value in the ROI, k_e, k_q, k_s is the electronic, quantum and structural noise terms, respectively which are specific to each DM system, E is the exposure level at the detector surface and G is the detector gain. In this, a in Equation 3.1 is replaced by G, the universal representation of gain and b is considered to be negligible, which is true in some of the commercial DM systems available currently.

For the purpose of modelling a simplistic uniform input image representative of the signal transfer property of the DM system, Equations 3.1 and 3.2 will be sufficient for modelling the pixel intensity values.

Clinical images are typically taken within the quantum-limited range; too low an exposure and the image may be too noisy to give enough information on possible lesions in the breast. On the other hand, too high an exposure would risk the patient receiving an excessively high dose without necessarily improving the diagnosis. The quantum-limited range differs from system to system. Typically, a screening mammogram is aimed to be less than 2mGy MGD per image[29]. Thus, Equation 3.3 should be sufficient for the purposes of characterising the mean pixel value to variance relationship. This will break down at very low or very high energies and Equation 3.5 would be more appropriate.

3.2 Modulation Transfer Function

The modulation transfer function (MTF) is a measure of the performance of an imaging system. MTF describes a system's signal transfer characteristics as a function of spatial frequency.

Mathematically, the MTF can be described as either the ratio of the frequency content output versus the frequency content of its input:

$$MTF(u,v) = \frac{|FT_{out}(u,v)|}{|FT_{in}(u,v)|} \tag{3.6}$$

or the Fourier amplitude of the response to a delta function input to the imaging system. This gives the optical transfer function, OTF, which is the Fourier transform of the point spread function (PSF).

$$OTF(u,v) = MTF(u,v).PTF(u,v) \tag{3.7}$$

$$PTF(u,v) = e^{-2.\pi.i.f(u,v)} \tag{3.8}$$

f is the spatial frequency. The OTF includes the magnitude (MTF) and phase components (phase transfer function, PTF). Thus, the MTF is the modulus of the OTF:

$$MTF(u,v) = |OTF(u,v)| \tag{3.9}$$

The resolution of a linear, shift-invariant system can be determined from the normalised output of an input delta function, i.e. the Point Spread Function in 2D or the Line Spread Function (LSF) in 1D. The OTF can be derived through the Fourier Transform of the LSF in 1D:

$$OTF = \int_{-\infty}^{\infty} LSF(x)e^{-2.\pi.i.x}dx \tag{3.10}$$

As defined in Equation 3.9, the MTF is the modulus of the OTF.

Equations 3.7 to 3.10 assumes the imaging system is shift invariant, thus the phase needs not be considered as the system's transfer function will be isotropic. However, due to the sampling nature of the digital detector, this assumption is, in actuality, violated. An imaging system is defined as shift-invariant if and only if a shift in its input is equal to a shift in its output. In the case of the digital imaging system, this is not strictly true as the system is based around discrete digital samples[53]. This issue will be discussed further in the following section, as it has important consequences for the work in this thesis.

3.2.1 Measuring the MTF

There are various ways in which the MTF can be measured in mammography, such as with an edge device[54, 47, 55, 56, 10] or slit device[57, 58]. The slit method has been well documented by Fujita et al[57] and measures the mammography system's response to an impulse function (LSF). This is in contrast to a delta function which a wire test phantom would give. The slit method, however, requires very high exposure as MTF measurements (obtainable from multiple exposures) are susceptible to noise, particularly with respect to assessing the high frequency components.

The alternative, more widely accepted method[54, 47, 50, 56, 55, 10] is with the use of an edge device, typically of high Z material (lead or tungsten). From an edge device, an edge spread function (ESF) can be obtained and differentiated to obtained the LSF.

The detector presampled MTF is defined by Dobbins as the "*system response up to, but not including, the stage of sampling*"[58]. "System response" encompasses the whole geometric setup of the mammography system. For clarification, the detector presampled MTF in particular is the blurring due to the detector only. To measure the detector presampled MTF, any scattering material such as PMMA slabs or the compression plate is taken out of the beam[54]. The anti-scatter grid is also taken out of the X-ray beam's path and the edge device is placed directly on the detector (Figure 3.2). In a clinical setup, the image resolution can be affected by many factors: focal spot size, geometry of the system and scatter from sources such as the breast tissue. As the ultimate goal of this work is to simulate realistic clinical images, it would seem

to be logical to include all these factors. However, these factors are not intrinsic to the detector, and liable to change for differing imaging conditions. Therefore, it would be more appropriate to look at only measuring the detector MTF and consider other factors as separate elements.

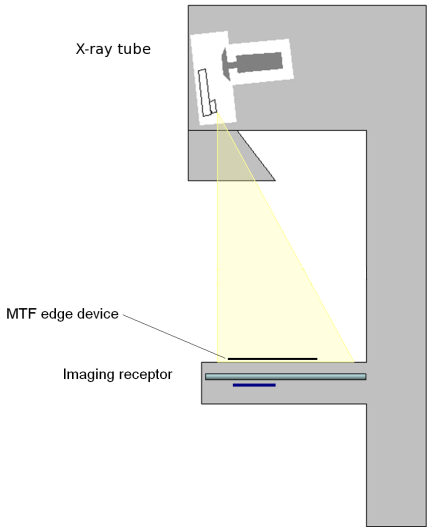


Figure 3.2: Geometric setup for MTF measurement.

There are two areas of differences in measuring the MTF: (i) set up of the MTF edge; (ii) the edge analysis techniques. Both aspects have been investigated and compared by Samei et al[54, 7]. In assessing the set up, the two methods mentioned above were assessed, the slit and edge method. The edge method was further split into the device implemented: radio-translucent and radio-opaque. The slit was constructed of two 2mm thick pieces of Pb with their polished edges placed $12.5\mu m$ apart. The translucent edge was constructed of a 0.1mm thick $Pt_{0.9}Ir_{0.1}$ alloy foil, laminated between two thin slabs of acrylic, polished on all sides. The opaque edge was made of 2mm of thick W slab, polished on one side and surrounded by Pb on the remaining sides.

Samei et al's work[54, 7] concluded that the slit method offers the highest precision across all the spatial frequency range. However, measurements were heavily affected by the presence of glare in the form of a low frequency drop in the MTF. Glare can affect the contrast through scattered X-ray photons. Although the edge device offers less precision, it is more convenient in that it requires less rigorous alignment (measurements were unaffected by misalignments up to 6cm) and will still provide good definition at low spatial frequencies. This is important as the MTF is used to calculate the DQE, which is only defined up to the Nyquist frequency of the system sampling size. The opaque edge was considered to be the preferred technique as it was less susceptible to generating secondary radiation at high energies like the translucent edge. Thus the opaque edge device has been established as the standardised method[47, 49].

It is appropriate to describe the basic principles of the edge methodology for measuring the MTF before continuing with the literature review of the variations upon the methodology here. An edge device is placed upon the detector for imaging at a

small angle (1-3°) with respect to either the horizontal or vertical axes of the detector plane. The edge angle is important as it enables finer sampling of the edge than the physical detector pixels would allow. Once the edge angle is determined through a variety of methods as described below, a set of profiles are extracted from the edge to create a supersampled ESF. This is has been the focus of most of the algorithms as any inaccuracies in the ESF will propagate to the final calculation of the MTF.

Samei et al[7] compared a range of six published algorithms focussing on edge analysis techniques published (Buhr et al[55], Granfors and Aufrichtig[59], Samei and Flynn[60], Saunders and Samei[61], Samei et al[7] and Reichenbach et al[62]) to derive MTFs from 14 edge images; 12 were experimentally acquired images whilst two were simulated edge images with and without noise added. Each algorithm followed four main steps in obtaining the MTF from an ESF:

1. Determine the edge angle. Buhr et al[55], Granfors and Aufrichtig[59] and Reichenbach et al[62] all used linear regression by fitting a straight line through the individual edge position estimates. Edge positions can be determined from the ends of the edge within the images (Samei et al[7]). Alternatively Radon or Hough transforms were implemented by Samei and Flynn[60] and Saunders and Samei[61].

2. A regular subsampling grid was obtained for further analysis of the ESF. Some algorithms rebinned the raw ESF into a fixed bin sizes ranging from 0.05 - 0.25 of the pixel pitch. Other algorithms implemented a 'natural' subsampling pixel pitch dependent on the edge angle. Smoothing methods were used on the ESF in some cases. Oversampling of the ESF overcomes the aliasing effects of the undersampled digital imaging system. This is discussed further in the next section.

3. All algorithms used a discrete finite element differentiation of the ESF.

4. All algorithms calculated the MTF using the absolute value of a fast Fourier transform.

The MTFs obtained using the above algorithms were found to be in good agreement with less than 0.02 difference between individual MTFs and the mean MTF. To validate this further with known MTFs, Samei et al[7] synthesised two edge images, one noise-free (Image 7 in Figure 3.3) and one with noise (Image 8 in Figure 3.3). The results improved further with the simulated edge images with less than 0.01 difference between the individually calculated MTFs and the true MTF, leading to the conclusion that the different algorithms can generate reliable and accurate results provided the images are not excessively noisy.

All current DM systems are undersampled[63, 11], with the possible exception of CR systems[1]. Undersampling occurs when the image is not sampled finely enough to record all the spatial frequencies present without aliasing. The next section will discuss the implications of undersampling.

[1]CR systems currently have relatively poor MTFs. Thus, despite the use of finer pixel sampling, there is little to be gained as the MTF will be close to zero by the Nyquist frequency.

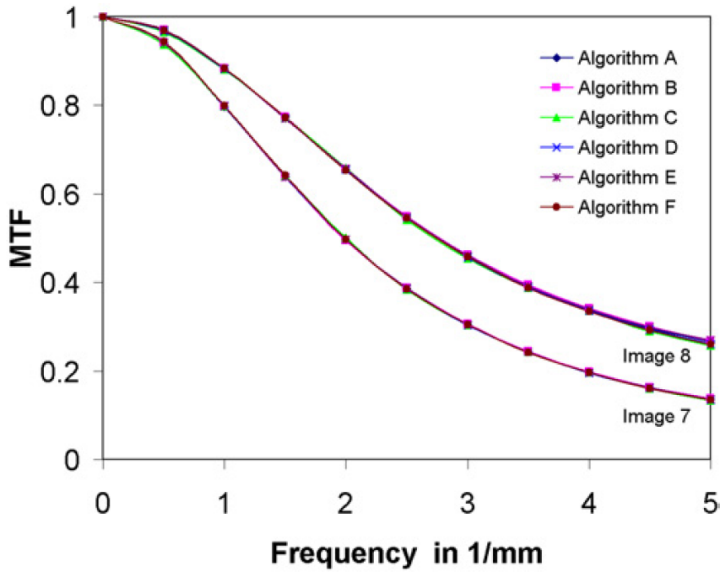


Figure 3.3: The MTF calculated by each of the algorithms assessed by Samei et al[7] for the noise free simulated edge image (Image 7) and the simulated edge image with noise (Image 8). Algorithms A - F are published algorithms by a range of authors as outlined in the text. Taken from Samei et al[7]

3.2.2 The effects of undersampling

At high spatial frequencies there is aliasing within the MTF of frequency components above the Nyquist frequency of the detector due to the undersampling effect in DM systems. The Nyquist frequency, f_N, is defined as half of the sampling frequency,f_s:

$$f_s = \frac{1}{\Delta x} \tag{3.11}$$

$$f_N = \frac{f_s}{2} \tag{3.12}$$

where Δx represents the del pitch in one direction. Undersampling has been thoroughly investigated in the work by Dobbins[63]. Dobbins' work found that the effect of undersampling affects the determination of the MTF in two ways:

- The digital MTF no longer describes the amplitude of a single frequency passed by the system.
- The digital MTF is phase dependent, therefore it is not spatially invariant. This violates the linear system's definition of MTF, which requires the system to have stationarity. Dobbins suggests averaging the MTF over all phases to give the expectation MTF (EMTF).

Supersampling of the ESF is the method adopted by other authors[55, 64, 53, 56] to mitigate this issue of sampling. This provides the effective sampling required to sample the image adequately without aliasing. However, there may be aliasing still within the

MTF measurement due to the the sampling measurement. Supersampling is typically undertaken at one tenth of the pixel sampling, therefore aliasing is considered negligible at the spatial frequencies the MTF considered.

3.2.3 Comparison of experimental detector MTFs

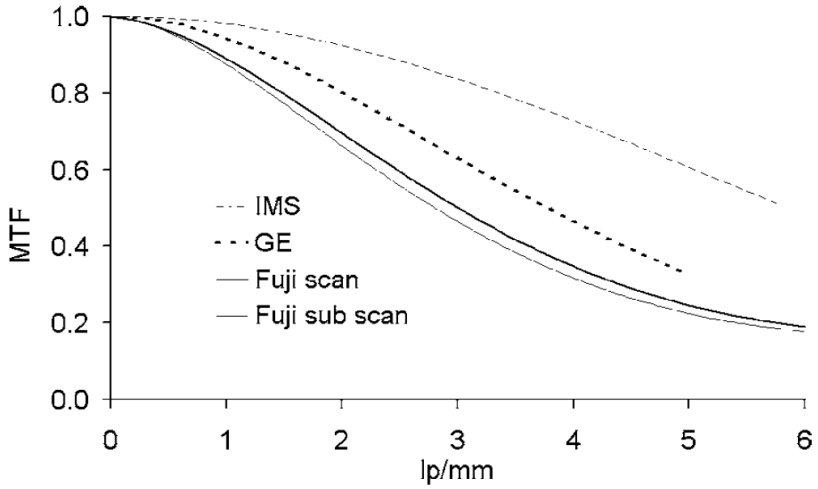


Figure 3.4: A range of MTFs acquired by Rivetti et al[8]. IMS refers to an a-Se system, GE is a CsI scintillator system, Fuji is a CR system taken in the scan and subscan directions. The scan direction is defined as the direction of the laser as it reads from left to right across the image. The subscan direction is perpendicular to this and is the direction of the plate as it moves along the reader.

Figure 3.4 gives an example of a range of detectors assessed by Rivetti et al[8]. Typically, amorphous selenium systems (IMS in Figure 3.4) have the most superior MTFs in the currently available clinical DM detectors, as the MTF does not deteriorate at the same rate as other systems. The GE system uses a CsI scintillator flat-panel technology. This system typically varies in MTF performance between the direct technology and CR technology. Flat-panel detectors are typically isotropic, hence only one directional/averaged MTF will be shown.

The two Fuji CR MTFs shown in Figure 3.4 represent the MTF in the two directions, scan and subscan directions. This phenomenon has been described by Monnin et al[65] in his work comparing screen-film technology with CR technology. The laser dwell time per pixel as the laser beam scans across is lower than the luminescence decay time[65]. Thus, in one direction, the MTF is decreased by luminescence from adjacent areas that the laser has passed. Therefore, the subscan MTF is not affected by such afterglow effects.

Currently CR systems offer poorer MTFs than DR systems, although attempts have been made to improve this with the use of finer sampling sizes. However, there is a limitation in creating very fine pixel size and the CR phosphor technology inherently suffers light spread. Needle crystal phosphors have been introduced to alleviate this

light spread. As discussed in the previous chapter, the needle crystals channel the light and reduce the light spread within the scintillator. The MTFs of two CR systems (typical powdered phosphor and needle crystal phosphor technologies) are shown in Figure 3.5. As can be seen the needle crystal phosphor technology provides an improved MTF compared with its powdered phosphor counterpart.

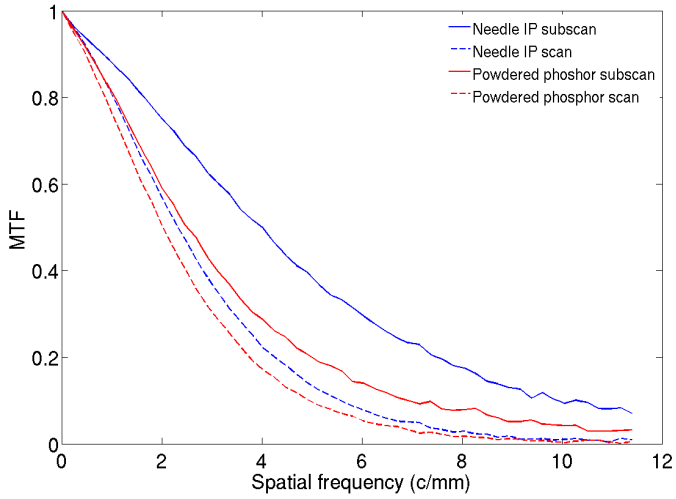


Figure 3.5: MTF of powdered phosphor CR detector compared with needle imaging plate CR. The two systems are both from Agfa as measured from experimentally acquired images. Images were acquired as part of a study of Agfa NIP and MM3 systems found in a report by NHSBSP[9]

There are alternative methods in measurement of the MTF, also known as the 'system' MTF. In the Figure 3.6, the results were obtained from experimentally acquired images of this system MTF. In this, there is a noticeable low-frequency drop in the MTF. This is an artefact of the measurement. A block of Perspex (a scattering material) had been placed in between the X-ray source and MTF edge during image acquisition. The Perspex had been placed during acquisition to emulate the scattering of the breast in a clinical image. This work has been further investigated by Rogge et al[56]. Although there is scattering in the breast during image acquisition, it degrades the contrast but not the MTF in the image. This had been apparent at the low frequency in the MTF as this is a global effect. To describe the detector presampled MTF only, scattering material should not be included in the image acquisition.

3.3 Noise Power Spectrum (NPS)

The NPS describes the noise variance per frequency interval in an image as a function of spatial frequency. The measurement of NPS is based on linear system theory, with the added assumption that the noise in the image is ergodic. The noise is ergodic if expectation values obtained from data samples at various locations in the image are equivalent to ensemble averages obtained from repeated measurements under identical

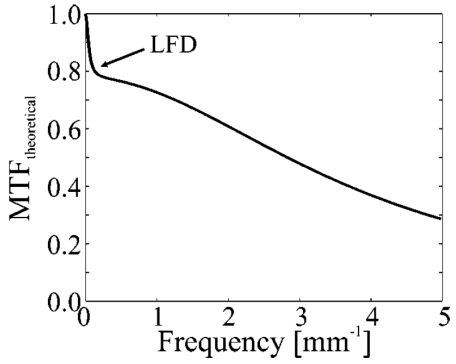


Figure 3.6: The low frequency drop (LFD) present in the MTF due to scattering material[10] in the set up

conditions at a single location. Thus it is possible to average spectra obtained from several areas of the image. However, due to factors such as heel effect, the system is not truly ergodic. It is nonetheless common to estimate the NPS from a limited area of a series of images. A stationary imaging system is given as one where the noise statistics are independent of position in the image and temporally between images. This is only true in radiography if the noise samples are obtained from spatially uniform exposures and there is no spatially fixed correlated noise from the detector.

The NPS can be calculated with the following equation:

$$NPS(u,v) = \lim_{X,Y\to\infty} \frac{1}{X.Y} \left| \int_{-X/2}^{X/2} \int_{-Y/2}^{Y/2} f(x,y) e^{-2\pi i(ux+vy)} dxdy \right|^2 \tag{3.13}$$

which can be rewritten as:

$$NPS(u,v) = \lim_{X,Y\to\infty} \frac{1}{XY} |F(u,v)|^2 \tag{3.14}$$

where $F(u,v)$ is the Fourier Transform of the pixel intensity value. The NPS measurement assumes infinite summation over the spatial domain as well as over the number of samples to determine the true NPS. There is therefore an intrinsic compromise in the form of the size and number of ROIs used for analysis. In addition, the above equations are relevant to an analogue system. Issues highlighted with the MTF measurement in terms of the digital sampling will affect the NPS measurement also. The following section will discuss the subject of measuring NPS for digital systems.

3.3.1 Measuring the NPS for a digital system

Measurement of the NPS for a digital system has been well documented by authors such as Williams et al[11], Dobbins et al[23] and Jiang et al[66]. For a digital system, the continuous expression given in Equation 3.14 needs to be rewritten in terms of discrete variables. In a digital system producing M×N sized images, the continuous image function $p(x,y)$ is sampled at regular intervals $(m\Delta x, n\Delta y)$, where $m = 1...M$ and

$n = 1...N$. Thus, the image can be expressed with image samples $f(m, n)$. In addition, the spatial frequency variables u and v can be evaluated at discrete frequencies given by $u = k\Delta u$ and $v = l\Delta v$, where $k = 0, \pm 1, \pm 2...K$ and $l = 0, \pm 1 \pm 2...L$. The maximum spatial frequency sampled, known as the Nyquist frequency is defined as $u_N = 1/(2\Delta x)$. The digital NPS can be evaluated by its values at discrete frequencies given by $(k\Delta u, l\Delta v)$:

$$\begin{aligned} NPS_d(u,v) &= NPS(k\Delta u, l\Delta v) \\ &= \frac{1}{MN\Delta x\Delta y}\left|\Delta x\Delta y\sum_{n=1}^{N-1}\sum_{m=1}^{M-1} f(m\Delta x, n\Delta y)e^{-2\pi i(k\Delta u)(l\Delta v)}\right|^2 \\ &= \lim_{M\Delta x, N\Delta y\to\infty}\frac{\Delta x\Delta y}{MN}\left|\sum_{n=0}^{N-1}\sum_{m=0}^{M-1} f(m\Delta x, n\Delta y)e^{-2\pi i(k\Delta u)(l\Delta v)}\right|^2 \end{aligned}$$

If this stationary random noise process is also assumed to be ergodic[11], then the NPS can be found by ensemble averaging. Thus:

$$NPS_d(u,v) = \lim_{M\Delta x, N\Delta y, Q\to\infty}\frac{\Delta x\Delta y}{MN.Q}\sum_{q=1}^{Q}\left\langle\left|\sum_{n=1}^{N}\sum_{m=1}^{M} f(x,y).e^{-2\pi(ux+vy)}dxdy\right|^2\right\rangle \tag{3.15}$$

where the $< . >$ indicate ensemble averaging, an average of spectra obtained from a series of uniform irradiation images, taken at identical exposures. Q denotes the number of regions used in the ensemble averaging. Influential work by Williams et al[11] explored how the experimentally determined NPS_d differs from the underlying analogue NPS:

1. The noise has been convolved with a box function given by the pixel aperture. Thus, the NPS that is measured experimentally is known as the presampled NPS:

$$NPS_{pre}(u,v) = NPS_{int}\,|sinc(au)sinc(bv)| \tag{3.16}$$

   where NPS_{int} is the underlying intrinsic or analogue NPS and a and b are the pixel aperture dimensions.

2. The image, from which the spectra has been estimated, has been sampled at discrete intervals. This is equivalent to multiplying by a Comb function. Thus, the digital NPS is given as:

$$NPS_d(u,v) = NPS_{pre}(u,v) \otimes\otimes \left(u, v; \frac{1}{\Delta x}\frac{1}{\Delta y}\right) \tag{3.17}$$

   where $\otimes\otimes$ denotes a two-dimensional convolution. The Comb function consists of an infinite array of delta functions mutiplied by two times the Nyquist frequency. Thus the NPS_d is an infinite 2D array of replications of NPS_{pre}. This means that there is aliasing of noise at frequencies above the Nyquist frequency into frequencies below the Nyquist frequency. As pixel pitch increases the aliasing becomes more severe[67, 11, 43, 68]. However, supersampling techniques employed

in MTF measurements detailed in Section 3.2.1 cannot be used to directly measure the presampled NPS as the phases of the Fourier components in the noise image are random[11, 57, 67].

Giger et al[67] theorized that as the pixel aperture increases, larger than the pixel pitch, the NPS_d decreases. The reason for this is that the sampling MTF smooths the noise prior to sampling. Therefore, the high frequency quantum noise components contributing to the aliasing effect are reduced. If the septa between pixels are large, leading to smaller pixel apertures compared to pixel pitch, the NPS_d will increase at low spatial frequencies.

3. The image data used to estimate the spectra has been truncated from its original infinite length to the number of samples (pixels) times the sampling interval. This is equivalent to multiplying the data with a box function with dimensions $M\Delta x \times N\Delta y$:

$$NPS_{d,w}(u,v) = NPS_d(u,v) \otimes\otimes |W(u,v)|^2 \tag{3.18}$$

where the $NPS_d(u,v)$ is the measured digital NPS and $W(u,v)$ is the frequency window, a Fourier Transform of the data window $w(x,y)$. If the image data were simply truncated after $M \times N$ points, the NPS is convolved with a frequency window with modulus

$$|W(u,v)| = M\Delta x N\Delta y \frac{sin(\pi M\Delta x u) sin(\pi N\Delta y v)}{\pi^2 M\Delta x u N\Delta y v} \tag{3.19}$$

which can be rewritten as:

$$|W(u,v)| = M\Delta x N\Delta y.sinc(xu).sinc(yv) \tag{3.20}$$

Different windows have been used depending on the characteristics of the particular spectrum being characterised[11, 61, 23, 66, 67]. The data window serves to reduce spectral leakage, where noise power from adjacent frequencies are mixed in the convolution process shown in Equation 3.18. Minimising the magnitude of the side lobes assists in distinguishing small amplitude features adjacent to large peaks in cases where there are strong periodic components.

It is important to know how the measured digital NPS differs from the underlying analogue NPS and how it is related, it may be necessary to understand the implications in noise simulation. The implications described above show that the NPS measured is, in actuality, the digital NPS, a product of the the digitally sampled presampled NPS. The NPS is specific to the imaging system, it is influenced by the doses implemented, the technology and the pixel size of the detector. The next section will describe methods in measuring the NPS.

The same group at the Duke Advanced Imaging Laboratory (North Carolina, USA) who had made a comparison of MTF measurement techniques described in Section 3.2.1, also reviewed the techniques in NPS measurement[23]. A prominent paper by Dobbins et al[23] reviewed only three main techniques from the current literature, details of which are given in the Table 3.1 .

Table 3.1: Parameters for the NPS methods evaluated in the work by Dobbins[23]. Methods A, B, C represent the methods published by different authors. NOL and OL represent non overlapping and overlapping ROIs used. Detrending refers to the polynomial function fitted to remove the low frequency shape across the image. Data rows averaged indicate how many rows on either side of the u or v axis in the 2D NPS were averaged to give the 1D NPS.

Method	Number of ROIs	ROI size (pixels)	Detrending method	Data rows averaged
Method A[63]	64 NOL	128 × 128	2D (first order)	8 (axis excluded)
Method B[60]	343 OL	128 × 128	2D (second order)	15 (axis included)
Method C[48]	160 OL	256× 256	2D (second order)	14 (axis excluded)

The methods referred to in Table 3.1 were assessed with a range of images, with differing parameters applied such as the size of the area within in the image for analysis, size of ROIs or whether or not the ROIs were overlapping. Detrending refers to the polynomial function fitted to remove the low frequency shape across the image. Current manufactured digital mammography systems require a flat-fielding algorithm to remove any large area non-uniformities and possible bad pixels. This is carried out at acceptance testing by the manufacturer's engineer who will average a number of uniform images to create a map. This map is greyscale inverted and applied to all subsequent images from the system. However, this may be incomplete[11, 43] and inhomogeneities may still be present in a flat field image. Therefore, it is typical to detrend the image data beforehand.

Detrending is a process to remove the intensity bias in the image, typically through the use of 2D first or second order polynomial fittings[53, 11] or with the use of a smoothing filter[11]. In addition, as the noise in radiographic images are not typically zero mean, the background signal should be subtracted from the image prior to NPS analysis. Often this is bypassed through ignoring the zero-frequency component as it is difficult to measure accurately[23].

The conclusion of Dobbins' work[23] was that the methods do not impact on the NPS measured. However, Dobbins had not included the effects of using a filter to detrend the ROI instead of a polynomial fit. Williams et al[11] has also investigated thoroughly the NPS of DM systems in particular. The work focuses on the theory of the NPS measurement with respect to digital imaging, as well as factors affecting the measurement as described above. In addition, their work looked at the effects of filtering the ROIs to detrend for NPS analysis compared to fitting a polynomial detrending method. The latter method dramatically increases processing time compared to smoothing filter.

Williams et al[11] assessed the effects of the detrending techniques on a synthesized data set, with and without a background trend applied. The background trend was applied with linear and quadratic trends. 2D fitting of the ROI yielded the best result in terms of removing the trend as shown in Figure 3.7, evident by the near-zero spatial frequency reduction. Another point to note in the NPS plot, is that there is a spike

at approximately 0.08 (arbitrary units) which would correspond to an excessive noise component at that specific frequency. Typically this may appear in an image as stripes across the image[11] or from the antiscatter grid if there is a contribution from both x and y directions[50]. The effects of the anti-scatter grid on the 2D NNPS is shown in Figure 3.8.

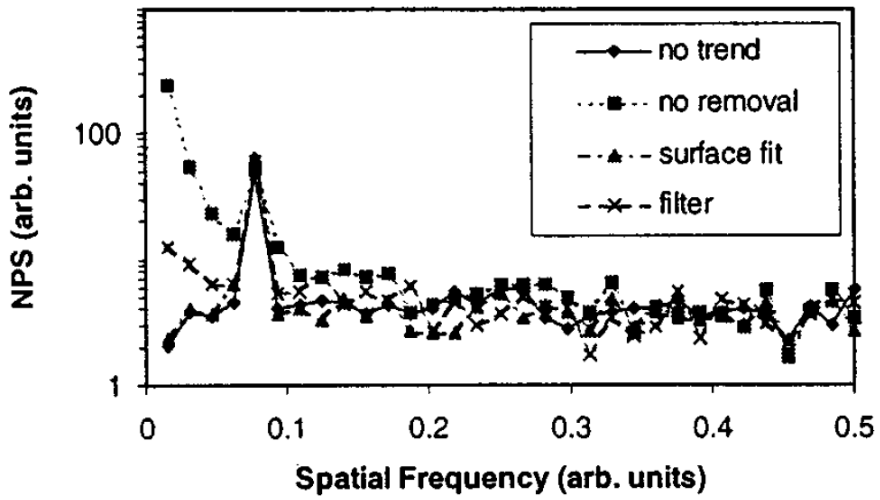


Figure 3.7: A comparison of the effects of background trend removal techniques on NPS estimation, using a synthesized data set from Williams et al[11]. The NPS is presented with no background trend applied to the synthetic data (diamonds), with background trend added but no removal technique applied (squares), with a 2D second order polynomial fit to the data (triangles), and a low-pass filtered version of the data (crosses).

3.3.2 Measuring the NPS clinically

IEC protocols[49] outline a method in measuring the NPS that has been implemented more recently[50, 69, 52, 51] and is described here. The NPS is estimated from a region extracted from flat field images, approximately 1088 x 1088 pixels[50]. ROIs of size 128×128 pixels are extracted from this selected region. A second order polynomial fit or smoothing filter is applied to each ROI and subtracted to remove the influence of large area non-uniformities.

Each ROI is then fast Fourier Transformed, squared and added to the NPS ensemble. The selected area was divided into a number of 128 × 128 pixel ROIs, overlapping each other by 64 pixels both horizontally and vertically. For purposes of direct comparison between systems and precision of noise power measurements[23], NPS is often presented as the normalised noise power spectrum (NNPS):

$$NNPS(u,v) = \frac{NPS(u,v)}{(S_0(E))^2} \tag{3.21}$$

$S_0(E)$ is measured as the pixel value linearised to the exposure. The NNPS is given in mm^2.

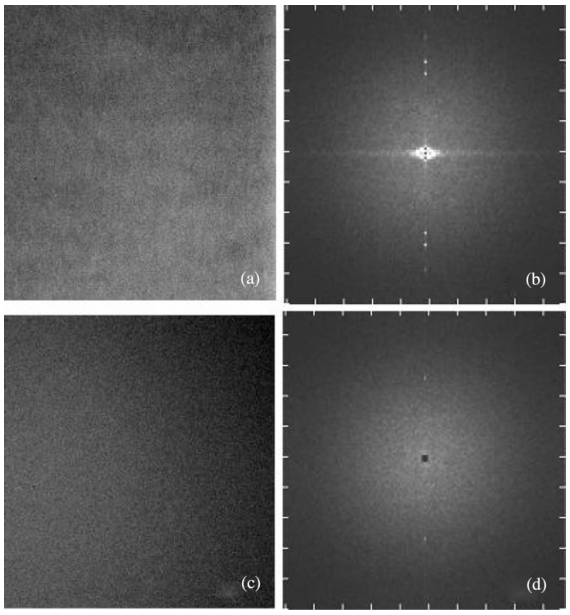


Figure 3.8: (a) Region obtained from a uniform image, acquired with an anti-scatter grid in place. (b) The 2D NNPS for region shown in (a). (c) The same region obtained from a uniform image, acquired without an anti-scatter grid in place. (d) The 2D NNPS for the region shown in (c). Figure is from Marshall's publication[12]

3.3.3 NPS as a function of dose

As discussed in Section 3.1, the total noise measured in an image can be attributed to different sources. The NPS is a spectral decomposition of noise variance as a function of spatial frequency[53]. Thus integration of this NPS will give the total variance in the image data used for the estimate:

$$\int_{-f_N}^{f_N} NPS_d(u,v) = \sigma^2 \tag{3.22}$$

Therefore, the relationship defined in Equation 3.5 can also be be expressed via the NPS in the form[51]:

$$NPS_t(u,v) = NPS_q(u,v) + NPS_e(u,v) + NPS_s(u,v) \tag{3.23}$$

where the total NPS, $NPS_t(u,v)$ is the sum of the quantum NPS, $NPS_q(u,v)$, the electronic NPS, $NPS_e(u,v)$, and the structural NPS, $NPS_S(u,v)$. As discussed in Section 3.1, the electronic noise is independent of energy absorbed by the detector. Quantum noise increases proportionally to energy absorbed, whereas structural noise increases with the square of the energy absorbed. Thus the $NPS_t(u,v)$ can be written with respect to air kerma at the detector, K:

$$NPS_t(u,v;K) = NPS_q(u,v).K + NPS_e(u,v) + NPS_s(u,v).K^2 \tag{3.24}$$

Equation 3.21 shows that the NNPS is calculated by dividing the NPS by the large area signal, relative to exposure. Thus, Equation 3.24 can be rewritten as:

$$NNPS(u,v;K) = NNPS_Q(u,v).\frac{1}{K} + NNPS_e(u,v)\frac{1}{K^2} + NNPS_S(u,v) \tag{3.25}$$

Thus far, the chapter has discussed different methods of characterising mammography systems, with particular attention to digital systems. It is with these image quality metrics that the simulation methodology will be developed. These are considered as objective analysis, as observer perception do not affect the result. Observer perception will be needed as part of validation of the image simulation framework. The next section will look at quantifying subjective image analysis.

3.4 Subjective Image Quality Analysis

Subjective image analysis takes account of the observer in the imaging chain. This is a very important part of the analysis, as the observer is the one who considers the image presented and makes a decision based on their finding. For a comprehensive assessment of a system, ROC analysis is typically employed. Such analysis can be time consuming and difficult to set up to assess each aspect of the mammography image optimisation. Thus contrast-detail test object phantoms have been developed to attempt to bridge the gap between objective and subjective image analysis. One such test object phantom is the CDMAM, illustrated in Figure 3.9. This test phantom is used widely across Europe for assessing the imaging performance of mammography systems and is proposed for assessment of digital systems also[47]. The CDMAM will be discussed further, exploring its use in a clinical environment and how it is scored for assessment of a digital system. This chapter will conclude with a discussion on ROC analysis.

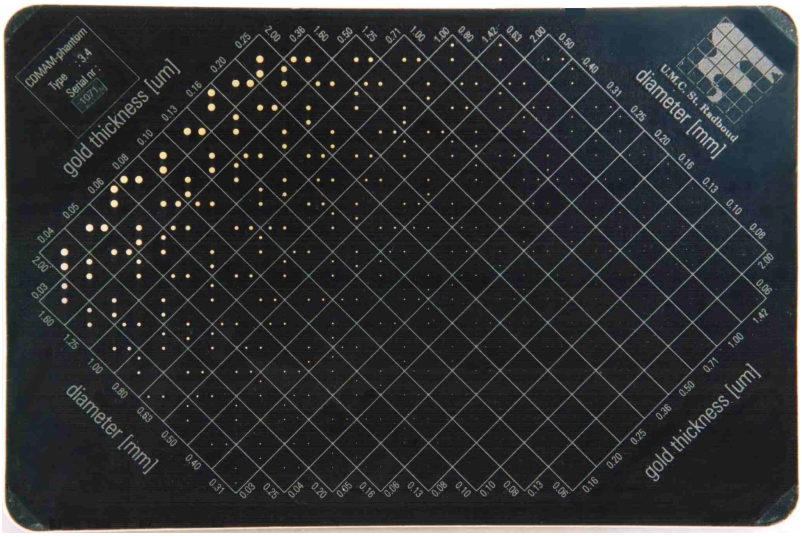


Figure 3.9: A photograph image of a CDMAM test object phantom. Multiple X-ray exposures of this test object is made for assessment of the digital mammography system at various X-ray settings.

3.4.1 The CDMAM test phantom

The CDMAM test phantom is made up of a layer of aluminium with a grid and numerals etched into its surface. Within the grid cells, two identical gold discs have been arranged such that one is placed in the centre and one is placed randomly in one of the four quadrants of the cell. These gold discs are arranged such that they decrease in diameter (2.00 - 0.06mm) and gold thickness ($2.00\mu m$ - $0.03\mu m$) in the rows and columns, respectively. During X-ray exposure, the CDMAM is placed between two slabs of 2cm thick PMMA. The attenuation of the PMMA slabs and the CDMAM phantom is equivalent to 5cm of PMMA thickness, which is equivalent to a 6cm thickness of breast with 50:50 fat:glandular composition[70].

During the experiment, this CDMAM setup is exposed to a 'normal' dose for the typical compressed breast thickness of 6cm with a 50:50 fat:glandular composition, typically 1mGy mean glandular dose (MGD)[2]. This is undertaken usually either 8 or 16 times with a slight translational shift applied to the CDMAM phantom for each exposure to the X-ray beam. This has been found to be the minimum number of readings to give the results with acceptable errors. For any fine disc detail that falls between two or more pixels in an image, its pixel value intensity will be spread out over those pixels meaning its peak intensity is lower than it would be if it were to have appeared in a single pixel. Therefore, acquiring multiple exposures with a slight translational shiftf each time ensures that any fine disc details approximately equivalent in size to the detector pixel do not bias the results. Furthermore, this is repeated for different doses such that the minimum dose for the acceptable image quality standard defined in the European guidelines[24] can be determined as shown in Table 3.2. European guidelines outline the minimum contrast thresholds which the system must achieve for detection to be within *acceptable* levels. *Achieveable* levels in Table 3.2 represent the contrast threshold levels achievable with the best possible systems.

Table 3.2: Acceptable and achievable levels published in the European protocol.[24]. Acceptable levels indicate the minimum detection levels, whilst achievable levels indicate the upper limits of detection levels.

Threshold Gold Thickness (μm)		
Disc Diameter (mm)	Acceptable Value	Achieveable Value
2	0.069	0.038
1	0.091	0.056
0.5	0.150	0.103
0.25	0.352	0.244
0.1	1.68	1.10

During scoring, human observers are asked to read each CDMAM image, identifying the location of the eccentric disc within each cell, one row at a time. In this manner, for each diameter, the lowest constrast theshold thickness can be correctly identified for the observer. Average scoring results from all images at the same X-ray setting are

[2]Mean glandular dose is indirectly calculated by measuring the breast skin entrance exposure and applying published conversion factors [70].

assessed and processed to obtain a *contrast-detail curve*. Processing involves applying a model fit[71] to the scoring data. This model fit describes the probability of detection of an object of diameter d as a function of its signal contrast in the form of a psychometric curve.

A psychometric function relates a physical stimulus to an observer's response. Typically, the relationship between the probability of correct responses to the physical parameter has a sigmoid shape. Thus, for a very large stimulus, such as a large disc with high contrast, the observer will always respond correctly. In the absence of a stimulus, the observer's response will lead to results of random guessing. Between these two extremes, there is a shift in the results where the observer's response is not completely 100% correct nor less than the random guessing rate. The threshold of detection is defined as the stimulus (disc contrast in this case) that will lead to the probability of correct reponses at 50% of the psychometric function.

Mathematically, this is defined as:

$$P(x) = \gamma + (1 - \lambda - \gamma)p(x) \tag{3.26}$$

where $\gamma = P(0)$, the lower asymptote; $1 - \lambda$ is the upper asymptote; $p(x)$ is the psychometric curve ranging from 0-100%, $P(x)$ is the psychometric curve ranging from the lower to upper asymptote and x is the stimulus strength (the contrast of the disc). The sigmoid shape of psychometric curve is defined as $p(x) \approx \frac{1}{1+e^{-x}}$ with the threshold and deflection point at $x = 0$. $P(x)$ represents the probability of correct observer responses in the CDMAM scoring, which is typically 25% when the disc is not present (related to the four quadrants of the cells in which the disc may be). Therefore, $\gamma = P(0) = 0.25$. Thus, the psychometric curve fitting for CDMAM scoring is given as:

$$P(t) = \frac{0.75}{1 + e^{f(C_T - C)}} + 0.25 \tag{3.27}$$

where $P(t)$ is the probability of detecting a disc of a certain diameter and thickness. C, $(= log(1 - e^{-\mu t}))$, is the contrast of a disc with thickness t, and linear attenuation μ, C_T is the threshold contrast corresponding to a detectability of 62.5% and f is a fitted parameter. Curves are fitted to the data using a least squares procedure[17, 71].

Human observer reading sessions can be time consuming, taking approximately 30-60 minutes per image depending on the experience of the reader. For this reason, automated CDMAM scoring software has been made widely available by EUREF[3], called CDCOM. This tool can help eliminate read-out variations inherent to human observers. This software makes a decision as to the location of the eccentric disc within each cell based on the average signal of the disc in relation to its local backround. CDCOM had initially been developed to mimick human observer scoring levels, but since improvements were made, the results are now typically superior to those of human observers. Thus, work has been carried out by Young et al to adjust the results of the automated scoring to predict human observer readings[17, 16].

Figure 3.10 is an example of a contrast-detail curve derived for the unadjusted CDCOM in comparison to human readers for the same set of images acquired on one digital

[3]European Reference Organisation for Quality Assured Breast Screening and Diagnostic Services

mammography system. As the curve shifts down, this indicates a reduced threshold contrast thickness for the corresponding disc diameter and thus indicating improved image quality.

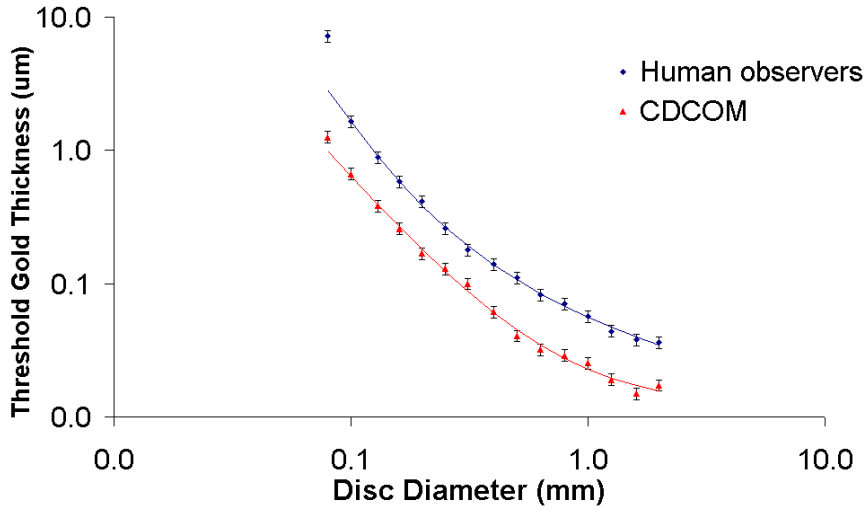


Figure 3.10: Two contrast-detail curves for the average of two human observers and CDCOM, plotting threshold gold thickness against disc diameter for the same set of CDMAM images. Results were derived from a previous study[13]

The limitation of the CDMAM phantom is that the increments in diameter and gold thickness (and hence contrast) are relatively coarse, limiting the precision of the resulting measurements. With monitor display windowing, CDMAM images from digital mammography systems are superior to images from conventional mammography systems. With current new technology, the current choices of disc thickness and diameter can be limiting and further choices may be more appropriate. In addition, the fixed locations of the disc layout leads to possible memorizing of the disc locations in certain cells. This has been acknowledged by other authors and as such a software that presents only single cells to the reader is available to counteract this issue[72].

Contrast-detail curves can be related to imaging characteristics of the system, previously discussed in the objective analysis portion of this chapter. The gradient of the slope of the contrast detail curves represent the deterioration of the disc visibility as the diameters decrease. Thus, a DM system with high MTF across all spatial frequencies will have a shallower gradient. Whereas a poor MTF will lead to a steep curve, indicating that the contrast of the discs are being degraded severely at smaller disc diameters as the MTF at corresponding spatial frequencies is diminished. This is illustrated in Figure 3.11. Dose also affects the contrast-detail curves in the form of shifts of the curve with increasing or decreasing dose. This is reflected in plots with scoring results from multiple doses shown in Figure 3.12.

Correspondences such as those described above could indicate that objective measurements could be used to predict subjective measurements. Marshall[53] has investigated comparing objective and subjective image quality measurements specifically for a full field digital mammography (FFDM) system. Marshall utilised previous methods of

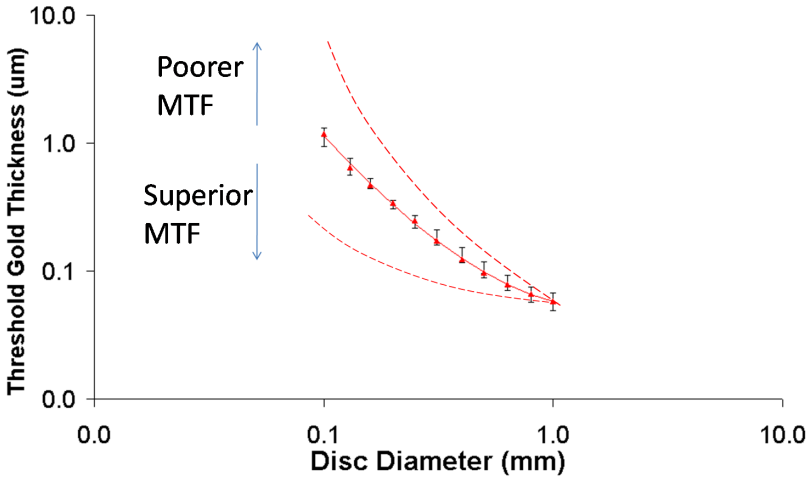


Figure 3.11: The effects of MTF upon the contrast-detail curve. A *superior* MTF would cause the gradient of the contrast-detail curve to become shallow. However, a *poorer* MTF would cause the gradient of the contrast-detail curve to increase. The contrast-detail curve was derived from images acquired in a study as part of the NHSBSP technical report[14].

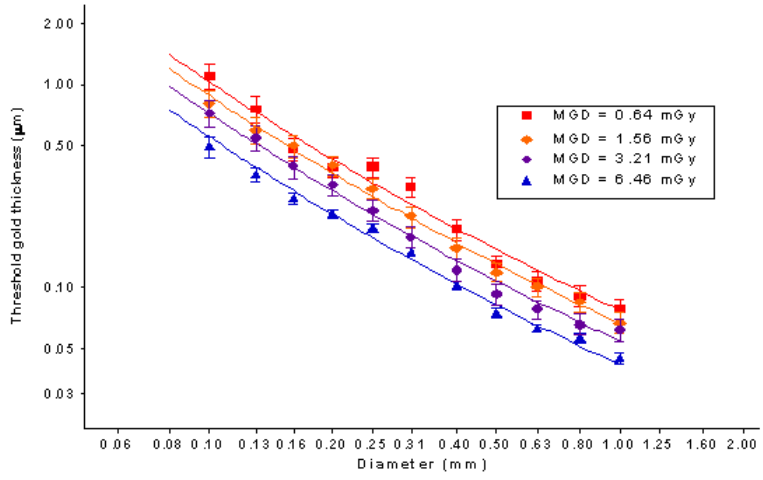


Figure 3.12: Contrast detail curves for the same system using different doses. Contrast detail curves were derived from images acquired in a study as part of the NHSBSP technical report[15]

predicting the contrast thresholds for digital mammography systems using objective measurements. This will be described further in the following section.

Detectability of an object in an image is determined by the signal difference of the object with its background, and the fluctuations (noise) in the image. Contrast is measured experimentally with the use of an aluminium square (1cm x 1cm) placed upon 5cm of PMMA on the detector. The following equation is used to calculate the contrast, C:

$$C = \frac{P_b - P_{Ob}}{P_b} \tag{3.28}$$

where P_{Ob}, P_b is the pixel value intensity of the transmitted radiation through the object and its neighbouring PMMA background, respectively. Care is needed to ensure that the ROI chosen for measurement is placed in the centre of the aluminium square such that the edge effect of the square does not affect the mean pixel value intensity measured. The noise fluctations can also be measured in the same ROIs, and the CNR is found using the background standard deviation, σ_b[73, 74]:

$$CNR = \frac{P_b - P_{Ob}}{\sigma_b} \tag{3.29}$$

CNR changes with dose and X-ray spectrum[47, 73]. This concept can be extended to the detectability of the gold discs within a CDMAM phantom. As the gold discs diminish in diameter, the contrast is increasingly affected by the blurring MTF of the detector. In detecting objects approximate in size and intensity to the local noise signals, this task is proven to be more difficult. This problem can be described by signal detection theory.

3.4.2 Signal Detection Theory

Signal detection theory (SDT) originates from statistical decision theory. Signal detection theory describes the decision an observer may make dependent on the information given to them. It has been implemented for decades, primarily from a psychology point of view to determine the sensitivity of a signal in the presence of noise. With the publication of work by Green and Swets[75], SDT has been applied to performance evaluation of human observer detection.

Returning to the CDMAM scenario, this type of classification task is known as a *signal-known-exactly* (SKE), *background-known-exactly* (BKE) detection task. Aufrichtig[76] and Marshall[53] have published work on finding the probability of detecting a disc object imaged against a homogeneous noisy background relating to signal-to-noise-ratios (SNRs):

$$SNR = \frac{C \int\int |S(u,v)\, MTF(u,v)\, O(u,v)|^2 dudv}{\left(\int\int |S(u,v)\, MTF^2(u,v)\, O^2(u,v)|^2 \left(q_0 DQE(u,v)\right)^{-1} dudv\right)^{1/2}} \tag{3.30}$$

where C is the contrast of the object, $S(u,v)$ is the spectrum of the target object in frequency space, $MTF(u,v)$ and $DQE(u,v)$ refer to the imaging system's MTF and DQE. $O(u,v)$ represents the spatial frequency response function of the observer's (human or modelled) visual system. Therefore, $O(u,v)$ models the observer's finite ability to visualise specific details. q_0 is the X-ray fluence incident upon the imaging detector. For detection to occur according to this model, the SNR will need to have exceeded some threshold criterion for detection, k for example, held by the observer. Thus, the threshold contrast for disc detection can be defined as:

$$C_T = k \left[\frac{C \int\int |S(u,v)\, MTF(u,v)\, O(u,v)|^2 dudv}{\left(\int\int |S(u,v)\, MTF^2(u,v)\, O^2(u,v)|^2 \left(q_0 DQE(u,v)\right)^{-1} dudv \right)^{1/2}} \right]^{-1} \tag{3.31}$$

Marshall[53] has studied the effect of modelling the spatial frequency response of the observer, utilising that published by Kelly[77] as well as setting $O(u,v) = 1$ (no spatial filtering by the observer). The model was applied to the objects in a CDMAM test phantom. With no spatial filtering by the human observer, effectively an ideal human observer, the modelled contrast-detail curves closely matched experimental data. Results were improved when published data by Kelly[77] and magnification effects were taken into account. The characteristic 'bowing' of experimental contrast-detail curves had been replicated in the theoretical data. Marshall[53] recognised the strong correlation between objective and subjective metrics. However, it was recognised that Equation 3.31 required modification to more accurately model the human visual system. This work has also been developed by Young et al[78] to predict the contrast-detail performance of five different digital mammography systems with similar results. Potentially this may replace the need to acquire multiple CDMAM images for scoring by using objective metrics alone, such as MTF and DQE. It may be worth noting that this may require more resources and calculations to measure to MTF and DQE accurately than to acquire and read sixteen CDMAM images.

The CDMAM is a simplified detection task, in a clinical environment the observer would be asked to detect, classify and identify signs of cancer in a mammogram which would be cluttered with system noise as well as anatomical noise.

Signal detection in medical imaging is task based. An imaging system optimised for one task maybe suboptimal for another task. The task a radiologist must undertake in mammography is classification, i.e. detection, discrimination and identification of signs of abnormality in an image. For example, a radiologist will have some form of decision criterion they may have to diagnose a patient with breast cancer based on the mammograms shown to them. Figure 3.13 is a graph illustrating the decision variable histograms for distributions of cases where there is a signal present (diseased, positive) or a signal is not present (non-diseased, negative). In an ideal system, these distributions would not overlap and 100% sensitivity and specificity is achieved. Sensitivity describes the fraction of diseased patients that are correctly diagnosed. Specificity describes the probability of a negative test resulting in non-diseased individuals.

In reality, these probability distributions overlap. Thus any threshold value will lead to misclassification of some diseased patients as normal or vice versa. An example decision threshold is indicated in Figure 3.13 by the vertical lines. The fraction of truly negative cases with decision variable values above the decision threshold is the false-positive fraction (FPF). The fraction of truly positive cases with decision variable values above the decision threshold is the true-positive fraction (TPF). A radiologist that is more likely to diagnose patients with breast cancer may achieve a higher true-positive rate, however, they may also generate a high false-positive rating. Although this may be acceptable for one radiologist, it may not be acceptable for another radiologist for which a high false positive rating is not worth the stress and expense of recalling a patient for biopsy. There are, however, standards set for this such as double-reading of a mammogram and scoring.

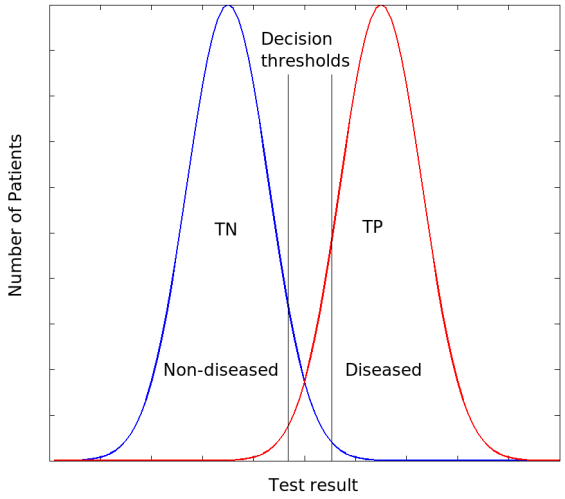


Figure 3.13: Schematic diagram showing the overlap between decision variable histograms of case images with truly positive and truly negative populations. Variation of the threshold value will change both sensitivity and specificity. Applying a lower threshold value results in the fraction of true positives (TPF) will be higher but the false negative fraction (FNF) will decrease (higher sensitivity) . A lower threshold value will reduce the fraction of true negatives (TNF) and increase the false positive fraction (FPF) (lower specificity).

The ability of a system to be able to differentiate between data taken from two populations can be quantified by examining the results produced by a decision-maker (the radiologist) who, when given the data from the imaging system is asked which of the two populations the data belong to. The decision maker will use some type of decision criterion to classify the image, such as the presence of patterns characteristic of masses, microcalcifications or architectual distortion of the tissue. If a large number of images are classified and assigned a decision variable, a histogram of the resulting values would result in a graph resembling Figure 3.13. Plotting the TPF against the FPF would give what is known as the Receiver-Operator Characteristic (ROC) curve. There is a large amount of literature regarding ROC analysis in medical imaging. However,

this is not within the scope of this thesis, the reader may find more regarding ROC analysis[79, 80, 81] and its application in [82, 33, 83, 84].

3.5 Summary

This chapter has presented the two different aspects of imaging analysis: objective and subjective approaches. Measurement of signal and noise transfer properties in the form of detector response, MTF and NPS have been presented along with careful consideration necessary for accurate characterisation of DM systems. Such measurements only describe the physical performance of the system and do not take account of the observer perception.

Subjective image quality analysis considered the inclusion of task-based performance metrics that included the observer. Contrast-detail test objects such as the CDMAM were considered as a bridging between objective and subjective measurements. The use of the CDMAM phantom and its interpretation was thoroughly explored as this will be used as a form of validation for the image simulation framework. Signal detection theory was discussed to introduce the the possibility of the link between objective and subjective image quality metrics. However, it must be borne in mind that the contrast-detail tasks described here limited in that there are still dissimilarities in its composition compared with real mammograms.

Thus far, this work has considered the background of mammography and the motivation behind this thesis. Methods of characterisation and image quality analysis of the DM systems have been investigated in detail. Using this knowledge, the next chapter will go on to describe a comprehensive approach to the simulation of digital mammography images based on such performance characteristics starting with a literature review and following with an application of an image simulation methodology.

Chapter 4

Developing the Image Simulation Chain

Image quality metrics such as MTF and NPS are determined by the physical processes in the formation of a radiographic image. With the added advantage that such metrics are measured routinely in the clinical environment, it is possible to create visually realistic, synthetic, mammographic images with such information. With this in mind, efforts to simulate images have involved using the imaging system's signal and noise transfer properties to degrade an idealised template image. The first step was to create idealised images which could be degraded using image quality metrics of digital mammography systems. In describing the development of the image simulation chain, it will be split into two parts: MTF blurring and noise creation. These will be discussed in detail separately, each section containing image simulation methodology, validation methodology and results.

4.1 Literature review

In a linear system, the input image, $f(x, y)$, is related to the output image, $g(x, y)$, through the following relationship.

$$g(x, y) = h(x, y) \star f(x, y) + \eta(x, y) \tag{4.1}$$

where $h(x, y)$ is the spatial representation of the degradation function which is convolved ($\star$) with the input image and added to the noise image, $\eta(x, y)$ to give the output image of a linear system. $h(x, y)$ can be considered as the PSF of the detector. Convolution in the spatial domain is equivalent to multiplication in the frequency domain, thus Equation 4.1 can be rewritten as:

$$G(u, v) = H(u, v).F(u, v) + N(u, v) \tag{4.2}$$

the terms in capital letters are the Fourier transforms of the corresponding terms in Equation 4.1, where $H(u, v)$ can be considered to be the MTF of the detector. It is upon this basis that simulation (and restoration) of images are formed[85].

There are two ways in which the resolution properties of a radiographic image has been simulated in the medical imaging field. The first method is based on the principle the input image, $f(x, y)$, used is ideal, has no noise and infinite resolution[61, 86, 87]. The second method begins from a clinical radiographic image as the input image[88, 64, 82, 37, 89]. Both these methods will be described below, along with their advantages and disadvantages.

4.1.1 Starting from an ideal image

An influential paper in this field by Saunders and Samei[61] outlines a method to modify the MTF of an image from an ideal image. Resolution characteristics of a digital X-ray system was applied to an ideal image and resampled to include the impact of the MTF and digitization on the image resolution. Resolution modification routine implemented an isotropic presampled MTF to apply the resolution characteristics to a synthetic edge image. The presampled MTF had been divided by a sinc function associated with the final sampling aperture, as the final resampling step causes the MTF to be multiplied by the corresponding sinc function. The MTF was multiplied with the Fourier Transform of the ideal image and the product was inverse Fourier Transformed. This modified image was resampled to the the desired sampling size with the use of a neighbourhood averaging routine.

The routine described implies that the presampled MTF is independent of sampling and thus the sinc function applied is associated with the final resampling step. This is contradictory to the definition of presampled MTF by Dobbins[58] which defines the presampled MTF to include sampling in the detector but not the digitisation step. This would be of little consequence as the desired sampling is the same as the original sampling of the presampled MTF. If, however, one were intending to apply the presampled MTF properties of a specific technology but with differing pixel size than is currently available, this could add inaccuracies to the simulation.

Grosjean et al[86] and Gong et al[87] both employed the use of physical models to create an ideal image. The physical models were implemented with the use of Monte Carlo techniques. Ideal images were created with the use of specific X-ray spectra and digital mammography setups, with knowledge of the detector absorption efficiencies and detector gain factors. Once the ideal image was created, the presampled MTF was applied as detailed in Saunders and Samei's[61] work. Validation of the models by Grosjean et al[86] was with the use of a CDMAM phantom, as the focus of the work was to assess the effect of a textured background on the detection rate of the CDMAM phantom. Comparison was made with a singular global value encompassing the scoring results of all the discs in the CDMAM phantom. This makes it difficult to clearly assess the effects of the image simulation model on the individual contrast and detail sizes. For example, one setup may result in improved scoring for large discs and poorer scoring for small discs compared with another system setup. However, the single global value would misconstrue this result to mean that the two systems had the same performance.

Saunders and Samei[61] also provide a method of simulating radiographic images with the correct level of noise as well as the correct NPS as that for specific doses. The

routine described by Saunders and Samei creates a Gaussian noise image which is filtered in Fourier space with the relevant NNPS of the detector to be simulated. The filtered noise image is inverse Fourier Transformed into real space and scaled according to a mean variance relationship to the radiographic image. This process assumes there is little or no noise already present in the image to be modified. Thus the modification routine may not be applicable to a lot of clinical images which will have their own noise properties inherent in the image. In addition, the process requires that the system be isotropic, which is applicable to most DR systems. However, this assumption is violated for a lot of CR system which may have anisotropic MTF and therefore NPS as well.

Creating radiographic images from an ideal image derived from models would enable the user to simulate images for any X-ray setup with different beam qualities, exposure, MTF and NPS characteristics. Monte Carlo can offer a lot of information on the physical processes in digital mammography. However, it requires in-depth knowledge of the geometrical setup of each component in the digital mammography system and rigorous validation of the applied models with experimental measurements. Moreover, adequate photon statistics would be needed to create a satisfactory image; for a full sized image, this is more than 10^{12} photons that may be needed for modelling. This could lead to days if not weeks of computing time in order to simulate one image.

4.1.2 Modifying a clinical image

It is possible to take a clinical image and degrade it to the imaging characteristics of another. Work in this area has been very much observer-performance study driven. In moving to digital mammography, there has been great interest in optimising the imaging systems (acquisition, processing and observer included). Thus far, modification of clinical images has been focused on two main areas also: resolution and noise.

In terms of resolution, a group in Katholieke Universiteit Leuven have experimented with extracted microcalcifications from mammograms. These extracted microcalcification templates had their MTF characteristics modified and their contrast altered to simulate acquisition settings of another system. The modified microcalcifications were then added into clinical mammograms for the purpose of observer performance studies by Zanca et al[82, 90, 91] and her predecessor Carton et al[64, 92, 10].

This work has helped understand the effects of image processing packages in detection of fine details such as microcalfications which are considered the limits of detection capabilities. However, the work does not consider the effects of noise in its resolution modification process. Arguably, with the nature of the templates modified, at only 20×20 pixels in size, it may be considered negligible. The noise should be correlated over the whole image, including the inserted microcalcifications. Moreover, in the microcalcification insertion process, it is necessary to take care in placement of the microcalcifications (single or clusters) as edge effects make lead to unrealistic appearance of the lesions in a mammogram.

Highnam et al [93] introduced a method to model 3D shapes of masses as well as modelling surrounding tissue to extract masses for implanting into another mammogram. The Highnam et al method uses the h_{int} representation which claims to provide

accurate and realistic simulation without the need to vary parameters to achieve an 'appropriate' appearance of the lesion in the mammogram. h_{int} represents the thickness of fat and non-fat tissue between the detector and the X-ray source. To simulate disease, adds to the h_{int} the corresponding h_{int} representation of an object/mass and perform an X-ray simulation to obtain the final simulated image. Results showed that extraction of masses from one mammogram for introduction into another mammogram proved the more successful as realistic features such as spicules and vessels surrounding the mass could be included in the extraction. Synthetic objects such as spheres and sharp spiculated 3D shapes were also generated. However, it would seem that the simple shapes were easy to identify as simulated masses compared with the extractions. The h_{int} representation provides a useful method to classify the types of tissue present in a mammogram. However, accurate knowledge of the X-ray beam and scatter effect is needed. The h_{int} representation lends itself easily to simulations with different exposure levels. However, it must be borne in mind that the image's resolution can only be degraded and not improved as no further information can be recovered.

Observer performance studies involving the use of radiographic images (mammograms and chest X-rays) that have been systematically dose reduced have been carried out by Workman[88], Båth et al[94], Ruschin et al[33], Svalkvist and Bäth[95], Samei et al[32] and Veldkamp et al[96]. This was based on creating a noise image equal to the difference in noise level and property (NPS) between the original image and an image acquired at a lower dose. With the exception of Veldkamp et al, most authors[88, 94, 33, 32] filtered the noise image with a frequency filter equal to the difference between the original dose and the lower dose. The methodology of Veldkamp et al is simplistic and assumes the noise to be added is not correlated. Therefore a Gaussian noise image equal in standard deviation to the difference between the original and lower dose image was used. This produced a synthetic clinical image with the correct standard deviation. However, the shape of the NPS did not match, meaning that the correlation of the noise was incorrectly modelled. Veldkamp et al argued that other methodologies may be computationally exhaustive for most clinical environments and that this method is a satisfactory compromise for small scale dose reduction studies.

Svalkvist and Båth[95, 97] developed upon the methodology published by Båth et al[94]. Svalkvist and Båth developed the model primarily for tomosynthesis images, where the previous assumption that the DQE remained unchanged across the image and across each projection was no longer valid. The methodology was validated by degrading 2D digital radiographic images as if collected at a lower dose level and comparing this with radiographic images acquired at this lower dose. By reducing the dose by 73% of the original dose, error in the integrated NNPS was reduced from more than 20% with the methodology developed by Båth et al[94] to 4% with the new methodology[95, 97].

Ruschin et al[33] and Samei et al[32] undertook a ROC study on the effect of dose reduction on observer performance. The dose of clinical images were reduced by adding an increased level of noise to the images. Both groups came to the conclusion that the dose of current digital mammography images could be reduced by one half without great detriment to the detection of lesions, in particular masses. For microcalcifications, as their size is comparable to the high frequency of the added noise, detection of these clusters were affected more.

One salient point in modifying clinical images is that the clinical image will have its own inherent image quality characteristics from the detector. These clinical images can only be degraded as it is not possible to 'improve' the image quality as the information is not there. For this reason, in some instances, simulation from ideal images would provide the most flexibility in studying the effects of imaging system characteristics on observer performance. In this chapter, simulation from ideal images has been chosen as a method of validation of modelling the blurring and noise only.

The remaining chapter will discuss the blurring MTF and noise simulation separately; presenting the image simulation methodology, validation methodology and results for each section. Details of the digital mammography systems modelled are given in Table 4.1. The systems chosen for simulation in this work provides a broad scope of technologies currently available on the commercial market. This ranges from the perceived lower image quality of CR system to the higher image quality from the direct conversion systems.

Table 4.1: Description of the digital mammography systems modelled

Imaging System	Pixel Spacing (μm)	Detector Type	Technology
Hologic Selenia	70	Direct	a-Se + TFT
GE Essential	100	Indirect	CsI + a-Si
Agfa Needle IP[a]	50	Indirect - CR	BrFl

[a]CR HM5.0 mammography detector used with a Siemens Mammomat 3000 Nova

4.2 Detector response

For the MTF and NNPS characterisation to be carried out correctly, each system modelled in this work had to be checked for linearity. Both the Hologic Selenia and GE Essential system followed this linearity assumption. The Hologic Selenia system had a slight offset in pixel value, such that when extrapolating the detector response curve to zero exposure at the detector, there was a value of 50 pixel intensity values. In previous experience with other Hologic detectors, this varied between 35 – 63 pixel intensity values and was found to be a idiosyncrasy of this type of detector.

However, the Agfa CR system used in this work needed to be linearised before further characterisation could take place. The pixel value intensity was measured for a range of different air kerma at the detector surface (16.8 - 504 μGy), K, and was found to follow a logarithmic relationship:

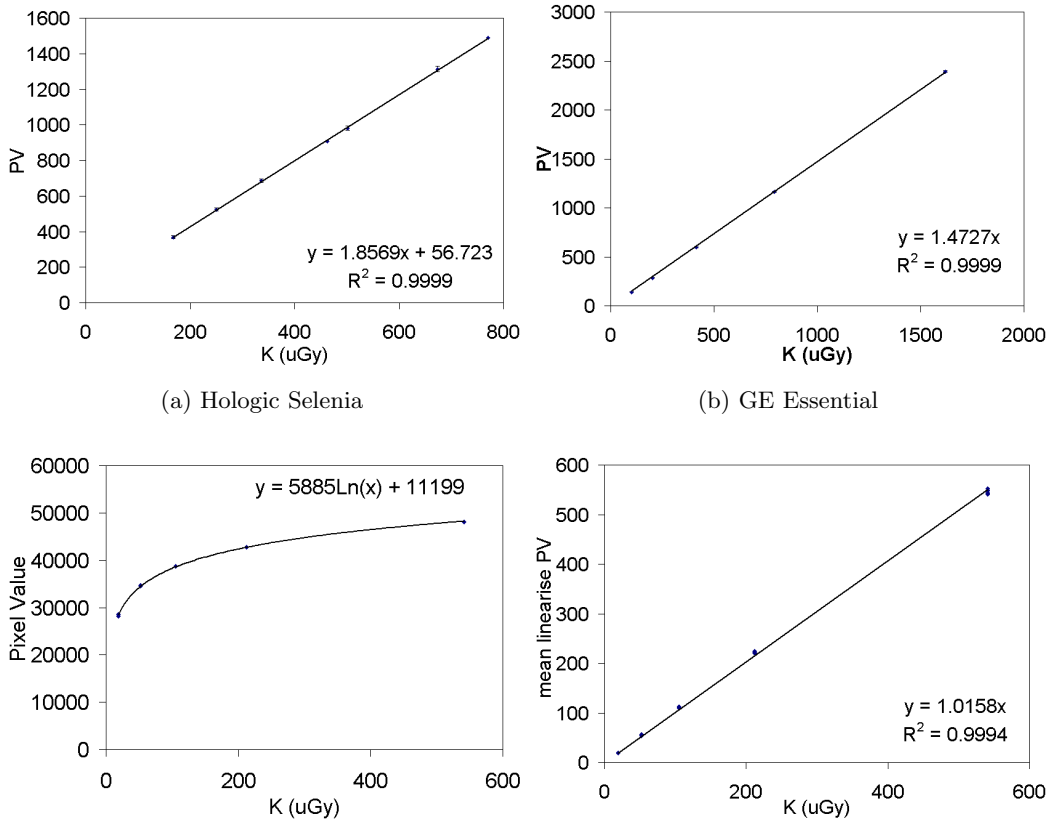
$$P_{CR} = A + Bln(K) \tag{4.3}$$

where A and B are constants. When linearised, the images followed a detector response in the form of:

$$P_{lin} = e^{((P_{CR}-A)/B)} \tag{4.4}$$

It is noted that after linearising the images, the fit of the σ_{lin} to P_{lin} largely follows that expected for a quantum-limited system. However, the σ_{lin} deviates further from P_{lin} at higher doses. This indicates that between 200-500μGy, structural noise is becoming

a more dominant noise source in the system. As such, it is possible the dose simulation will be complicated in this range as it no longer follows Poisson statistics which the simulation process relies on. Figure 4.1 shows the linearised detector response of each detector used in this study for a set up with 5cm PMMA.



(a) Hologic Selenia

(b) GE Essential

(c) Agfa CR

(d) Agfa CR linearised

Figure 4.1: Detector response of the three systems used in this study. Note that the Hologic Selenia system has an offset shown in (a). (b) shows the detector response for the GE Essential system.(c) and (d) show the detector response for the Agfa CR system before and after the images were linearised as in Equation 4.4.

4.3 MTF Blurring and Resampling of the Images

This section will present the methodology involved in the resolution part of the image simulation chain. The work will separate the two main defining factors affecting resolution: MTF blurring and resampling. Validation methodology of this will be described and its results will be presented afterwards. The noise simulation part of the chain will also follow this section with the same format.

4.3.1 Developing the blurring and resampling simulation chain

An ideal image in this context is defined as having infinitely high spatial resolution with zero noise. For this purpose, an ideal image was approximated using a $10\mu m$ pixel size. $10\mu m$ was chosen as it was a compromise between having high resolution that would not affect the images within the range of the considered spatial frequencies whilst enabling efficient image creation with the computing facilities available. This was further verified with a short experiment described in Section 4.3.4. Resolution of digital images is affected not only by the system's MTF, but also its pixel sampling. Modelling of these components will be discussed in the following sections. Figure 4.2 shows the process in which the blurring of the idealised image, $I_{idealised}$, undertakes to produce the synthetic blurred image at the pixel size of the detector system.

4.3.2 MTF

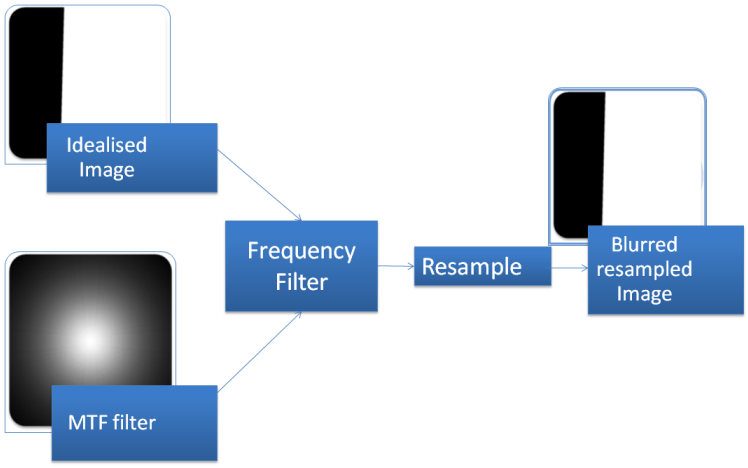


Figure 4.2: Flow chart illustrating the process to simulate resolution properties of digital mammography system images. An idealised image is created (as described below) and filtered with the MTF filter in the frequency domain. The MTF filter described here is derived from the detector presampled MTF. The inverse Fourier transform of this resultant image is resampled to the pixel size representing the digital mammography system to be modelled.

In radiography, the MTF is a measure of a system's spatial frequency response. As discussed in the previous chapter, the MTF can be measured for either the digital mammography system setup or for the detector only. In the interest of simulating the digital mammography system faithfully for different acquisition setups, only the detector MTF will be considered in the simulation. The detector MTF, defined as a presampled MTF, includes the unsharpness due to the detector substrate (CsI phosphor or a-Se) and the detector aperture. The detector aperture, in flat-panel imagers is defined as the active pixel size. In CR systems, this is modelled on the characteristics of the laser scanner[58] as well as the pixel size.

The presampled MTF was measured experimentally as outlined in the previous chapter. A sharp edge phantom was used, tilted between 1° to 3° in the horizontal and vertical axis, in two different exposures to ensure that the MTF was the same in both directions. It is assumed this will indicate an isotropic MTF from the detector. This was found to be the case in the flat-panel imagers. However, for CR, the MTF may have a tendency to be poorer in the scanning direction (of the laser beam) than the subscanning direction.

Raw images were obtained for each system and the MTF measured using an ImageJ[98] plugin developed for this purpose[1]. In the case of the flat-panel imagers (Hologic Selenia and GE Essential), the MTF was found to be the same in both directions as illustrated in Figure 4.3. The Hologic Selenia system can be seen to have the best MTF. The GE Essential system MTF approximates that of the Agfa CR system.

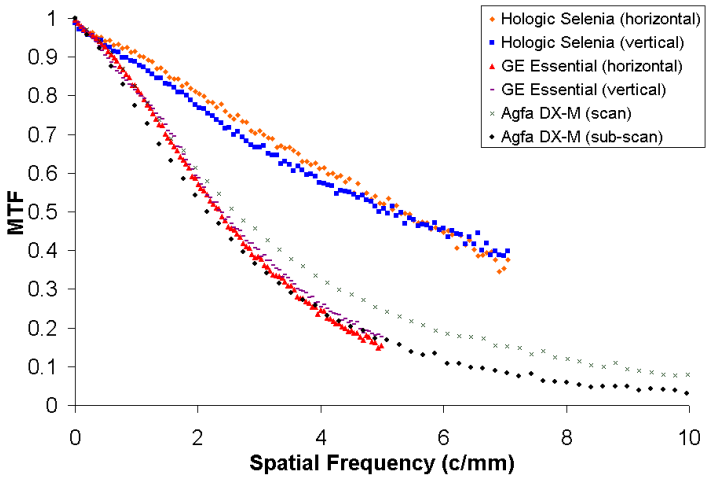


Figure 4.3: Experimental presampled MTF in horizontal and vertical directions for digital mammography systems modelled.

As discussed in the previous chapter, the presampled MTF is ideally rotationally symmetric, representing an isotropic system. In the case of the flat-panel imaging systems, this can be approximately true, the MTF profiles for each system have been averaged between the horizontal and vertical axes and a curve was fitted to the data for use as a MTF filter.

The one-dimensional presampled MTF is only defined up to the Nyquist frequency for the sub-sampling steps in the MTF measurement process (typically one tenth of the detector pixel size), beyond which there are aliasing issues[58]. However, the presampled MTF will typically be plotted up to the Nyquist frequency of the detector pixel size as there is no information beyond the detector's Nyquist frequency in the image.

As the MTF will be applied to an idealised image at $10\mu m$ pixel sampling, the MTF needs to be defined up to the Nyquist frequency at this sampling (50 cycles per millimetre). Therefore, a double Gaussian model was used to fit to the measured presampled

[1]QAdistri plugin was developed for the purpose of quality assessment in digital radiography by Frank Rogge at the LUCMFR, UZ Leuven.

MTF and extrapolated to 50c/mm:

$$MTF_{fit}(f) = C_1.e^{(f-k_1/m_1)^2} + C_2.e^{(f-k_2/m_2)^2} \tag{4.5}$$

where $C_1, C_2, k_1, k_2, m_1, m_2$ are parameters to be fitted using least squares fitting, $MTF_{fit}(f)$ is a function of the spatial frequency f. Using a Gaussian fit ensures that the tails of the curves taper to zero as expected for the MTF. The fits were in excellent agreement with the measured data as shown in Figure 4.4, with approximately 0.97% - 1.7% relative difference between MTF_{fit} and the experimental presampled MTF, between the range of 0 - Nyquist frequency for each system. In addition, the curve fitting mitigated the effects of the noise in the measurements.

MTF_{fit} was interpolated to obtain a two dimensional MTF filter. Data points at (u,v) in MTF_{2D} were calculated based on its distance f from the centre frequency point (0,0) and correlating this to the respective frequency component in the MTF_{fit} profile in both directions. The contribution from MTF_{fit} from either direction was weighted based on how close it was to either profile.

$$MTF_{2D}(u,v) = MTF_{fit,u}(f).W_u + MTF_{fit,v}(f).W_v \tag{4.6}$$

where

$$f = sqrt(u^2 + v^2) \tag{4.7}$$

$$W_u = tan(v/u) \tag{4.8}$$

$$W_v = 1 - W_u \tag{4.9}$$

As the presampled MTF includes the sampling of the digital detector, it is important to take account of this in the following resampling stage. Digital detectors use square pixels, which in the spatial domain are modelled as a *rect* function. In the frequency domain, this is represented as a *sinc* function. To remove the sampling effect of the digital detector, the MTF needs to be divided by a *sinc* function in both directions:

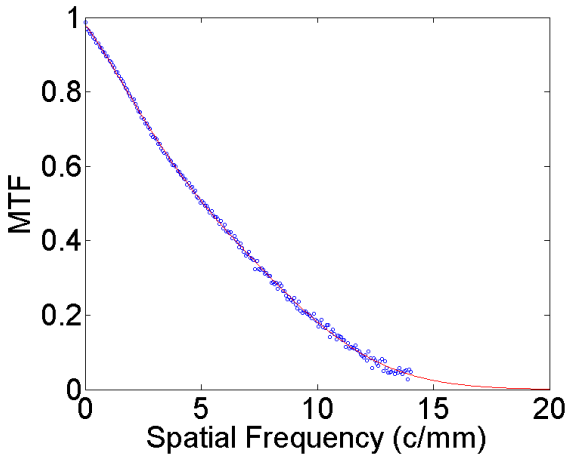
$$MTF_{filt}(u,v) = \frac{MTF_{2D}(u,v)}{sinc(au).sinc(bv)} \tag{4.10}$$

where MTF_{filt} is the input MTF filter function to be used to filter the idealised image, MTF_{2D} is the two-dimensional representation of the fitted presampled MTF, u and v are spatial frequencies conjugate to x and y, a and b refer to the detector's pixel aperture dimensions from which the MTF_{pre} originates. The MTF_{filt} can be considered the *intrinsic MTF* for the detector system.

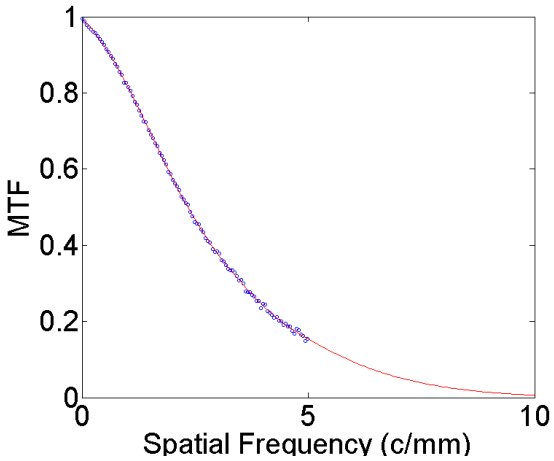
To maintain the same sampling intervals in frequency space in both directions, a block of zero values was added to the idealised image such that the number of pixels in the x direction equalled that in the y direction. The MTF_{filter} is defined upto the Nyquist frequency of the idealised image's sampling ($10\mu m$, f_N = 50c/mm) to the spatial dimensions of the image.

$$I_B(x,y) = IFFT\left(FT\left(I_{idealised}(x,y)\right).MTF_{filt}(u,v)\right) \tag{4.11}$$

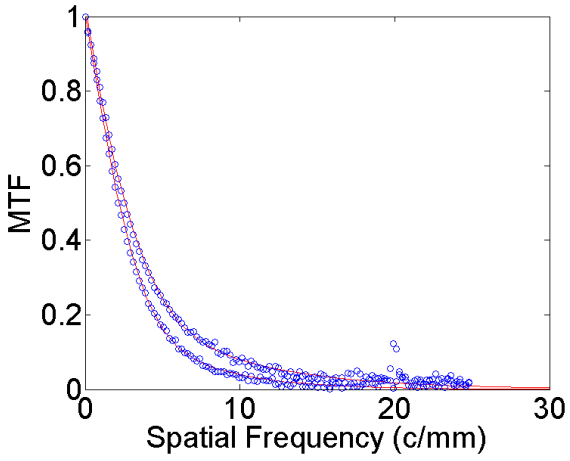
After the inverse Fourier transform, the block of zero values were cropped from the blurred image, I_B. The next stage requires the image to be downsampled to the coarser pixel sampling of the digital mammography detector under investigation.



(a) Hologic Selenia



(b) GE Essential



(c) Agfa

Figure 4.4: Examples of the Gaussian curve (red) fitted to the measured MTF data (blue o), extrapolated to show the model tapers to zero.

4.3.3 Resampling

The blurred image, $I_B(x, y)$, is at the same sampling as the idealised image of $10\mu m$ per pixel. The pixel size and detector technologies developed within this work are detailed in Table 4.1. Resampling was carried out with the neighbourhood averaging method. This closely matches the physical process of sampling as the charge from detected photons are collected and integrated into one pixel bin. Thus, in the case of the Hologic Selenia system which has $70\mu m$ pixel sampling, the pixel intensity in a group of 7x7 pixels in the I_B is averaged and assigned to one pixel in the blurred resampled image, $I_{B,R}$, as illustrated in Figure 4.5. This process is repeated by taking the next consecutive 7x7 pixel region in $I_B(x_i, y_j)$ to generate the pixel value intensity in the next pixel of $I_{B,R}(x_k, y_l)$.

$$I_{B,R}(x_k, y_l) = \frac{\sum_{i,j=1}^{X_N, Y_N} I_B(x_i, y_j)}{M^2} \tag{4.12}$$

where X_N and Y_N are the maximum number of pixels in the x and y direction, respectively, whilst M is the number of pixels within the neighbourhood, in the case of the Hologic Selenia system this is 7x7 pixels.

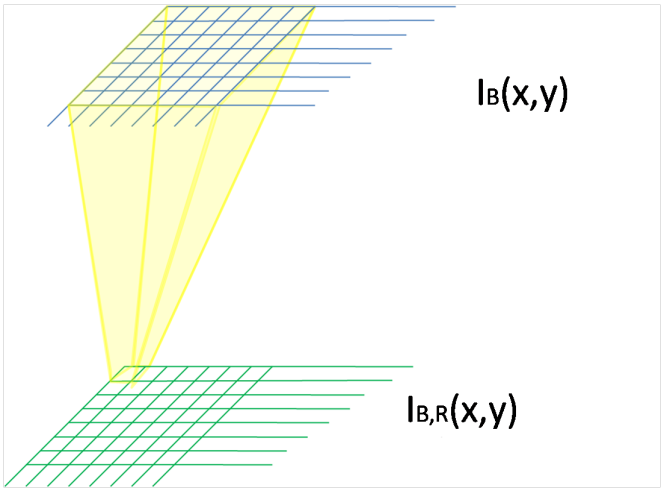


Figure 4.5: Neighbourhood averaging of pixels in $I_B(x, y)$ into $I_{B,R}(x, y)$

4.3.4 Finding the minimum sampling ratio

Based on work by Saunders and Samei[61], there was concern that the sampling ratio between the idealised image, $I_{idealised}$, and the blurred resampled image, $I_{B,R}$, was only 5:1, less than the recommended 8:1 ratio given in their work. It is recognised that there would be aliasing inherent as all digital mammography systems are undersampled[58]. However, we do not want to introduce further artifactual aliasing into the synthetic image. Therefore, the edge was sampled with either 5:1 (idealised image with $10\mu m$

pixel size) or 10:1 (idealised image with $5\mu m$ pixel size) ratios, and the resultant MTF from the $I_{B,R}$ was compared. The results of this are shown in Figure 4.6 and compared with the experimental MTF (averaged from the two directions). The relative difference for the 5:1 ratio sampling was 1.5% compared with 10:1 ratio sampling of 1.3%. As there was only a small effect on the resultant MTF, a ratio of 5:1 sampling was considered sufficient for the simulation procedure for all the systems modelled.

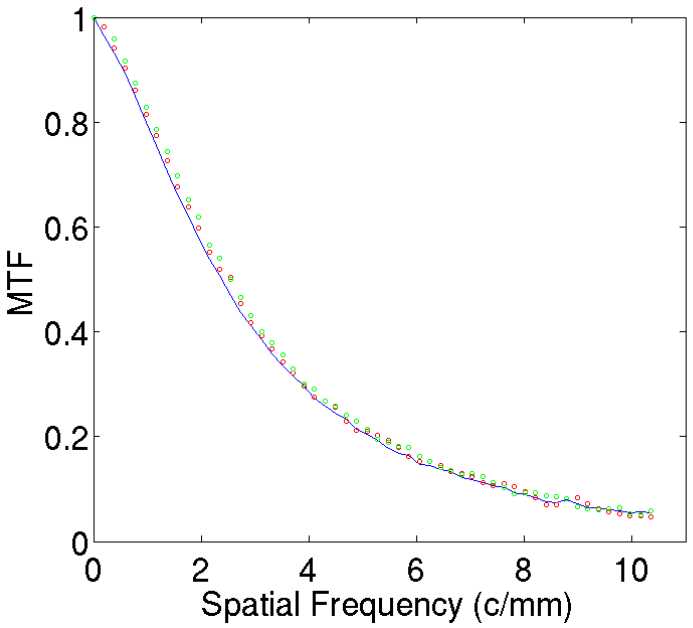


Figure 4.6: The experimentally measured MTF (blue curve) plotted against presampled MTFs measured from synthetic edge images. The synthetic edge resampled at 5:1 ratio is shown in red and the synthetic edge resampled at 10:1 is shown in green.

4.3.5 Validation methodology

To model the MTF in synthetic images, an idealised image of a synthetic edge image was created. A blank background image was created with pixel size corresponding to $10\mu m$, with pixel intensity value of 600 arbitrary units. An edge was created by placing a rectangular foreground shape with a pixel intensity value of 60 arbitrary units(corresponding to 10% edge transmission) and tilted at 1.3°. This was carried out with the use of MATLAB's [99]built-in function *imrotate* using a bilinear interpolation method. The MTF was measured for this edge to verify the only blurring effect in the image at this point is due to the subpixel sampling of the MTF measurement. ImageJ measures the MTF with a subpixel sampling of one tenth of the pixel, in this case equivalent to $1\mu m$. The results of went smoothly to zero at the Nyquist frequency associated with the subpixel sampling (0.1 x 10μm) as shown in Figure 4.7.

From this, it can be inferred that there is no blurring effect from the *imrotate* procedure on the edge and the approximation to an idealised edge image is as expected, with only the effects of the subsampling in the measurements affecting the MTF from the images.

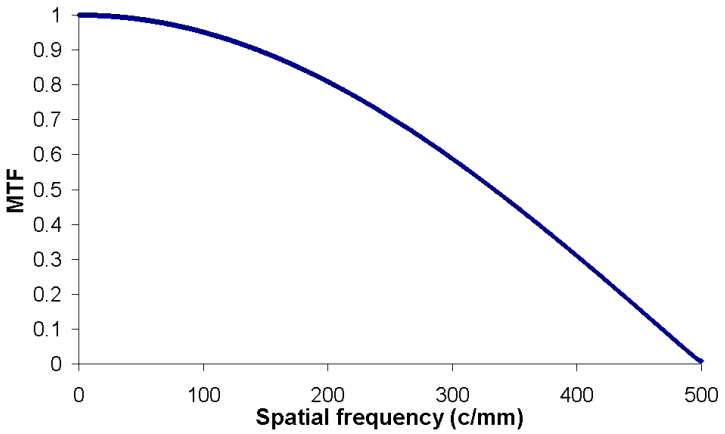


Figure 4.7: Presampled MTF measured from a sharp edge image of $10\mu m$ pixel size. The data falls to zero at the Nyquist frequency for the subpixel sampling of $1\mu m$.

The next step required filtering with the MTF filter. Each system's presampled MTF was divided by the sinc function associated with the particular system's intrinsic detector pixel size. The MTF filter was interpolated to the image dimensions of the idealised edge image and used to filter the image in Fourier space. The subsequent blurred image was then resampled to the pixel size of the system as outlined in Section 4.3.3.

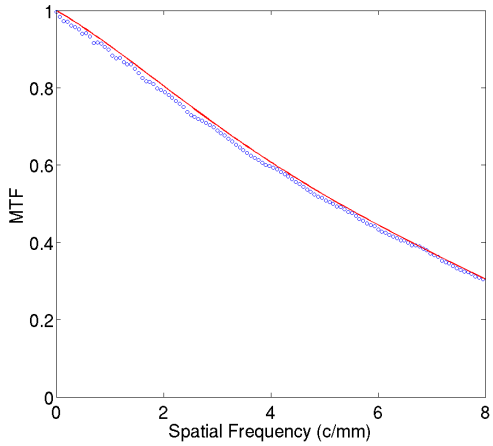
4.3.6 Validation Results

Comparison of the synthetic MTF and experimental MTF are shown in 4.8 for all three systems.

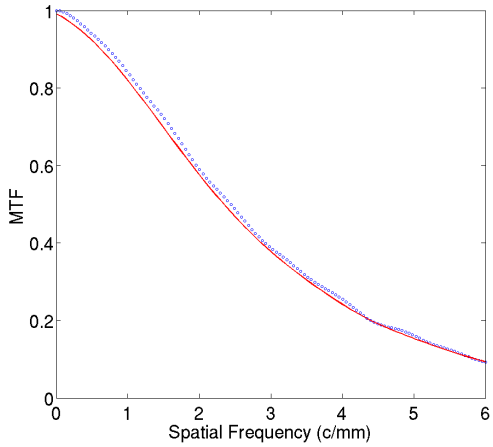
The difference between experimental (fitted) and simulated curves were calculated as[61] between the frequency range of $0 - f_n$ for all systems:

$$MTF_{diff} = \frac{\Sigma_i \mid MTF_{exp,i} - MTF_{sim,i} \mid}{\Sigma_i MTF_{exp,i}} \times 100\% \tag{4.13}$$

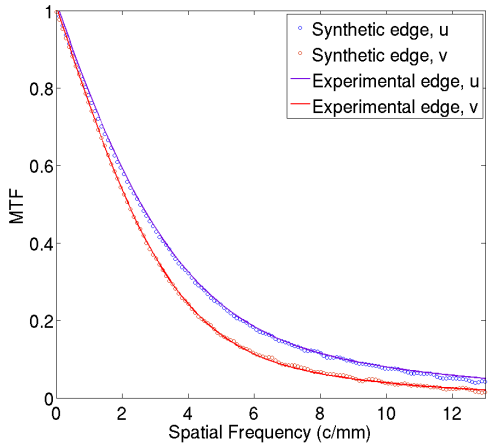
where Δ is the interval width, $MTF_{exp,i}$ and $MTF_{sim,i}$ refers to the experimental and simulated MTF curves, respectively. The experimental MTF in this case refers to the curve fitted to the original experimental data as this will not have noise included. For the Hologic Selenia system the Nyquist frequency is 7.14c/mm, the GE Essential system has a Nyquist frequency of 5.00c/mm and for the Agfa the Nyquist frequency is 10.00c/mm. Table 4.2 displays the relative differences at zero to one quarter, to one half, to three quarters and to the maxmimum of their respective Nyquist frequencies.



(a) Hologic Selenia



(b) GE Essential



(c) Agfa

Figure 4.8: MTF profiles derived from synthetically derived edge images compared with the experimentally acquired counterparts.

From the data in Table 4.2, For all systems, the difference between MTF_{sim} and MTF_{exp} increases with increasing spatial frequency. Overall, the relative difference has been found to be less than 2%, showing agreement with Saunders and Samei[61]. Increased error at higher spatial frequencies suggest increased level of noise at this range which can be expected for this method of MTF measurement.

Table 4.2: Relative difference between experimental and simulated MTF curves at respective spatial frequencies for each imaging system for different ranges up to the Nyquist frequency. Brackets denote the v direction in the Agfa system.

Spatial frequency range	Hologic Selenia %	GE Essential %	Agfa %
0 – 0.25	1.50	1.4	1.25 (0.51)
0 – 0.50	1.78	1.78	0.77 (0.35)
0 – 0.75	1.80	1.96	0.82 (0.32)
0 – f_n	1.81	1.96	0.89 (0.24)

4.4 Intrinsic Sampling MTF

Despite the misnoma of the "presampled" MTF, $MTF_{pre}(u, v)$ includes the blurring effects from digital pixel sampling, $S(u, v)$, as well as those of the physical MTF blurring, $MTF_{int}(u, v)$, associated with the imaging system itself[58]. Pixel apertures are typically square, thus, the MTF due to discrete pixel sampling can be modelled as a sinc function:

$$S(u, v) = sinc(au).sinc(bv) \tag{4.14}$$

where a and b are the pixel dimensions. The presampled MTF is therefore a product of these two processes:

$$MTF_{pre}(u, v) = MTF_{int}(u, v).S(u, v) \tag{4.15}$$

Providing the sampling is sufficiently fine so as not to affect the intrinsic MTF of the detector then $S(u, v)$ is insignificant. However, in actuality, the digitisation process (pixel sampling) may well impose upon the $MTF(u, v)$. In image processing, it is well-established that interpolation methods impose their own filtering effects upon the resampled image[100, 85, 101]. This interpolation method applies a sinc function.

The presampled MTF used to model the blurring effects of the DM system has the blurring effects of the pixel sampling aperture. Having now accounted for pixel sampling and the intrinsic MTF blurring, we now account for any change in the pixel sampling dimensions. This may be needed, for example, in considering the optimisation of an imaging detector.

4.4.1 Resolution modification of idealised images

Prior work addressing this issue[61, 88, 102] has divided the filter function by the sinc function associated with the final sampling aperture. This suggests that the sinc

function is used to account for the downsampling stage in the blurring image simulation chain. This is not strictly accurate. Due to the way the presampled MTF is measured, sampling is inherent in the pixel sampling, but not digitisation[58]. Therefore, we propose it is necessary to account for the pixel aperture of the system for which the presampled MTF was measured in order to accurately model the blurring process in the simulated image.

This is particularly important if the aim is to modify an image from one system to appear as if acquired from another imaging system with a different MTF. If a filter function is to be applied to an idealised image in preparation for the resampling stage, the filter function $MTF_{filt}(u,v)$ must not have the sampling from the original system. For the sake of clarity, we rewrite Equation 4.15:

$$MTF_{filt}(u,v) = \frac{MTF_{pre,o}(u,v)}{S_o(u,v)} = MTF_{int,o}(u,v) \tag{4.16}$$

The subscript 'o' refers to the original imaging system. When this $MTF_{filt}(u,v)$ is applied to filter an idealised image which is subsequently sampled to the pixel size of the original system, the effects of $S_o(u,v)$ will be have been mitigated.

Alternatively, it may be that one wishes to study the effects of sampling an image with same $MTF_{int,o}(u,v)$ with a different pixel size. In which case, equation 4.16 still applies as it can be seen that $MTF_{filt}(u,v) = MTF_{int,o}(u,v)$. Thus subsequent sampling to an alternative pixel size will provide the correct representation of an image for a system with the intrinsic MTF of the original system but with a different pixel size.

Starting with the case where it is only the pixel resampling that is affected and the intrinsic MTF remains the same:

$$MTF_{pre,A}(u,v) = MTF_{int,A}(u,v).S_A(u,v) \tag{4.17}$$
$$MTF_{pre,B}(u,v) = MTF_{int,B}(u,v).S_B(u,v) \tag{4.18}$$

For the particular case, where $MTF_{int,A}(u,v) = MTF_{int,B}(u,v)$ but the pixel size for system A and B are different. In order to correctly filter an idealised image, $F(u,v)$, as defined in Equation 4.2 with the correct resolution (blurring and sampling), it can be seen that Equation 4.16 will provide the correct filter for blurring an image for resampling to the pixel size of system B:

$$G_{sim,B}(u,v) = F(u,v).MTF_{int,A}(u,v).S_B(u,v) \tag{4.19}$$

This theory will be applied to idealised images in Section 4.4.3. Before doing so, we extend the above to converting resolution properties of clinical images from one system to appear as if acquired on another system.

4.4.2 Clinical Image Synthesis

Significant research is focussed on imaging system performance to understand its impact on diagnostic performance such as cancer detection[32, 33, 82, 88, 103]. In such studies, a large number of data sets are needed in order to measure the significance

of optimising observer performance with respect to specific parameters in the imaging chain. Obtaining statistically significant numbers of images is often a major challenge. Thus an image simulation tool that can synthesise image of one imaging system, when actually acquired on another system, would provide a powerful method for creating such data sets. In such studies, one needs to be confident that any modification to the original images applied does not introduce new image artefacts. This section therefore introduces theory which ensures pixel sampling and intrinsic MTF blurring effects are correctly accounted for. The key difference here is that we start with a clinical rather than idealised image.

In assessing resolution properties of such systems, one may wish to take a clinical image with the inherent imaging properties of system A and process the image such that it appears as if acquired from system B. Unlike the previous section, system A and B referred here do not have the same intrinsic MTF. In converting an image from one system to appear as if acquired on another system, one needs to also take account of how the signal and noise transfer properties change from one system to another. In radiological applications, effects such as beam hardening, beam quality and scatter will need to be taken into account. However, this is deemed outside the scope of this current work, but this is addressed in [88, 103]. Considering only MTF blurring effects, the following theory can be applied to convert images from system A to synthesise an image from system B.

Consider $G_A(u,v)$, the Fourier transform of an image acquired from imaging system A with MTF blurring properties described by $MTF_{pre,A}(u,v)$. To convert $G_A(u,v)$ to appear as if acquired on system B, the process begins with deconvolving the image with the blurring properties of system A:

$$G(u,v) = G_A(u,v).\left(MTF_{pre,A}(u,v)\right)^{-1} \tag{4.20}$$

Here, the blurring and sampling effects of system A has been theoretically deconvolved from the image $G_A(u,v)$. Next, the intrinsic blurring of system B will need to be applied without the intrinsic sampling effects of system B. The reason for this is that $G_A(u,v)$ still has the sampling rate of system A, therefore the resulting filtered image will need to be resampled after the filtering process.

$$G_{sim,B}(u,v) = G(u,v).\left(\frac{MTF_{pre,B}(u,v)}{S_B(u,v)}\right) \tag{4.21}$$

$G_{sim,B}(u,v)$ will subsequently be resampled to the pixel size of system B using neighbourhood averaging methods.

The next section demonstrates the effects of correcting for the resolution modification process with the sinc function derived either from the presampled MTF or the final resampling process. In addition, investigation will be made into how this affects image blurring when upsampling or downsampling an image for various study purposes. It must be borne in mind that upsampling an image will not increase the information in the image. Correcting for the upsampling will ensure that the image will not be further degraded unnecessarily.

The first part will validate this process with the use of hypothetical presampled MTFs and the second part will apply this knowledge to correctly degrade an experimentally

acquired X-ray image from one system to appear as if acquired on another system. For most intents and purposes, applying the MTF of one digital imaging system and resampling the image to the same pixel size poses no problem.

4.4.3 Validation results

To validate the theory described in the previous section, idealised edge images were created with unit sampling a, which is assumed to be fine enough not to affect the subsequent MTF measurements. This idealised image was filtered with MTFs and sampled to multiples of the pixel sampling a to represent systems A and B and as described below. The presampled MTFs were measured from these synthetic images and compared with theory.

Starting from idealised images

Considering the initial case discussed in section 4.4.1, a validation of the required $S(u, v)$ was carried out. Two presampled MTFs were created with the same intrinsic MTF and different $S(u, v)$ to represent two different imaging systems as described in Equations 4.18.

Idealised images of an edge were filtered with $MTF_{int}(u, v)$ and sampled for system A and B. This is shown in Figure 4.9.

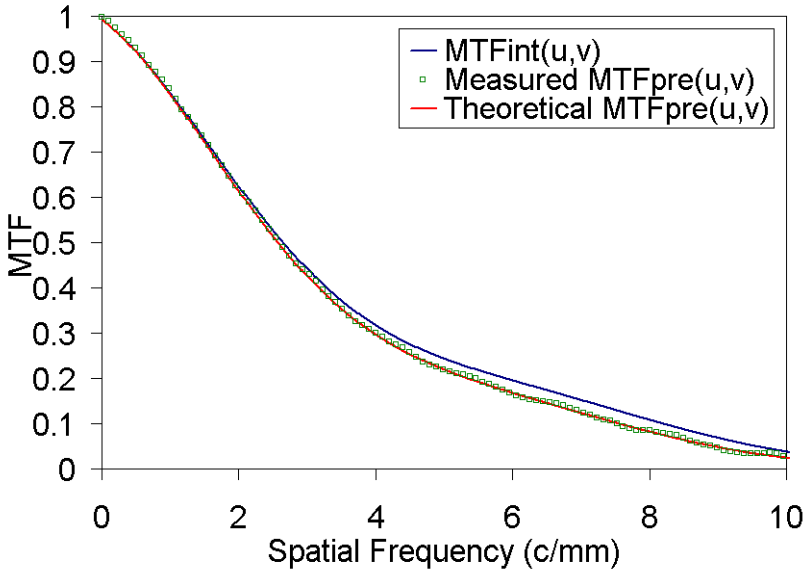


Figure 4.9: The modelled intrinsic MTF (blue curve) was used to filter a $7a$ pixel edge image and the resultant measured presampled MTF (green data points) was compared with the theoretical presampled MTF (red curve).

To validate the image simulation process, images with the same intrinsic MTF and different pixel size were created. This was undertaken by deriving $MTF_{filt}(u, v)$ as in

equation 4.16 from $MTF_{int,A}(u,v)$ and filtering the idealised images. Next the filtered images were sampled to the pixel size of system B. It can be seen in Figure 4.10 that using the $S(u,v)$ from system A, there was excellent agreement between the $MTF'_{pre,B}$ and the presampled MTF of the simulated image.

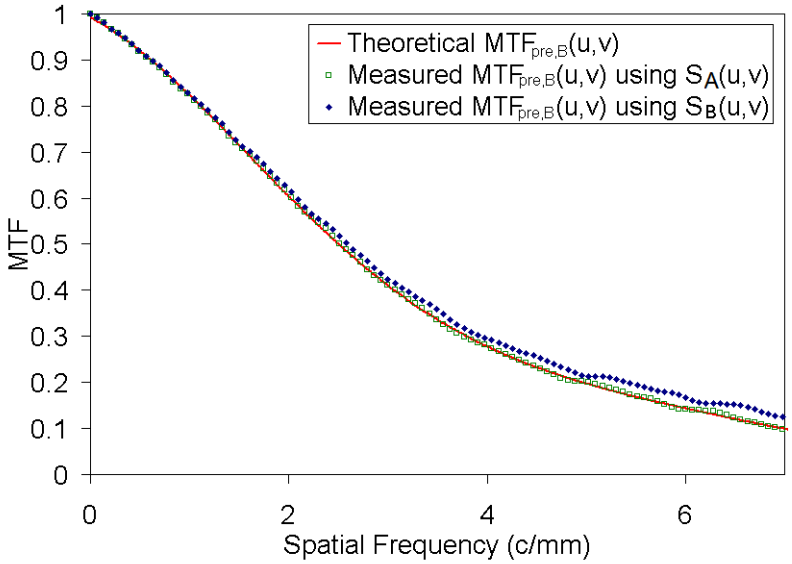


Figure 4.10: The measured presampled MTF was used to filter an edge image sampled at $5a$. The theoretical MTF for system B is shown in red. Different sinc functions were applied to the presampled MTF for filtering the $5a$ edge image, denoted in brackets.

Simulating different systems

Theory described in section 4.4.2 will be explored here. Images of an edge phantom was experimentally acquired from two systems. The image from system 1 was filtered as follows:

$$G_{sim,B}(u,v) = G_A(u,v).\left(\frac{MTF_{pre,B}(u,v)}{MTF_{pre,A}(u,v).S_B(u,v)}\right) \tag{4.22}$$

$G_{sim,B}(u,v)$ was inverse fourier transformed and downsampled to the pixel size of system B with neighbourhood averaging. The effect of this is presented in Figure 4.11.

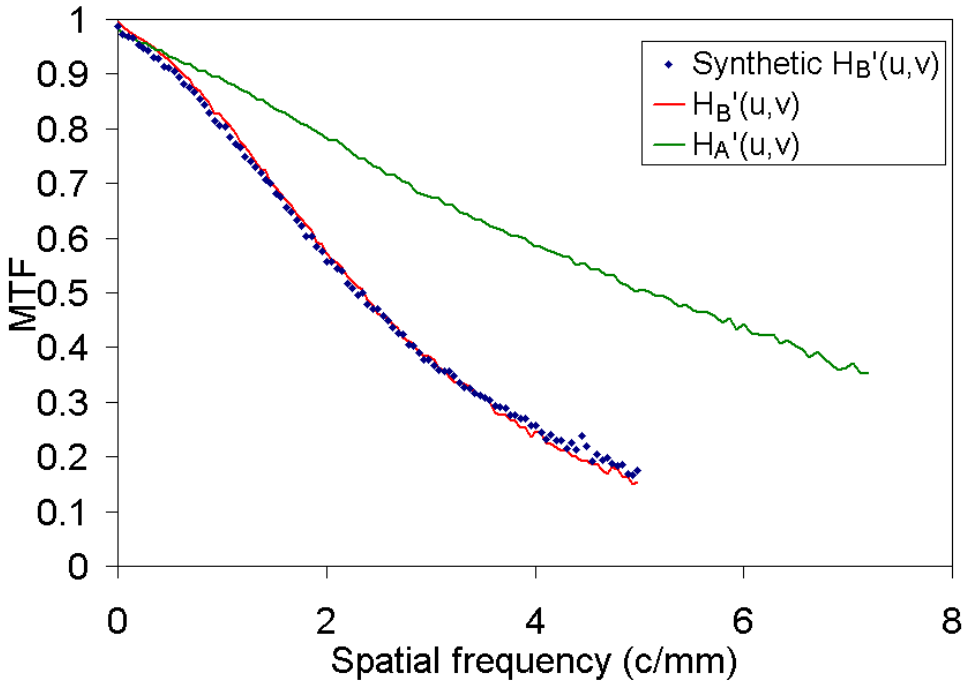


Figure 4.11: Presampled MTFs acquired from an edge image from the Hologic Selenia system (green) and GE Essential system (red). The edge image from the Hologic Selnia system was filtered and resampled to appear as if acquired on the GE Essential system and the presampled MTF measured (blue).

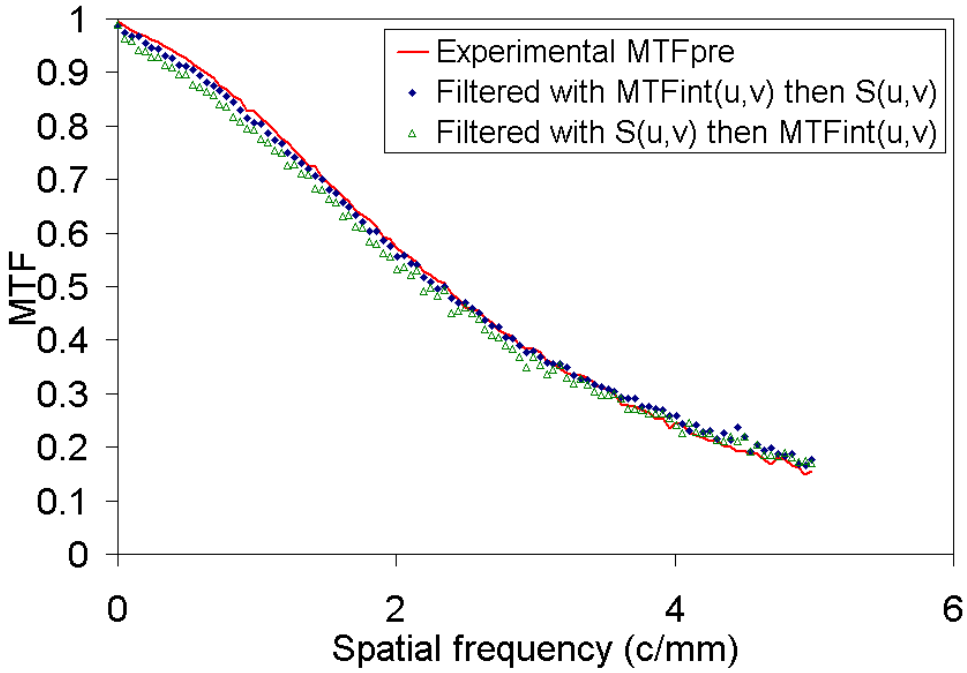


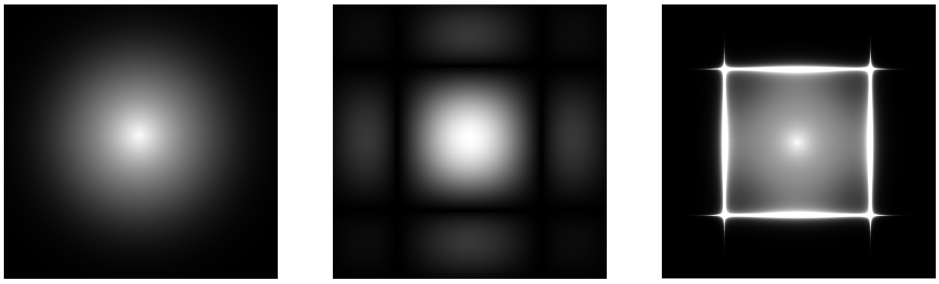
Figure 4.12: The effects of resampling before or after the filtering stage in an image simulation chain for a clinical edge image.

As can be seen, there is an excellent agreement between the presampled MTF of the clinical image from system B and the synthetic image for the same system. Furthermore, the effect of resampling the image before or after the filtering process was investigated as shown in Figure 4.12. It can be seen that there is there is better agreement in the final synthetic $MTF_{pre}(u, v)$ and experimental $MTF_{pre}(u, v)$ if the resampling is carried out after the filtering process. The $MTF_{pre}(u, v)$ improved with the simulation process where the resampling process was undertaken *after* the filtering stage by 2%. The reason for this is that if the image is resampled before filtering, even though the image is deconvolved with the relevant $S(u, v)$, information lost in the image from the resampling cannot be recovered.

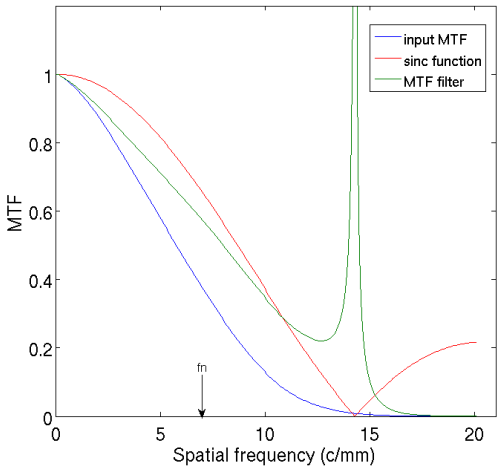
4.5 MTF analysis

We now consider the effects of the intrinsic MTF and pixel sampling on the resultant observed MTF. It was noted that if the spatial frequency spectrum was extended beyond the Nyquist frequency of the imaging receptor, a sharp spike occurred. Further investigation into this found that this occurred at the point at which the sinc function falls to zero, below the presampled MTF. This results in the MTF filter exceeding unity and causes the artefact illustrated in Figure 4.13c. In the spatial domain the image exhibited ringing artefacts. In the case of neighbourhood averaging, which is modelled by a sinc function in the frequency domain. It is known that the sinc function of the resampling process will have considerable energy beyond the Nyquist frequency as discussed by Parker et al[100], causing the extensive ringing artefacts.

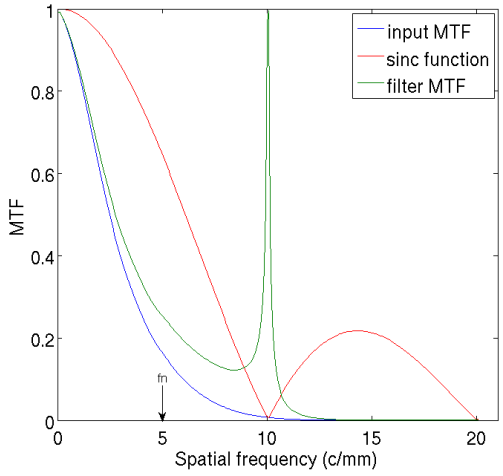
Typically the Nyquist frequency is approximately half the frequency at which the sinc function reaches zero, therefore there should be no information after this point. However, this spike causes ringing artefacts in the final simulated edge image. There are concerns that if a presampled MTF is obtained from a system with a pixel size double that of a system which we would like to simulate, there maybe difficulties in effectively removing this spike artefact without distorting the MTF_{filt}. If the presampled MTF does not sufficiently go to zero before the sinc function zero point, there will be a spike in the MTF filter at the Nyquist frequency that will visibly distort the image without windowing. Other authors[61, 88, 100] suggest use of a window function to force the MTF_{filt} to zero before the sinc function reached this point. The limitation of this is that for each system with different pixel size the Hann window will need to be configured individually.



(a) $MTF_{pre}(u,v)$ (b) $S(u,v)$ (c) $MTF_{filt}(u,v)$



(d) Profile of each function, for the Hologic Selenia system



(e) Profile of each function, for the GE Essential system

Figure 4.13: Effects of the sinc function on the presampled MTF. (a) is the presampled input MTF, (b) is the 2D sinc function corresponding to the original sampling of the presampled MTF, (c) is the resultant MTF filter after division of the input MTF by the sinc function. A clearer idea of the effects is shown in the profile in (d) for the Hologic system.(e) reiterates this point with an example for the GE Essential system.

Since the intrinsic MTF is expected to be isotropic and it is from the sampling aperture that the anistropy occurs, the 1D presampled MTF was divided by the correct sinc function. The result was fitted with a double Gaussian model, such that the model fitted smoothly through the spike. This fitted 1D profile was interpolated into a 2D MTF_{filt}. Figure 4.14 presents the Hann windowed synthetic presampled MTF compared with the modelled synthetic presampled MTF. The Hann windowing method lead to a synthetic presampled MTF that deviated on average 0.0077 ± 0.0021 from the experimentally acquired MTF. The Gaussian model method lead to a synthetic presampled MTF that deviated 0.0046 ± 0.0019. This is a very small difference, but still gives satisfactory if not improved results. As mentioned earlier the issue with using the Hann windowing method is that a lot of trial and error is required for each system set up to ensure that the artefact of the spike is removed in each case.

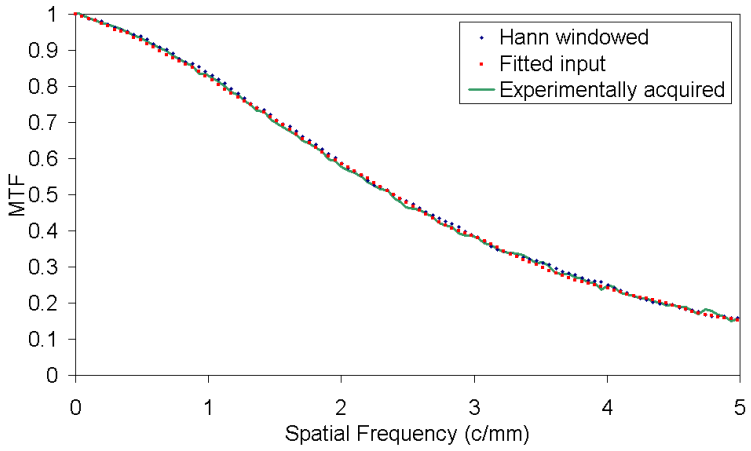


Figure 4.14: An example of the synthetic MTF derived from a Hann windowed MTF filter (blue points) compared with that derived from a Gaussian modelled MTF filter (red points). Both MTFs have been compared with the experimentally acquired MTF to be modelled (solid green curve).

4.6 Noise Simulation

The NPS was experimentally measured from a uniform image of PMMA using the particular detector systems to be simulated over a range of doses. Doses in this experiment have been calculated for incident air kerma at the surface (IAKS) of the detector without backscatter. DM systems are operated in the quantum limited range of doses, where the quantum noise (from X-ray photon fluctuation) is the dominant source of noise. Quantum noise is Poisson noise. However, with increasing n, in this case number of photons (n>20)[104], a Poisson distribution can be modelled by a Gaussian distribution with a probability density distribution given by:

$$p(z) = \frac{1}{sqrt(2\pi\sigma)} e^{-(z-\bar{z})^2/2\sigma^2} \tag{4.23}$$

where the mean, $\bar{z}$, is equal to zero and the variance, σ^2, is scaled such that it is equal to unity.

For this work, as we do not operate at excessively low doses clinically, a Gaussian noise field has been chosen as the noise model. A Gaussian noise field is generated randomly with the same dimensions as the blurred resampled image. This is to ensure that when it is applied to the $I_{B,R}(x, y)$ created earlier, it does not change the overall mean pixel intensity.

The next step is to filter the Gaussian noise field with the digital mammography system's NPS in frequency space as seen in Figure 4.15.

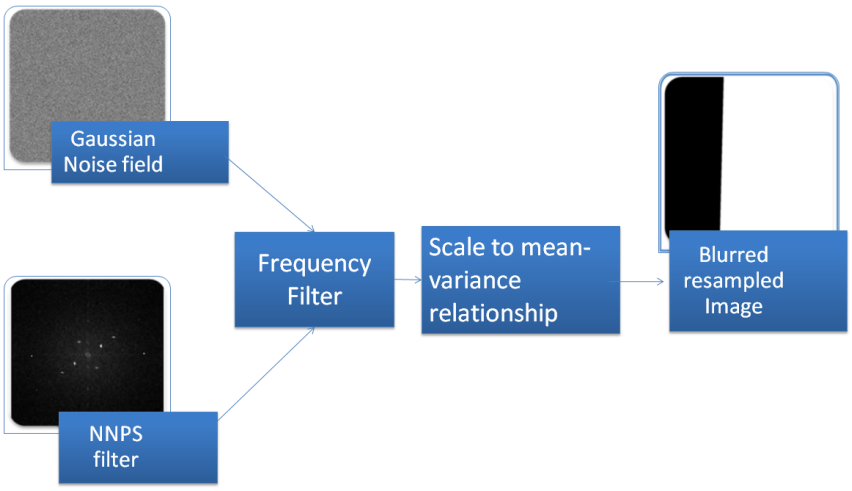


Figure 4.15: Flow chart to depicting the process to simulate the noise properties of digital mammography images.

4.6.1 NPS filter

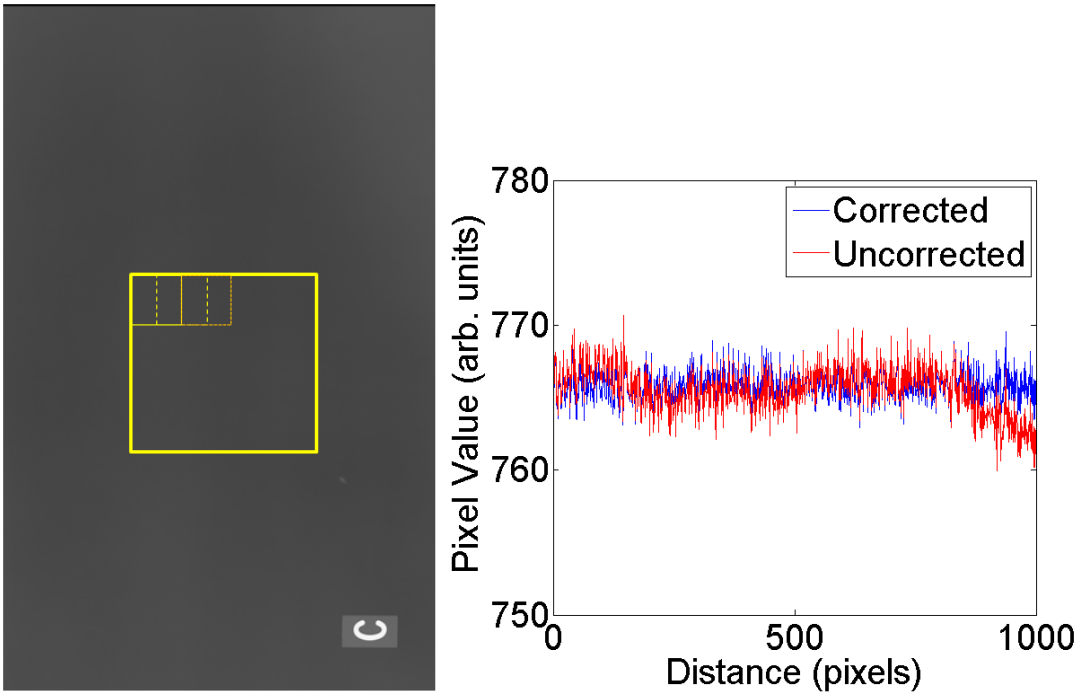
The NPS was measured from an experimentally acquired uniform image as outlined by Marshall[50]. Care was taken to ensure the region of interest (ROI) was placed in the centre of the uniform PMMA phantom. In digital mammography, it is necessary to remove the heel effect to improve image quality of clinical images. This is carried out with the use of a flat-fielding algorithm during acceptance testing. Prior personal experience showed that residual effects of the heel effect remained in the images. Prior to NPS measurement, the residual heel effect was removed from the uniform ROI as will be described below. The heel effect presents itself in an image as a slowly varying intensity inhomogeneity. Removal of this effect will be described before the measurement of NPS is made. This will be followed by discussion of simulating different dose levels from available dose references.

In order to remove the heel effect from the uniform image, the noise needs to be removed. There are two main methods published in which to remove the heel effect for NPS measurement as described in Chapter 3. The heel effect can be removed using a 2D polynomial fit or with the use of a smoothing filter. Although the polynomial fit provided a more accurate measure of the NPS at low frequencies, a median filter was chosen to remove the heel effect bias in each ROI used for NPS measurement. It is considered in this case that the more important information is found in the higher frequencies and the use of a median filter to remove the heel effect would reduce the processing time drastically.

A median filter with kernel size of 100 x 100 pixels was applied to the ROI. The corrected image, I_{corr}, is the uniform image, I_U, corrected for the heel effect:

$$I_{corr}(x,y) = I_U(x,y).\frac{I_U(x,y)}{medfilter\{I_U(x,y)\}} \tag{4.24}$$

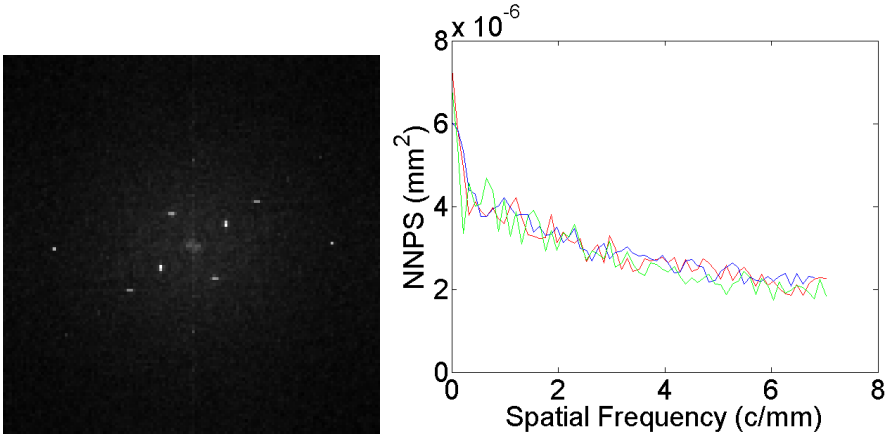
225 sample ROIs with dimensions of 128 x 128 pixels were placed at half overlapping ROI intervals in the large ROI as shown in Figure 4.16a. Profiles in Figure 4.16b the effect of applying Equation 4.24 to the large ROI. In this case for the Hologic Selenia system, the pixel value intensity deviated by less than 1%. This increased to 1.5 and 3% for the GE Essential and Agfa CR systems, respectively. It has been quoted [67] that 128x128 pixel sample ROIs can lead to spectral leakage, therefore before the NPS was calculated from the samples, each window was applied a Hanning window. The NPS was calculated as in Equation 3.15 for each sample ROI and averaged over the sample ROIs. Typically the (0,0) frequency in the NPS was overestimated[11, 50]. A polynomial fit was made to the radial averaged NPS (without the zeroth frequency) and used to extrapolate to find a new value.



(a) (b)

Figure 4.16: (a) Sample ROIs defined within the uniform PMMA image for NNPS measurement. (b) Profile across the ROI before and after correction for the residual heel effect.

The 2D NNPS was found to contain spikes in the u-v axis, as shown in Figure 4.17a, which are attributed to the anti-scatter grid[50, 55]. These are artefacts in the image which should not be included in the noise measurement. In addition, due to the relatively small number and size of sample ROIs available from which to take an averaged NPS, it was decided that it would be more accurate to obtain a fitted radial NPS and interpolate this isotropically into a 2D NPS. The original 2D NPS was radially averaged to obtain a 1D plot. This was then interpolated into 2D as described in Equation 4.6. Figure 4.17b shows the NNPS averaged in the x and y axes and at 45°, illustrating that the isotropic assumption was adequate for this work. To obtain the noise filter for the Gaussian noise image, this fitted NPS was divided by the maximum value found in the



(a) 2D NNPS (b) 1D NNPS representations in x and y axis

Figure 4.17: (a)2D NNPS illustrating the spikes in the x and y axis and 45°. (b) shows the NNPS in the x, y and 45° axes (blue, red and green respectively).

NPS. This gives the noise transfer function with which to filter the noise image:

$$NTF(u,v) = \sqrt{\frac{NPS(u,v)}{max(NPS(u,v))}} \tag{4.25}$$

This NTF was interpolated to the frequencies corresponding to the Gaussian noise image, $I_N(x,y)$, and used to filter this noise image in Fourier space:

$$I_{N,corr}(x,y) = IFFT\left[FT\left(I_N(x,y)\right).NTF(u,v)\right] \tag{4.26}$$

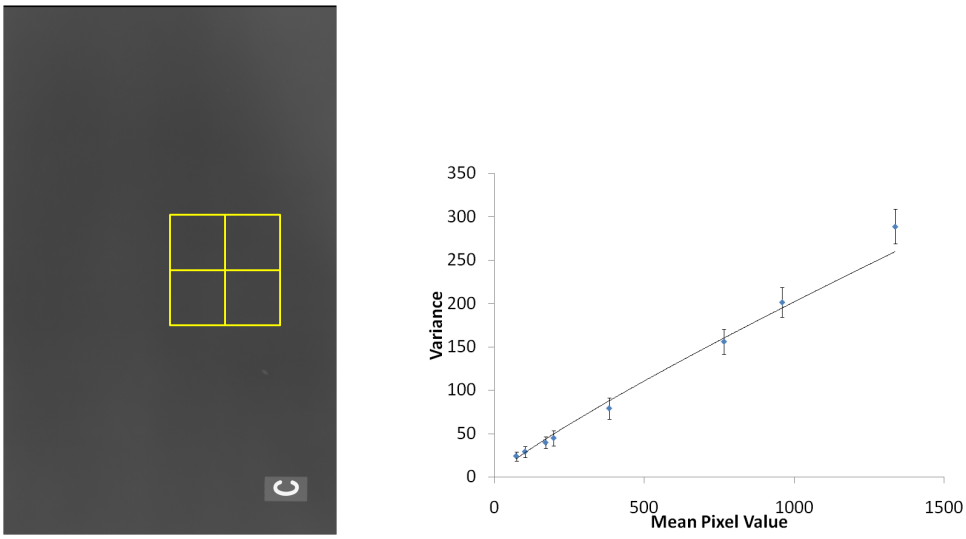
Where the $I_{N,corr}$ is the correlated noise image, a noise image filtered by the NPS filter.

4.6.2 Dose simulation

As the X-ray image noise follows a Poisson distribution in the quantum limited range, the noise variance in mammographic images is a function of the mean pixel value (which can be directly related to the dose absorbed). Therefore, a mean variance relationship was measured from experimental image data acquired from all of the mammography systems to be simulated over a variety of doses. Use of large ROIs to measure the variance leads to inaccuracies. Therefore smaller ROIs are needed to get a more accurate measure of the relative noise without the heel effect - in terms of mean pixel value or variance. Figure 4.18 shows how the mean variance was measured, with an example of the mean variance relationship plotted for one of the Hologic Selenia.

A 'clean' image, I_c, is created for a specific dose using the detector response shown in Figure 4.1. The correlated noise image, $I_{N,corr}(x,y)$, produced from the previous step is now related to I_c on a pixel by pixel basis using the mean-variance relationship to create the scaled correlated noise image, $I_{N,S}$:

$$I_{N,S}(x,y) = I_{N,corr}(x,y).\sqrt{k\left(I_c(x,y)\right)^n} \tag{4.27}$$



(a) ROIs used for measurement of mean and variance

(b) Mean variance relationship for the Hologic Selenia system

Figure 4.18: Measuring the mean-variance relationship.

where k and n are constants fitted to the mean-variance relationship. The noise image is scaled in accordance with the value of the $I_c(x, y)$ on a pixel by pixel basis to take into account the dependence of noise in the pixel values. This corrected noise, $I_{N,S}(x, y)$, image is now added to I_c to give the final simulated image, I_{sim}:

$$I_{sim}(x, y) = I_c(x, y) + I_{N,S}(x, y) \tag{4.28}$$

It is possible to replace the noiseless image with the blurred resampled image created in Section 4.3.2 to simulate a complete image purely from the detector characteristics.

Although we can alter the level of noise in an image, the shape of the NNPS alters with varying dose. This reflects the dominance of the different noise sources discussed earlier (electronic, quantum and structural) under different acquisition conditions. For example, purely quantum noise would present as white noise, which in a NNPS for an ideal detector would give a near flat shape. A real system would give correlated noise, thus the NNPS would approximate a flat shape multiplied by the MTF^2[68]. In addition there are other noise sources as discussed in previous chapters.

Although it is possible to obtain uniform images at any dose for simulation, it would be advantageous to be able to simulate different doses using a different dose level as a reference. This has been carried out previously by other authors, in particular Båth et al[94]. Using Equation 4.29, the NPS could be scaled to any dose required. This is, however, reliant on the DQE between the doses to be the same. This is a fair assumption for the DQE within limits, the major effect on the DQE is the beam quality[105]. Thus, it is preferable to use reference doses close to that which is to be simulated.

$$NPS_{sim} = NPS_{orig}.\left(\frac{D_{orig}}{D_{sim}}\right)^2 \tag{4.29}$$

where the dose is measured as incident air kerma at the surface (IAKS) of the detector.

To create a flat-field image at a dose which a reference NPS is not available for, it is possible to use Equation 4.29 to create a NPS. Assuming quantum noise is the dominant source of noise, the NPS of the higher dose image can be scaled with the square of the ratio of the original to simulated dose. NPS_{sim} was normalised as in Equation 4.25 and used to filter a Gaussian noise image.

$$I_{N,C} = IFFT(NTF_{sim}(u,v).FFT(I_G(x,y))) \tag{4.30}$$

This correlated noise image was scaled to the I_{clean} using the mean-variance relationship as described before. Flat field images from a range of doses(64-256μGy) were chosen as D_{orig} to simulate a lower dose D_{sim} of 48μGy. From this it can be established how accurately doses can be replicated when actual doses are not available to the user to use as a reference. Based on work by Veldkamp et al[96], it is expected that the standard deviation of the synthetic image would match that of the experimentally acquired image. However, as the original dose extends further from the simulated dose, the measured NNPS may begin to alter in shape.

4.6.3 Validation methodology

The goal of the validation of the noise image creation part of the chain is to validate its ability to create noise images for specific doses using the same dose for which the NNPS was obtained accurately. Secondly, it is necessary to understand how accurately the noise in an image can be simulated when applying the NNPS from a different dose.

To measure the NNPS in synthetic images, a synthetic uniform image was created. The pixel value intensity in the uniform image, P_{uni}, is calculated based on the detector response of the system in Equation 3.1. A uniform image with dimensions corresponding to the pixel size of the detector to be simulated was created. A Gaussian noise image was created with the same dimensions as the uniform image with zero mean and unit variance as defined earlier. This Gaussian noise image was filtered as described in Equation 4.26.

The resultant correlated noise image was inverse fourier transformed into the spatial domain and scaled to the blank image on a pixel-by-pixel basis using the mean-variance relationship described in Equation 4.27 for each system modelled. Various doses were simulated like-for-like, for all systems. In addition, reference (64-256μGy) doses were used and scaled as in Equation 4.29 to simulate an image as if acquired at 48μGy.

Noise in the images was measured in the spatial and Fourier domain. A ROI was defined in the central part of the image, equivalent to 10cm by 10cm for all systems. Within this ROI the relative noise was measured, given as the ratio of the noise (measured as standard deviation in the image) to the mean pixel value:

$$\sigma_{rel} = \frac{\sigma}{\mu} \tag{4.31}$$

The results for the three systems are given in Table 4.3, 4.4 and 4.5.

4.7 Validation Results

4.7.1 Noise

Results of the aforementioned spatial measurements between the experimental and synthetic images were in agreement with less than 0.5% relative error in all systems. The only exception was for the highest doses. At such high doses, the structural noise component was becoming a more dominant noise source and the mean-variance relationship defined in Equation 4.27 begins to break down at this point.

Table 4.3: Relative noise measured for the experimental and simulated images for the Hologic Selenia System. A set up of 31kVp W/Rh target/filter settings were used with a variety of tube current-time products to achieve different doses. All simulated images were simulated using the same reference dose.

Dose (μGy)	Relative noise % (Experimental)	Relative noise % (Simulated)
25.6	4.63	4.50
64.0	3.19	3.17
102.4	3.04	3.03
128.0	2.73	2.74
256.0	2.10	2.06
1410.2	1.87	1.61
2563.9	1.59	0.70

Table 4.4: Relative noise measured for the GE Essential System, for the experimental and simulated images. A set up of 29kVp Rh/Rh target/filter settings, using a variety of tube current-time products to achieve different doses. All simulated images were derived from using the same reference dose.

Dose (μGy)	Relative noise % (Experimental)	Relative noise % (Simulated)
29.3	4.82	4.85
58.5	2.66	2.68
91.1	1.86	1.91
184.2	1.23	1.19
360.0	0.797	0.786
737.0	0.547	0.552
1474.0	0.397	0.406
2337.1	0.328	0.338

In the Fourier domain, the NNPS of the experimental and simulated images were compared as illustrated in Figure 4.19 for the Hologic Selenia system. To measure the differences between the NNPS, the zero-frequency interval was ignored as this can include overestimates of noise. The integral difference was found to calculate the error

Table 4.5: Relative noise measurements for the Agfa System, for the experimental and simulated images. A set up of 29kVp Mo/Rh target/filter settings were used with a variety of tube current-time products to achieve different doses. All simulated images were generated using the same reference dose.

Dose (μGy)	Relative noise % (Experimental)	Relative noise % (Simulated)
16.8	3.21	3.02
50.2	1.82	1.68
102.7	1.31	1.17
204	0.987	0.843
504	0.753	0.579

in the radial NNPS:

$$NNPS_{diff} = \frac{\Sigma_i \mid NNPS_{exp,i} - NNPS_{sim,i} \mid}{\Sigma_i NNPS_{exp,i}} \times 100\% \tag{4.32}$$

Thus for the range up to f_n, the integral difference was found to be between 2.6% and 6.18% for the range of doses simulated for the Hologic Selenia. For the GE Essential system, the integral difference varied between 1.2 - 3.1%. Error increased with increasing doses.

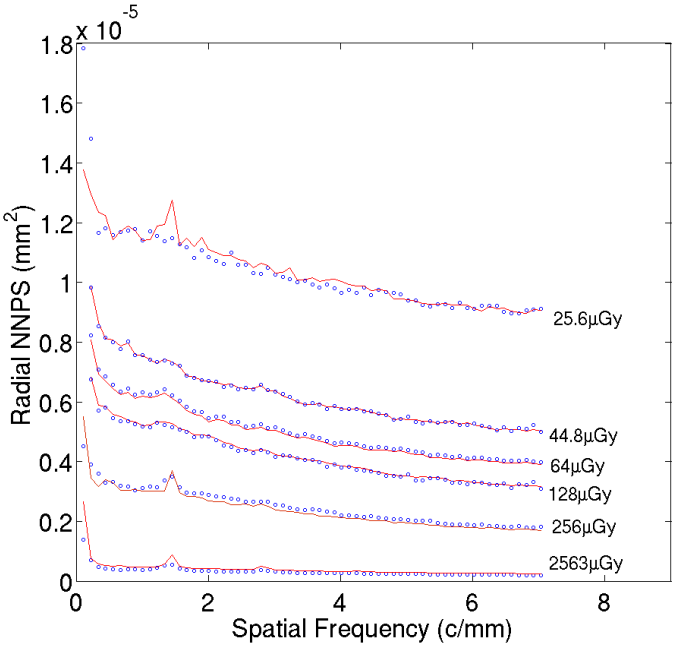


Figure 4.19: Radial NNPS of experimental (solid lines) compared to simulated (points) images for six doses for the Hologic Selenia.

Five doses were simulated and compared for the Agfa system: 16.8, 50.2, 102.7, 204 and 504 μGy. The results of the dose simulation are shown in Figure 4.21. For 16.8,

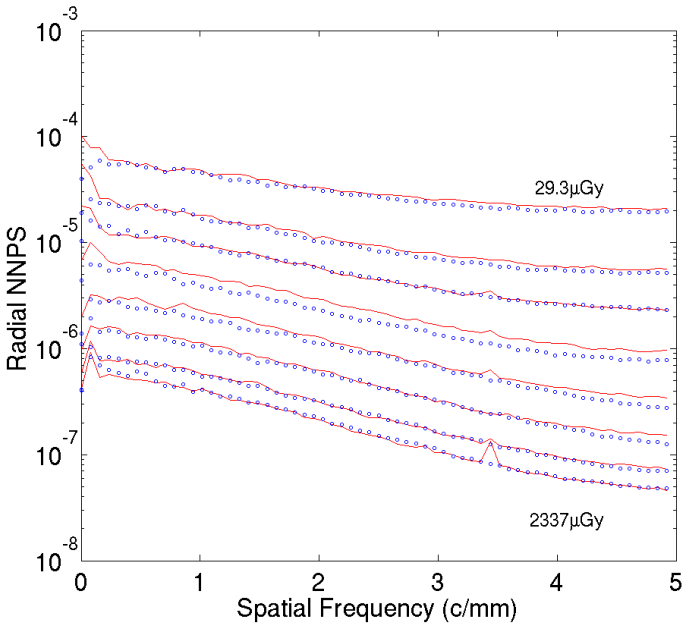


Figure 4.20: The radial NNPS for the GE Essential system. Solid curves show the radial NNPS of experimentally acquired images, circular points show the radial NNPS of the synthetic images. Doses correspond to those detailed in Table 4.4.

50.2, 102.7, 204 and 504μGy doses, the integral difference in the radial NNPS between experimental and simulated images are 4.75%, 16.0%, 36.0%, 37.0% and 28.0%, respectively up to the f_n spatial frequency range. This is much higher than the other two systems. In all cases, the simulation was found to be overestimating the noise power in the images, whereas the spatial measurements of the image showed the relative noise consistently lower than the experimental results.

Upon further investigation, the mean-variance relationship used was found to be overly simplistic. The mean-variance relationship assumes quantum noise to be the main contributor of noise which was applicable for the flat-panel detectors. However, for CR, there is a higher level of contributions from structural noise sources. Alternative noise sources are additive, therefore the total noise, σ_t, in the image can be found from summing the squared standard deviation from each source:

$$\sigma_t^2 = \sigma_e^2 + \sigma_q^2 + \sigma_s^2 \tag{4.33}$$

where σ_e,σ_q,σ_s are the standard deviation noise from electronic, quantum and structural sources, respectively. This can be re-written in terms of relative noise, σ_t/K, as[52]:

$$\frac{\sigma_t^2}{K^2} = \frac{\sigma_e^2 + \sigma_q^2 + \sigma_s^2}{G^2.K^2} = \left(\frac{k_e}{K}\right)^2 + \frac{k_q^2}{K} + k_s^2 \tag{4.34}$$

where P is the average pixel value in the ROI, k_e, k_q, k_s is the electronic, quantum and structural noise terms, respectively, E is the exposure level at the detector surface and G is the detector gain. Rearranging this for use as the new mean-variance relationship

$$\sigma_t^2 = k_e^2 + k_q^2.K + k_s^2.K^2 \tag{4.35}$$

This created a more accurate mean-variance relationship.

Fitting the data to Equation 3.5, there was a vast improvement with the radial NNPS measurements: integral difference fell from approximately 30% to 6% for the largest error seen in the five doses simulated. This is shown in Figure 4.21. The standard deviations in the simulated images are compared in Table 4.6 with the experimental results.

Equation 4.35 was also applied to the highest dose for the Hologic Selenia system, at 2563μGy, which exhibited the largest error. The resulting relative noise measurement from the synthetic image was seen to be 1.55%, a better agreement with the experimental relative noise of 1.59%. This suggests that for the amorphous selenium system (Hologic Selenia), the quantum noise assumption broke down at doses above $256\mu Gy$. The quantum-only noise assumption led to overestimation of the relative noise in the GE Essential as seen in Table 4.4. When the Equation 4.35 was applied, the maximum relative error between experimental and synthetic relative noise measurements fell from 3.1% to 0.9%. For the Agfa CR system, structural noise played a bigger part even at the lowest dose. The largest error was seen to be 23.1% in Table 4.5, compared with the largest error in Table 4.6 found to be 0.3%. For the CR system, the system is more susceptible to structural noise despite the use of needle imaging plate technology, therefore a quantum-only noise model is insufficient.

Table 4.6: Revised relative noise measurements for the Agfa System, for the experimental and simulated images using the mean-variance relationship developed in Equation 4.35. All simulated images were simulated using the same reference dose.

Dose (μGy)	Relative noise % (Experimental)	Relative noise % (Simulated)
16.8	3.21	3.37
50.2	1.82	1.79
102.7	1.31	1.31
204	0.987	0.992
504	0.753	0.755

The radial NNPS measured for the Agfa CR system in for experimental and synthetic images are shown in Figure 4.21. As the dose reduced in the Agfa setup, the simulated NNPS data was found to be higher than the experimental data, particularly prominent in the low frequency range. The integral error between the experimental and synthetic radial NNPS was found to range between 1.3 - 5.8% for the doses shown after the multiple noise source mean-variance relationship was applied.

To assess the effects of simulating images from alternative reference doses, two different doses were used to simulate an image at 44.8μGy for the Hologic Selenia system. The resultant radial NNPS curves are shown in Figure 4.22. The relative difference between the simulated dose to the experimental data was found to be 2.25% and 8.61% for the spatial frequency range up to f_n. The large error was found for the largest D_{orig}, 256μGy where the dose was approximately four times the dose to be simulated. Thus, if doses are to be modelled using alternative dose references, it must be borne in mind that the error will increase with the difference between D_{orig} and D_{sim}.

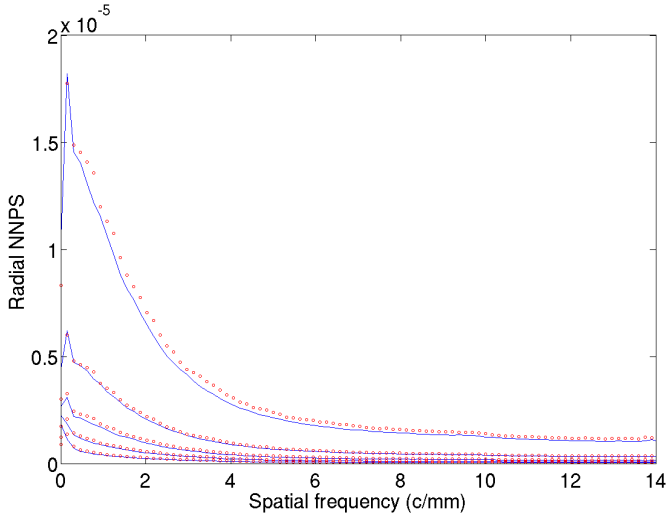


Figure 4.21: Comparison of radial NNPS from experimental (blue, green and orange curve) and simulated (red circles) images for the Agfa CR system. The doses (from top down) are 16.8, 50.2, 102.7, 204 and 504 μGy.

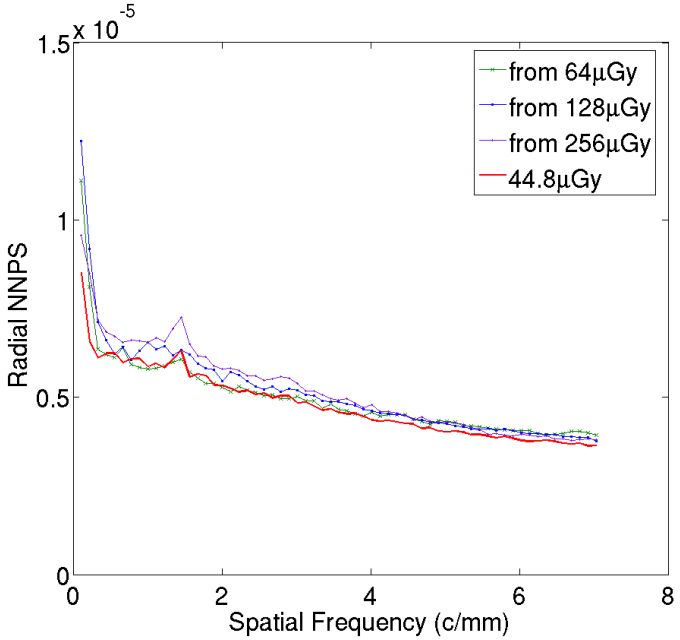


Figure 4.22: Radial NNPS of images simulated at 44.8μGy from different doses. The experimental NNPS is shown in the bold solid curve for comparison.

4.8 Discussion and Conclusions

Simulations for three systems have been carried out using the experimentally acquired spatial resolution and noise characteristic of each. MTF measured from synthetic edge images were seen to be within 2% of the experimental MTFs. Differences in the MTF were in agreement with those published by Saunders and Samei[61].

Further investigation into the resampling effects of the simulation chain has shed light onto the real steps in the process. It has been found that the presampled MTF is a misnoma, and in actuality includes the effects of sampling aperture from which the measurement was acquired. Work by Saunders and Samei[61] had assumed this was not the case, and thus used a sinc function related to the final sampling stage in the simulation chain. This contradictory theory was investigated with the use of a theoretical MTF model, as a known intrinsic MTF and resampled to two different system pixel sizes to produce effective presampled MTFs. This presampled MTF was used to look at simulating the same system with a new pixel sampling. It was found that indeed, the sinc function required in order to correctly simulate the system's images is related to the presampled MTF's original sampling.

Furthermore, a method to counteract the effects of MTF resampling artefacts was proposed and provided a more robust method of modelling the MTF for different DM systems when compared with previous Hann windowing methods.

Flat-field images were created to validate the noise simulation framework. It was seen that the detector response of each system could be faithfully simulated, with the correct mean pixel value corresponding to each dose. Variance for each system was effectively simulated for lower doses. However, very high doses pose a problem in simulation as we begin to leave the quantum limited range of the the system and structural noise poses more of a problem. The mean variance function measured for these systems begin to deteriorate at the higher doses. This was vastly improved with the use of a mean variance function with three components to model the electronic, quantum and structural noise. Relative error between the relative noise measurements for the three systems modelled ranged from 0.9 - 1.3%.

Analysis of the radial NNPS for simulated and experimental flat-field images showed a good agreement with integral difference ranging between 1.2 - 6.8% integral difference between the radial NNPS curves for all three DM systems presented in this study. Large improvements were seen when the mean-variance relationship was modelled on a multiple noise source assumption. Integral errors for the Agfa CR system radial NNPS reduced from 30% down to less than 6%.

The dose reduction methodology was implemented to simulate a low dose image with the use of NPS from a range of higher dose images. It was found that although the relative noise was accurately modelled, the shape of the NNPS measured from the synthetic images varied. The relative difference between experimental and synthetic NNPS varied between 2.51 - 8.61%. The error was larger as the original dose extended further from the dose to be simulated. This is to be expected as the NNPS of $I_{D_{orig}}$ used to filter the noise image to create the low dose synthetic image will not have changed shape, although it had been scaled to the correct level. Thus, in future use of

this methodology, it will be necessary to use D_{orig} as close as possible to the dose to be simulated.

Chapter 5

CDMAM Synthesis and Contrast Detail Analysis

In the previous chapter, the imaging chain to simulate the resolution and noise properties of the digital mammography system was thoroughly validated for three systems. Validation was carried out on simple clinical test objects, with uniform background or a straight edge. Typical clinical mammograms have a lot of clutter with a range of contrasts between structures. It is hard to validate simulation of such images, as there is little ground truth with which to assess the simulation. For a typical mammogram, it would present a major challenge to ascertain what tissues the X-ray photons traversed before reaching the detector. In contrast, Monte Carlo could provide exact details of the energies and paths traversed by each photon. However, the current available breast phantoms are not sufficiently realistic[36] or thoroughly validated[35] for such clinical tasks.

In the clinical environment, it is typical to assess the imaging system based on the observer's ability to detect subtle details in an image, akin to detecting signs of cancer in a mammogram. As discussed in Section 3.4, assessment of physical performance of an imaging system with consideration to the observer can be carried out with the CDMAM phantom. The CDMAM phantom is made up of gold discs with varying thickness and diameters.

There has been only one other author that has attempted to simulate images of the CDMAM phantom. Grosjean et al [86] has attempted to simulate CDMAM phantom images based on Monte Carlo methods with the aim to validate design options of digital mammography systems without the need for physical prototyping. A polychromatic X-ray spectrum was passed through individual cells of the CDMAM phantom to produce a setup of 4cm PMMA and the CDMAM aluminium and PMMA combination. The results was measured with the Image Quality Factor (IQF), which matched the experimentally acquired images across a range of doses. The IQF gives an average of the smallest disc diameter visible, $D_{i,min}$, for each disc thickness, C_i:

$$IQF = \frac{n}{\sum_{i=1}^{n} C_i D_{i,min}} \tag{5.1}$$

where n is equal to 16. Since the results were output as a single value for each dose, it is difficult to understand the effects of noise and blurring as the contrast and diameter of the disc changes. The detector was modelled on a CsI phosphor scintillator with the use of the energy absorption coefficient for the scintillator. The simulation process also employed the use of detector MTF. The different noise components (quantum, electronic and scintillation) were modelled separately in the process. The noise simulation implemented for this experiment has modelled noise components separately, unlike the noise creation process described and used elsewhere[64, 61].

The limitation of this work is that the individual blurring and noise simulation process were not validated. The CDMAM phantom was used as a point of validation for the simulation tool developed by Grosjean et al. However, each cell was simulated individually on the basis that the image was uniform. Effects from residual heel effect and scatter were not included. Also, the noise model described was specific to scintillator technology as this is the chosen technology of the author's institution (GE Healthcare). It may be applied to other technologies by replacing the scintillation techology with others such as a-Se or CR phosphor plates. In addition, Monte Carlo methods can be a complex process to implement as it requires in-depth understanding of the physical composition and properties of the X-ray system. Therefore, it can take several hours to create one image. The method presented in this thesis can take between 10 – 60 minutes to create one image, depending on the nature of the image. In addition, as the imaging properties of the system is modelled on the MTF and NPS, the image simulation chain can be applied to any detector technology.

This chapter presents the simulation images of the CDMAM phantom. Through combining the blurring and noise creation imaging chains from the previous chapter, the CDMAM phantom image creation process can be modelled from an idealised image to the final simulated image. Methodology of the validation process for the CDMAM phantom image is presented with the use of the CDCOM software[38] as well as the methodology for an in-house developed CDMAM phantom scoring software that provides additional information on the contrast to noise ratio of discs within the CDMAM phantom image. Experimental CDMAM phantom images were compared with the simulated images for three digital mammography systems with the use of automated scoring softwares. The CDMAM phantom image simulation framework was evaluated and subsequent requirements of image simulation framework was also explored.

5.1 Methodology

This section discusses the methodology of the simulation and evaluation of the CDMAM phantom. The following section describes the creation of an idealised CDMAM phantom image as an input for the image simulation framework described in the previous chapter. The idealised image of the CDMAM phantom was created through use

of a template for the CDMAM phantom grid and numerals. Within this grid, discs of varying contrast and diameter were inserted to represent the different disc thicknesses and diameters present in the phantom. Images from a DM system for different settings such as beam quality, exposure levels or technology were simulated using the image simulation framework desribed in the previous chapter.

5.1.1 Modelling the CDMAM Phantom

In acquiring CDMAM phantom images, the CDMAM phantom is placed between two slabs of 20mm thick PMMA on top of the detector surface. The set up of this is shown in Figure 5.1. The CDMAM phantom is made up of 5mm of PMMA and 3mm of aluminium, this has an X-ray attenuation equivalency of 10mm PMMA in total.

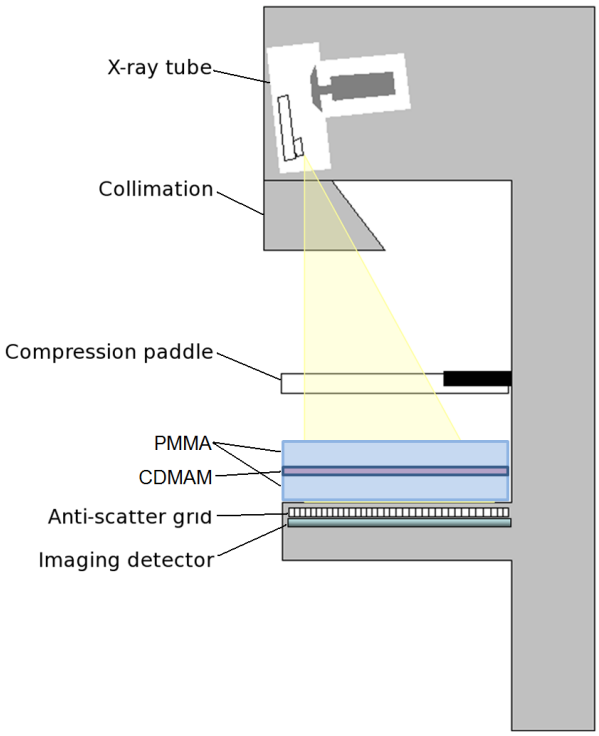


Figure 5.1: Set up for the acquisition of a CDMAM image

The composition of the CDMAM phantom was discussed in Section 3.4. It was seen that the phantom comprises a grid and numerals for reference in scoring the gold discs. To create the idealised image of the CDMAM phantom, this grid was replicated through thresholding of an actual X-ray image of a CDMAM phantom. A high dose X-ray image was selected to provide the highest resolution representation of a CDMAM test phantom with the lowest relative noise. For this reason, an image was obtained from a Hologic Selenia system, with a pixel size of $70\mu m$ at an MGD of 4mGy (approximately 2 times the clinical dose[29]). From the thresholded image, noise artefacts and discs were removed manually and the lines were sharpened to create the CDMAM phantom

template. The binary image resultant of the thresholding process is shown in Figure 5.2.

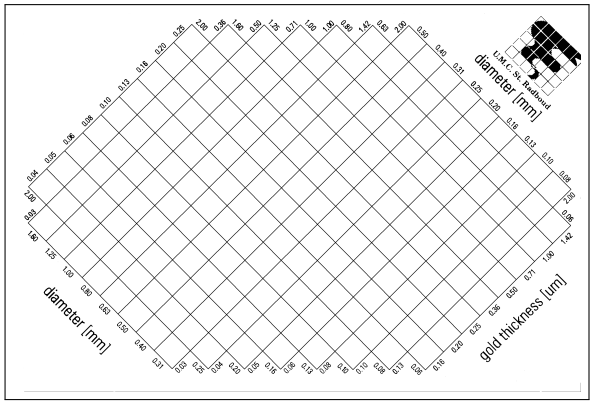


Figure 5.2: The CDMAM phantom binary template created from thresholding an X-ray image of the test phantom.

To create the idealised image, the background pixels of the CDMAM phantom binary template were assigned an intensity consistent with the detector response at the dose to be simulated. This required a detector response measurement as described in Section 3.1 applied to a set of CDMAM phantom images at different doses. Pixels within the grid lines and numerals were consequently assigned an intensity at approximately 20% of the background intensity. This had been chosen as the grid lines are irrelevant in scoring the CDMAM and there was difficulty in determining the exact pixel value intensity from images as there were too few pixels from which to draw a true value from.

The idealised image is at the same pixel size that the template had originated from, $70\mu m$. To create an idealised image input that is applicable to all the detector pixel sizes currently available, the idealised image was upsampled to $10\mu m$ per pixel using bilinear interpolation methods. This method was chosen to conserve the idealised nature of the image with minimal inconsistencies in the lines. Further to the process of creating the idealised image, discs were placed within the grid at $10\mu m$ sampling. Physically, the discs vary in diameter between 0.03-2.00mm in 16 approximately logarithmic intervals, and in thickness between 0.06-2.00μm in 16 approximately logarithmic intervals. There are two things to consider when creating discs: the discs need to be inserted into the idealised image input with the correct size and the discs need to have the correct contrast with respect to the local background representative of its gold thickness.

5.1.2 Creating the discs

Each gold disc was created in a template of 200 x 200 pixels, this was equivalent to 2.00mm, the largest disc diameter. Within this template, D, the size of the disc is defined using the radius specified. Any pixel at a distance less than or equal to the specified integer radius from the centre is included and defined as part of the disc.

$$D(x,y) = \begin{cases} P_{disc} & \text{if } x^2 + y^2 \leq r^2 \\ P_{bgd} & \text{otherwise} \end{cases}$$

The background of the template of the disc is assigned a pixel value intensity based on the local background of the idealised image input P_{bgd}, which, as defined before is related to the dose which the image is to represent.

The disc within the template was assigned a pixel value intensity to give a contrast relating to the gold thickness with which the disc represents. This contrast-thickness relationship was defined through manual analysis of discs within linearised X-ray images of a CDMAM phantom for different beam qualities. The contrast of the discs is affected by the X-ray beam quality. Consequently, it was advantageous to measure the contrast from an image using the highest dose available for the beam quality with which to simulate. As the discs reduce in diameter, the effect of blurring reduces the contrast of the disc resulting from X-ray attenuation only. Therefore, it was necessary to measure the signal within the largest disc for each disc thickness, using a circular ROI smaller than the disc itself to avoid the reduced pixel value intensities on the edges. Due to the limited number of pixels available to measure this signal within the disc (less than 100 pixels per disc), the signal was measured within the same disc for five different images taken at the same exposure and the average taken. This is illustrated in the Figure 5.3 with ROIs defined to show how the background pixel value intensity was defined also.

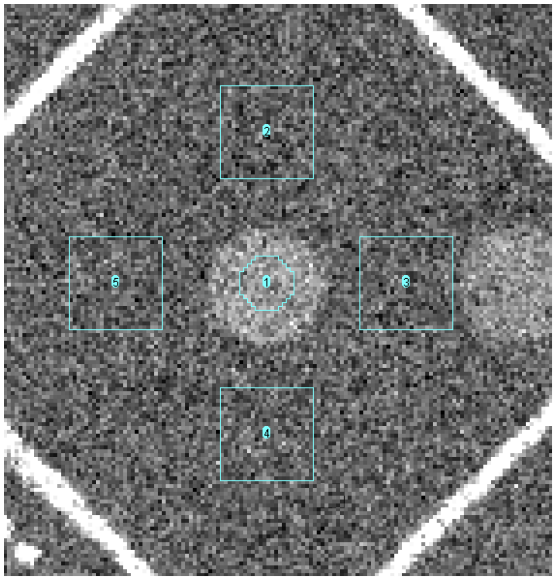


Figure 5.3: ROIs used for measuring the pixel value within the discs and local background.

The relative contrast, C, of the disc was calculated as follows:

$$C = \frac{P_{bgd} - P_{disc}}{P_{bgd}} \tag{5.2}$$

where P_{bgd} and P_{disc} refer to the background and disc pixel value intensities, respectively.

To model the contrast of a disc, the following set up is considered: a polychromatic X-ray beam traverses the CDMAM set up (4.5cm PMMA, 0.3cm aluminium). X-ray spectra for specific beam qualities is used to model the polychromatic X-ray beam. To simplify notation, the following equations are derived for a monochromatic X-ray beam. The number of the photons that traverse the background of the CDMAM phantom is N_1, equal to scatter and primary photons:

$$N_1 = P + S = P(1 + S/P) \tag{5.3}$$

The number of photons of a certain energy that traverse the CDMAM phantom layers plus the gold disc is N_2, assuming the scatter remains the same:

$$N_2 = Pe^{-\Delta\mu.t} + S \tag{5.4}$$

where $\Delta\mu$ is the linear attenuation coefficient of the layers of the CDMAM phantom setup. Equations 5.3 to 5.4 are defined for a monochromatic X-ray beam. In this work, polychromatic X-ray beams were used by implementing X-ray spectra for specific beam qualities from the IPEM database[106]. The number of photons and linear attenuation coefficients were defined for each corresponding energy interval within the spectra. The number of photons that traverses the defined layers are summated and used to calculate the contrast of the gold discs.

To find the contrast of the gold discs, Equation 5.2 can be used:

$$\begin{aligned} C &= \frac{P(1 - e^{-\Delta\mu t})}{P(1 + S/P)} \\ &= \frac{1 - e^{-\Delta\mu t}}{(1 + S/P)} \end{aligned} \tag{5.5}$$

where $\Delta\mu$ is the difference between the background CDMAM and the CDMAM and gold disc, S/P is the scatter to primary ratio. To relate this to the observed contrast, C_{obs}, measured from the experimental images, Equation 5.5 can be rewritten as[107]:

$$C_{obs} = \frac{C_p}{(1 + S/P)} \tag{5.6}$$

where C_p is the contrast of the disc due to primary photons only, i.e. no scatter.

C_p was derived by using Lambert-Beer's law and known linear attenuation coefficients[1] for PMMA, gold, aluminium etc; a variety of X-ray spectra (tube voltage, target/filter materials) with the same beam quality as used in acquiring the experimental images was passed through 4.5cm of PMMA slabs, the aluminium layer of the CDMAM phantom and the gold discs. The number of the X-ray photons was calculated for each energy in the polyenergetic spectrum for this set up before and after passing through the specified gold thicknesses used in the CDMAM phantom to obtain the relative contrast of the discs. Lambert-Beer's law (Equation 5.7) was fitted to the resulting analytical data:

$$I = I_0.e^{-\mu t} \tag{5.7}$$

$$\begin{aligned} Cp &= \frac{I_2 - I_1}{I_2} = \frac{I_0.(e^{-\mu_2.t} - e^{-\mu_1.t})}{I_0.e^{-\mu_2.t}} \\ &= 1 - e^{-\Delta\mu_a t} \end{aligned} \tag{5.8}$$

[1] Taken from XCOM Photon Cross Section database and calculated for specific densities of materials: http://www.nist.gov/pml/data/xcom/index.cfm.

The measured contrasts of the discs were fitted to Equation 5.9 to compare the relative difference with primary-only model for C_p. The corresponding linear attenuation coefficient for each system's beam quality, $\Delta\mu_a$, from the analytical model was compared with the experimentally measured $\Delta\mu_{fit}$.

$$C_{fit} = 1 - e^{-\Delta\mu_{fit}.t} \tag{5.9}$$

Discrepancies between $\Delta\mu_{fit}$ and $\Delta\mu_a$ were found to be due to the assumption of a scatter-free set up. Futhermore, the analytical model did not consider the compression paddle nor the detector efficiency for each detector technology used in this study. It has been seen that the compression paddle would contribute to the scatter[108, 109] in an image. The detector efficiency would also change with respect to energy and the detector composition. These factors were assumed to be small in this study. It was quoted[110] that the spectra used may have had up to 1kVp difference in its beam quality. This led to approximately 10% error in its final calculation of its attenuation coefficient. The effects of this are displayed in Figure 5.4.

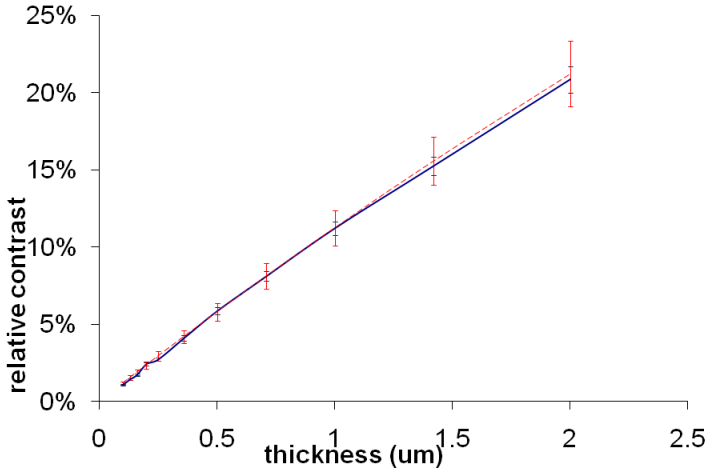


Figure 5.4: Comparison of the measured (solid blue curve) contrast-thickness relationship with the analytical model (dashed red curve) for the same beam quality (32kVp, Mo/Rh). The red error bars indicate the 10% error associated with the analytical model, whereas the dark blue error bars give the standard mean error for the measured data.

For S/P, there was no available data or software to create a map of the varying scatter across the detector for a CDMAM phantom set up. Fitting C_{obs} with C_p using Equation 5.6, assuming the above analytical model for C_p was correct with only the absence of the scatter degradation contributing to its difference from C_{obs}, the S/P was found to be equivalent to .111±0.011 (mean ± standard deviation) for 29kVp Rh/Rh beam quality for the GE Essential setup. This is a relatively low value of S/P for mammography, the value was quoted as 18% for work carried out by Boone et al[111, 112] and Dance and Day[108]. The reason for this could be that the contrast measurements for each disc thickness were undertaken for the largest discs for each thickness. This results in measurements made at the beginning of each row, where there is relatively less scatter

compared to the centre of the CDMAM phantom. This is because there is little material on the edge of the CDMAM phantom for photons to be scattered back in for detection by the receptor.

For the Hologic Selenia system, the S/P was found to be 0.060± 0.012%. For the Agfa system the S/P was found to be 0.218±0.030%. The large variations in S/P can be attributed to the different anti-scatter grids employed by each system (linear for GE Essential and the Agfa plate which used a Siemens X-ray set up, cellular for the Hologic Selenia) as well as slight variations in the location of the CDMAM and PMMA set up on the detector plate. The assumption of uniform scatter may be sufficient as the scatter model is a relatively slow-varying shape across the detector for a large phantom as the CDMAM phantom and PMMA set up. It is difficult to calculate accurately from images alone what the scatter contributions are at each location on the detector for each beam quality without the use of Monte Carlo.

Table 5.1 shows how the analytical $\Delta\mu_a$ (with S/P = 11%) compared with the C_{fit}. Relative differences were calculated between the measured disc contrasts, C, and analytical, C_{obs}, and fitted, C_{fit}, models.

$$\Delta_{obs} = \frac{C - C_{obs}}{C} \tag{5.10}$$

$$\Delta_{fit} = \frac{C - C_{fit}}{C} \tag{5.11}$$

On average, for the discs compared, relative Δ_{obs} was found to be -0.22±0.002% (mean ± standard deviation), and the relative Δ_{fit} equalled 0.04±0.002%. The error between the two calculations of disc thickness is not significant.

Table 5.1: Relative differences in C_{obs} and C_{fit} of gold discs in the CDMAM phantom for the 29kVp RhRh beam quality compared with C using Equations 5.10 and 5.11. Measured C for each disc thickness is compared with analytically calculated C_p. C_{obs} was derived from Equation 5.9

Disc Thickness (μm)	Measured C	C_p	C_{obs}	C_{fit}	Relative Δ_{obs}	Relative Δ_{fit}
0.10	0.987	0.988	0.988	0.988	-0.21%	-0.15%
0.13	0.986	0.984	0.985	0.984	0.06%	0.14%
0.16	0.982	0.980	0.982	0.981	0.03%	0.12%
0.20	0.971	0.975	0.977	0.976	-0.63%	-0.51%
0.25	0.970	0.969	0.972	0.971	-0.23%	-0.08%
0.36	0.959	0.956	0.960	0.958	-0.17%	0.04%
0.50	0.943	0.939	0.945	0.942	-0.24%	0.07%
0.71	0.919	0.914	0.923	0.919	-0.42%	0.02%

The limitation of this method is the assumption of a uniform scatter model, also the S/P value was derived from disc measurements only. The S/P may be more accurately derived from image measurements or Monte Carlo calculations which were not available at this time. Further investigation into this is made in the next Chapter. The next step was to insert the discs into the idealised CDMAM phantom image.

5.1.3 Inserting the Discs

Within each cell, there are two discs: one central disc and one eccentric disc placed according to a random pattern in one of the four quadrants of the cell. A schematic of the true locations of the eccentric disc within each cell was used to set up a 16 x 16 cell array. Each cell of this eccentric disc array had a number of 1 to 4 inclusive to indicate the orientation of the eccentric disc with respect to the central disc. The discs were inserted into the grid of the synthetic idealised CDMAM phantom image cell by cell, row by row. For this, a further two arrays were used to define the thickness and diameter of the discs in descending order.

Starting on the first row, in the first cell, where the disc diameter is equal to 2.00mm and the thickness is equal to $0.25\mu m$, the coordinates of the central disc were calculated to be in the centre of the cell. From centre to centre, the eccentric disc was located one half of the distance between the central disc to the axis of the cell. This was found to be, on average, 66 pixels in a set of experimental images either horizontally or vertically displaced from the central disc as shown in Figure 5.5. As the idealised CDMAM phantom image is at 10μm per pixel, the experimental image from which the CDMAM phantom template had been obtained was at 70μm per pixel, a factor of 7 is used to achieve the correct scale. Thus the eccentric disc was inserted at 7 x 66 pixels away from the centre of the central gold disc within the cell of the upsampled CDMAM phantom image input. The location of the central disc in the following cell in the same row was found to be 107 pixels shifted down and across from the central disc in the first cell in both the x and y direction. This is shown in Figure 5.5.

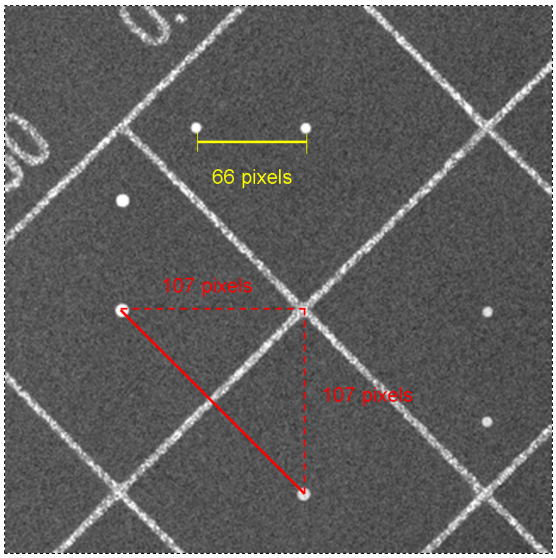


Figure 5.5: Illustration of the distances used to locate each disc, from central to central disc and from central to eccentric disc. Each pixel was equivalent to $70\mu m$.

This second central disc is inserted with the same disc diameter but the next thickness in the array is implemented. An identical disc is inserted in one of the four quadrants of the cell with reference to the eccentric disc matrix. This process is repeated through

each cell along the row using descending disc thicknesses before beginning a new row with a new disc diameter. This process is further repeated for each disc diameter until all cells have been allocated with two discs.

The idealised image has now had all the discs inserted at the correct locations in the grid with the appropriate disc diameters and contrasts. As described in Section 3.4.1, sixteen images of the CDMAM phantom with the same radiological settings were generated to introduce randomization into the measurements. The pixel intensity value of any small discs imaged between two or more pixels will be reduced compared to if the disc had appeared within a pixel. Thus very slight rotations in the CDMAM phantom will remove any possible biasing in the scoring results. This element of randomization to the synthetic CDMAM phantom images was introduced to mimic the clinical environment. The idealised CDMAM phantom image input was rotated using affine transformations.

The image (x, y) was rotated to (x', y') using the following matrix:

$$\left[x'\,y'\right] = \left[x\,y\right] \begin{bmatrix} cos\theta & sin\theta \\ -sin\theta & cos\theta \end{bmatrix}$$

θ was determined randomly at each image creation up to 2° in either the clockwise or anticlockwise direction.

This ends the creation of the idealised CDMAM phantom image. The idealised image can be inserted into the image simulation framework shown in Figure 5.6. This image simulation framework is based on the work developed in the preceding chapter to synthesise an image with the resolution and noise properties of a chosen DM system. Therefore, the next step was to apply the resolution limiting properties of the digital mammography system to the image. The idealised image was 15778x23268 pixels in size. In order to be filtered in Fourier space, the image was padded to the nearest value of 2^n. A 32768x32768 pixel blank image equal to mean of the idealised CDMAM image pixel intensity was created and the idealised CDMAM image was placed in the middle. The padded idealised CDMAM image was filtered in frequency space with the MTF_{filt} as described in Section 4.3.2 to create the blurred image, I_B. I_B was downsampled to the pixel size of the detector to be simulated using neighbourhood averaging methods as outlined in Section 4.3.3 to create the blurred, resampled image, $I_{B,R}$.

In the next step, $I_{B,R}$ was used as an input for scaling the standard deviation in $I_{N,C}$ to $I_{N,S}$ as in Equation 5.12 using the mean variance relationship. It is important that the $I_{B,R}$ was created before scaling the noise image, this ensures the noise image is correlated correctly at each point using the multiple noise source model for the standard deviation in Equation 4.35.

$$I_{N,S}(x,y) = I_{N,corr}(x,y).\sqrt{\left(k_e^2 + k_Q^2.(I_{B,R}(x,y)) + k_s^2.(I_{B,R}(x,y))^2\right)} \tag{5.12}$$

Finally the $I_{N,S}$ was added to the $I_{B,R}$ of the CDMAM phantom image.

$$I_{sim} = I_{N,S} + I_{B,R} \tag{5.13}$$

$I_{B,R}$ replaces I_c in equation 4.28 in the previous chapter to give equation 5.13. This synthetic image was then cropped to the final dimensions of the CDMAM phantom to

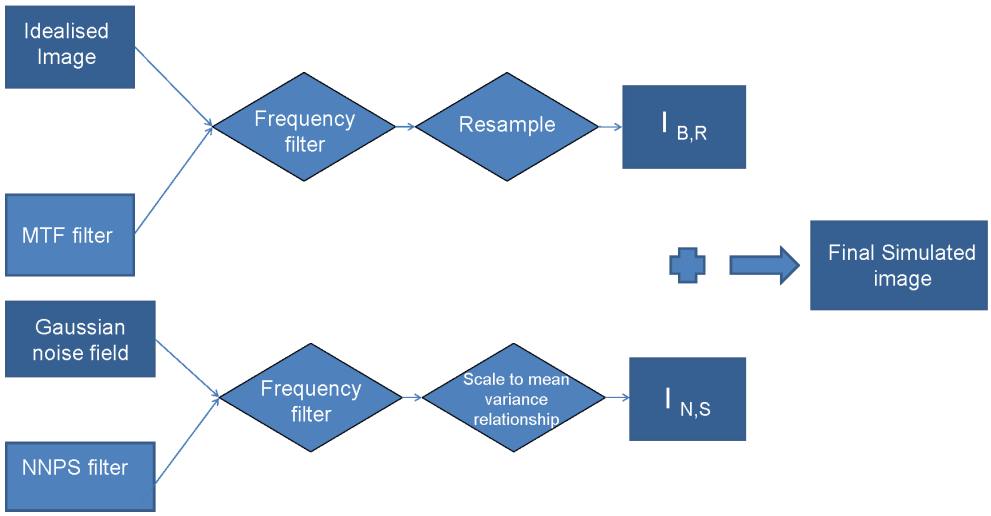


Figure 5.6: The image simulation framework to synthesise an image with the resolution and noise properties of a user-defined digital mammography system. $I_{B,R}$ is the blurred, resampled image whilst $I_{N,S}$ is the scaled, noise image.

remove the padding introduced earlier. From this, it is possible to create an image as if from a digital mammography detector entirely from physical models and characteristics of the detector.

Sixteen images were created at the same X-ray beam quality settings as those acquired for the systems modelled, for different doses. Sixteen images were created as this was found to be the optimum number of scoring results needed[17]. Three digital mamography systems were modelled to compare directly with experimental images.

Table 5.2 shows the settings used experimentally for each image set, for each imaging system. Synthetic CDMAM images were created to emulate these same experimental setups.

The next section discusses the evaluation methods used. Due to the large number of images to be assessed, automated scoring tools were used. Two automated scoring tools were used, a commercially available CDCOM software tool[2][71] and an in-house developed Quantitative Assessment Software (QAS)[13]. The QAS has been validated and the work published by the author[13]. Evaluation methods will be discussed before the results are presented.

5.2 Evaluation methodology

Evaluation of the CDMAM phantom images encompasses the assessment of the imaging chain with the observer taken into consideration. In human reading, the task of the observer is to correctly identify the location of the eccentric disc within each cell. This is

[2]The CDCOM software is available at http://www.euref.org/dmwg/templatedmwg.aspx?page=cdmamreadout.asp Last accessed June 2010.

Table 5.2: Settings for the CDMAM images acquired experimentally.

Imaging system	Beam Quality (kVp, target/filter)	Tube Current time product (mAs)	MGD (mGy)[a]	No. of Images
Hologic Selenia	30 W/Rh	61 91 122 182 245	0.84 1.25 1.68 2.50 3.37	16
GE Essential	29 Rh/Rh	14 28 57.3 110 225	0.24 0.52 1.06 2.04 4.16	16
Agfa NIP	28 Mo/Rh	40 80 160	0.84 1.68 3.35	16

[a]This Mean Glandular Dose was calculated for a breast thickness of 6cm with 50:50 fat/glandular equivalency which the set up was intended. Typically the MGD of a clinical image is approximately 2mGy[29]

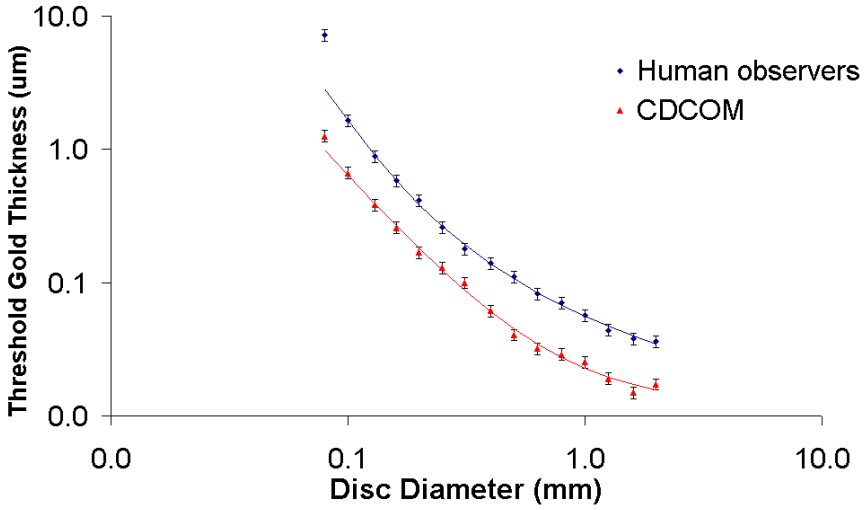
a time-consuming task, and is subject to inter- and intra-observer variability in scoring. Therefore, an alternative assessment approach in digital imaging is to use an automated scoring tool known as CDCOM[71, 38]. However, the exact methodology adopted within the CDCOM framework and further information on the Signal-to-Noise Ratio (SNR) and Contrast-Noise Ratio (CNR) of the detected discs is not available to the user. This has motivated the development of an in-house automated scoring software tool, QAS, to provide additional information on the discs as they are assessed. From this additional information, data such as SNR and contrast properties of the system can be obtained for further analysis. Despite this, CDCOM still provides a validated format in which CDMAM can be scored[16, 17, 71], providing direct comparison with published data on CDMAM, experimentally acquired and simulated[86].

The next two sections will discuss how CDCOM and QAS operate and how they were implemented to assess the CDMAM test phantom images.

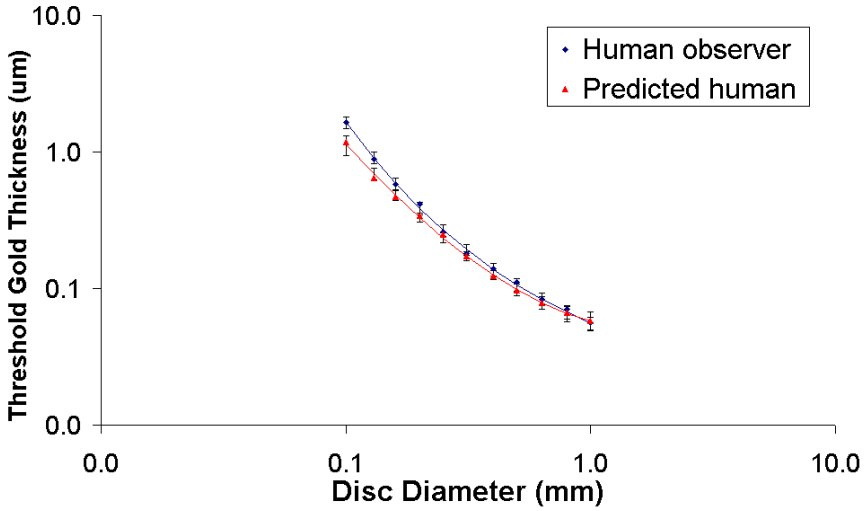
5.2.1 CDCOM software

Based on published papers[71, 38], CDCOM crops the CDMAM phantom image such that the overexposed areas in the image are removed and do not distract from the grid determination. From the cropped image, the grid lines are found using a Hough transform and the cells determined from the intersections of the lines detected in the CDMAM phantom image. The cell quadrants are then each searched using an appropriately sized circular template to calculate the mean signal of the potential disc. If the circular template falls on top of the actual disc, it is expected a maximum contrast is found and in which case, the decision is made that the disc is in that quadrant.

The CDCOM software performs exceptionally well in scoring, performing better than humans as shown in Figure 5.7a, demonstrated by the lower threshold gold thickness curve (Section 3.4.1 discusses the interpretation of the contrast-detail curves). As mentioned in Chapter 3, work by Young et al has utilised this software to create contrast-



(a)



(b)

Figure 5.7: Contrast detail curves resulting from one set of images scored by (a) CDCOM scoring unaltered compared with human observers, (b) CDCOM scoring fitted to predict human scoring implementing Young et al's[16, 17] methodology compared to the same human observer scoring results from (a).

detail curves as well as to predict human observer performance from the CDCOM results[16, 17]. It was found that the raw CDCOM results had a linear relationship to the human observer scoring results, thus human readings could be reliably predicted from the CDCOM results. To illustrate this, the same human scoring results have been plotted in Figure 5.7b and Figure 5.7a with CDCOM scoring results fitted to predict human scoring in Figure 5.7b and left unaltered in Figure 5.7a.

The results from CDCOM adjusted to predict human observer readings were used to

evaluate the scoring of the CDMAM images both from experimental and synthetic setups. However, comparison of contrast-detail curves is somewhat limited in its analysis of the data available in such images. Thus the QAS was developed to enable access to the data that an automated CDMAM scoring program can obtain throughout its process.

Converting to DICOM images

The CDCOM software was developed to score DICOM images of the CDMAM phantom. To compare the synthetic images created with the experimental images, it was necessary to '*dicomise*' the synthetic images for input into the CDCOM. The synthetic images were created as 16 bits unsigned integer raw files to retain as much information as possible. DICOM images also hold extra information about the image in the form of a header file. Within the header file there can be information about the pixel size used, the number of slices taken (in the case of CT or MRI volume images), the beam quality, the exposure time etc.. The information that CDCOM requires is the pixel size to deduce the correct location and expected size of gold discs within the CDMAM phantom[38]. Also, information about the *Pixel Intensity Relationship Sign* is required to indicate whether the pixel intensity values increase or decrease with increasing X-ray exposure[38]. These were not present in the experimental DICOM image headers. Therefore, in light of this, the CDCOM manual suggested CDCOM could deduce the same information from *Photometric Interpretation* instead. An ImageJ plugin was utilised to convert the raw images into DICOM images. With the use of OFFIS DICOM Toolkit DCMTK©, the header files of dicomised images were altered to the settings of the system simulated.

5.2.2 Quantitative Assessment System (QAS)

To obtain more objective assessment of the CDMAM phantom images it is desirable to measure the contrast of the discs and explore the effects of MTF blurring on the discs. As CDCOM does not provide this data, an in-house CDMAM assessment software was developed to extract such data from the CDMAM phantom images. The operation of the QAS is described in the next section along with details of how the data was used for analysis of the CDMAM phantom images.

The first task of such an automated CDMAM scoring system is to locate the discs within each cell of the CDMAM phantom image. This was divided into two major processing steps: (i) A pre-processing stage, for determination of grid lines and their intersections within the CDMAM phantom image, in order to locate each cell; (ii) A disc detection algorithm to be executed within each of the four quadrants of every cell.

Pre-processing

The CDMAM image may contain overexposed areas outside the phantom image which need to be removed before processing, therefore the phantom image was cropped so

that the following processes of edge detection were not distracted. In order to account for variations in the manufacture of the cells within the CDMAM phantom, search templates need to be correctly aligned for each image being assessed. The CDMAM phantom image was binarised using a Canny edge detector to find the edges within the grid. This searches for the local maxima of the gradient in the image, calculated using a derivative of a Gaussian filter. It uses two thresholds, to detect strong and weak edges, and includes weak edges in the output only if they are connected to the strong edges.

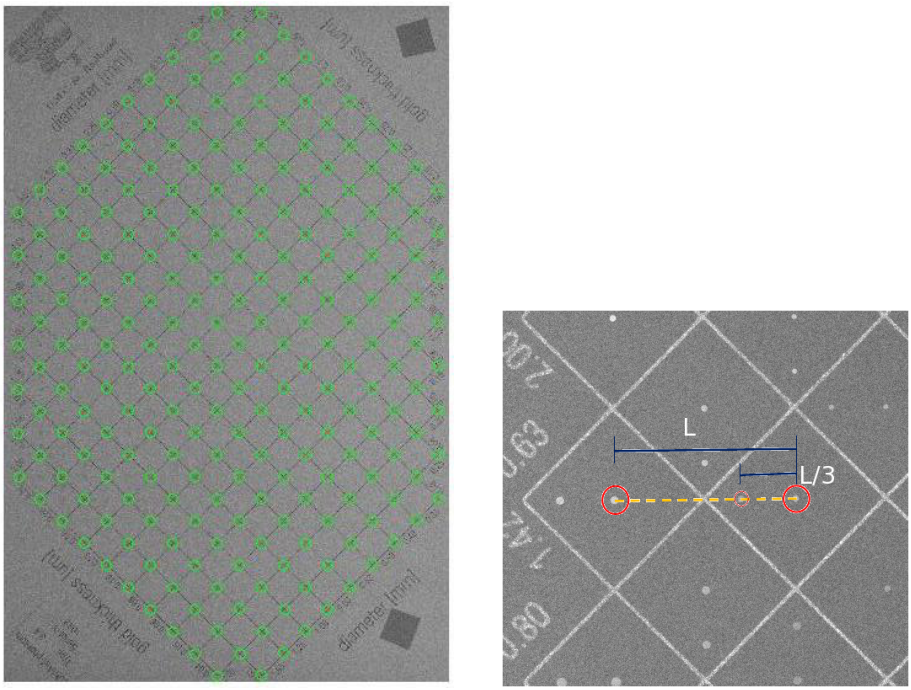
The image was downsampled by a factor of 2 to speed up processing for a Hough transform to be applied, in order to extract the binarised grid lines from the image. Coordinates of the intersection of the lines were then calculated as illustrated in Figure 5.8a. The intersections were grouped in a vertical fashion to define the four corners of each of the 205 cells, ready for the implementation of the disc detector algorithm.

Implementation of a disc detection algorithm

Search areas were created and applied to each cell within the grid structure using the intersection information found in the pre-processing stage. The corner search areas were located at a pre-defined position from the centre of the cell, assuming the central disc is at this point. The pre-defined position was assumed to be approximately one third of the distance between the central discs of two adjacent cells as illustrated in Figure 5.8b. These search areas were eroded by 85% to ensure that the finite thickness of the grid lines did not interfere with the disc detection process. Five search areas were defined per cell as shown in Figure 5.9 and the disc detector algorithm was then applied to each.

Search areas were further eroded to twice the diameter of the disc of interest, with an exception for the smallest discs which may appear in the image as only one pixel in diameter. Search areas were defined to be twice the diameter of the disc of interest to ensure the search area covers the area in which the disc is most likely to be located. The search areas for the smallest discs (less than 0.20mm in diameter) were eroded to 5 times the disc diameter, again to ensure the disc is within the search area. A circular region, the disc template, equal to the known size of the gold disc in the cell was scanned across the search area, using single pixel steps. The average pixel value within this disc template was calculated. Ideally, signal intensity and contrast measured should be maximal when the disc is correctly located within the search window. This may not be the case when the contrast is very low and the noise distorts the information which QAS's disc algorithm is given. This is very similar to a human observer's visual detection process: human observers are typically unable to visualise an object with signal-to-noise ratio below a certain point. This is further hindered if noise is comparable to the signal to be detected in the image.

For each of the decision criteria: maximum contrast and maximum signal, along with its similarity in its signal and contrast to the central disc; a vote is cast upon which corner the algorithm believes the eccentric disc to be in. The vote system, based on the above four criteria, determines the location of the disc within each cell. For this work,



(a) (b)

Figure 5.8: (a) Illustrates the intersections of the grid within the CDMAM image. (b) Calculation of the corner disc coordinates in relation to the central discs from adjacent cells. The distance between the central disc (large red circle) and the eccentric disc (small red circle) is approximately one third of the distance between the central discs of adjacent cells.

equal weighting for each criteria was determined to provide the best scoring results overall.

From prior experiments[13], it was found that the QAS did not perform as well as the CDCOM, but provided better readings than human observer readings. The merit of the QAS is that from the correctly detected discs, contrast and noise information can be extracted for use in analysis.

5.3 Preliminary Results

CDMAM images from three systems were simulated as described in Section 5.1.1 and compared with experimental images from the same systems: Hologic Selenia, GE Essential and Agfa Needle-IP CR system. The technical specifications of the systems can be found in Chapter 4. Figure 5.10 shows examples of 0.25mm diameter discs in experimental and synthetic images for all three systems.

Contrast-detail curves were obtained for each system, for each setting, using CDCOM (fitted to predict human observers as described in Section 5.2.1). The same images were further analysed using QAS to assess CNR of the discs themselves. Below is an example of a experimental CDMAM phantom images with their synthetic counterparts.

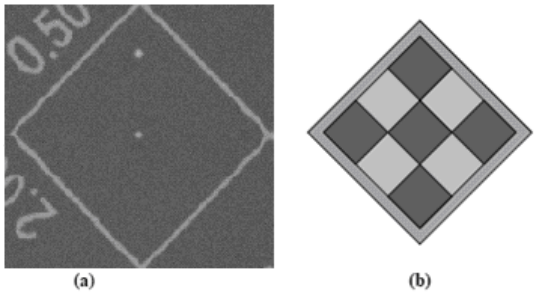


Figure 5.9: Example of the search area construction (a) Original cell in CDMAM phantom (b) Diagrammatic of a CDMAM cell. Border shows cell eroded to 85% of the cell area, to avoid grid lines. Placement of five search areas within the cell is shown with dark squares.

5.3.1 Contrast-detail Curves

Figures 5.11,5.13 and 5.15 are derived from CDCOM scoring output.

Figure 5.11 shows the contrast detail curves derived from CDCOM scoring fitted to human predicted scoring for the Hologic Selenia system, for experimental and synthetic images. In both cases the contrast-detail curves for each dose appear to be well defined as the curves are shifted down with increasing dose. A salient point to note is that the experimental data show an increased amount of curvature. The contrast-detail curves from the synthetic images appear linear, suggesting there may be other sources of blurring in the experimental images that were not taken into account in simulation such as magnification as mentioned by Marshall[53]. Currently in this chapter, simulations do not take account of magnification of the discs nor the geometric blurring associated with not placing the CDMAM phantom directly on the detector.

Figure 5.12 shows how the contrast-detail curves for experimental and synthetic images appear when overlapped for each dose for the Hologic system. Contrast-detail curves are shown for each dose individually for clarity in the B.

A ratio for each disc diameter, d_i, of the threshold gold thicknesses, t, of experimental to synthetic images was calculated as follows:

$$R_{d_i} = \frac{t_{exp,d_i}}{t_{sim,d_i}} \tag{5.14}$$

The ratio of experimental to simulated fitted contrast detail curves was calculated as in Equation 5.14. For all doses and disc diameters for the Hologic Selenia, the average ratio was approximately 1.01±0.14 (mean± standard deviation). The plot of ratios shown in Figure 5.12b are close to unity, indicating a good agreement between the synthetic and experimental CDMAM images. The $R_{d_{all}}$ ranged from 0.86 – 1.47 for all doses, with the largest error for the smallest disc diameter in the readings, $0.10\mu m$. This may indicate that the MTF blurring is insufficient at these disc diameters.

Figure 5.13 presents the contrast-detail curves for the GE Essential system.

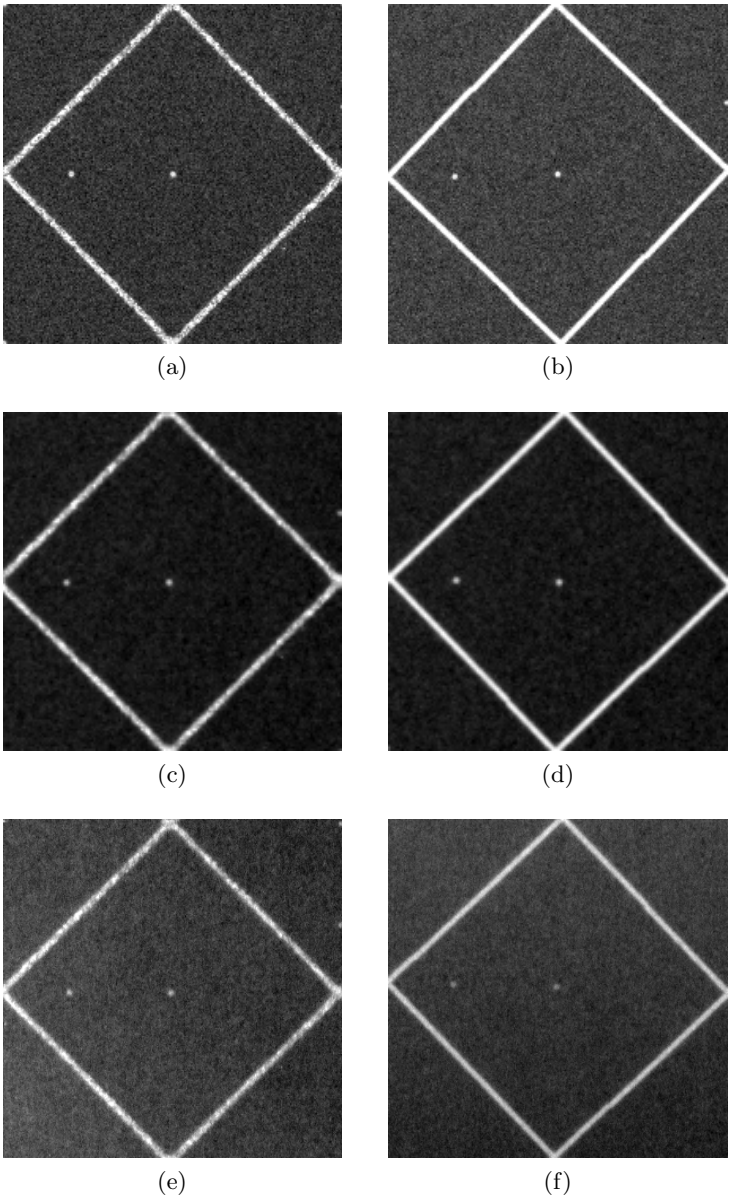
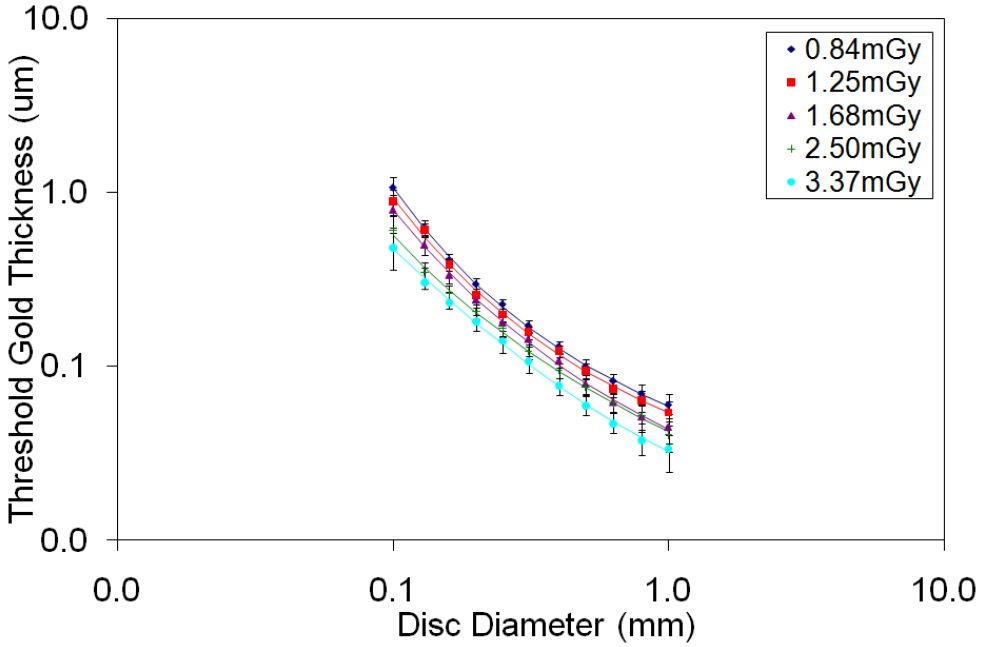
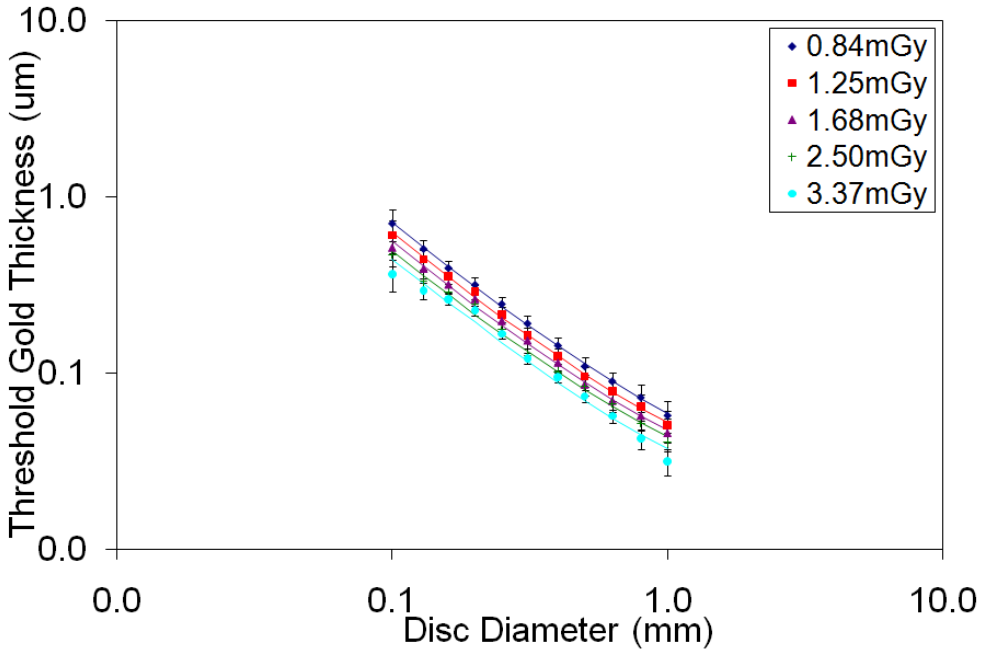


Figure 5.10: Comparison of 0.25m diameter disc in an experimentally acquired and synthetic CDMAM images. Images on the left show the experimentally acquired and image on the right show the synthetic. (a) and (b) show the disc for the Hologic Selenia system for 3.37mGy MGD. (c) and (d) show the disc for the GE Essential system for 4.16mGy MGD. (e) and (f) show the disc for the Agfa CR system for 3.35mGy.



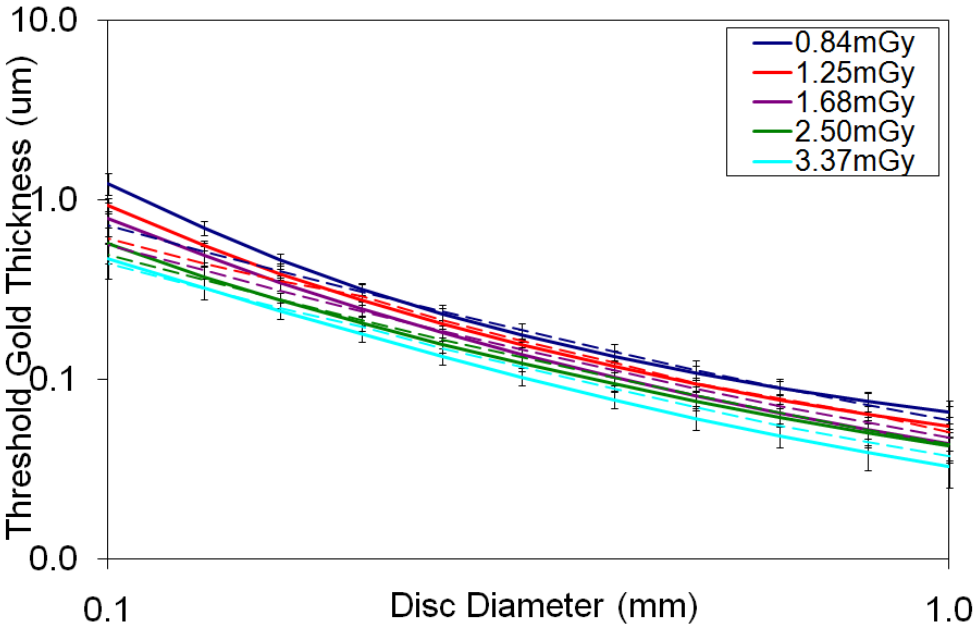
(a) Experimental



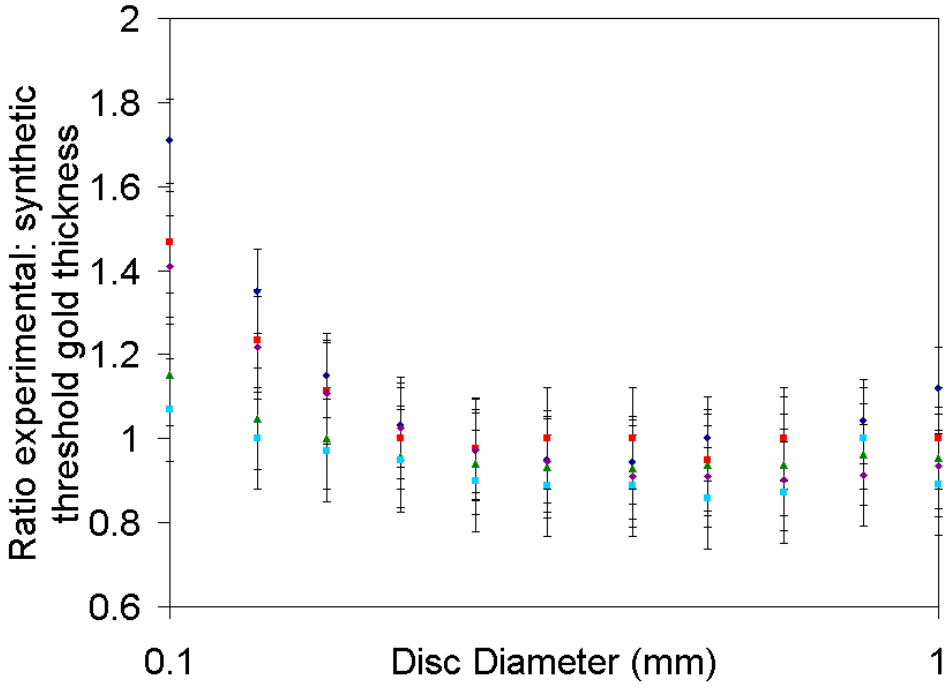
(b) Synthetic

Figure 5.11: Comparison of the contrast-detail curves for experimental (a) and synthetic (b) images for the Hologic Selenia system. Error bars denote two standard errors of mean.

The experimental contrast-detail curves were plotted alonside the synthetic contrast-detail curves to further investigation in Figure 5.14. The overall curvature of the fitted

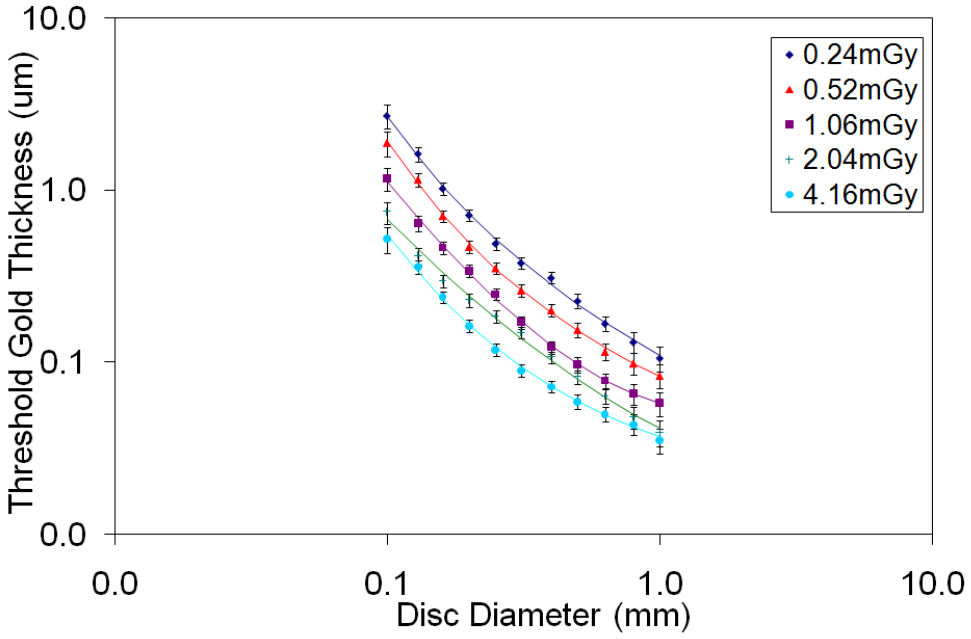


(a) Contrast-detail curves

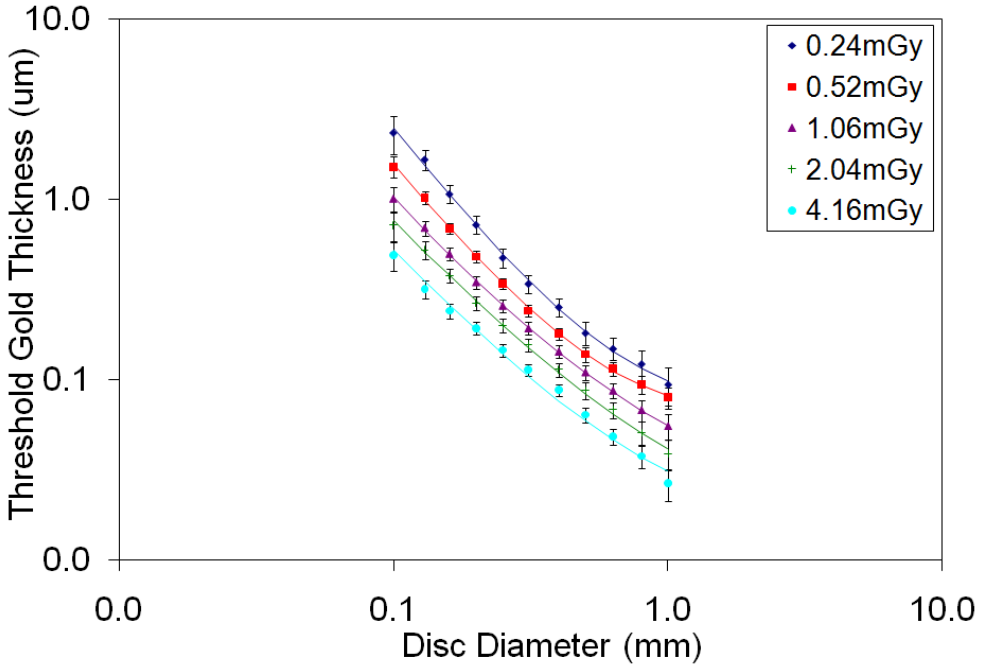


(b) Ratios

Figure 5.12: (a)Direct comparison of the contrast-detail curves for experimental (solid) and synthetic (dashed) images for the Hologic Selenia system at each dose. (b) R_{d_i} for each dose. Error bars denote two standard errors of mean.



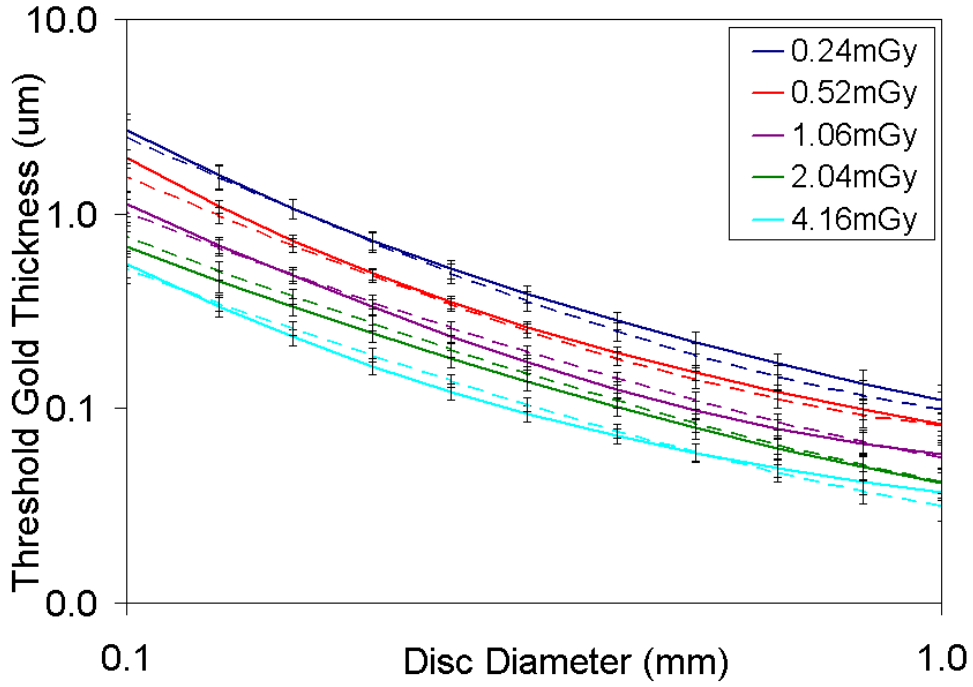
(a) Experimental



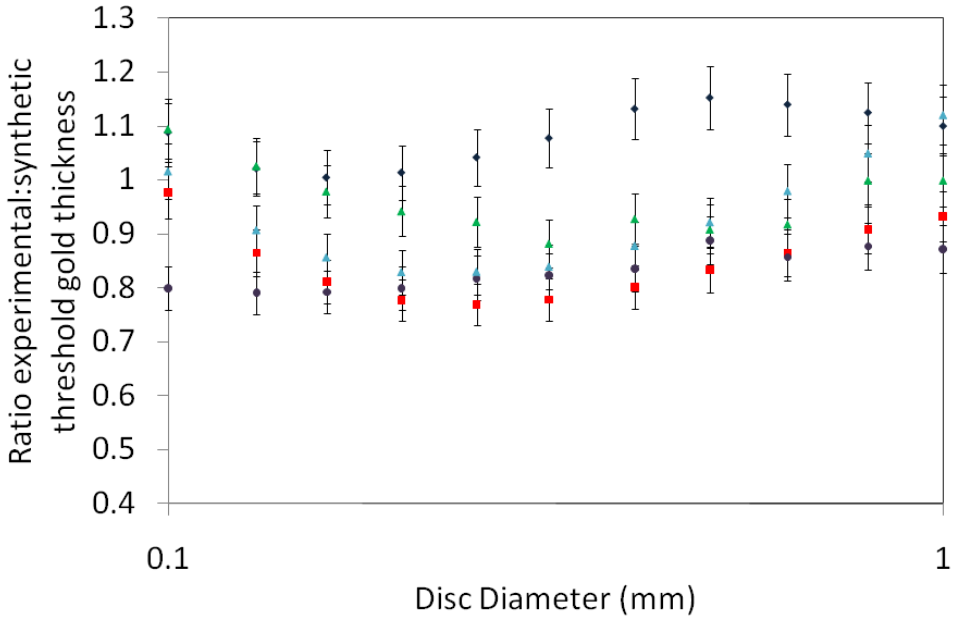
(b) Synthetic

Figure 5.13: Comparison of the contrast-detail curves for experimental (a) and synthetic (b) images for the GE Essential system. Error bars denote two standard errors of mean.

curves of the simulated and experimental data is similar, suggesting the blurring effects of the MTF was correctly modelled.



(a)



(b)

Figure 5.14: (a)Direct comparison of the contrast-detail curves for experimental (solid curves) and synthetic (dashed curves) images for the GE Essential system at each dose.(b) R_{d_i} for each dose. Error bars denote two standard errors of mean.

The ratio of threshold gold thicknesses of experimental to synthetic images, R_{d_all}, varied between 0.76 – 1.15, when further averaged across all discs for each dose. The average ratio of threshold gold thicknesses for experimental to synthetic images for all doses was 0.93±0.11 (mean± standard deviation). This shows that typically, the simulated images had slightly increased threshold gold thickness readings from CDCOM.

Contrast-detail curves presented in Figure 5.16 are for the Agfa CR system, all the contrast-detail curves for the simulated images have a slightly higher threshold gold thickness than that of the experimental data. The ratio, R_{d_all}, of the experimental to synthetic was between 0.77 – 1.14. Averaging across all three doses, the ratio was 0.86 ± 0.08 (mean ± standard deviation). The poorer detection in the synthetic images, despite correct application of blurring and noise properties as discussed in the previous chapter hints at other effects not modelled in the current framework.

CDCOM detects discs when the quadrant contains the lowest average signal compared to the other quadrants of cell. CDCOM does not provide any information additional to scoring results. Therefore it is not possible to directly determine how much of the contrast of the discs were reduced due to the MTF blurring. Howeverm it is possible to use the QAS to assess the CNR of the discs gave a clearer idea of how the implementation of altered MTFs in simulation may cause the difference from the experimental data.

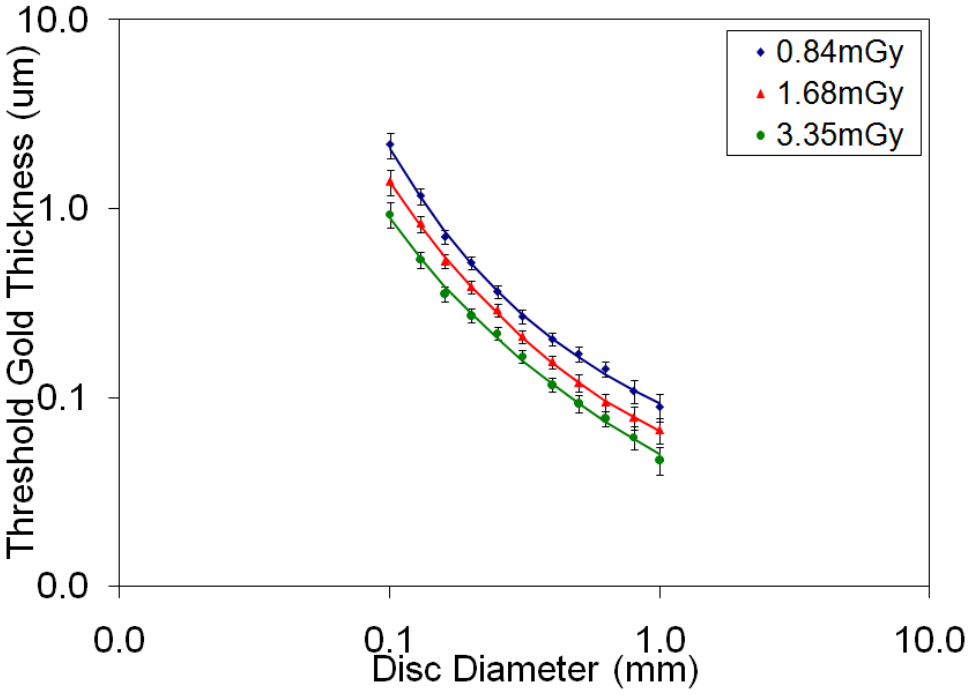
5.3.2 Contrast and Noise Measurements

Figures 5.18 to 5.23 have been derived from QAS output data. Figure 5.17 shows the cells used for analysis in the CDMAM phantom images. For the CNR measurements, accurate measures of the disc contrasts were required, therefore the larger discs were used. It was seen that there were mitigating factors in the CNR measurement due to varying standard deviation measurements local to the discs, therefore only the data from the highlighted cells were used. Investigations into the MTF blurring was made with measurements of the contrast of the discs of varying diameter. As the disc diameter reduced, the contrast of the disc was degraded by the MTF. This was measured as Contrast Degradation Factor for each disc diameter d, CDF_d:

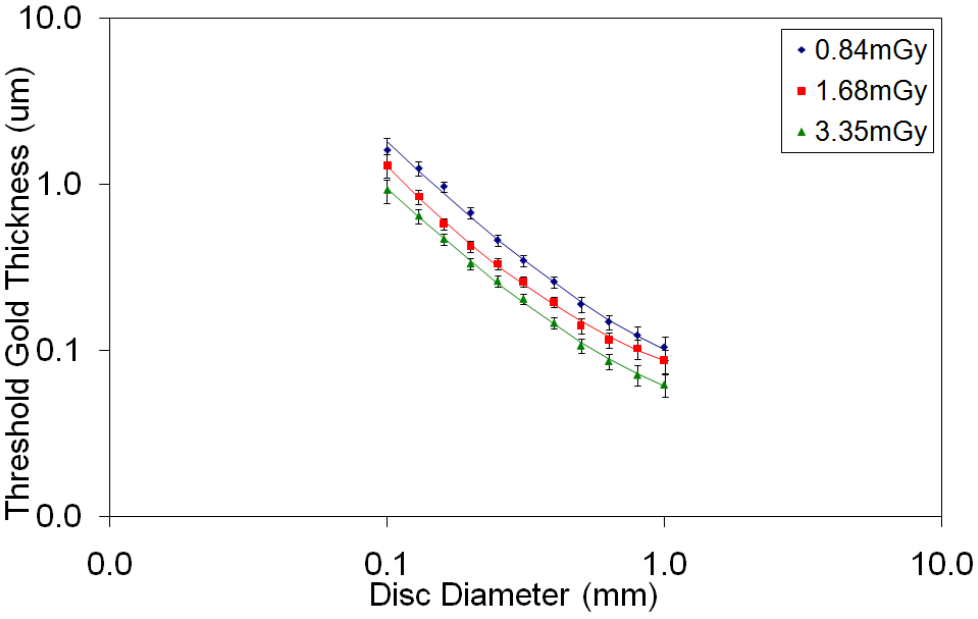
$$CDF_d = \frac{C_{obs,d}}{C_{meas,d}} \tag{5.15}$$

$C_{obs,d}$ is the contrast of the disc derived in Equation 5.6, used as the input to the simulation model and measured from experimental images. $C_{meas,d}$ is the contrast measured by QAS from the discs in the image. CDF and contrast measurements are shown in Figures 5.18, 5.20 and 5.22 for the three systems modelled.

Further investigation into the individual contrast and noise (measured as standard deviation of the local background to the discs) was made and presented in Figure 5.19 for the Hologic Selenia system. Contrast was plotted against disc thickness, as noted earlier the blurring of the system reduces the expected contrast of the discs. Therefore, the contrast was extracted for disc diameters up to 0.5mm for which the contrast was degraded by the MTF.



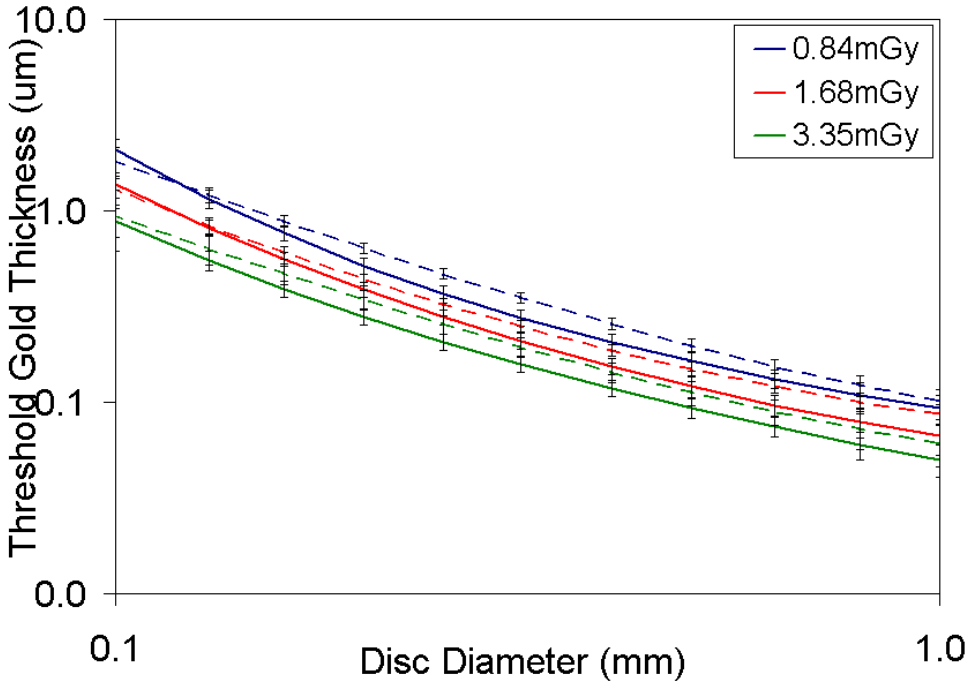
(a) Experimental



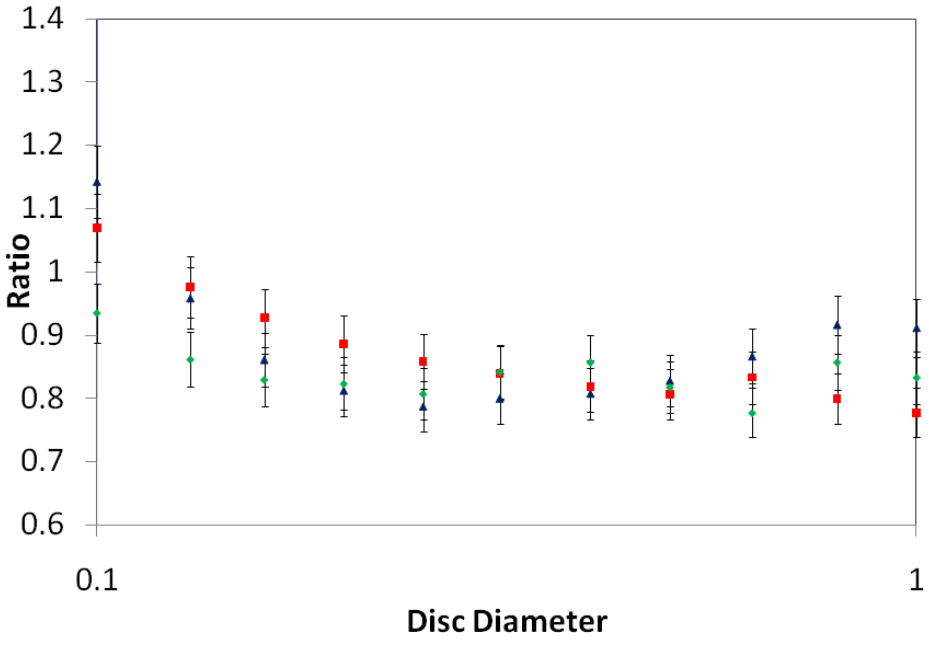
(b) Synthetic

Figure 5.15: Comparison of the contrast-detail curves for experimental (a) and synthetic (b) images for the Agfa CR system. Error bars denote two standard errors of mean.

Results gathered from the QAS have shown agreement in the CDF of experimentally acquired images and synthetically generated images. However, CDFs for the experi-



(a)



(b)

Figure 5.16: (a)Direct comparison of the contrast-detail curves for experimental(solid curves) and synthetic (dashed curves) images for the Agfa CR system at each dose. (b) R_{d_i} for all doses. Error bars denote two standard errors of mean.

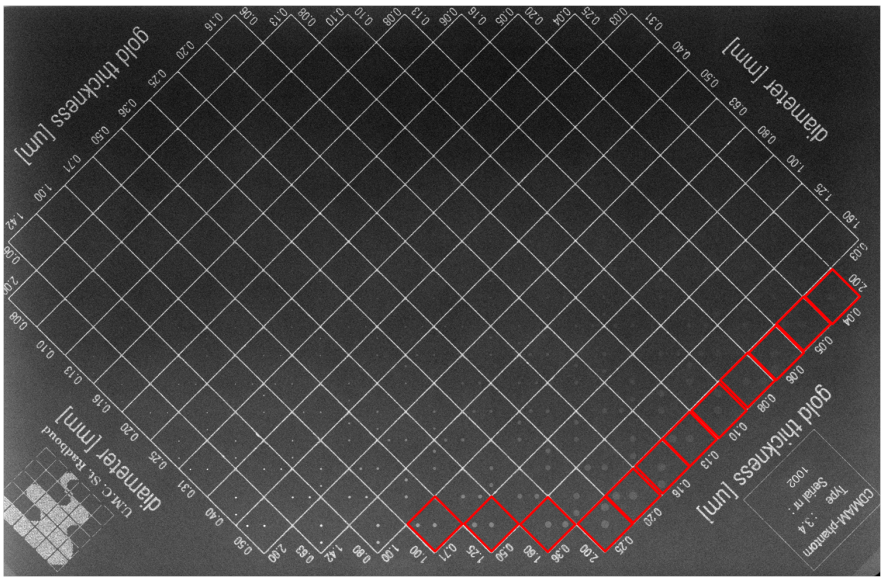


Figure 5.17: Red cells denote the cells that were used for CNR measurements

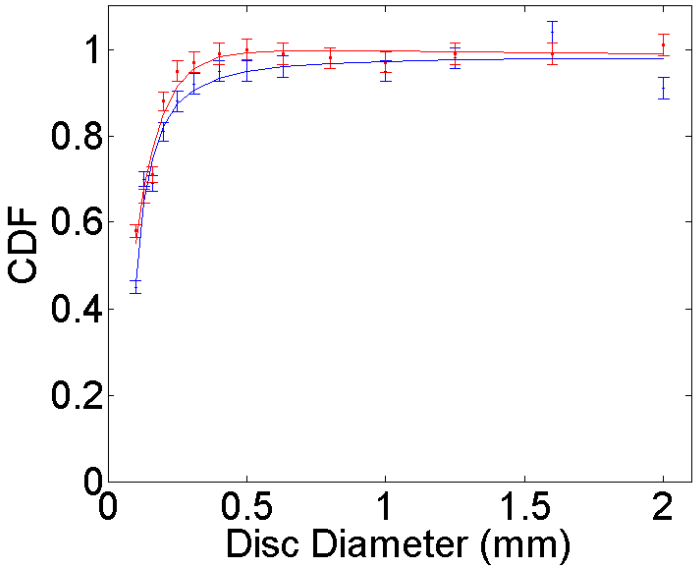
mentally acquired images were found to degrade at an earlier stage. The disc diameter at which the CDF was found to equal 0.5 is shown in Table 5.3. In comparison, the synthetic images degrade to CDF value of 0.5 at smaller disc diameters. This suggests the presampled MTF blurring introduced in the image simulation framework may not be sufficiently modelling all the blurring factors in the CDMAM images.

Table 5.3: Disc diameter at which CDF(0.5) was found for all systems modelled, for synthetic and experimentally acquired images. Error denotes standard error mean.

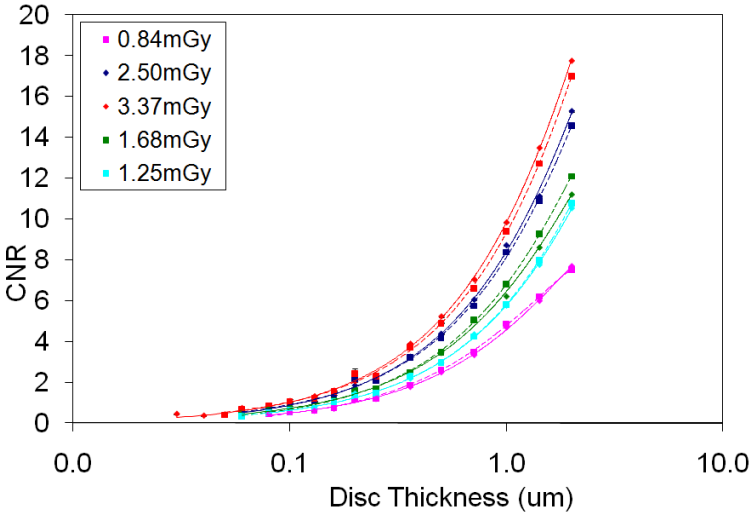
System	Experimental d(CDF = 0.5) (mm)	Synthetic d(CDF = 0.5) (mm)
Hologic Selenia (a-Se flat panel)	1.05 ± 0.02	0.90 ±0.02
GE Essential (CsI phosphor flat panel)	0.188 ± 0.02	0.166 ± 0.02
Agfa Needle IP (CsBr plate)	0.195 ± 0.02	0.160 ± 0.02

The were discrepancies in the CNR measurements between the experimental and synthetic images. Further investigation into the individual measurements showed that although the contrasts between experimental and synthetic images matched, the noise (measured as local background standard deviation) did not. The salient point found in all the systems modelled was that the noise varied with location in the experimental images, which is not apparent in the uniform models of the CDMAM phantom images. For each system, the relative error in the CNR for disc diameter, i, and dose K was calculated as follows:

$$\Delta_{CNR} = \frac{\Sigma_{i,K} \left| CNR_{i,K,exp} - CNR_{i,K,sim} \right|}{\Sigma_{i,K} CNR_{i,K,exp}} \times 100\% \tag{5.16}$$



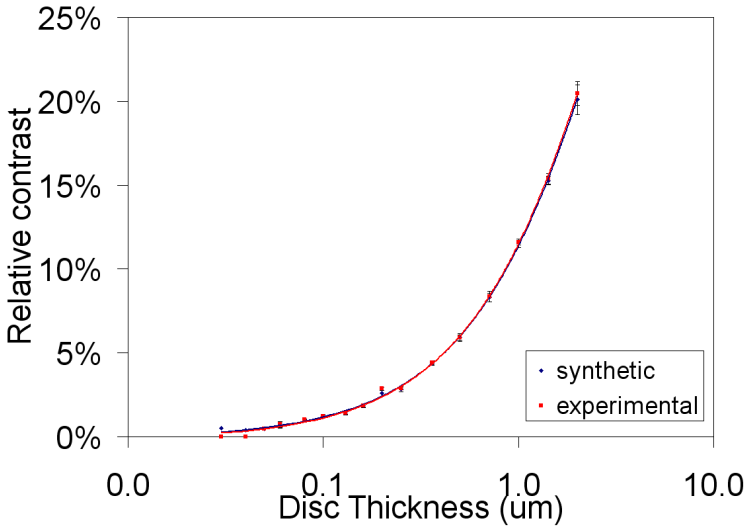
(a)



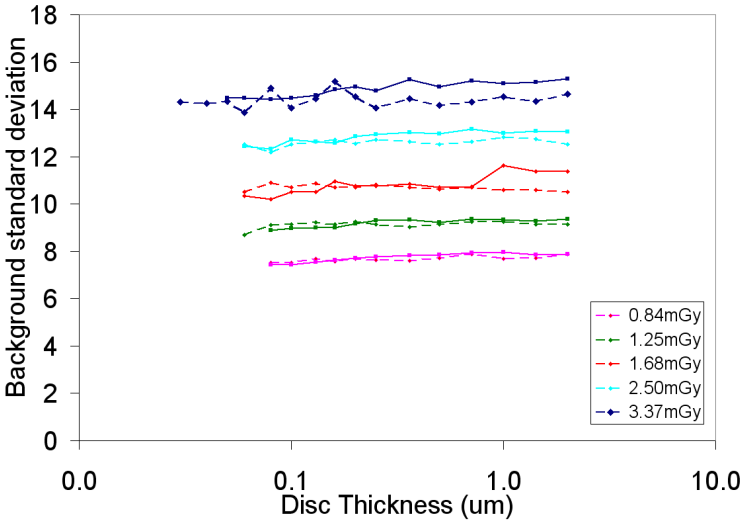
(b)

Figure 5.18: (a) CDF measured from experimentally acquired and synthetically generated images for the Hologic Selenia system.(b) CNR measured from experimentally acquired and synthetically generated images for the Hologic Selenia system. Solid curves show lines of best fit for experimentally acquired images and dashed curves represent the lines of best fit for synthetically generated images. Error bars denote two standard error means

Average relative differences in the CNR for all disc diameters and doses were seen to be 1.52%, 1.05% and 14.9% for the Hologic Selenia, GE Essential and Agfa CR systems, respectively.



(a)

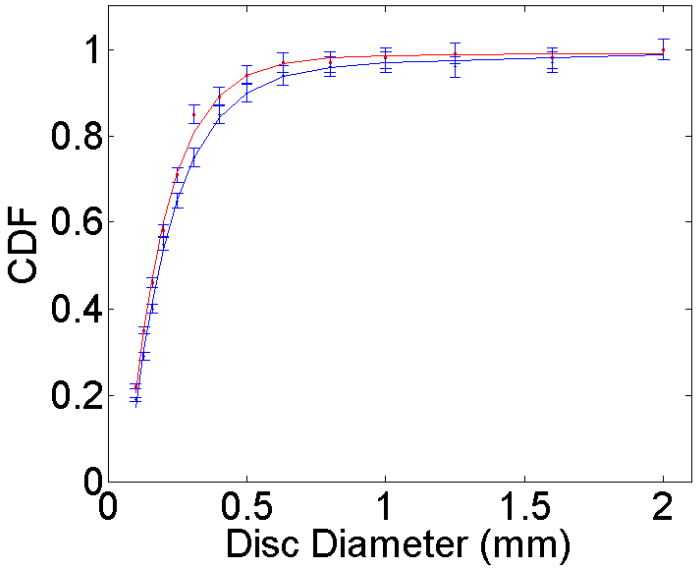


(b)

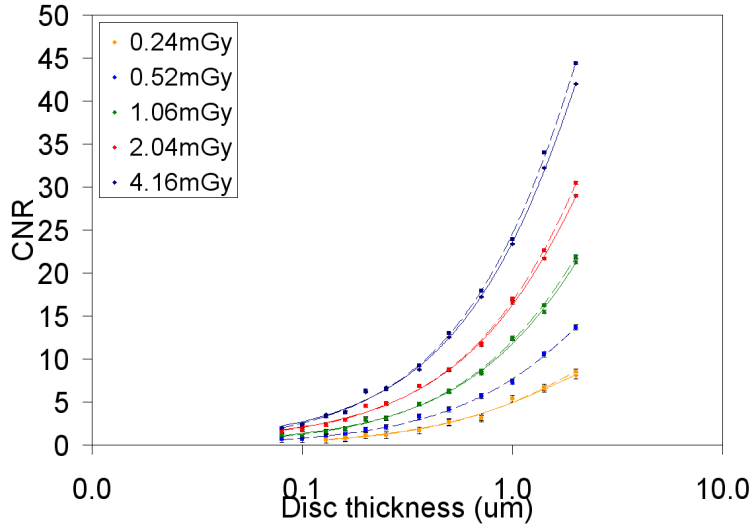
Figure 5.19: (a) Contrast measurements for all doses, from synthetic and experimentally acquired images, for the Hologic Selenia system. Error bars show two standard errors of mean. (b) Standard deviation measurements local to discs measured in (a), from synthetic and experimentally acquired images (dashed and solid lines respectively).

5.4 Limitations and Subsequent Requirements

This chapter has explored the use of the CDMAM phantom and implemented a method to simulate the CDMAM phantom images. The image simulation chain from the previous chapter has been adapted to simulate the CDMAM phantom images. The CDMAM phantom images were evaluated using two software systems developed for the purpose. CDCOM was used to predict contrast-detail curves as if obtained from human observer



(a)

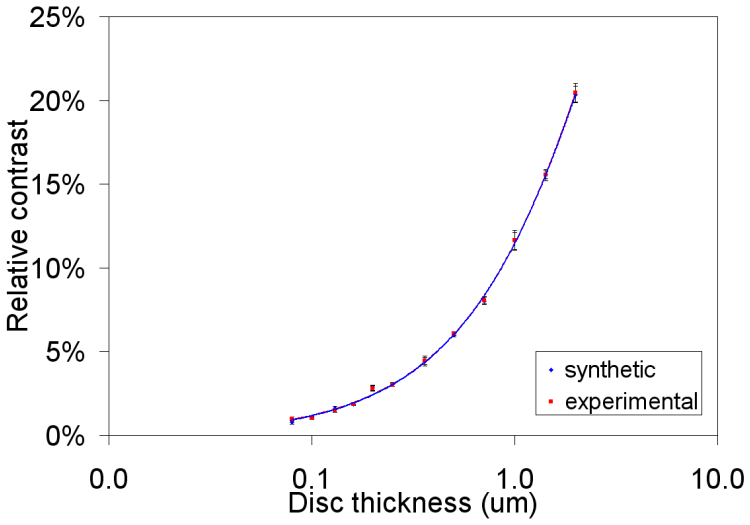


(b)

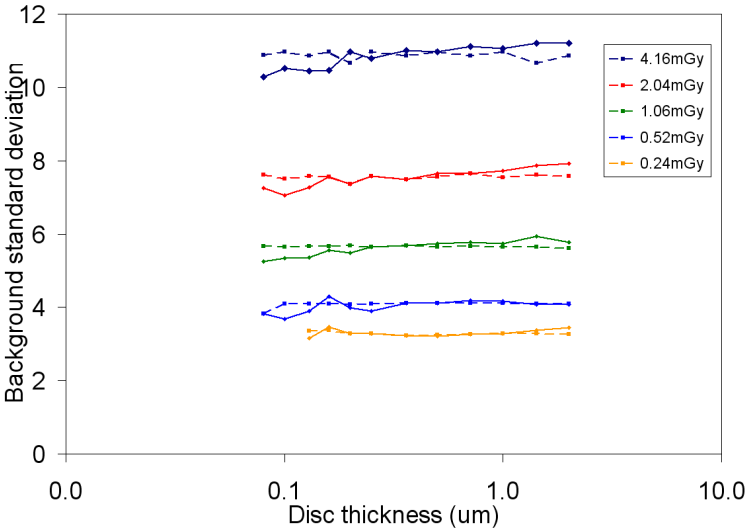
Figure 5.20: (a) CDF measured from experimentally acquired and synthetically generated images for the GE Essential system.(b) CNR measured from experimentally acquired and synthetically generated images for the GE Essential system. Solid curves show the lines of best fit for experimentally acquired images and dashed curves represent the lines of best fit for synthetically generated images. Error bars denote two standard error means

scoring. QAS was implemented to assess the contrast and noise properties of individual discs within the images.

Scoring results from CDCOM indicated that the CDMAM phantom image simulation



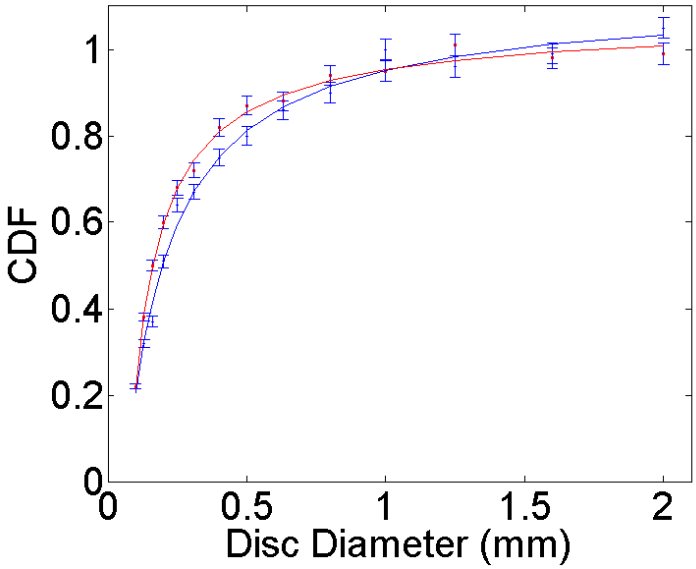
(a)



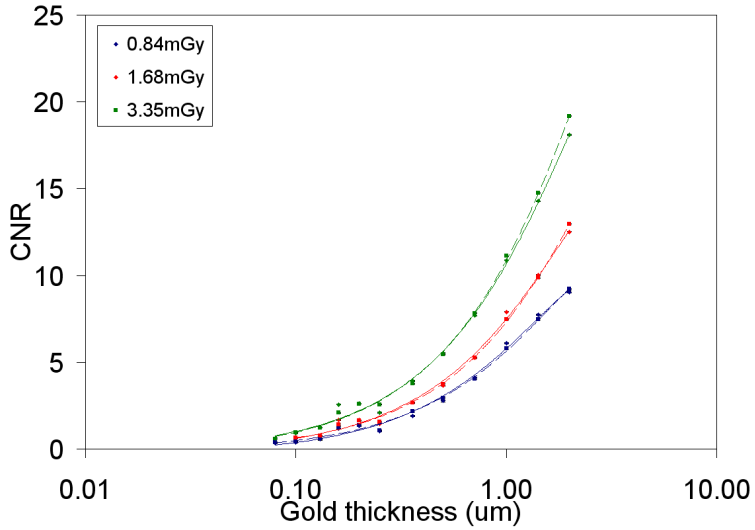
(b)

Figure 5.21: (a) Contrast measurements for all doses, from synthetic and experimentally acquired images, for the GE Essential system. (b) Standard deviation measurements local to discs measured in (a), from synthetic and experimentally acquired images (dashed and solid lines respectively).

was successful for some of the image sets. The a-Se system (Hologic Selenia) provided the best results with averaged ratio of the experimental to synthetic threshold gold discs, $R_{d_{all}}$, of 1.01± 0.14. CsI phosphor system (GE Essential) had an average $R_{d_{all}}$ of 0.93±0.11, suggesting overestimated threshold gold thicknesses for the synthetic images. The simulations for the CR system (Agfa) performed the worst with $R_{d_{all}}$ = 0.86±0.08. Further investigations in to the contrast and noise in the experimental and synthetic CDMAM phantom images found that although the contrast was well



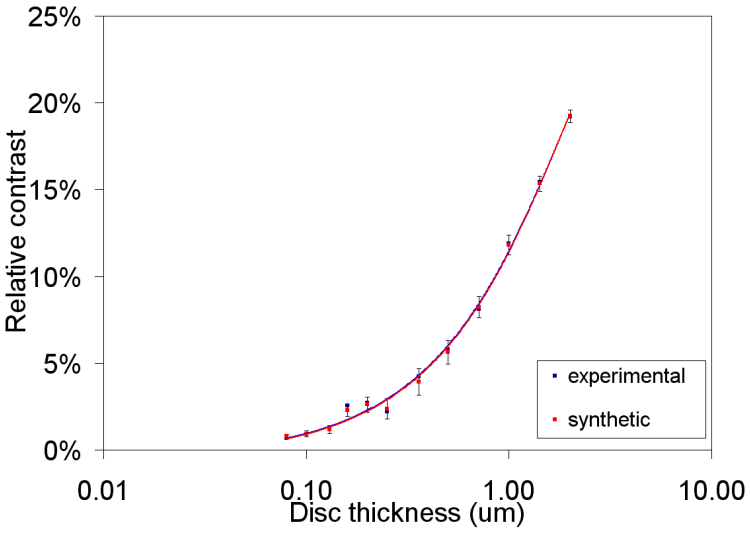
(a)



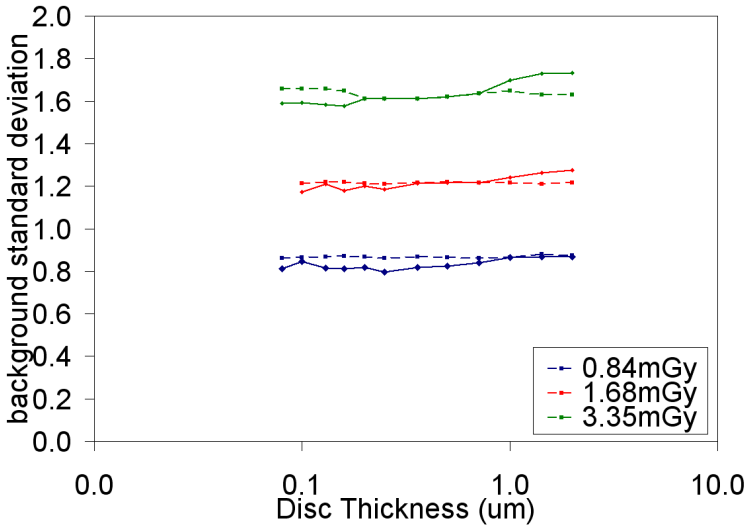
(b)

Figure 5.22: (a) CDF measured from experimentally acquired and synthetically generated images for the Agfa CR system.(b) CNR measured from experimentally acquired and synthetically generated images for the Agfa CR system. Solid curves show the lines of best fit for experimentally acquired images and dashed curves represent the lines of best fit for synthetically generated images. Error bars denote two standard error means

modelled, the blurring was insufficient. This lead to slight deviations in the CDF of the synthetic images when compared with the experimental images. The larger effect was attributed to the noise modelled in the synthetic images. The noise did not vary with location in the image, thus the CNR measurements of the gold discs of the synthetic



(a)



(b)

Figure 5.23: (a) Contrast measurements for all doses, from synthetic and experimentally acquired images, for the Agfa CR system. (b) Standard deviation measurements local to discs measured in (a), from synthetic and experimentally acquired images (dashed and solid lines respectively). Error bars denote two standard error means.

CDMAM phantom images deviated between 1.05 - 14.9% from the experimentally acquired counterparts.

Although the previous chapter had indicated the MTF and noise properties had been well simulated, the observer scoring task set in this chapter has highlighted the subtleties in the mammography images not accounted for. Analysis of the simulation chain had been based on comparing the output with its input, on global measures, as such it

would be expected that the results were similar. In the case of the CDMAM phantom, there are more subtleties to consider. There are local variations that the current image simulation chain does not take into account. The images were assumed to be uniform, which in reality is not true. The simulations presented in this chapter lack the residual low frequency pixel intensity variation across the detector. This in turn would alter the variance measured at different points in the image as the mean-variance relationship that the noise image is scaled to is carried out on a pixel-by-pixel basis in relation to $I_{B,R}$.

In addition, relative noise across the detector can vary greatly as was seen in measurements with the QAS. Although experimental contrast measurements matched that in synthetic CDMAM phantom images, the varying standard deviations in the experimental CDMAM phantom images led to dissimilar CNR measurements. Although typical mammography systems have flat-fielding algorithms applied, this alters the pixel values for each pixel. However, this algorithm does not take into account the variance as a function of location on the detector. This phenomenon occurs due to the heel-effect and should be addressed accordingly.

The CDMAM phantom set up described in this chapter also leads to another issue: the geometric blurring due to the fact that the gold discs are not placed directly upon the detector. The distance between the gold discs and the detector leads to magnification of the details. As such, CDCOM may not be using the correct sized search template as the software uses the a-priori knowledge of the pixel size, disc diameter as well as the actual distance of the intersections of the grid in the CDMAM phantom to deduce the correct search template size.

Non-uniformities described were not of interest in the previous chapter as the measurement of MTF and NPS required detrending of the image to remove such artefacts. Thus, the results of the synthetic images were in agreement with the experimental images. The observer detection task in this chapter has highlighted the non-uniformity artefacts that affect an observer's ability to detect specific details. In the next chapter, addition of non-uniformity models will be presented along with results showing their effects upon the CDMAM phantom scoring results.

Chapter 6

Non-Uniformity Considerations

This chapter presents the development of the image simulation chain to incorporate non-uniformity effects. Thus far, the image simulation chain has been based upon previous authors' models [61, 94, 10] and applied to clinical test objects which have not been previously considered. MTF and NPS comparisons were consistent with published papers[61, 96, 94]. The scoring results of the CDMAM phantom images were illustrative of the effects of the MTF and noise upon the detectability of the discs. Images synthesised with the same image quality metrics as the system setups provided comparative results with that of the experimental images acquired. Some of the discrepancies in the contrast-detail curves indicated that there were further aspects in the image simulation chain needing to be considered, primarily thought to be obfuscating non-uniformity effects in the image.

This chapter is divided into four parts to introduce the different non-uniformity considerations made to improve the image simulation chain: spatial intensity variation, variance map, geometric MTF and scatter. Each section is split into theory, methodology. Results of the combined effects upon the CDMAM scoring will be presented.

All the effects of the non-uniformity considerations will be systematically incorporated into the image simulation chain and the resulting synthesised images assessed using contrast-detail curves as before. Finally the complete image simulation chain will be presented with all non-uniformity considerations taken in to account.

6.1 Spatial Intensity Variation

The most significant spatial intensity variation issue in diagnostic radiography is caused by the heel-effect. Despite this, few authors have considered including the heel-effect in radiographic image simulation. Typically the goal of previous authors has been to remove this effect[18, 20, 113, 19] from clinical images. Within this section, methods of modelling the heel-effect will be reviewed. The sources of the spatial intensity variation, such as path obliquity, spectral beam hardening and inverse-square law, are often ignored in modelling as their effects are smaller compared to the heel-effect. Nevertheless, these effects will also be discussed in the following section.

6.1.1 Causes of the Spatial Intensity Variation

There are a number of causes of the spatial intensity variation as aforementioned. The main cause is the heel-effect. This has been discussed in Chapter 2 but a more indepth explanation will be given here to understand what needs to be incorporated into the image simulation chain.

Within the X-ray tube, the electrons are fired at the anode as shown in the inset of Figure 6.1. There is a specific range at which the electrons will penetrate the anode target. However, the resultant X-rays will traverse different path lengths as they leave the anode. As the resultant X-rays leave the anode target, the energy dissipated within it is dependent on the path length traversed, thus the X-ray beam is non-uniform. Investigations by Terry et al[114] have found the difference in pixel intensity values from one side to another, along the anode-cathode axis, can vary between 16-40% in mammography. The difference in the orthogonal direction to this anode-cathode axis is more modest at only 1-9%. The next source of spatial intensity variation is path

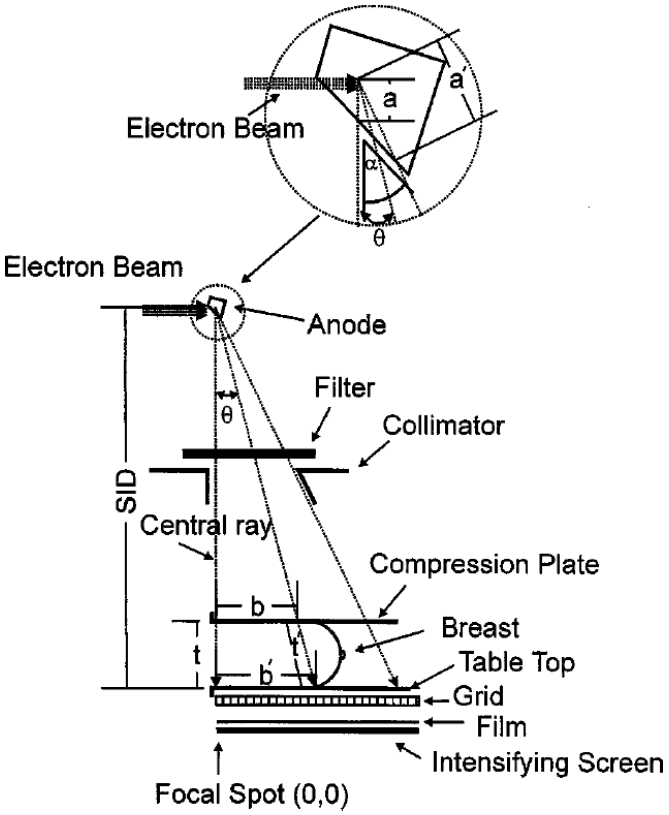


Figure 6.1: Schematic of the contributing factors to spatial intensity variation in mammography. The differing path lengths a to a' leads to an inhomogenous intensity beam exiting the X-ray tube, this phenomena is known as the heel-effect. Path obliquity is demonstrated by the differing path lengths within the object, t compared to t' would lead to greater attenuation at the point under t'.SID is the source-to-imager distance. Image taken from [18].

obliquity. Figure 6.1 shows the effect of path obliquity. The tilted X-ray tube and

intrinsic target angle of the anode combine to yield an angulation of the target with respect to the beam that is orthogonal to the plane of the image receptor. In the Figure 6.1, the path length t directly below the focal spot is shorter than t', a ray passing through at another angle. This path obliquity occurs in all objects in the field of view, thus the X-ray beam is non-uniformly attenuated through the filter, the compression paddle, test object/breast, anti-scatter grid and imaging plate. Beam hardening occurs when lower energy X-rays being attenuated more than higher energy X-rays. As the tilted anode angle and obliquity of the beam contributes to the beam hardening, the mean beam energy increases with increasing θ whilst the relative noise increases due to greater attentuation. The path obliquity occurs in both directions from the focal spot.

The final source of X-ray field non-uniformity is the inverse square law. This occurs due to the divergence of the X-rays as they move further away from the source, thus the X-ray fluence reduces as the distance in the image from the central ray increases.

The effect of the aforementioned spatial intensity variation in the image is that the contrast measurement will be dependent on its location. Figure 6.2 shows a 3D plot of five identical discs on a uniform background from a digitized radiographic image, in the presence of the heel-effect. As can be seen the heel effect rapidly alters the local spatial intensity. Measurements based on intensity values alone would be inaccurate.

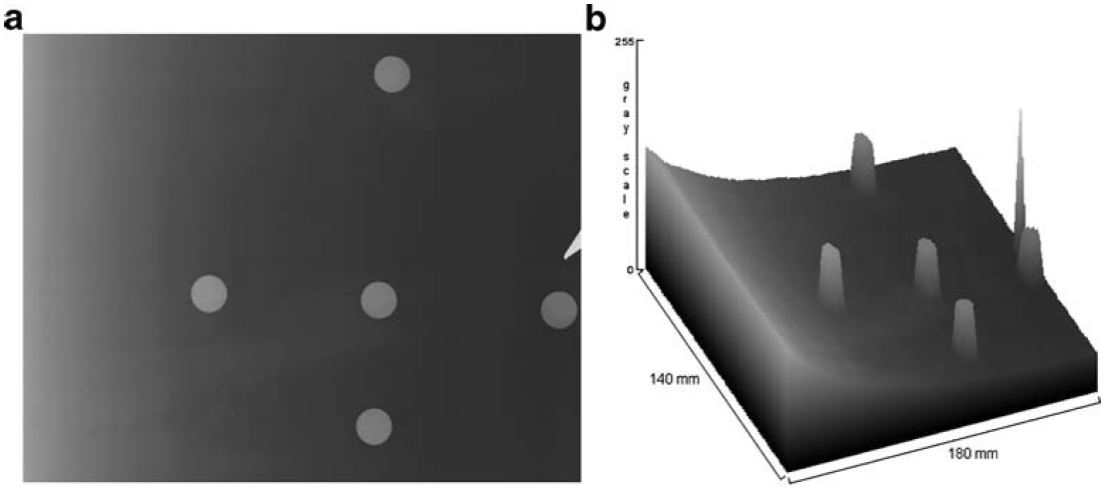


Figure 6.2: An example of the heel-effect upon the contrast of a set of identical discs on a uniform background. (a) shows the X-ray image and (b) shows the 3D plot of the same image[19]. The sharp artefact in the right hand side of the image is a pointer.

Burgess[115] investigated the background non-uniformity of a flat-field image obtained with a mammography system: A 0.1×0.1cm box function kernel was applied to a flat-field image and found that there was band-like modulation in the image. When this was carried out for the same mammography system at another institution, the pattern differed from the first image. One noteable artefact was a *cupping* artefact around the edge of the image[115]. Burgess hypothesised that during system calibration, the flat-field images were created with the compression plate removed and 2.5cm thick PMMA placed directly on the detector. Due to scatter pattern from the PMMA, subsequent images flat-fielded from this map will have spatial variations introduced by

the non-uniform scatter pattern. From this, it can be inferred that a model to the spatial intensity variation will be individual to each system, despite the use of the same technology. The next section will review the literature on the approaches taken to model the heel effect of an image in other areas of diagnostic radiography.

6.1.2 Modelling the spatial intensity variation: a literature review

From the literature reviewed there are two main methods of modelling the heel-effect, by processing experimental images[113] and with theoretical models[18, 20, 19]. Each methodology will be reviewed below.

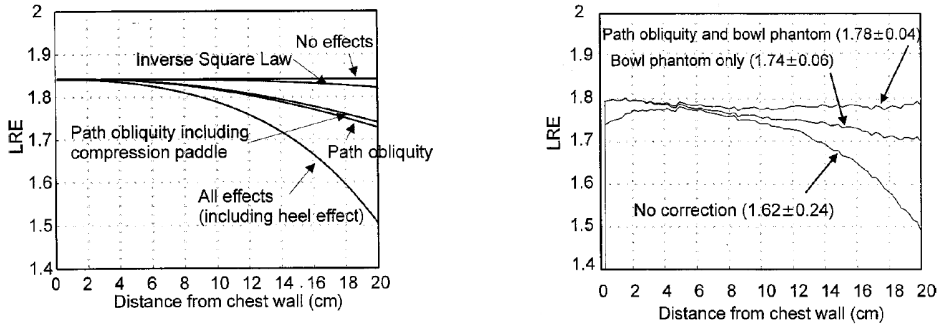
As noted previously, heel-effect modelling has often been undertaken for the purpose of correcting radiographic images. Despite the efforts of the flat-fielding algorithm, there are residual effects.

Pawluczyk and Yaffe[18] have corrected the spatial intensity variations produced by the heel-effect in digitized mammograms[1]. Simulated images were calculated with a range of formulae to account for non-uniformity effects. Experimental set up to emulate this was carried out with a 'bowl' shaped PMMA phantom. This phantom had been produced such that at any point in the (x, y) plane, the thickness $t = t'$ (in Figure 6.1). This phantom negated any path obliquity present in images of uniform slabs of PMMA. This bowl-shaped phantom allowed a correction matrix to be constructed and applied to subsequent images.

Results of the profiles of the simulation and the experimental correction method are shown in Figure 6.3. Figure 6.3b shows the profile of the uniform PMMA slab with and without the empirically derived correction matrix. Path obliquity correction was also applied to improve the results. The simulation results were in line with the experimental data with one exception, the simulation did not fully explain the gradual increase in intensity from the chest wall to a position 6cm away. This effect is shown in Figure 6.3. Pawluczyk and Yaffe concluded that the modelled non-uniformity corrections were similar to experimental results. However, they were insufficiently accurate to correct for all the non-uniformities. To provide a versatile and robust method of removing the non-uniformities, a combination of the simulation and empirical methods was employed.

Behiels et al[20] developed a fully automated mathematical model to correct the heel-effect in radiographic images of the hand. Behiels et al's method involved fitting a mathematical model derived from the geometrical setup of a typical radiography system. Two assumptions were made: firstly, the heel effect had an exponential profile along the anode-cathode axis; and secondly, that the heel-effect is constant in the perpendicular direction. The background region of the image was extracted to estimate the parameters of the mathematical model. The fitted model is used to correct the whole image and a new background region is extracted from the corrected image and model parameters estimated. This process was repeated until no significant changes in the background region and the mathematical model estimation were found.

[1] Digitized mammograms were a compromise between screen-film technology and digital technology. Screen-films were processed through a digitizer to produce digital images.



(a) Simulated (b) Experimental

Figure 6.3: (a)The results of a simulation of a 4cm slab of PMMA with 28kVp spectrum. The curves show the individual effects of the inverse-square law, path obliquity with and without the compression paddle and all effects including the heel-effect. All curves were shifted to provide the same signal intensity at the chest wall. (b) Experimental profile results of a 4cm slab of PMMA with 28kVp spectrum. The profiles are shown with and without correction with mean and standard deviations [18].

The method was effective, as shown in Figure 6.4. The methodology was applied to 137 hand X-ray images. However, the model needed to be refined through an iterative process and only assumed change in the heel-effect in one direction (which may have been sufficient for the images that were used). Most of the resulting image was occupied by the hand and it appeared that the anode-cathode axis was along the length of the hand, where background inhomogeneity was most noticeable. The heel effect was more prominent in the direction of the hand to forearm in the X-ray images. Therefore, Behiels et al only considered a model that was dependent on the distance in the direction of the hand to forearm. It would be appropriate to alter the mathematical model to include variations in the perpendicular direction for mammography imaging. Other limitations of this method includes the necessity of several iterations for each image for an accurate model to be derived.

do Nascimento et al[19] developed an automatic correction method to correct for the spatial intensity variations by the heel-effect without the use of reference images or previous experiments to detect the centre of the X-ray field. All calculations were determined from the one image to be corrected. do Nascimento et al's method involved simulating an image based on the radiological image formation process utilising ray-tracing methods that accounted for the heel-effect. Once the simulated image was created, this was subtracted from the radiological image to provide a heel-effect corrected image.

The removal was considered a success, with minimal difference between experimental images and the modelled image. In addition, do Nascimento et al considered the physical behaviour of the X-ray generation accurately. Consequently, it was claimed that noise (measured as standard deviation) in the mammogram can be removed with-

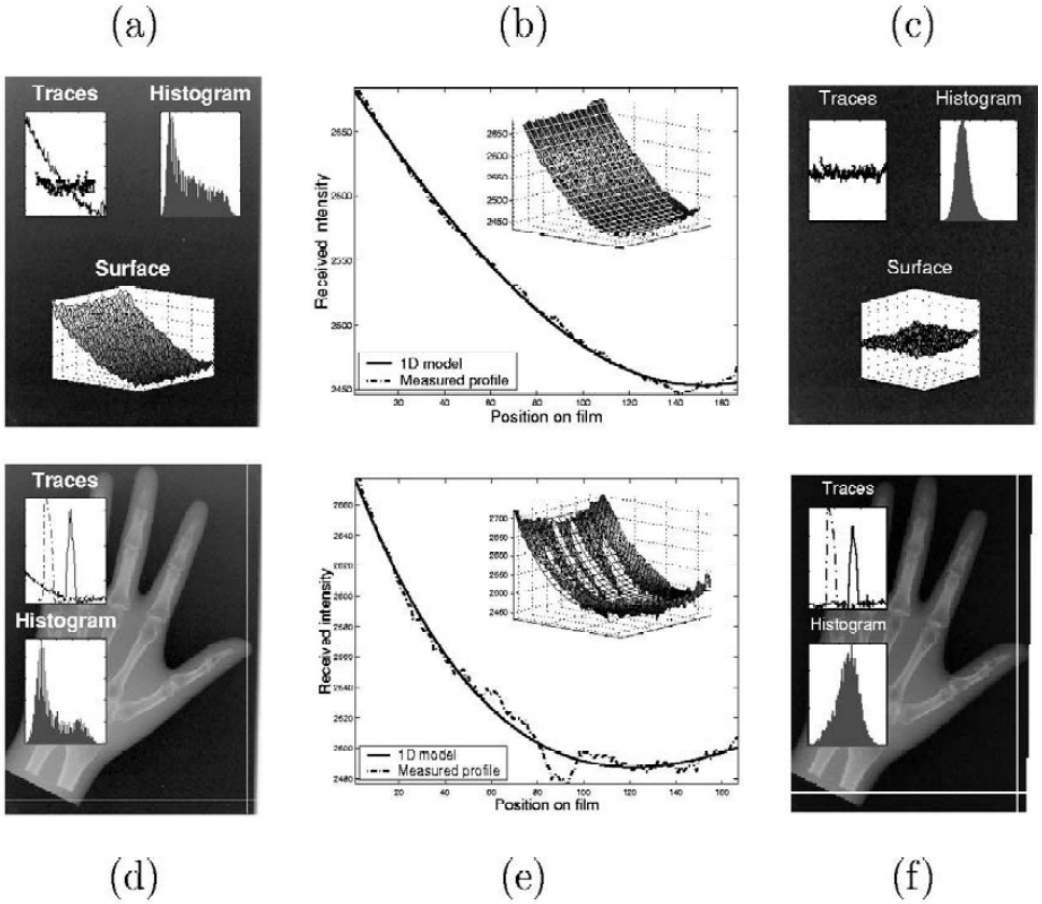


Figure 6.4: (a)Flat field image presented as a surface with its histogram and profile along the anode-cathode axis (solid line) and perpendicular to this axis (dotted line). (b) Averaged profile (dotted line) and the fitted model (solid line) of the flat field image. The subimage presents the fitted model as the white grid overlaid on the rendered surface of the flat field image. (c) Surface, histogram and profile of the corrected flat field image. (d) same as (a) for the hand image. (e) same as (b) for the hand image. (f) same as (c) for the corrected hand image. Image taken from [20].

out affecting structure relevant to diagnosis. However, this was not fully assessed and proven with ROC analysis. As this model was developed for digitized mammograms, consideration of the flat-fielding effects were not needed. It would be difficult to accurately predict how the flat-fielding algorithm would have attempted to correct for this heel-effect.

Alsager et al[113] also developed a method to remove the heel effect from images to improve CNR measurements. The CNR was measured from an image acquired with 45mm PMMA and an aluminium square in the directly below the focal spot. From this image, ROIs were placed on the four sides of the aluminium square, as well as within the aluminium square. The work found a method to improve the CNR measurement in the images by correcting for the heel effect.

With the repetitive use of a 7×7 pixel Gaussian filter applied to an image, high frequency noise arising from the detector was eliminated and low frequency noise from the heel effect was retained. This created a smoothed image, I_B, with which to divide the image to be corrected from the heel effect, I_A. This was then multiplied by a scaling factor, F_S, to produce the heel-effect corrected image with 'average' mean pixel intensity values:

$$I_C = \frac{I_A}{I_B}.F_S \tag{6.1}$$

The scaling factor was defined as the mean pixel value of the image. This method provided effective removal of the heel-effect in digital mammography images, especially the CR systems, improving consistency of CNR measurements.

In summary, both methods of modelling the heel-effect, processing experimental images [113] and with theoretical models[18, 20, 19], have been applied in correcting the heel effect from images and appear to be effective. Pawluczyk and Yaffe, Behiels et al and Nascimento's methods were all applied to digitized film-screen images. These typically have no prior spatial intensity correction applied, unlike digital mammography images. Images acquired on current digital mammography systems can only be acquired with this flat-fielding algorithm applied. As the flat-fielding algorithm does not remove the heel effect completely in all images, there are residual effects present. Thus, modelling based on the assumption that the digital mammography image is subject to all the aforementioned effects would be an overcompensation. Therefore, for work in this thesis, a method based on Alsager et al[113], which used digital mammography images which had been flat-field corrected, would be most appropriate.

6.1.3 Modelling the Residual Heel-effect

To simulate the CDMAM with the residual heel-effect as accurately as possible to include effects of obliquity and possible scattering effects as discussed earlier[115], the experimental image acquired in the same conditions as the CDMAM phantom image is needed. That is, the same geometrical set up as the CDMAM is needed: 40mm PMMA with a CDMAM phantom. The CDMAM phantom is assembled with 5mm PMMA and a 3mm aluminium plate where the gold discs are inserted.

Ideally, a uniform image acquired with a 50mm thick block of PMMA should be used to obtain the heel-effect mask. As mentioned previously, the attenuation properties of

the CDMAM phantom can be approximated with a 10mm thick block of PMMA. This ensures that all path obliquity, inverse-square law and heel effect issues that are present in acquired CDMAM phantom images (and subsequently corrected for using the flat-fielding algorithm) are included. However, in early studies of this work, such images were not available. Uniformity images that were available were acquired with 45mm PMMA according to European guidelines[24] for the purpose of NPS measurement. If such an image is used, the pixel intensity value may be overestimated and the spatial intensity non-uniformity may not be correctly modelled. To overcome this obstacle, CDMAM phantom images were used. CDMAM phantom images contain all the details of the test object, but with the correct filter kernel size. The high frequency noise of the details as well as the local quantum noise was removed whilst retaining the low-frequency residual heel-effect across the image as detailed in Alsager et al[113].

A median filter was chosen to smooth the CDMAM phantom image. This removes the high frequency details such as the grid and discs, as well as the noise in the image, to leave the slow varying shape of the heel effect. Alsager et al[113] implemented a Gaussian filter on a single uniform image 20 times[113] in order to attain the same heel-effect mask. Let S_{xy} represent the set of coordinates of an ROI of size (m $\times$ n) at point (x, y). The median filter calculates the median value of the CDMAM image, $g(x, y)$, within the defined ROI. Therefore, the resultant smoothed image, $f(x, y)$, at point (x,y) is the median value using the pixels in the ROI defined by S_{xy}:

$$f(x, y) = \underset{(s,t)\in S_{xy}}{median} \{g(s, t)\} \tag{6.2}$$

To remove details such as the grid, discs and noise from the CDMAM image effectively, a set of 3 kernels were investigated: with equal in size to the CDMAM cells in the image (200 pixels, pixel size of 70μm), less than the the size of the cells in the image (150 pixels) and a factor of 1.5 times the size of the cells in the image (300 pixels). Figure 6.5 shows the effects of the varying filter kernel sizes overlayed on the original CDMAM profile without filtering. It can be seen that the kernel with a factor 1.5 times the cells diameter in the image was most effective in removing the high frequency details whilst retaining the shape of the heel-effect. For the other systems modelled in this study, the GE Essential system with 100μm pixel size required a kernel of 210x210 pixels. The Agfa CR system with 50μm pixel size required a kernel of 420x420 pixels. The next step was to apply this heel-effect mask to the synthetic CDMAM images.

The primary image referred to here is created based on the detector response i.e. the idealised image, I_{ideal} created in Chapter 4 and 5. Equation 6.1 was rearranged to create the heel-effected image, I_{heel} :

$$I_{heel} = \frac{I_{ideal}}{\mu(I_{smoothed})} \times I_{smoothed} \tag{6.3}$$

where $I_{smoothed}$ is the median filtered experimental image acquired in the same conditions as the image to be created. The scaling factor in Equation 6.1 was replaced with the known mean pixel intensity value in the smoothed image, such that the simulated image is scaled and is always relevant to the exposure setting to be simulated.

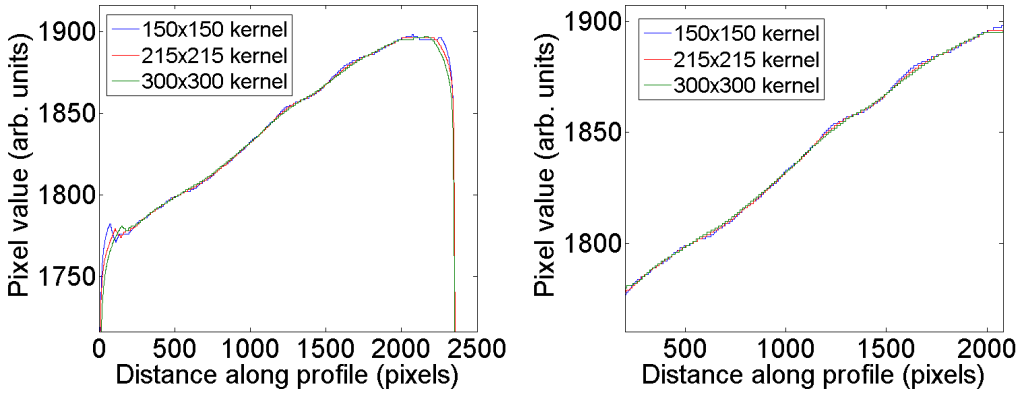


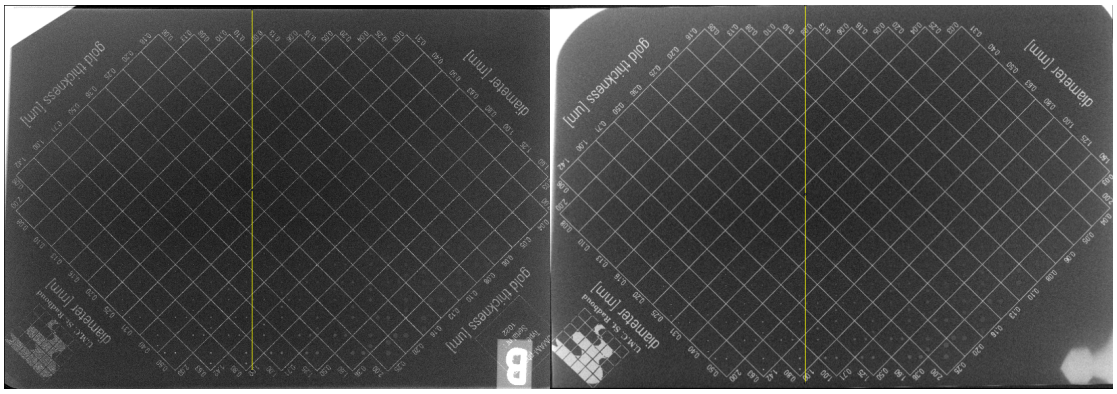
Figure 6.5: Profile taken of the heel effect masks derived using median filter kernels of size 150x150, 200x200 and 300x300 pixels.(a) shows the profile across the image. (b) shows a cropped region of (a) for clarification on the rippling effect.

The advantage of this method is that the median filter need only be applied once, unlike Alsager et al's[113] approach where the Gaussian filter was applied multiple times to remove the quantum noise effectively. In addition, the required set up to obtain the residual spatial intensity variation is retained for application to the CDMAM image without need for precise physical modelling of the geometrical set up for each simulation. One possible drawback is that a reference radiological image is required per system at the same set up as the CDMAM image. However, with the type of images obtainable in acceptance testing of a mammography system such as MTF and NPS, CDMAM images are typically acquired and this work has shown that median filtering of the CDMAM image is sufficient for simulating the residual heel-effect. Figure 6.6 shows the heel-effect modelled in a synthetic CDMAM compared with an experimentally acquired CDMAM image. The effects of including the residual heel-effects are shown in Section 6.1.4.

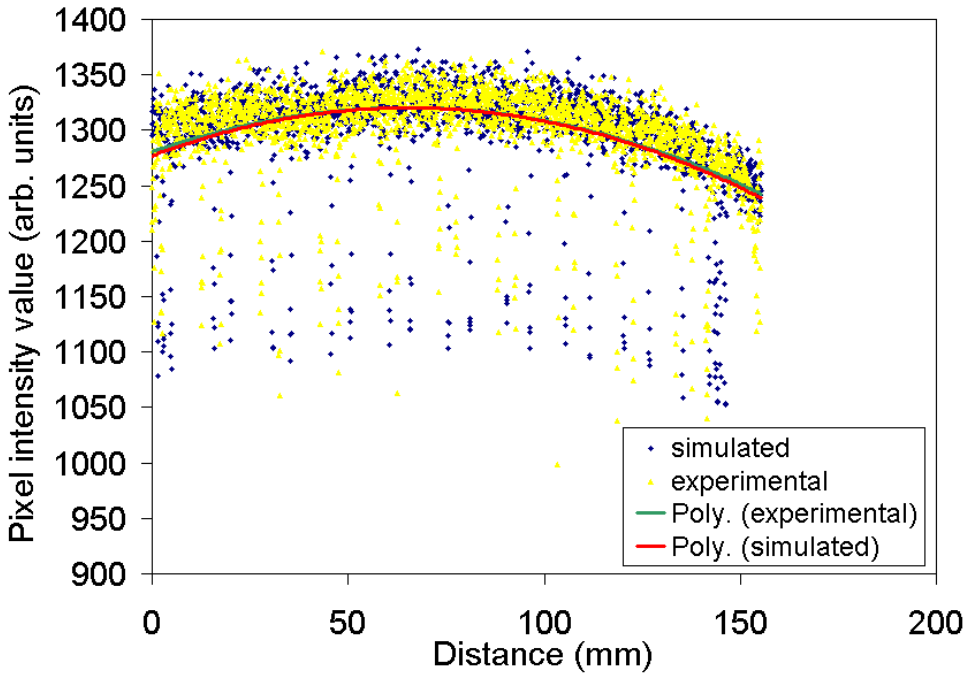
Addition of the heel effect mask will not affect the contrast of the discs as they are modelled in reference to the local background. However, as variance in the image is modelled on a pixel-by-pixel basis, this will increase or decrease the variance in local areas of the X-ray field accordingly.

6.1.4 Spatial intensity variation for the three systems

The heel-effect mask was acquired from all systems simulated in this work thus far: Hologic Selenia, GE Essential, Agfa CR. From these masks, the amount of residual heel-effect could be determined: the Hologic Selenia (a-Se technology) had 6.6% relative difference from the chest to the nipple side of the detector, in the perpendicular direction, the relative difference was 5.6%. The GE Essential (CsI scintillator) had 2.0% difference from the chest to the nipple side of the detector, and 1.4% in the perpendicular direction. The Agfa CR had 17% difference from the chest to the nipple side of the detector, compared with 20.6% in the perpendicular direction. The reason



(a) (b)



(c)

Figure 6.6: (a) An experimentally acquired CDMAM image for the Hologic Selenia system. (b) A simulated CDMAM image with heel effect mask applied for the same system. The yellow lines show the location of the profiles taken for comparison in (c). There are sharp spikes in the profiles relate to the grid lines in the CDMAM phantom image. Polynomial fits to the experimental and simulated data are shown in red and green for clarity.

for this is that CR system does not have any flat-field correction applied. The results are within range of the that quoted by Terry et al[114]. The heel-effect mask for each system is shown in Figure 6.7.



(a) Hologic Selenia (b) GE Essential (c) Agfa CR

Figure 6.7: Normalised heel-effect masks implemented for each system. The smudge in the corner of (a) is an artefact from implementation of the median filter upon a high pixel intensity value object in the corner of the CDMAM phantom image. This does not affect the analysis of the CDMAM phantom image. There is a blur in the heel effect mask for (a) due to the presence of a high pixel intensity object in the corner of the original CDMAM image (an image identifier). It was possible to acquire the CDMAM images for GE and Agfa systems without the identifier present.

6.2 Pixel Intensity Variance across the Detector

Although the flat-fielding algorithm corrects for the pixel intensity value variation across the detector, it is not possible to correct for the pixel value variance. In the remainder of this section, the consequences of this will be considered. In addition, the methodology in modelling the variance across the detector will be outlined.

6.2.1 Consequences of Pixel Intensity Variance

Figure 6.8 shows how the signal variance across alters across a CsI scintillator detector. Pixels with high variance are shown in white and low variance is shown in black. As the distance from the central spot increases, so does the variance. This is because the spatially variant illumination, due to the heel-effect as described in the previous section, leads to varying signal variance. This is due to quantum statistics of the X-ray photons as mentioned in Equation 3.3: $\sigma = \sqrt{N_p}$.

The consequences of this effect are that the CNR of details is reduced by this process at outer edges of the detector where relative variance is higher. Figure 6.9 shows a set

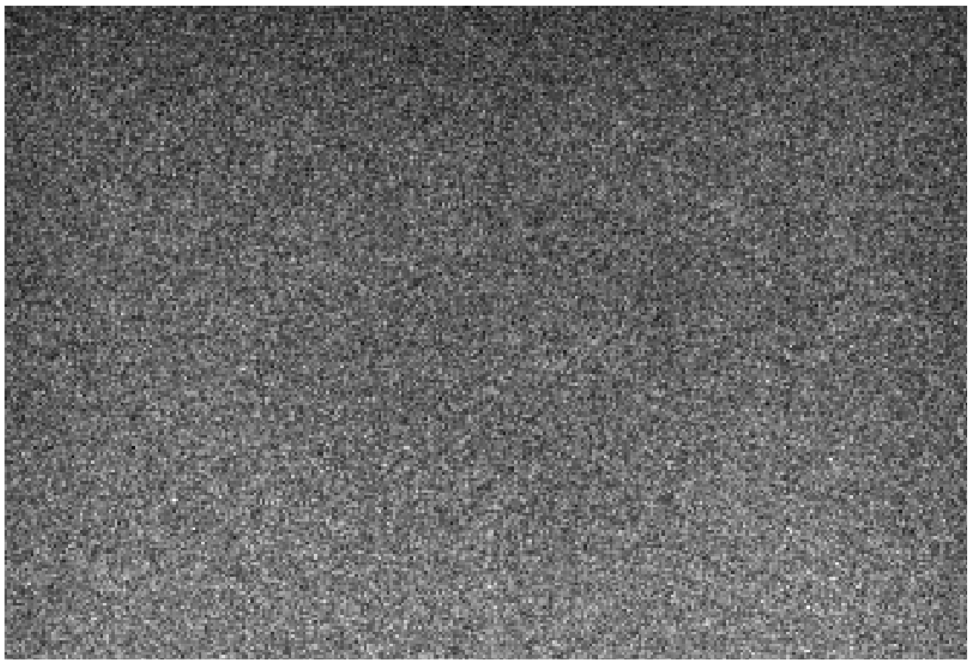
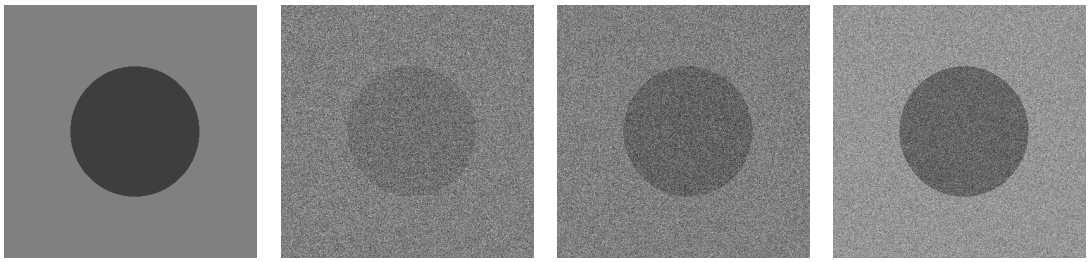


Figure 6.8: A 2D representation of the variance in a uniform image from a CsI scintillator detector. High variance is represented by white pixels whilst the low variance is shown in black. The chest wall of this image is at the bottom.

of identical details where the contrast remains the same whilst the noise increases, thus the CNR decreases.

Marshall[50] implemented a variance image to check for uniformity of the variance across the detector, else any gross artefacts may violate the assumptions of ergodicity and stationarity required for the NPS analysis. Marshall assumes that for a normally functioning detector, the image variance would be dominated by the X-ray statistics of the beam, with some variation due to the heel effect[50, 53]. Any deviation from this indicates artefacts in the detector. Such gross spatial artefacts should be rectified in a clinical environment, i.e. by replacing the detector. Variance maps were found to be useful tools to give an indication of such artefacts.

The variance map will provide a measure of the statistical uncertainty at each point in the image, the contributions of which will be from the statistical fluctuations associated with photons as well as local fixed pattern and electronic noise. Fixed pattern noise may arise from local non-uniformities in the detector as some pixels may not be as sensitive as others. For example, in CR imaging plates, fixed pattern noise may arise from the granular nature of the powdered phosphor layer.



(a) No noise (b) CNR = 0.5 (c) CNR = 1 (d) CNR = 2

Figure 6.9: An example of disc details simulated with differing CNR levels.

Thus far, no author has presented a method to simulate the increased geometric variance across an imaging detector. It is potentially arguable that this may not affect detection when considering the anatomical clutter noise in a clinical mammogram. However, for a CDMAM phantom image where the discs are placed on a uniform background, aside from MTF blurring, quantum noise will be a major factor obfuscating disc detection. Thus non-stationary variance such as that described above may reduce the CNR of the discs and therefore affect detection rates. Applying a spatially dependent variance 'map' may improve detection of certain discs whilst decreasing the detection of others based on their location in the image. This may lead to a shift in the contrast-detail curve either globally, or at its ends.

6.2.2 Introducing the effects of the Pixel Intensity Variance

The increased variance with increased distance from the central focus in the detector is due to the heel effect[50]. If a non-uniformity heel effect mask is added to the image simulation chain, with the added effect of the pixel-by-pixel mean-variance function applied to the image, the variance should be modelled sufficiently to account for all major obfuscating effects. However, the previous chapter also explored the fact the flat-field algorithm does not alter the variance in the image. Thus, the variance in the resulting simulated image would only be the variance due to the *residual* heel-effect of the image, not the full heel-effect.

For this reason, it is necessary to add a location-dependent variance to the simulated image, which will need to originate from empirical measurements. A variance image was generated from uniform images of a 50mm PMMA slab using the method outlined by Marshall[50, 53]. A 10 x 10 pixel ROI was used to calculate the local variance in the uniform image. Beginning at the top left corner of an uniform image, I_u, the ROI estimates the variance and this value is used to replace the corresponding 1 x 1 pixel region in the variance image, $I_{var}(x, y)$.

$$I_{var}(x, y) = \sigma^2(I_u(x, y)) \tag{6.4}$$

Figure 6.8 is an example variance image from a CsI system simulated in this work. The variance smoothly varies from high to low variance from left to right as expected in relation to the number of photons. However, the variance image is still very noisy as

can be seen in Figure 6.8 and 6.10. Therefore a 2D polynomial fit was implemented. The 2D polynomial took the form of:

$$f(x, y) = b_0 + b_1 x + b_2 y + b_3 x^2 + b_4 xy + b_5 y^2 \tag{6.5}$$

b_{0-5} are the coefficients to be fitted. A polynomial regession model was used to fit the data.

A second order polynomial was confirmed to give the best fit; the error was reduced as the order of the polynomial used was increased. The root mean square error (RMSE) was calculated to be 11.14. This appears to be a high level of error but it should be borne in mind the original variance map is very noisy. The error only decreased by less than 1% each time after the initial error and was not a substantial improvement. The alternative fit to this was to use a median filter with a kernel size of 50 x 50 pixel a minimum of five times. The RMSE between the original variance map and the smoothed model was found to be 11.52 and was not found to be significant. Figure 6.10 shows the 2D fit with the variance data points overlaid.

This modelled variance image is used as a *map* of the changing variance across the imaging receptor. Therefore, this variance image was normalised to create a variance map, I_{vmap}. To introduce this into the image simulation chain, it was necessary to apply the variance map to the noise image in the spatial domain. Thus, the variance map was multiplied with the correlated noise image, $I_{N,corr}$, as illustrated in Figure 6.11. The resulting correlated noise image with variance map applied was then corrected to the mean-variance relationship on a pixel-by-pixel basis as described in Section 4.6.2.

It is expected that the spatially dependent pixel intensity variance will cause a slight shift in the contrast-detail curves. The low contrast details may become harder to detect, the smaller details will be degraded more so as the detail diameter tends towards the size of the detector pixel.

6.3 Magnification through Geometric Setup

Another factor of blurring in radiography results from the geometrical set up. As discussed in Chapter 3, the presampled MTF is a measure of the detector MTF and sampling effects only. Additional sources of blurring need to be included separately such as the geometric blurring.

In mammography, there may be situations where magnification of a suspicious lesion is necessary. This may be achieved in two ways: a small field digital mammography (SFDM) system with finer resolution ($24\mu m$ per pixel[88]); alternatively, the object of interest may be imaged with an air gap between it and the detector.

Due to the divergent X-ray beam, magnification of an object with the use of an air gap will introduce blurring. This is known as geometric blurring. Geometric blurring has been modelled by Sandborg et al[116, 117]. Sandborg et al state that the geometric blurring is caused by the focal spot and varies with magnification[116].

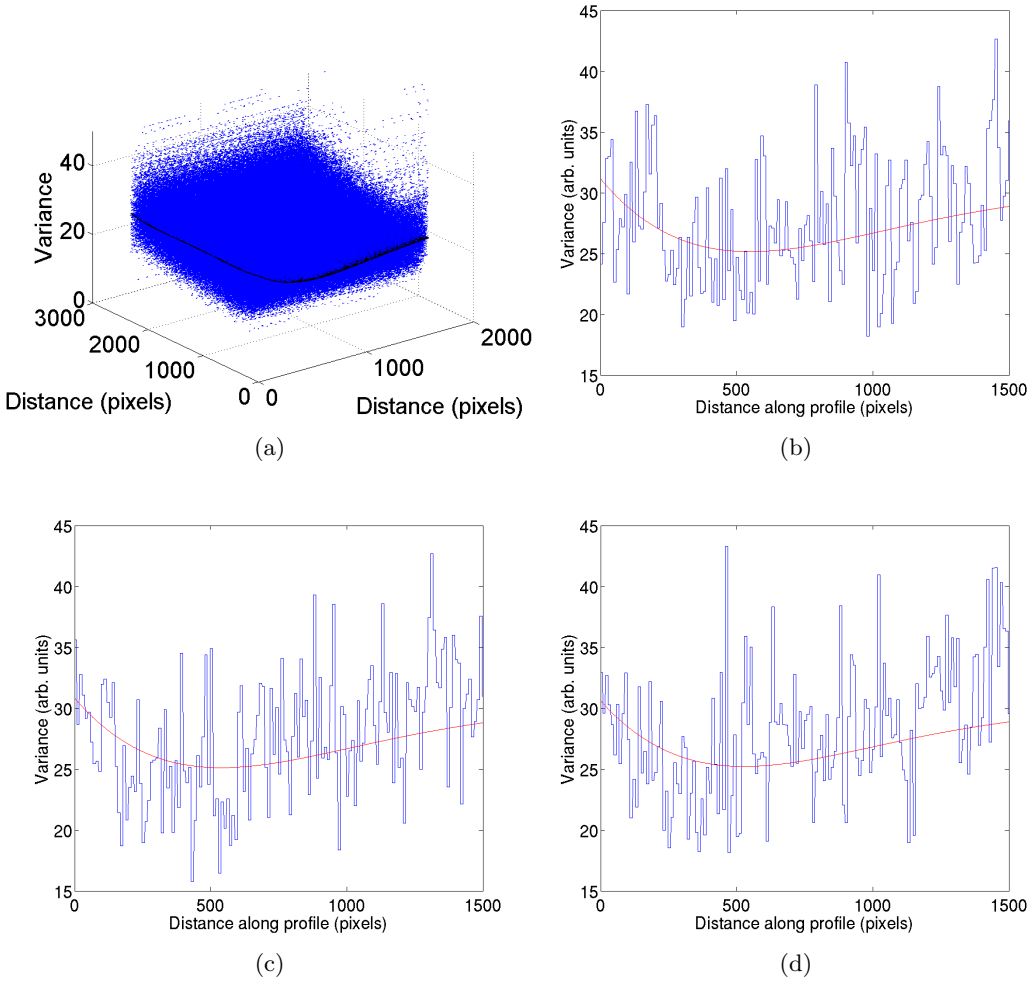


Figure 6.10: (a)The surface plot (black) modelled on the variance image (blue points) created from the GE Essential system. (b-d) shows profiles from the chest wall to the nipple side of the variance image at three profiles along the perpendicular direction of the image. The red curve is the 2D polynomial fit to the variance image (blue).

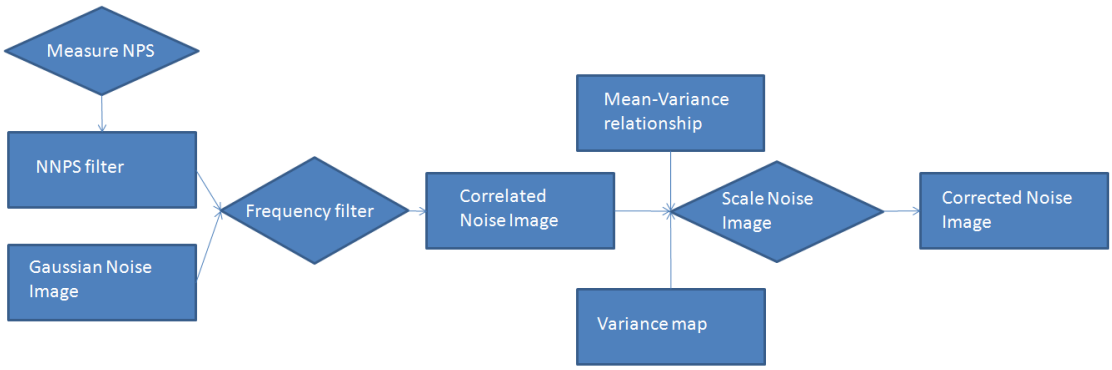


Figure 6.11: Detailed flow chart of the noise creation framework with alterations to include the variance map. The variance map is applied before the noise image is scaled to the mean-variance relationship to account for the relative change in variance across the detector.

The magnification is given by:

$$m = \frac{SID}{SDD} = 1 + \frac{DSD}{SDD} \tag{6.6}$$

SID is the source to imager distance, SDD is the source to detail distance. If the detail is thin, DSD can be defined as SID-SDD.

The focal spot can be characterised with direct measurement with a pinhole camera or with equipment that enables recording of a magnified image of the emission distribution from the focal spot[116].

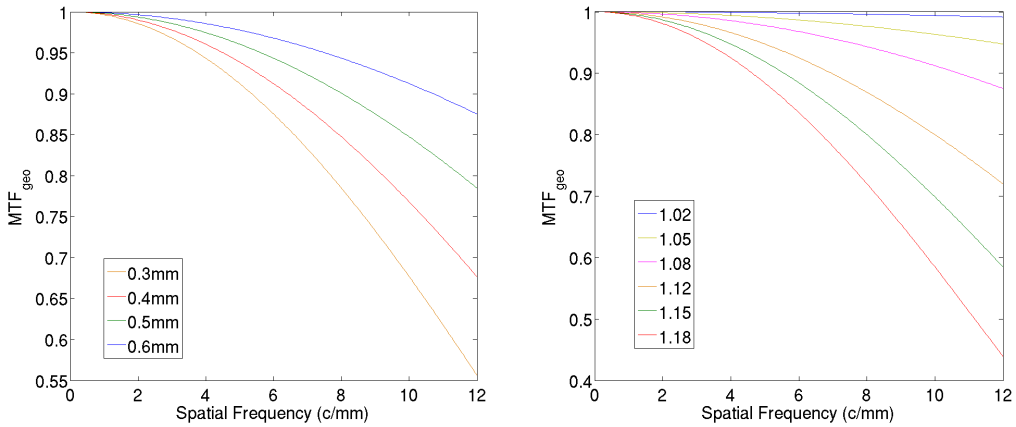
The focal spot was modelled on a box function, where an uniform emission distribution within a box side of s and no emission outside of this box. Sandborg et al[116] modelled the geometric blurring as a MTF_{geo}:

$$MTF_{geo} = \frac{|sin\left(\pi s f\left(m-1\right)\right)|}{\pi s f\left(m-1\right)} \tag{6.7}$$

where f is the spatial frequency. Sandborg et al define the spatial frequency, f, in the image plane in reference to the spatial frequency in the object plane, f_o:

$$f = \frac{f_o}{m} \tag{6.8}$$

Figure 6.12 shows examples of MTF_{geo}, with varying focal spot size and magnifications. As can be seen, the MTF_{geo} does not deviate greatly from unity (complete signal transfer) until the higher spatial frequencies. This means that the smaller discs will affected more by the MTF_{geo} than large discs ($f = 1/2 \times discsize$). In the previous chapter, the effect of the presampled MTF upon the contrast degradation of the discs was explored. Results showed that modelling the presampled MTF alone was insufficient in degrading the contrast of smaller discs.



(a) Focal spot sizes (b) Magnification

Figure 6.12: (a)MTF_{geo} for differing focal spot sizes and magnification of 1.08. (b) MTF_{geo} for different magnifications and focal spot size of 0.3mm.

The total MTF, MTF_t, of the imaging system can be computed as the product of the individual MTF components:

$$MTF_t = MTF_{det} \cdot MTF_{samp} \cdot MTF_{geo} \tag{6.9}$$

Thus, the geometric MTF was introduced into the image simulation chain through multiplication of the MTF_{det} by the MTF_{geo}. The resulting product was used to filter the idealised image, thus achieving MTF_t. In addition, the idealised image will need to be magnified by a factor m before it is filtered to include the magnification effects.

The SID, SDD, magnification and focal spot size was found to be the same across all systems modelled. SID and SDD were found to be 600 and 612mm, respectively, which led to a magnification of 1.08 and the focal spot size was modelled as 0.3mm.

6.3.1 Combining the non-uniformity effects

Figure 6.13 shows the image simulation chain for the CDMAM phantom with all non-uniformity considerations presented in this chapter included.

Initial investigations into each non-uniformity effect were carried out systematically to observe the effect of increasing sophistication of the image simulation framework. Ordinarily, it would not be possible to acquire an experimental X-ray image without the non-uniformity effects let alone with each effect isolated. As such, the effect of including each individual non-uniformity effect will be presented in Tables 6.1, 6.2 and 6.3 (and the contrast-detail curves presented in the Appendix). However, it is more apt to compare the results for the synthetic CDMAM phantom images with the non-uniformity effects combined for the remainder of this work as shown in Figures 6.14, 6.15 and 6.16 for all imaging systems.

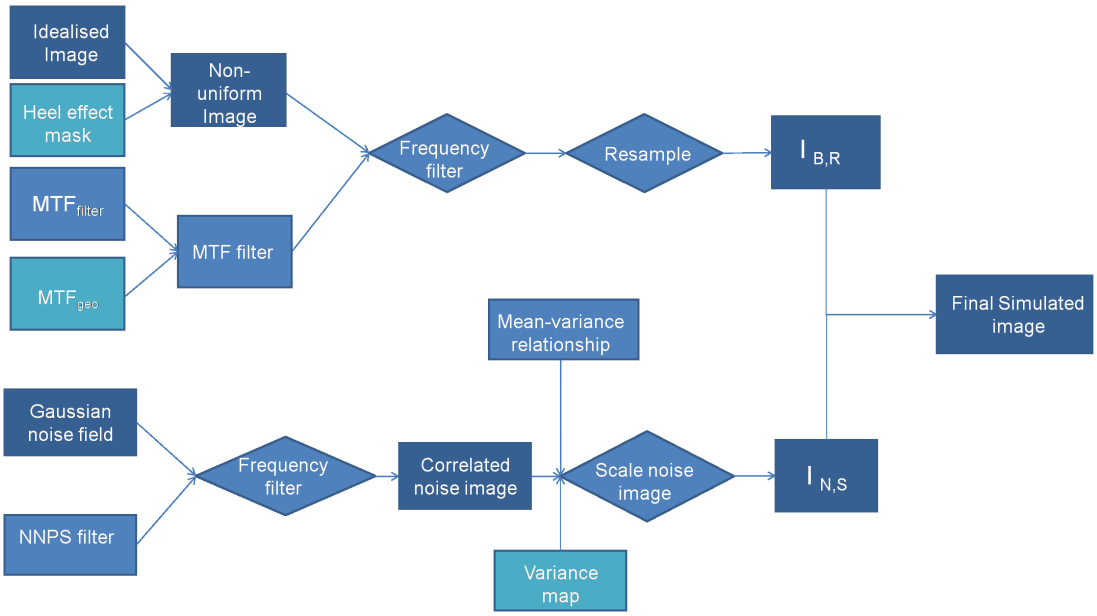


Figure 6.13: The image simulation framework with all non-uniformity considerations included. New additions to the image simulatio framework are shown in light blue.

Tables 6.1, 6.2 and 6.3 show the average, maximum, minimum ratio of threshold contrasts for experimental to synthetic scoring results, R_{d_all}, for all three systems modelled. In all cases, the spatial intensity variance and variance map worsens the overall ratio of threshold contrasts across all doses. Geometric MTF improved the scoring for all systems. When non-uniformity considerations were taken into account, the ratio of the threshold gold thickness drew closer to unity for all systems. In addition, the standard deviation of the ratios dimished when non-uniformity considerations were taken into account. The effect of non-uniformity considerations was more significant for the GE Essential and Agfa CR system because the non-uniformity effects were greater in magnitude compared with the Hologic Selenia system.

Table 6.1: Ratios of experimental to synthetic threshold gold thickness R_{d_all} averaged across all doses used in each study for the Hologic Selenia system.

	Uniform[a]	Spatial Intensity Variance	Variance map	Spatial Intensity Variance and Variance map	Geometric MTF	Combined
Average $R_{d_{all}}$	1.02	0.98	0.99	0.98	1.04	1.00
Maximum $R_{d_{all}}$	1.36	1.31	1.32	1.33	1.21	1.11
Minimum $R_{d_{all}}$	0.93	0.87	0.91	0.87	0.98	0.97
$\sigma(R_{d_{all}})$	0.13	0.13	0.13	0.14	0.07	0.04

[a] from previous chapter

Contrast-detail curves for the synthetic images of the Hologic Selenia (Figure 6.14) provide a good agreement with the experimentally acquired images. The largest discrepancy ($R_{d_i} = 1.13$) was seen at the smallest disc diameter 0.10mm, this may be attributed to possible anomalies the images causing the curves to deviate from that expected. The contrast-detail curves should exhibit the same curvature for each dose

Table 6.2: Ratios of experimental to synthetic threshold gold thickness $R_{d_{all}}$ averaged across all doses used in each study for the GE Essential system.

	Uniform[a]	Spatial Intensity Variance	Variance map	Spatial Intensity Variance and Variance map	Geometric MTF	Combined
Average $R_{d_{all}}$	0.95	0.89	0.86	0.86	0.99	0.99
Maximum $R_{d_{all}}$	1.03	0.98	0.96	0.94	1.12	1.19
Minimum $R_{d_{all}}$	0.89	0.84	0.82	0.82	0.94	0.92
$\sigma(R_{d_{all}})$	0.05	0.04	0.04	0.04	0.05	0.07

[a]from previous chapter

Table 6.3: Ratios of experimental to synthetic threshold gold thickness $R_{d_{all}}$ averaged across all doses used in each study for the Agfa CR system.

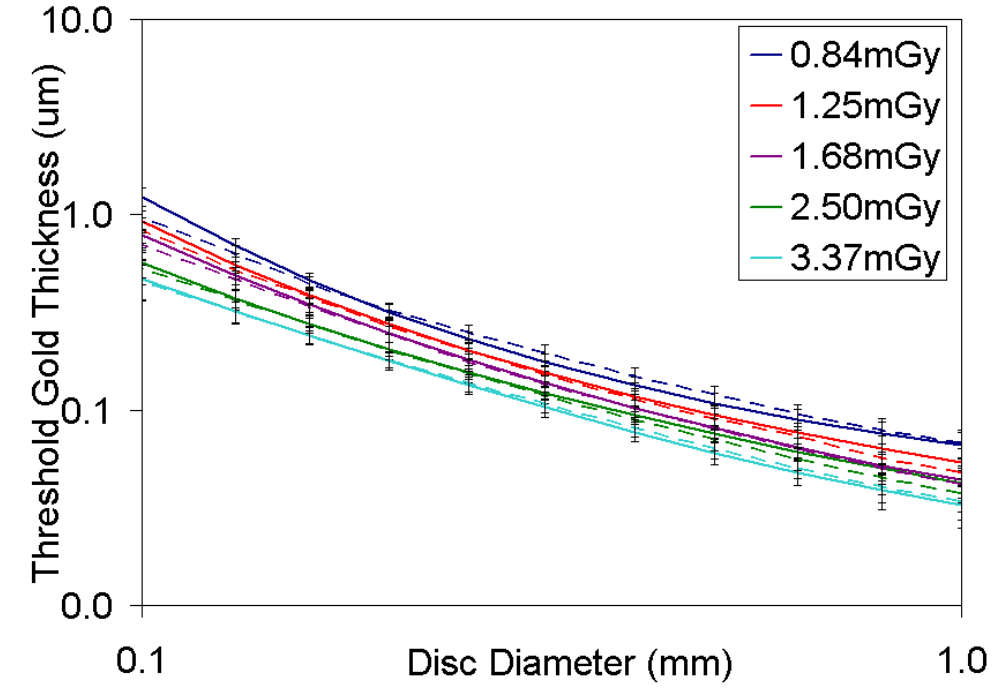
	Uniform[a]	Spatial Intensity Variance	Variance map	Spatial Intensity Variance and Variance map	Geometric MTF	Combined
Average $R_{d_{all}}$	0.86	0.86	0.84	0.83	0.90	1.01
Maximum $R_{d_{all}}$	1.14	1.07	1.07	1.10	1.16	1.39
Minimum $R_{d_{all}}$	0.78	0.75	0.72	0.70	0.79	0.90
$\sigma(R_{d_{all}})$	0.08	0.09	0.09	0.09	0.08	0.12

[a]from previous chapter

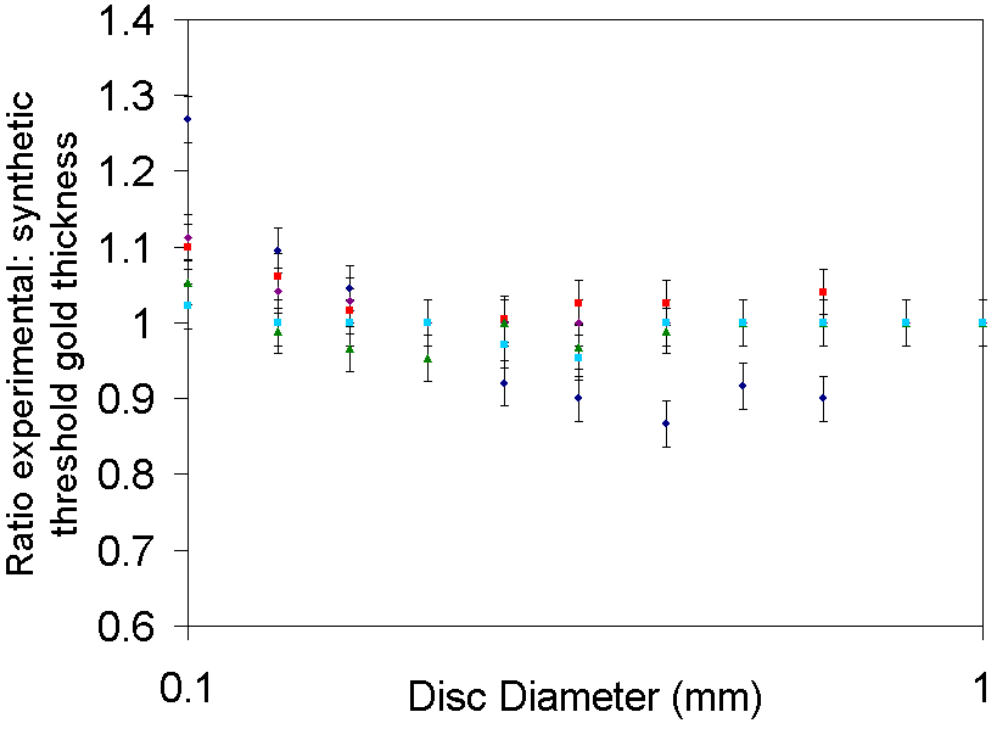
when all other settings remain the same. However, as can be seen, the experimental contrast-detail curves for 0.84 and 2.50mGy deviate from the others slightly. The deviation is due to natural statistical effects in the acquisition of the CDMAM phantom images. The error bars take account of the statistical differences between the CDMAM phantom images. For all contrast-detail curves, the synthetic data are within the error bars of the experimental data.

The maximum R_{d_i} found for the contrast-detail curves of experimental and synthetic GE Essential CDMAM phantom images. There is a larger curvature exhibited in the experimental contrast-detail curves, which synthetic data struggle to replicate. Although the geometric blurring has had an effect on the smallest discs, exhibited by the reduction in $R_{d_{0.10mm}}$ from 1.02 to 1.00 for the uniform to non-uniform model, there is still some discrepancy for the smaller discs. Again, one of the experimental contrast-detail curves deviate in curvature compared with the other doses, the 2.04mGy dose shows an improved threshold gold thickness for the smaller discs compared to the others (Figure 6.15a). In this case, this has an effect of shifting the ratio to unity. The average R_{d_i} of the contrast-detail curves for the synthetic images with non-uniformity considerations applied has improved from the uniform model, the value shifting from 0.95±0.05 to 0.99±0.08 (mean±standard deviation).

Contrast-detail curves for the synthetic Agfa CR CDMAM phantom images (Figure 6.16)exhibit the same parallel curvature as seen in the previous systems modelled. Contrast-detail curves for the experimental images, however, exhibit more curvature than the other two DM systems. The small details (<0.16mm) of the simulated images had lower threshold detection ratings than the experimental CDMAM phantom images. Although the presampled MTF of the Agfa CR system is very similar to that of the

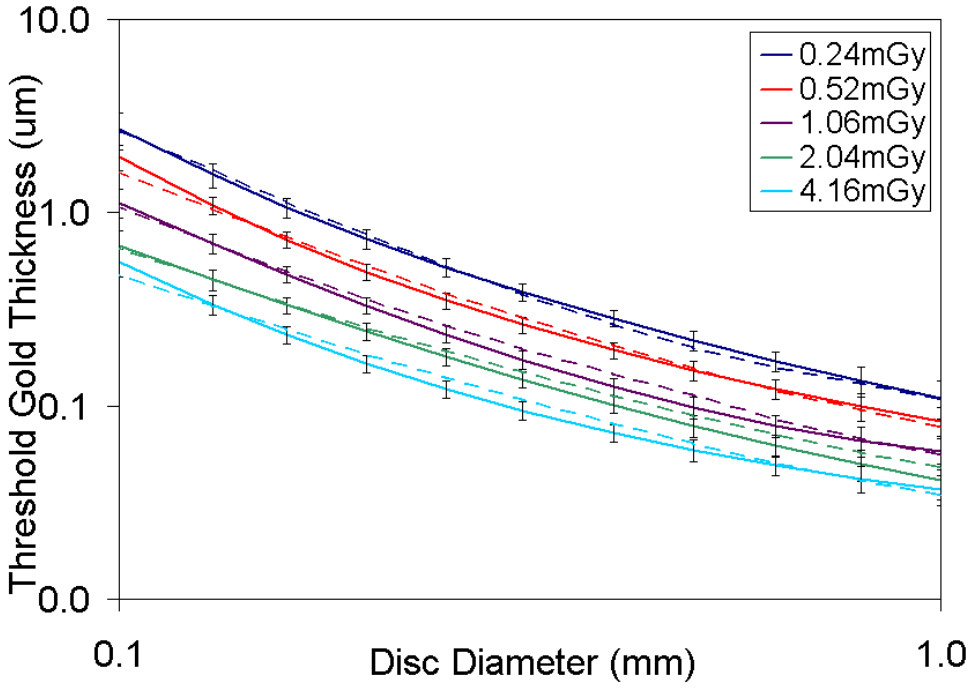


(a)

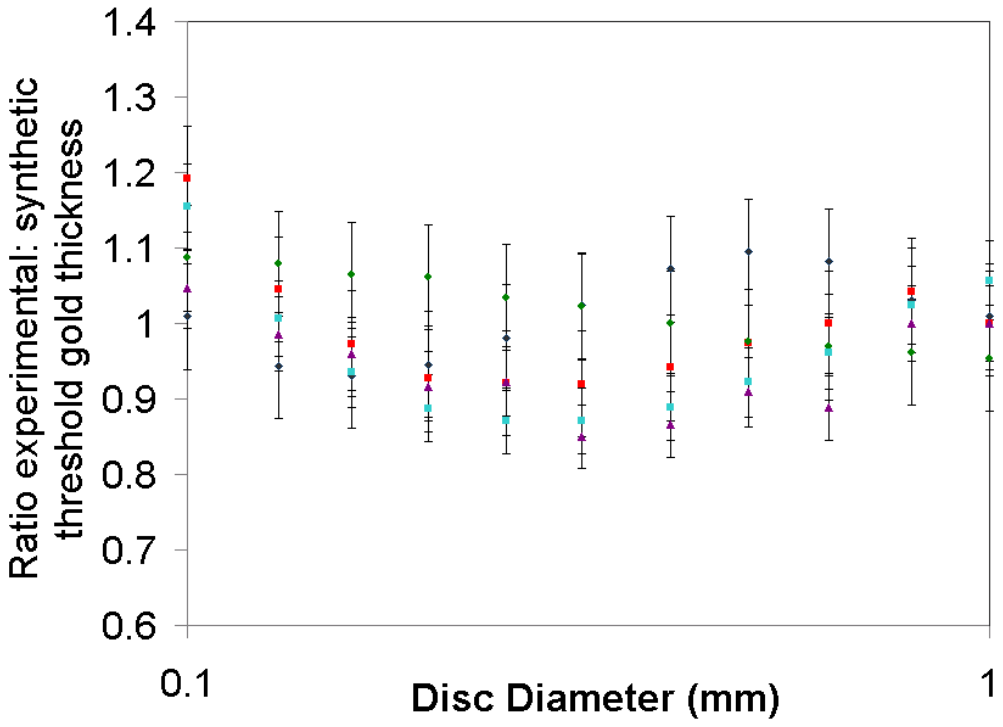


(b)

Figure 6.14: (a)Comparison of contrast detail curves for experimental and synthetic CDMAM images with heel-effect mask, variance map and geometric magnification applied for the Hologic Selenia system. (b) gives the ratio of the contrast-detail curves shown in (a). Error bars denote the standard deviation of the data.

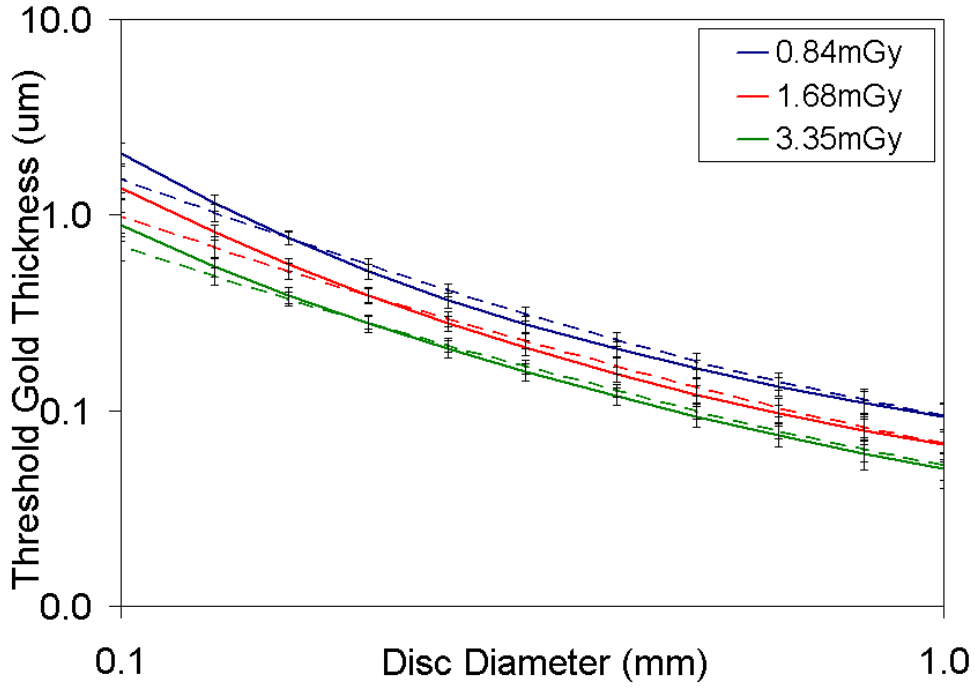


(a)

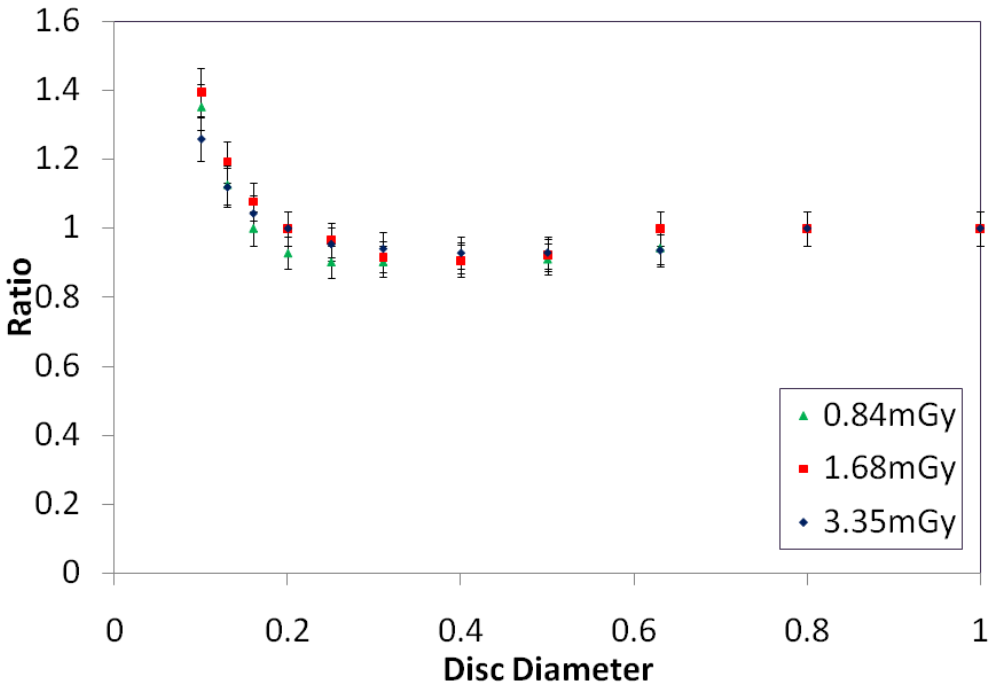


(b)

Figure 6.15: (a)Comparison of contrast detail curves for experimental and synthetic CDMAM images with heel-effect mask, variance map and geometric magnification applied for the GE Essential system. (b) gives the ratio of the contrast-detail curves shown in (a). Error bars give the standard deviation of the data.



(a)



(b)

Figure 6.16: (a)Comparison of contrast detail curves for experimental and synthetic CDMAM images with heel-effect mask, variance map and geometric magnification applied for the Agfa CR system. (b) gives the ratio of the contrast-detail curves shown in (a). Error bars denote the standard deviation of the data.

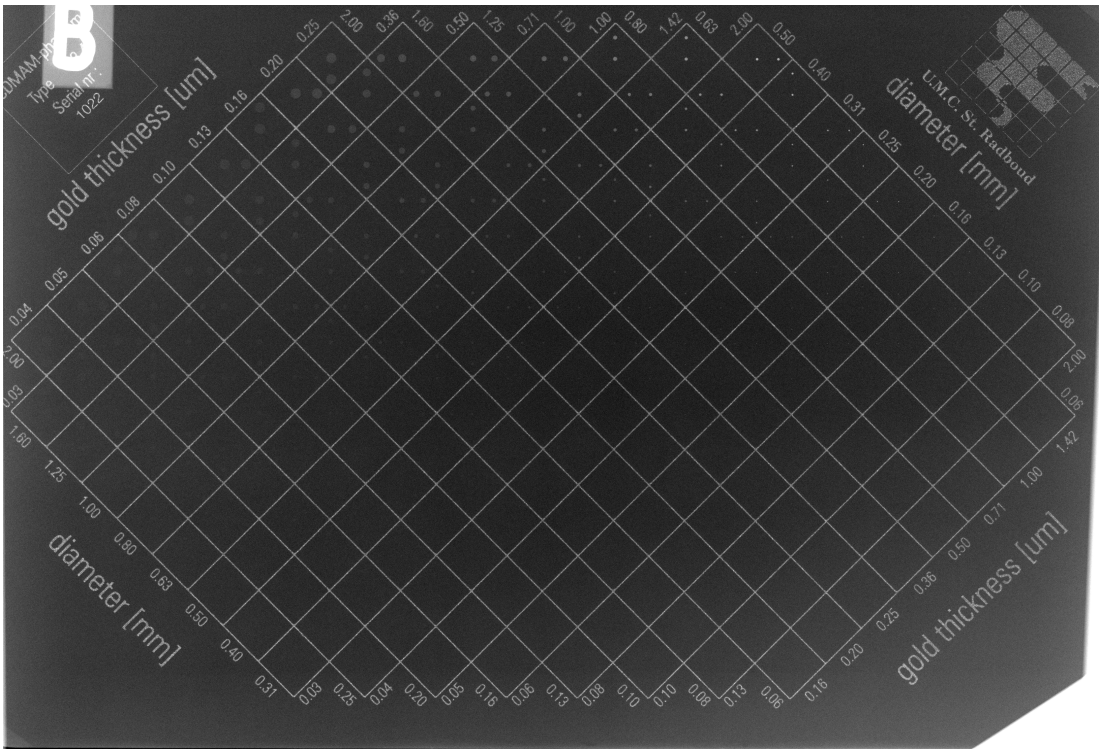
GE Essential system (Figure 4.3), the increased structure noise associated with the CR detector plate obfuscates the smaller details in an image. The NPS of the Agfa system has provided a good replication of structure (fixed pattern) noise expected in the Agfa CR image. However, the NPS only provides an averaged measure of the structure noise in one defined area of the imaging plate and as such cannot replicate the spatial dependence of the structure noise in the image. One method to extract the spatial dependence of the structure noise in the Agfa system would be to combine a number of high exposure flat-field images and divide the combined image by the mean pixel intensity value. This would emphasise the fixed pattern noise otherwise invisible in one exposure. Multiplying the structural noise image The system was not available for further study and this could not be confirmed with the images currently in possession.

The variance map was only acquired from one image, therefore any structure noise may not have been emphasised sufficiently. For a more accurate representation of the structural noise exhibited by the Agfa CR system would require a number of high exposure images to be combined and averaged. This was not possible as the high exposure images obtained for this system were not acquired with the same set up and the system was unavailable for further study.

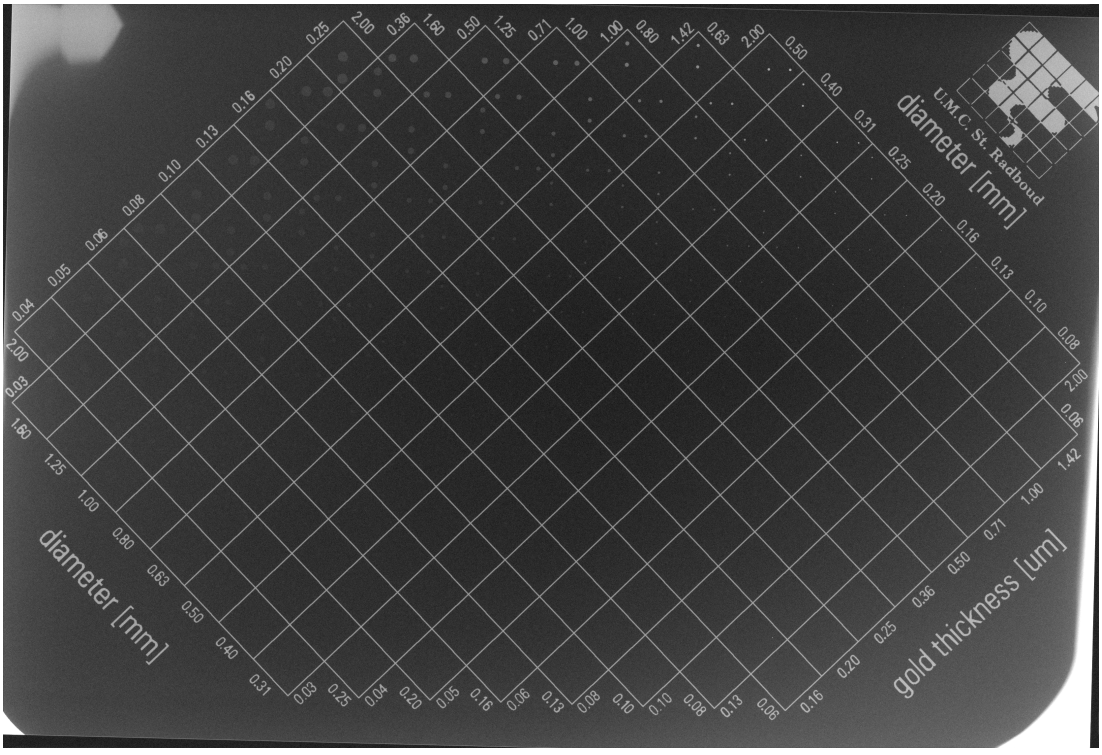
In spite of this, the non-uniformity considerations applied for the Agfa CR system has improved the average ratio, $R_{d_{all}}$, from 0.86±0.08 to 1.01±0.12. However, it must be noted that maximum $R_{d_{all}}$ has also shifted from 1.14 to 1.39. This shift in the ratios suggest that the inclusion of the non-uniformity effects has helped improve the overall detection of the discs in the synthetic images.

Figures 6.17, 6.18 and 6.19 show examplar CDMAM phantom images experimentally acquired and the corresponding synthetically generated for the systems modelled in this study.

With the CDMAM phantom image simulation framework in place, it is possible to validate a non-uniform scatter model with the results displayed thus far. The next section investigates scatter modelling with respect to the CDMAM phantom. The results will be compared with the results shown in Figures 6.14, 6.15 and 6.16 to assess the validity of the uniform scatter model introduced in the previous chapter.

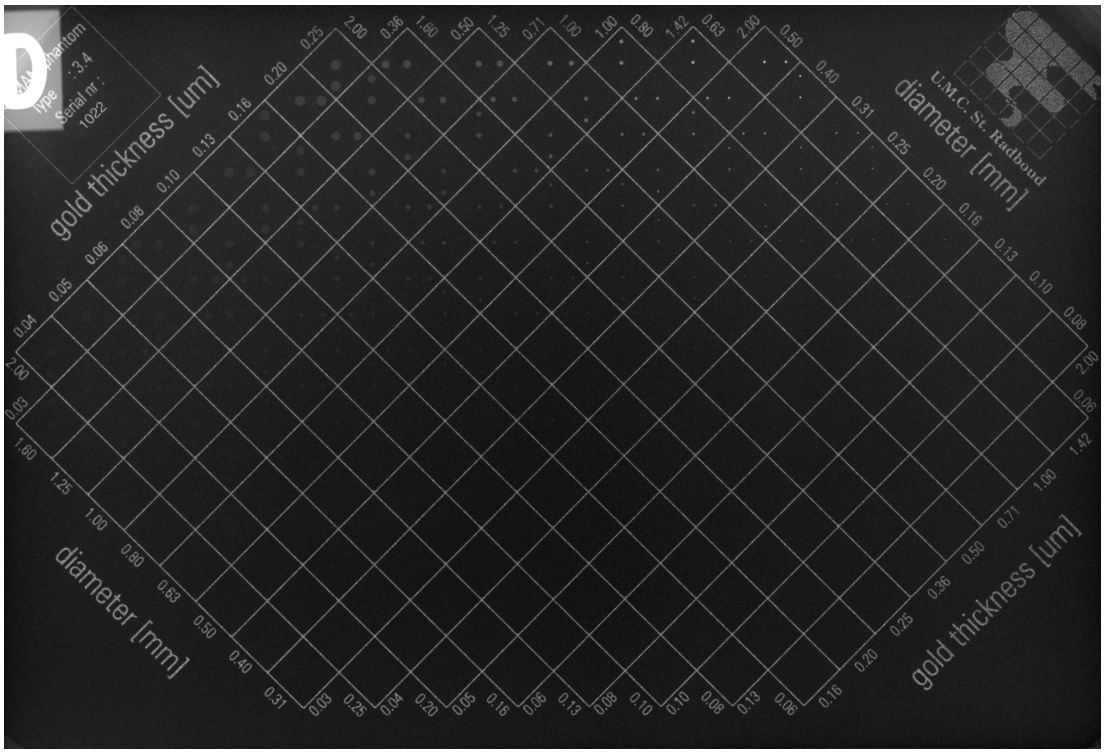


(a)

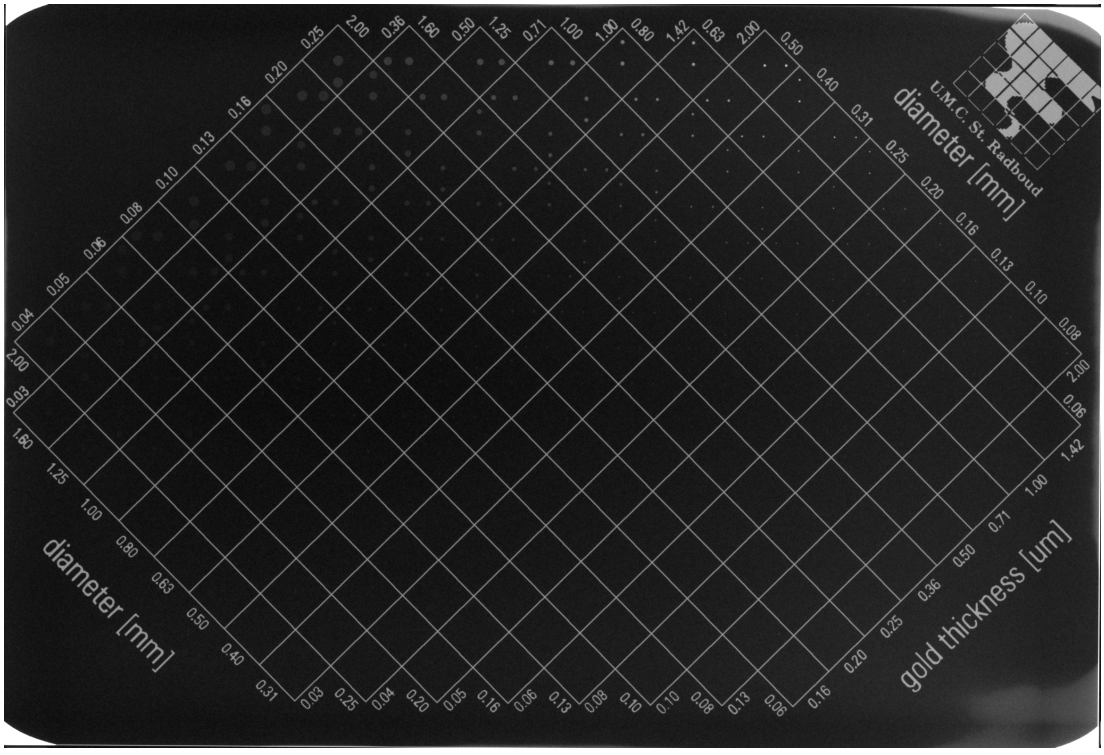


(b)

Figure 6.17: (a) Experimentally acquired and (b) synthetically generated CDMAM phantom images for the Hologic Selenia system at the highest dose for 28kVp MoRh beam quality.

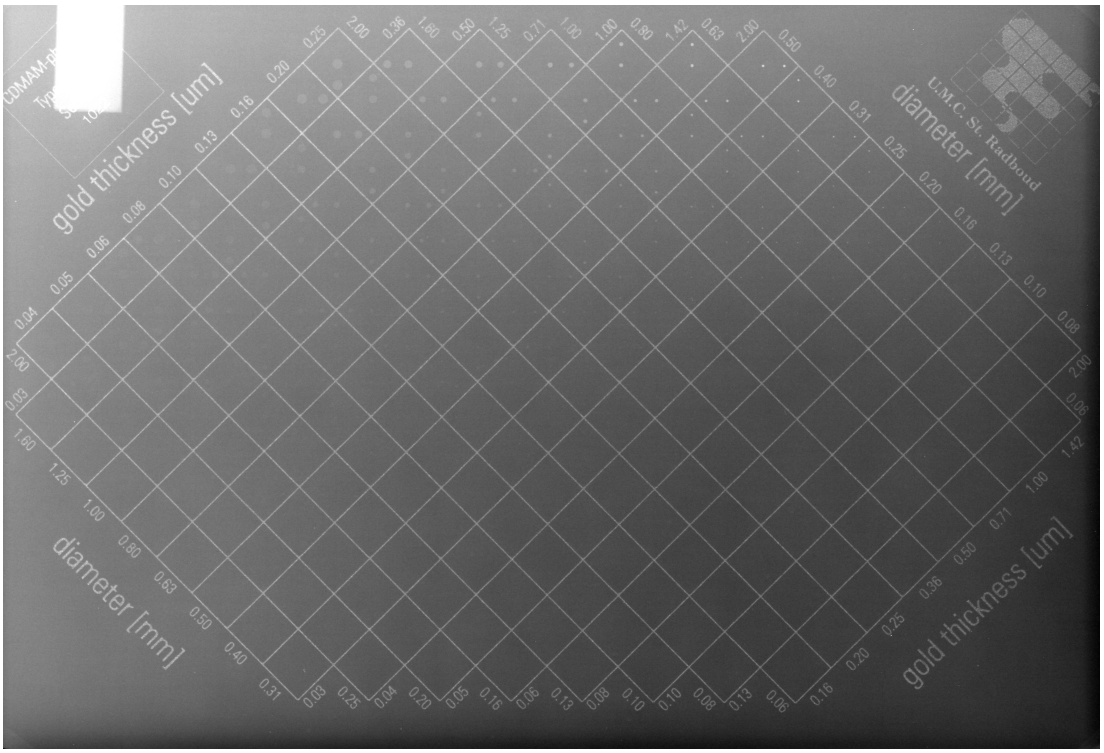


(a)

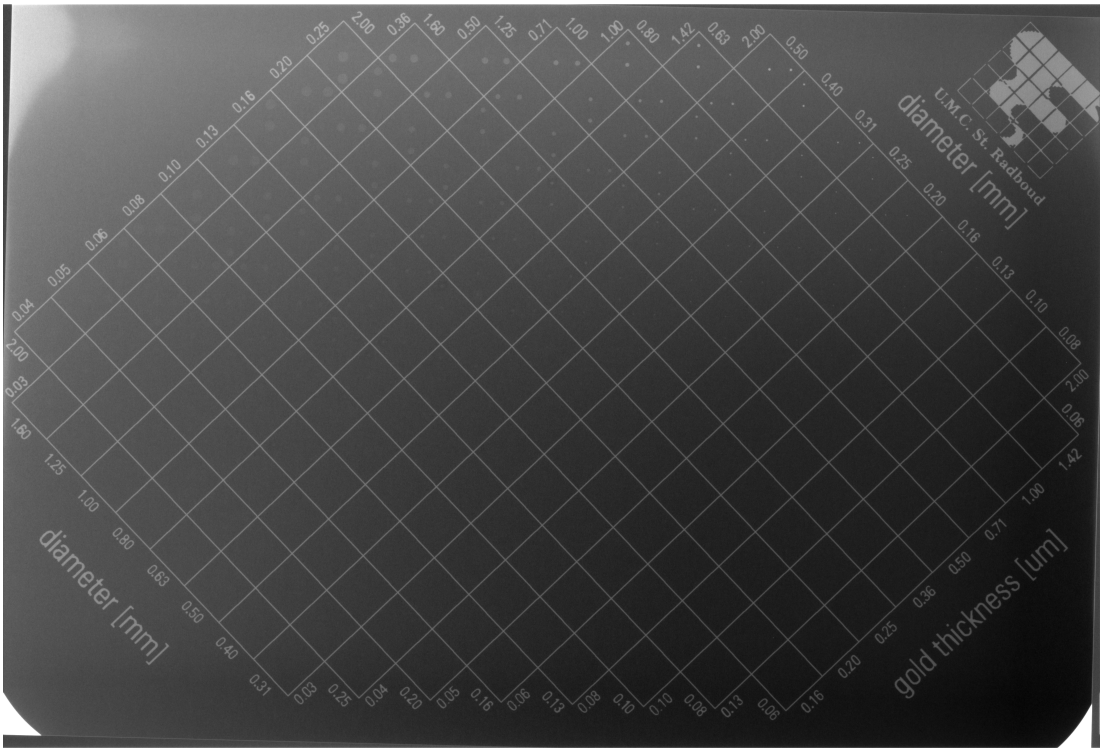


(b)

Figure 6.18: (a) Experimentally acquired and (b) synthetically generated CDMAM phantom images for the GE Essential system at the highest dose for 28kVp MoRh beam quality.



(a)



(b)

Figure 6.19: (a) Experimentally acquired and (b) synthetically generated CDMAM phantom images for the Agfa CR system at the highest dose for 28kVp MoRh beam quality.

6.4 Scatter Modelling

Thus far, the simulation chain has only considered the 'primary' photons in its simulation. The mean-variance relationship defined in Chapter 4 was an empirical measure of experimental images which include contributions from scatter and primary photons.

If the scatter was isotropic and constant over the image, this would not be an issue as the mean variance relationship would take this into account. However, the scatter is not isotropic[118, 111, 112, 108] as will be discussed in the next section. The consequences of this will be discussed with a short literature review of prior work that has simulated scatter in radiographic images. This will be followed by an outline of the Monte Carlo methodology employed here to create scatter to primary ratio maps with which to degrade the contrast of the discs.

6.4.1 Principles of Scatter

Chapter 2 discussed the different photon interactions in mammographic tissue such as photoelectric effect, coherent (Rayleigh) scattering and incoherent (Compton) scattering. The latter two interactions contribute to the scatter in an image. The consequence of photons scattering in the target object is that overall image contrast may be reduced as described by Equation 5.5.

The presence of scattered photons is dependent on several factors:

- The X-ray spectrum. The amount of detected scatter may increase with increasing energies, as opposed to lower energy photons that can be absorbed by the tissue or grid.
- Thickness of the scattering material - i.e. breast tissue or PMMA test phantom. There will be more scattering in the material as thickness increases.
- Density of the scattering material. Higher density materials are more likely to scatter X-rays.
- Size and shape of the field of view[111]. There is less scattering at the edges of the field of view upon a detector. Any scattered photons are likely to be removed more efficiently at the edges of an anti-scatter grid as the angle of the scattered photon's trajectory becomes more oblique. Also there is no scatter contribution from outside the sample/object.
- Detector composition and thickness. Dependent on the detector's composition, it maybe more predisposed to absorb energies of scattered photons than the energies of primary photons.
- Anti-scatter grid characteristics. The design of the anti-scatter grid (linear, cellular, hexagonal) and its operation (stationary/oscillatory) will affect the amount and directions of the scatter detected in the image receptor.
- Position of the ROI in the field of view. As there is less scatter at the edges of the field of view, the size and location of ROI to measure scatter is variable.

6.4.2 Prior work

Scatter is difficult to directly measure experimentally, although there are various methods available to measure the S/P such as the beam-stop method, the edge spread method and slat method[111]. To implement a robust method of simulating the scatter in the image based only on empirical measures such as those used until now would be difficult: all possible set ups used in mammography imaging assessment would need to be carried out. In simulating the scatter in radiography, in particular mammography, Monte Carlo methods have been used[111, 112, 118]. Monte Carlo is a statistical programming method used to estimate solutions to high dimensional problems that cannot be solved analytically.

Boone[111, 112] has carried out seminal work in the field of X-ray spectra, in particular in the field of mammography. With the use of Monte Carlo, Boone and Cooper[111] investigated the properties of the S/P when different parameters were altered such as X-ray energy, air gap, phantom thickness and phantom composition. Two methods to simulate scatter in Monte Carlo were presented: direct method and the convolution method.

The direct method implemented a geometrically accurate simulation procedure. The convolution method used an idealised geometry (monoenergetic, normally incident delta function input to the scattering medium) to produce scatter PSFs. Scatter PSFs were derived through imaging an edge phantom with a scattering material such as PMMA. An edge spread function is measured from this image and the PSF is derived. The scatter PSFs were weighted with the X-ray spectrum of interest and convolved with the field of view to estimate S/P values. Boone and Cooper[111] had found that the two methods gave very similar S/P results. The direct method required longer computation time than the convolution method (assuming the scatter PSF was pre-calculated).

Nykänen and Stiltanen[118] implemented a scattering point spread function (PSF) originally introduced by Seibert and Boone[119] to remove the scatter in mammograms from digital mammography systems. The method implemented was claimed to be non-iterative, robust against noise and worked for any level of scatter to primary ratio. The paper claims to take account of the spatial invariance that Boone and Cooper's method omitted[111]. Results appeared to successfully remove the scatter from clinical images. However, the method requires exhaustive measurements of the scatter PSF with validation of the Monte Carlo system.

With this in mind, it was decided that a direct calculation of the scatter-to-primary ratio at different points in an image would be the fastest and efficient method in which to implement a scatter model into the simulation for the CDMAM set up used so far. The methodology and technical considerations will be described in the following section.

6.4.3 The Scatter Model

The Monte Carlo package Geant4[2] was used to model the scatter in the images. Geant4 is a toolkit for the simulation of particles such as photons through matter. As mentioned in Chapter 4, Monte Carlo simulations can be used to create synthetic images

[2]Available from http://geant4.web.cern.ch/geant4/

by accounting for the physical processes, detector geometry, detector materials and efficiencies. This can be a complicated procedure, requiring a detailed knowledge of the geometric structure and physical processes in the detector and image acquisition process to achieve accurate modelling of the mammography system. With the use of Geant4, the amount of scatter can be calculated at each point upon the detector and the resulting model can be added to the simulation chain. The remainder of this section will describe the set up used to model the scatter in the synthetic CDMAM images.

The beam qualities and experimental set up used within the previous chapter for each system under study was reproduced in the Monte Carlo environment. With this set up, the deposited energies of the scattered and primary photons were integrated into E_S and E_P, respectively, and the scatter-to-primary ratio was calculated at each location (x, y) after the anti-scatter grid and before the detector. Three sets of images were created using 10^9 photons per image. These images were summated to create a representation of the S/P map. As the scatter distribution is expected to be a slowly varying function across the detector, the deposited energies were not binned in to the pixel sizes of the detector but to approximately 1mm^2 to provide a statistically less noisy representation of the SPR map. To this end, the S/P was further filtered using a median filter to smooth the image further.

Using Equation 5.5, with the C_p described in the previous chapter it is possible to find $C_{obs}(x., y)$ for each disc dependent on its location in the image:

$$C_{obs}(x, y) = \frac{C_p}{(1 + S/P(x, y))} \tag{6.10}$$

The S/P was derived for a location relating to the location of the disc in the image. However, as the S/P map was relatively noisy, an ROI of 100x100 pixels was averaged centered at this location for $S/P(x, y)$. This new $C_{obs,xy}$ was used for the contrast-thickness relationship for the discs in the image simulation framework.

In the previous chapter, the contrast of the discs had been modelled on an analytically calculated contrast in relation to its gold thickness with a uniform scatter model assumed. This may have been too simplistic, as this contrast degradation would be applied to all the discs across the image equally. With the S/P map, it is expected that C_p for each discs can be calculated analytically for different beam qualities and then synthetically degraded further dependent on its location in the image.

This purely analytically-derived method would remove the need for empirical measurements for each system simulated. The addition of the S/P map leads to a more robust method in correctly modelling the contrast of the discs. In addition, this would provide a more accurate model of the scatter across the field than the assumption made in the previous chapter.

6.4.4 Scatter-to-Primary Ratio Map

The S/P maps generated in Geant4 with the CDMAM set up on the detector plate. The S/P maps were cropped to the size of the CDMAM phantom are shown in Figure 6.20.

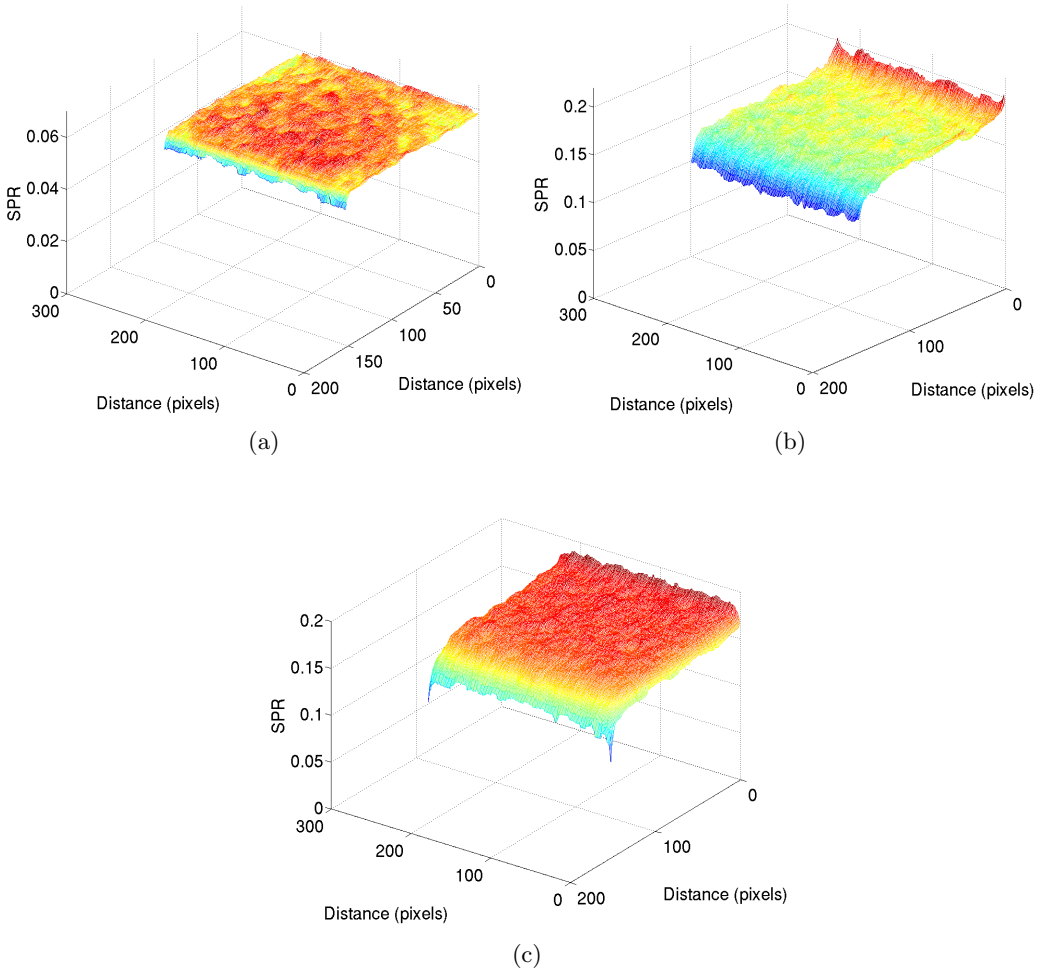


Figure 6.20: Surface plots of S/P for the three systems modelled (a) Hologic Selenia (b) GE Essential and (c) Agfa CR. The orientation is such that the chest wall to anode is from the left to rightof each plot.

For Hologic Selenia system, the S/P was 0.05 ± 0.01 compared with the GE Essential, the S/P was found to approximate 0.19±0.01. For the Agfa CR system, the S/P was found to be 0.17±0.01. The disparity between the systems may be due to different anti-scatter grid technologies. The Hologic system used a cellular grid compared with the GE and Agfa systems which used a linear grid. Figure 6.20 shows the S/P to be uniform across the detector, with the exception of the edges of the CDMAM phantom. At this point, the S/P fell sharply in all cases. In comparison, the S/P calculated in Chapter 5 based on empirical measurements were found to be 0.05± 0.01, 0.11±0.01% and 0.22±0.03% for the Hologic Selenia, GE Essential and Agfa CR systems, respectively.

The SPR maps were included in the image simulation framework shown in Figure 6.13 to include all non-uniformity considerations discussed in this chapter. The contrast-detail results for synthetic CDMAM images including the SPR for each system is shown in Figure 6.21, 6.22 and 6.23. For the Hologic Selenia system, the average of $R_{d_{all}}$ for all

doses and disc diameters was 1.14±0.17; suggesting the detection rate for the synthetic CDMAM images with the scatter model was better than the experimental CDMAM images.

Table 6.4 show the $R_{d_{all}}$ for the synthetic contrast-detail curves with the uniform scatter model and non-uniform scatter model derived with Monte Carlo. The scatter model introduced from the Monte Carlo simulations have increased the variability of the contrast-detail values. The simulated data for the Hologic Selenia system have been underestimated, suggesting the contrast of the discs may be too high. The opposite is true for the synthetic GE Essential CDMAM phantom images. The Agfa CR system simulations appear to have remained the same, however, the standard deviation has increased. Due to the larger discrepancies in the ratios of experimental to synthetic contrast detail curves, it suggests that the disc contrast calculations needs refining.

Table 6.4: Ratios of experimental to synthetic threshold gold thickness $R_{d_{all}}$ averaged across all doses used in each study.

	Uniform scatter model[a]				Non-uniform scatter model			
Imaging System	Average $R_{d_{all}}$	Minimum $R_{d_{all}}$	Maximum $R_{d_{all}}$	$\sigma(R_{d_{all}})$	Average $R_{d_{all}}$	Minimum $R_{d_{all}}$	Maximum $R_{d_{all}}$	$\sigma(R_{d_{all}})$
Hologic Selenia	1.00	0.97	1.08	0.03	1.10	0.97	1.46	0.16
GE Essential	0.99	0.92	1.19	0.08	0.94	0.83	1.07	0.07
Agfa CR	1.01	0.90	1.39	0.12	1.01	0.88	1.43	0.17

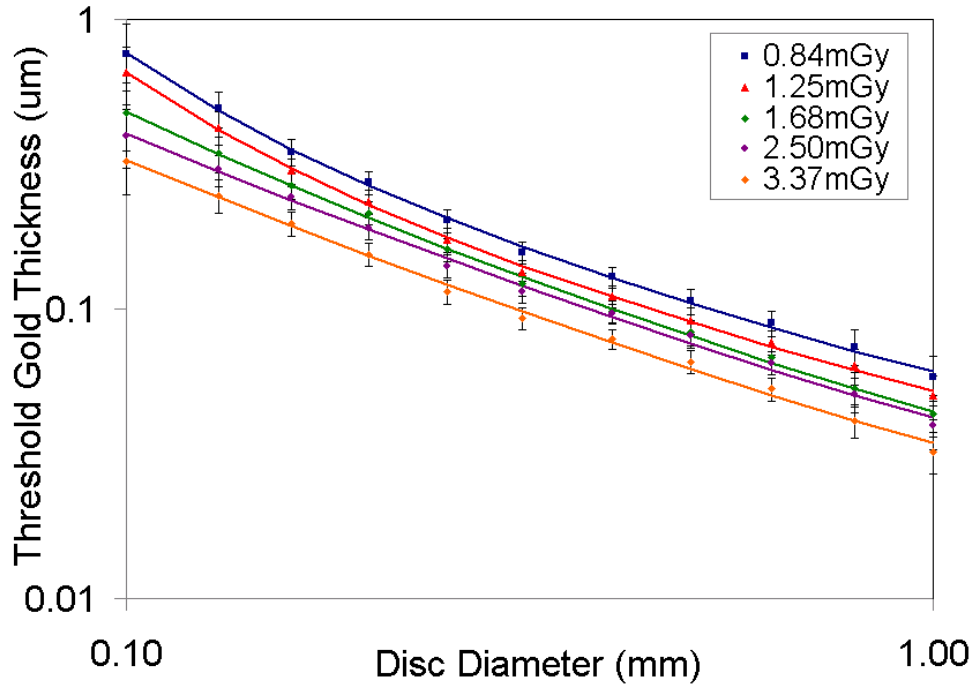
[a] from previous section

The next section investigates the sensitivity of the disc contrast calculations when other factors are taken into acount.

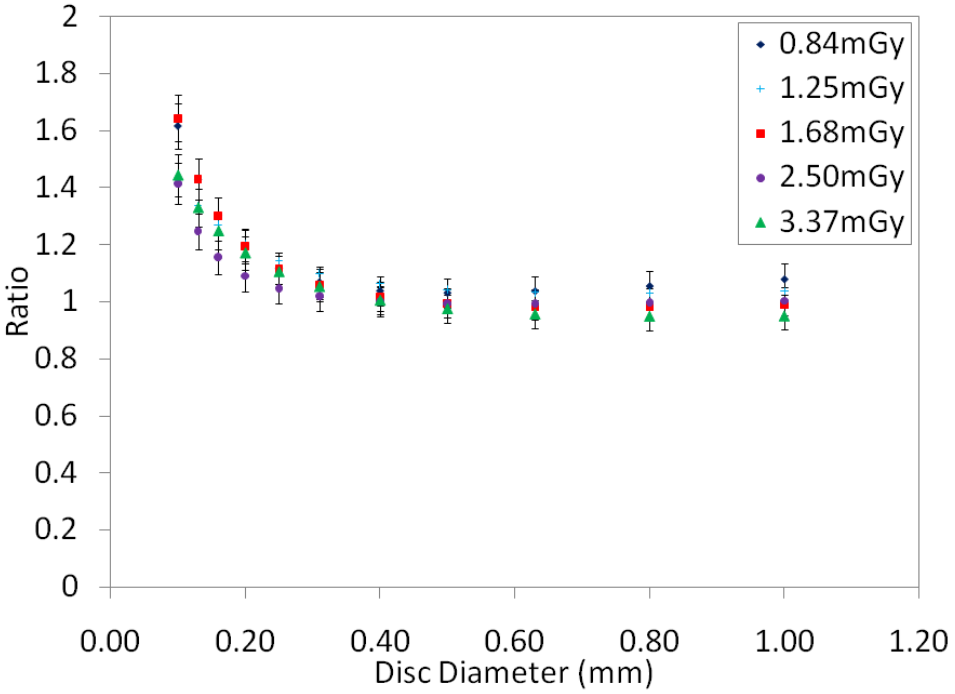
6.4.5 Sensitivity of Disc Contrast Calculations to Experimental Set Up Parameters

There were discrepancies in the contrast-detail curves for the simulated CDMAM phantom images where the non-uniform scatter model was incorporated. As the scatter model agrees with published data[111, 109, 108], it may be that the error lies in the original disc contrast calculations. Various factors were not included in the original calculations that may affect the final CDMAM phantom image simulation. Three factors were identified to have lead to discrepancies in the disc contrast calculations: the photon attenuation due to the compression paddle; modifying the X-ray spectrum to match the beam quality of the individual systems used; receptor efficiency. These factors are further investigated in Appendix C.

It can be seen that the previous gross assumption made in Chapter 5 had in effect been concealing other issues in the disc contrast calculations. It is with the sophisticated model of the scatter to primary ratio across the detector that this has become apparent. Increasing the level of complexity in this model has led to the need to further refine the disc contrast model for a more robust CDMAM phantom image simulation framework. This may be an area for further work. However, for the purpose of validating this image simulation framework, the remainder of this work will continue analysis with the

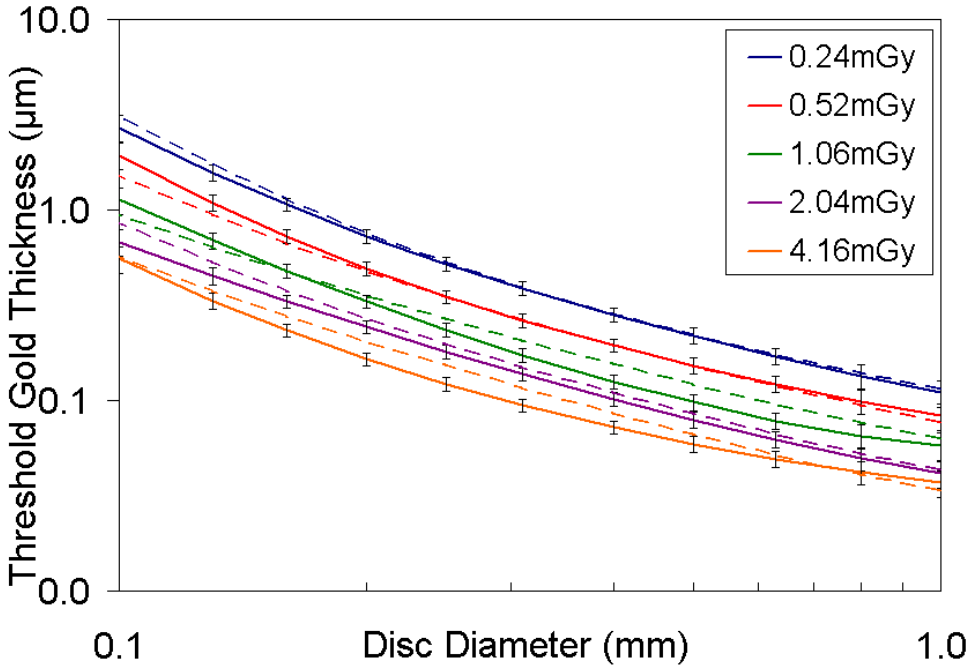


(a)

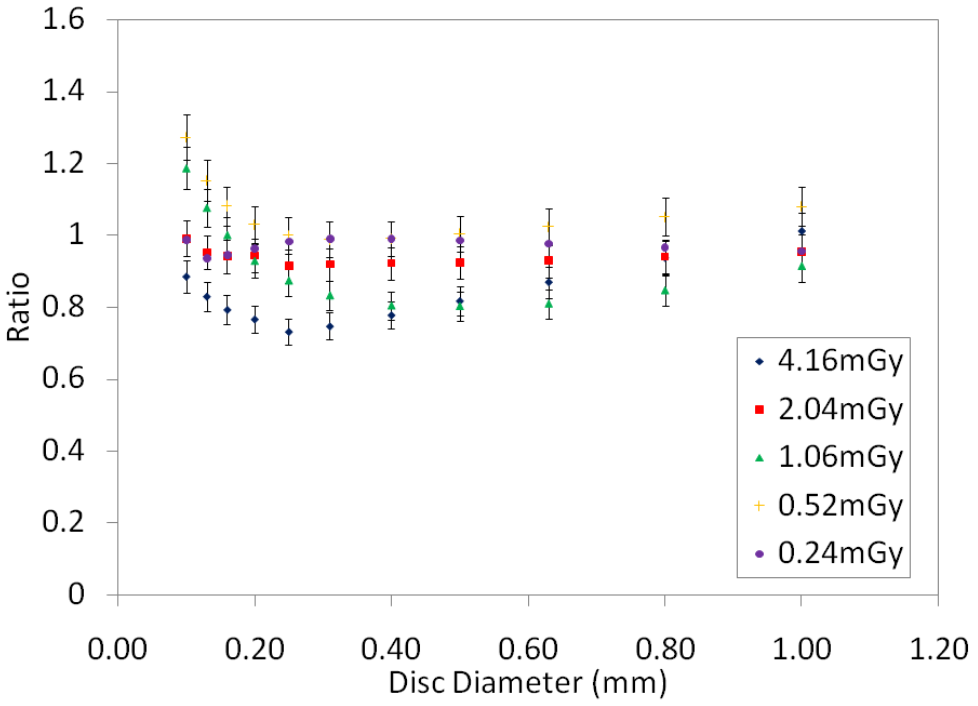


(b)

Figure 6.21: (a)Contrast-detail curves for experimental CDMAM images and synthetic CDMAM images with all non-uniformity considerations applied with the scatter model included for the Hologic Selenia system. (b) Ratio of contrast-detail curves found in (a). Error bars denote 2 standard error means.

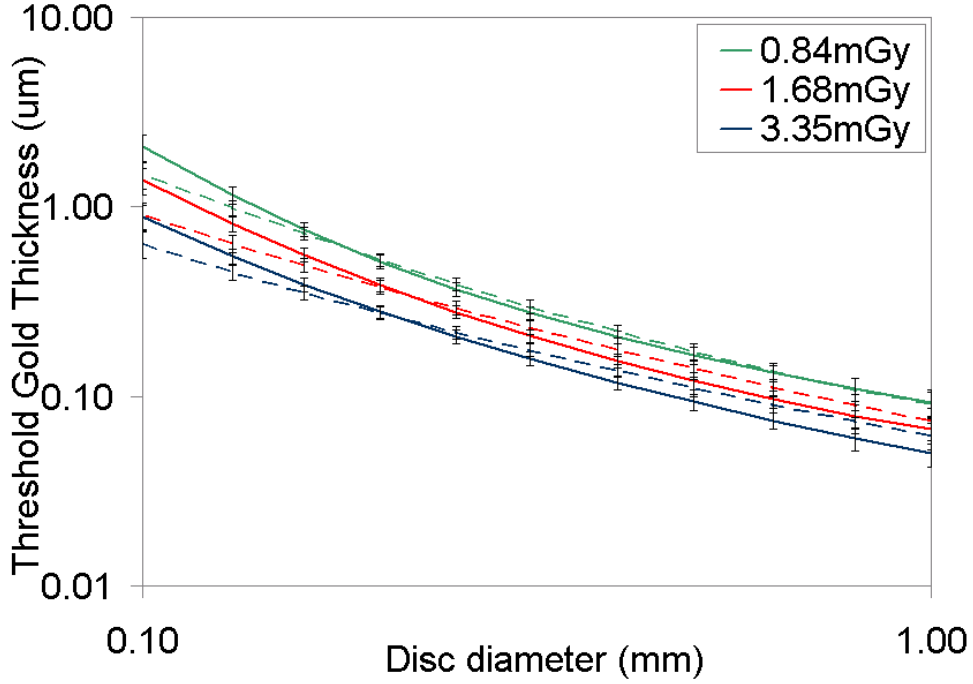


(a)

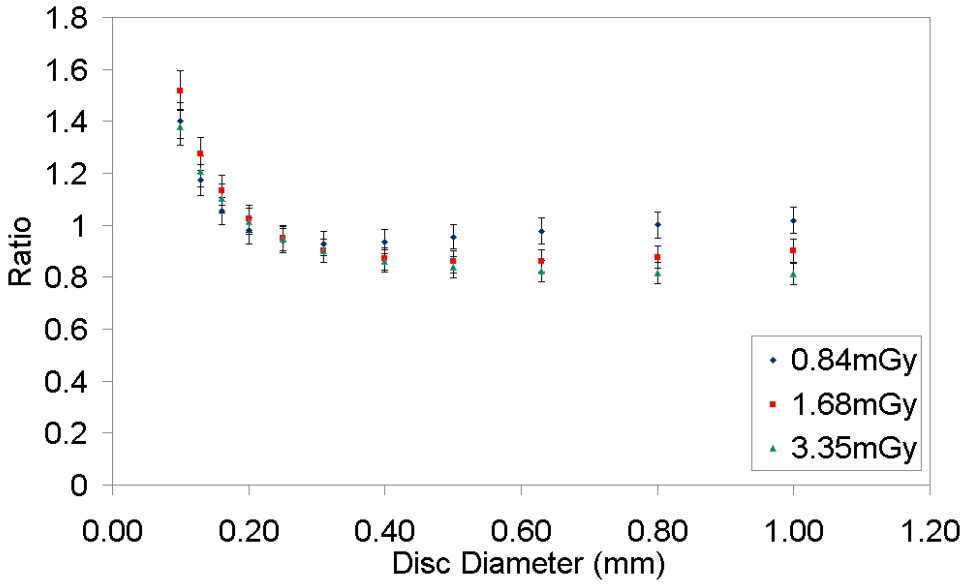


(b)

Figure 6.22: (a)Contrast-detail curves for experimental CDMAM images and synthetic CDMAM images with all non-uniformity considerations applied with the scatter model included for the GE Essential system. (b) Ratio of contrast-detail curves found in (a).Error bars denote 2 standard error means.



(a)



(b)

Figure 6.23: (a)Contrast-detail curves for experimental CDMAM images and synthetic CDMAM images with all non-uniformity considerations applied with the scatter model included for the Agfa CR system. (b) Ratio of contrast-detail curves found in (a).Error bars denote 2 standard error means.

CDMAM phantom images produced from the image simulation framework with the heel-effect mask, variance map and geometric MTF applied.

6.5 Contrast and Noise measurements from the synthetic CDMAM images

As at the end of the last chapter, QAS data were used for direct comparison of CNR data. The new addition to the image simulation framework has made an improvement to the standard deviation of the background pixel value measured locally to the discs. QAS was run on the images generated in the study from Section 6.3.1 as these provided the most accurate simulations so far. Therefore the synthetic disc contrasts still matched the experimental disc contrasts as in the previous chapter. Consequently, CNR calculations were seen to have improved for all three systems as shown in Figures 6.24, 6.25 and 6.26 as the non-uniformity effects were taken into account.

Introducing the non-uniformity has improved the CNR. Relative average discrepancies between synthetic and experimental calculations of CNR were found to be -0.10%, 0.58% and -0.27% for the Hologci Selenia, GE Essential and Agfa CR systems, respectively. This is a large improvement compared with the relative differences found in the previous chapter of 1.52%, 1.05% and 14.9%, respectively.

The uniform model implemented in the previous chapter showed that there were slight discrepancies in the CDF due to insufficient blurring. Figures 5.18a, 5.20a and 6.29 show how the CDF has been affected with the addition of the geometric blurring into the image simulation framework.

6.6 Discussion and Conclusions

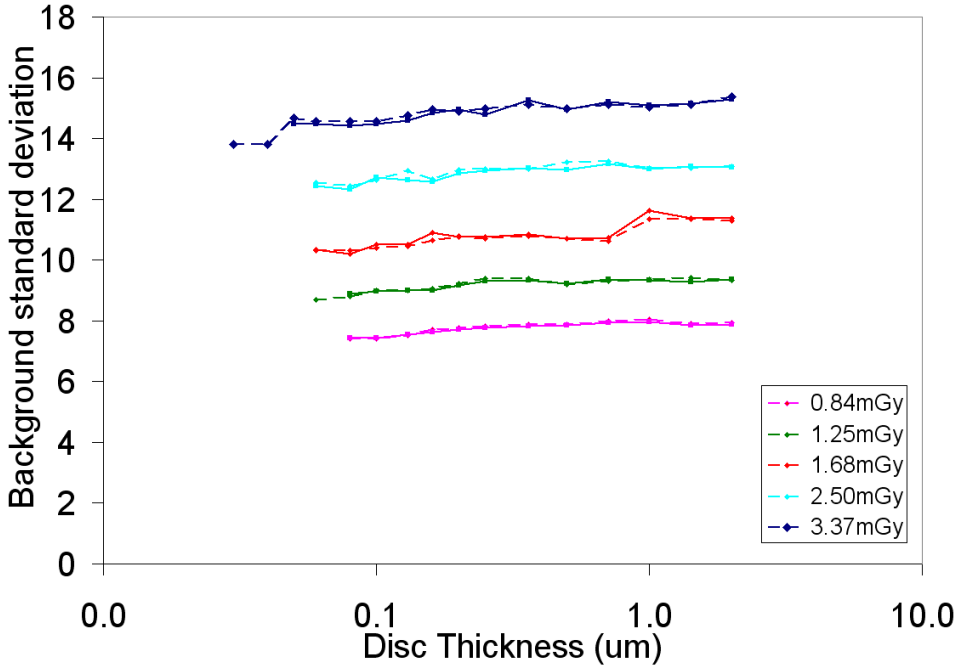
This chapter has presented the sources of non-uniformity, which, to the author's knowledge, has not previously been implemented in a similar image simulation methodology, either individually or together. Such thorough validation with a contrast-detail test object has not been undertaken until now.

A short literature review for each non-uniformity considered was carried out. The effects of the heel-effect mask, variance map and geometric blurring were combined into the image simulation framework to obtain new synthetic CDMAM phantom images for scoring. Relative differences in the ratio of experimental to synthetic contrast-detail curves for all doses, before and after non-uniformity effects were applied were seen to be larger for GE Essential and Agfa CR systems when compared with the Hologic Selenia system. The amorphous technology did not appear to be as susceptible to the non-uniformity effects introduced in this chapter. Ratio of the experimental to synthetic contrast-detail curves improved by an absolute amount of 0.01±0.03, 0.04±0.08, 0.15±0.12 in the $R_{d_{all}}$ for the Hologic Selenia, GE Essential and Agfa systems, respectively.

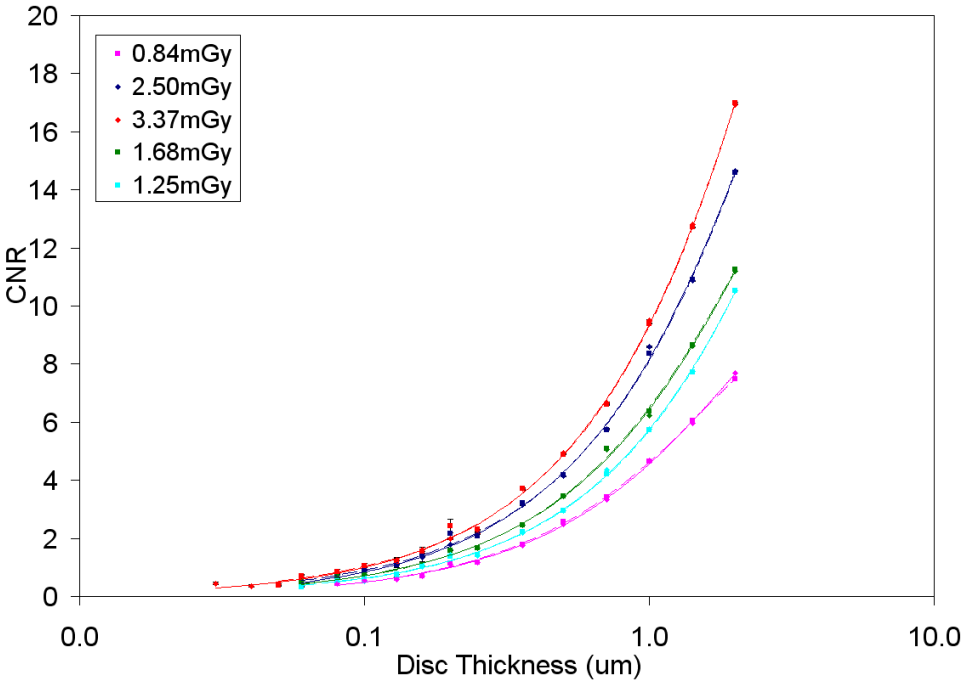
A scatter model was implemented to evaluate whether the uniform scatter model was a valid assumption. The S/P maps modelled for all DM systems used in this study had shown the uniform scatter model to be valid. The S/P maps were inserted into the image simulation framework for generating CDMAM phantom images. It was seen that the contrast-detail curves were poorer for the resultant synthetic images. The sophisticated S/P model has exposed the need to refine the original disc contrast calculations due to primary photons. The assumption of a uniform scatter was derived from empirical measurements. This had in effect obfuscated factors not modelled originally in the primary-only disc contrasts, C_p.

The contast-detail curves give a good indication of the overall detectability of the details in the CDMAM phantom, however, the averaging over a number of images causes certain factors such as the non-uniformity effects to be obfuscated. CNR and CDF measurements gave a clearer indication of the accuracy of the details simulated in the image. Non-uniformity effects led to a change in the CNR where the maximum relative difference was seen to be 0.58% compared with 14.9% found in the previous chapter when a uniform model was assumed.

The image simulation chain presents one of the most sophisticated method of simulating mammographic imaging systems. Thus far, the image simulation chain has been implemented for the simulation of test object images such as straight edges, flat-field and CDMAM phantom images. To assess the digital mammography systems with consideration to the observer performance, simple test objects are insufficient to completely model what would happen in a clinical detection task as the test objects have uniform background unlike the clutter present in mammograms. The overall goal of this image simulation framework is to assess the performance of the radiologist when different X-ray settings are implemented. The next chapter will explore a method of implementing the image simulation chain with clinical images with noise and blurring effects. As it is not possible to acquire images of the same patient with different acquisition conditions such as exposure, mastectomy images were obtained at different exposures for the purpose of comparison. The subtleties of this method of simulation will be discussed in the following chapter.

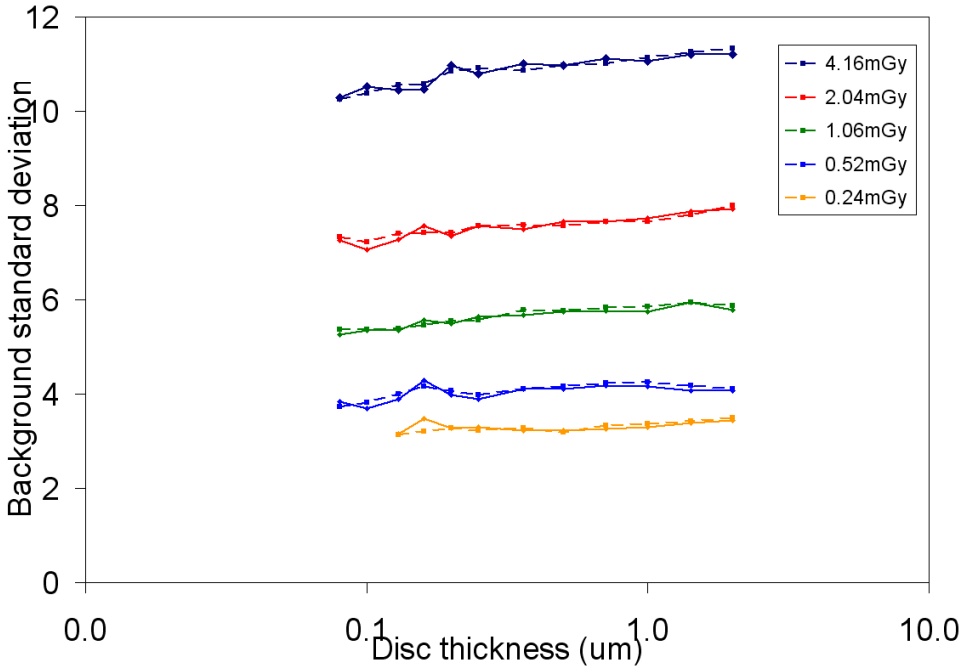


(a)

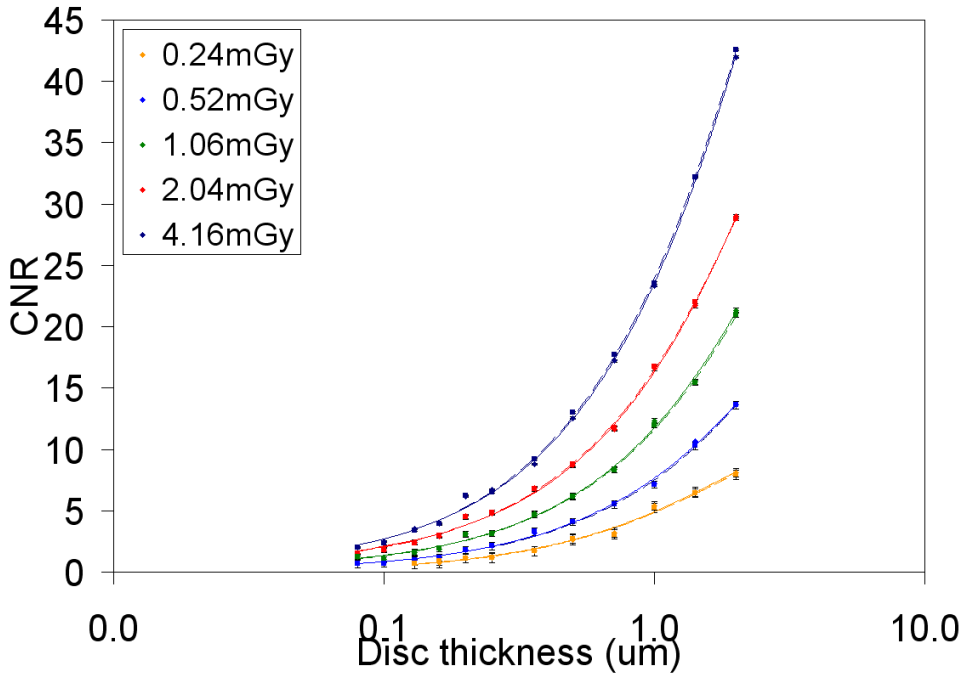


(b)

Figure 6.24: (a) Standard deviation measured in the local background to the discs for experimentally acquired (solid) and sythetically generated (dashed) images of the Hologic Selenia system. (b) Resulting CNR calculated with new standard deviation measured in (a). Data from experimentally acquired images is shown in solid curves and synthetically generated images is shown in dashed curves. Error bars denote two standard errors of mean.

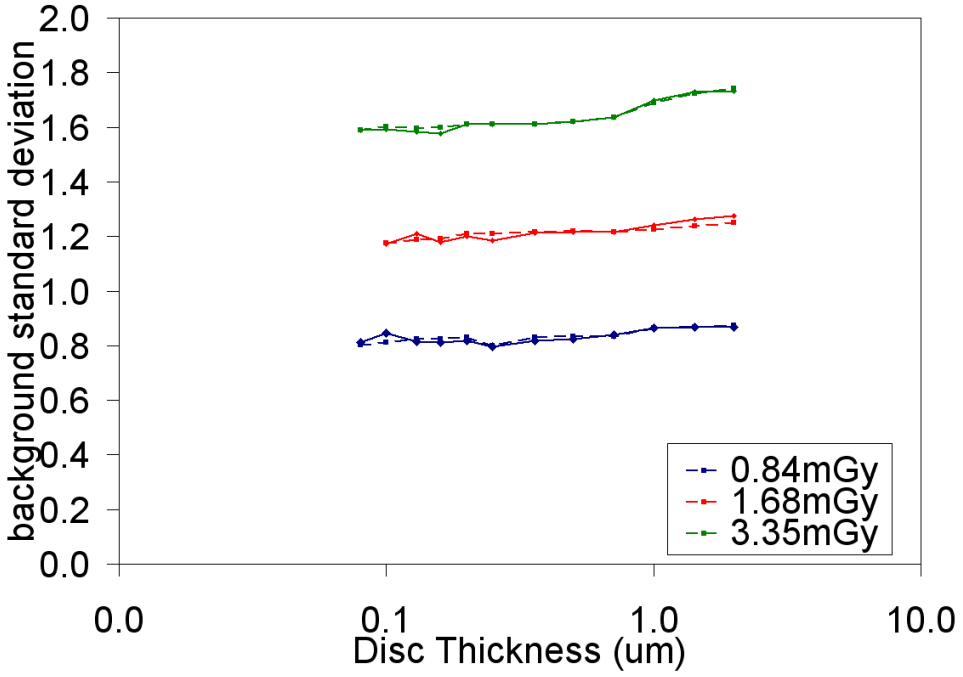


(a)

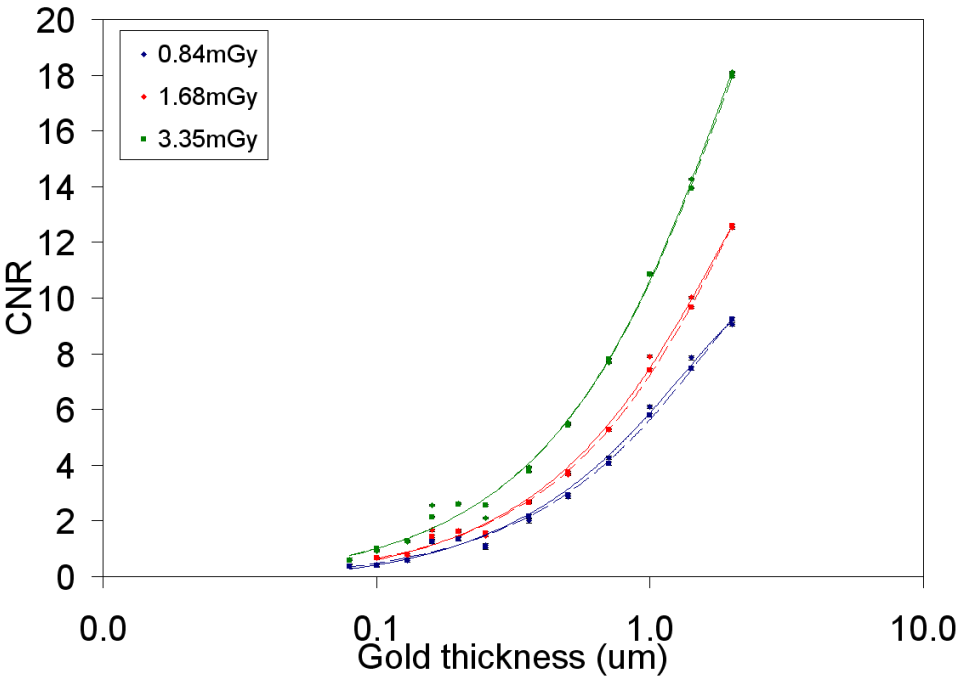


(b)

Figure 6.25: (a) Standard deviation measured in the local background to the discs for experimentally acquired (solid) and sythetically generated (dashed) images of the GE Essential system. (b) Resulting CNR calculated with new standard deviation measured in (a). Data from experimentally acquired images is shown in solid curves and synthetically generated images is shown in dashed curves. Error bars denote two standard errors of mean.



(a)



(b)

Figure 6.26: (a) Standard deviation measured in the local background to the discs for experimentally acquired (solid) and sythetically generated (dashed) images of the GE Essential system. (b) Resulting CNR calculated with new standard deviation measured in (a). Data from experimentally acquired images is shown in solid curves and synthetically generated images is shown in dashed curves. Error bars denote two standard errors of mean.

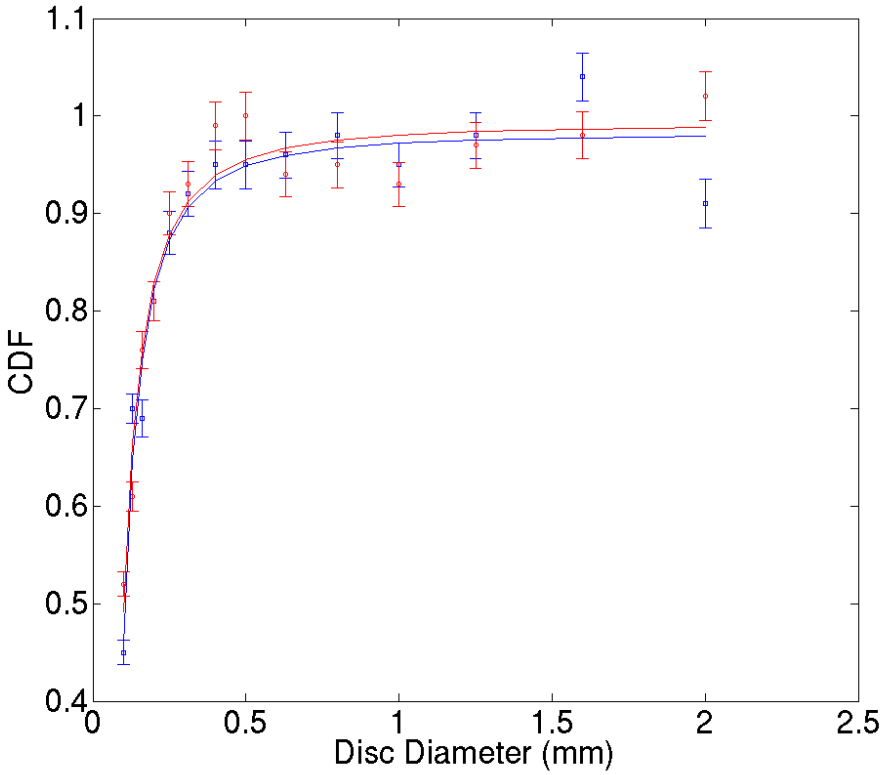


Figure 6.27: CDF measured from experimentally acquired and synthetically generated images for the Hologic Selenia system. Error bars denote two standard error means

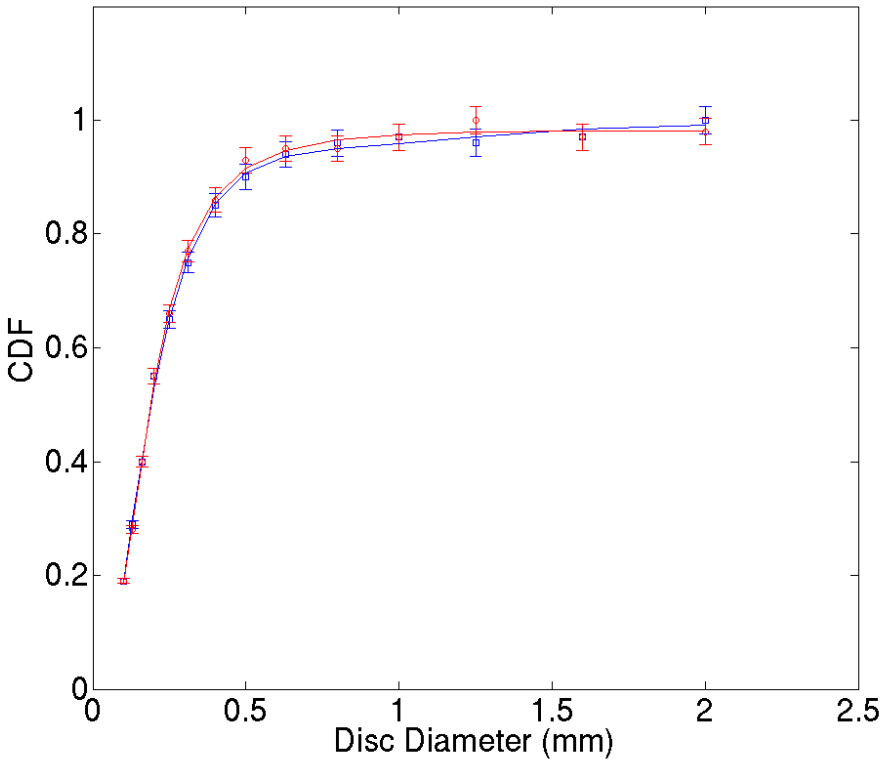


Figure 6.28: CDF measured from experimentally acquired and synthetically generated images for the GE Essential system.Error bars denote two standard error means.

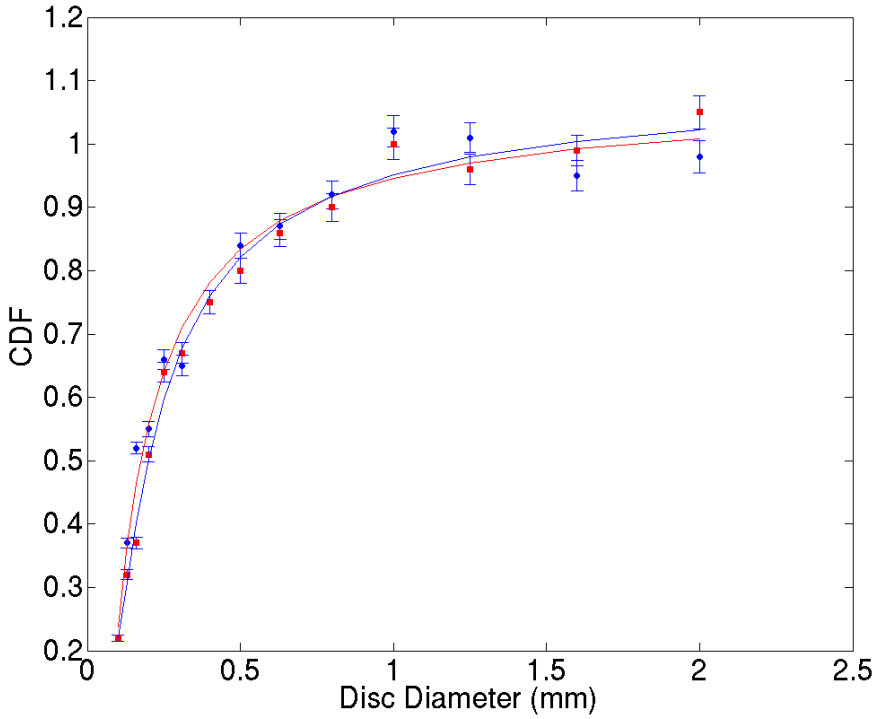


Figure 6.29: CDF measured from experimentally acquired and synthetically generated images for the Agfa CR system. Error bars denote two standard error means

Chapter 7

Application of the Image Simulation Framework to Clinical Images

The work presented thus far has been concerned with validating the image simulation framework with the use of test objects. Chapters 4, 5 and 6 have been a development of the complete image simulation chain, now incorporating the non-uniformity considerations which have not been included elsewhere in the field.

Images simulated have been from *idealised* images where the nature of the object images had been understood and modelled for the purpose of validating the image simulation chain. The ultimate goal of this work is to provide a framework with which to create images as if from DM systems for the purpose of comparing their clinical impact upon cancer detection. As has been discussed in previous chapters, for meaningful comparison of the digital mammography systems in terms of their clinical impact, the task must be relevant. This means that since these systems are to screen for signs of mammographic breast lesions, the gold standard method of comparing such systems is with ROC studies using clinical mammograms assessing the parameter of interest.

Ethical reasons prevent patients from being subjected to multiple radiation doses from different systems for such a clinical test. Therefore, image simulation is a more viable option to assessing clinical performance of the digital mammography systems. If images could be synthesised realistically, it would be possible to employ such a method in ROC analysis. Indeed, two such groups have been able to carry out this experiment[32, 33]. Validation of the dose reduction had been applied to flat field images in work prior to these studies[61, 94]. However, validation of the dose reduction process with respect to clinical images had not been published. To be sure that the dose reduction claimed was accurate would require validation with the clinical images.

More recently, Svalkist and Båth[97] have published a sophisticated dose reduction method applied to breast tomosynthesis images and have validated their method thoroughly with NPS flat-field images as well as clinical breast tomosynthesis images.

Thus far, the dose reduction described in the chapter 4 had been implemented upon the assumption that the dominant noise source is quantum-based. This has been a valid

assumption for the systems and dose ranges used so far. However, it could be seen that a quantum-only assumption broke down considerably when the difference was four-fold in chapter 4. Thus, for a fuller understanding of the noise model and to extend the limits of this dose range, it may be necessary to extend the noise model to include the major sources of noise: electronic, quantum and structure. This chapter extends the quantum-only noise model to include the structure and electronic noise sources. Three NPS arrays were derived to represent the three noise sources and from this, it is possible to simulate any dose level based on their relationship to exposure. Theory is described in Section 7.1 and continued with methodology to validate the theory with synthetic images as has been carried out in previous chapters: flat-field images and CDMAM images.

Flat-field images were created synthetically to compare NNPS measurements directly with experimentally acquired flat-field images. CDMAM phantom images were also synthesized from an idealised template as described in chapter 5 with the exception that the noise simulation was replaced with the multiple noise source model.

This chapter aims to bring into context the image simulation framework developed in the previous chapters. Therefore, the next step investigates the possibility of modifying the dose upon experimentally acquired flat field images from a Hologic Selenia system[1]. Following this, a set of experimentally acquired CDMAM phantom images was degraded to mimic reduced dose. Contrast-detail curves will be used to compare the effects of reducing the dose upon detection tasks.

Extending the work to some clinical images, four sets of clinical mastectomy images were also modified. Clinical mastectomy images were acquired on a Siemens Novation system at the Leuven Hospital, Belgium. The Siemens Mammomat Novation system uses a very similar detector to the Hologic Selenia, an amorphous selenium detector with $70\mu m$ pixel pitch.

Comparisons of the synthetically derived mastectomy images was carried out qualitatively with corresponding mastectomy images acquired at lower doses. Quantitative comparison involved the use of noise power spectra measurements. The chapter concludes with a discussion of this investigation.

7.1 Multiple noise source model

Evans et al[51] have described the NPS as having three main contributions of noise sources: electronic, quantum and structural and their relationship to energy deposited on the detector is given as follows:

$$NPS_t(u,v) = NPS_q(u,v) + NPS_e(u,v) + NPS_s(u,v) \tag{7.1}$$

Ravaglia et al[52] illustrated how these noise sources could be modelled separately in terms of NPS. Following this method, a curve was fitted at each point of the 2D

[1]This system was different from the Hologic Selenia system used in the previous chapters. This is because a new system was installed at St. Georges Hospital between the time that these experiments were conducted. A new detector response and noise model were derived for this system

representation of the NPS as a function of spatial frequency, (u, v), and dose (measured at the surface of the detector), K. The curve fitted followed the following form:

$$NPS_t(u, v; K) = NPS_q(u, v).K + NPS_e(u, v) + NPS_s(u, v).K^2 \tag{7.2}$$

This way, representations of the three noise sources in the form of NPS_e, NPS_q and NPS_s for electronic, quantum and structural noise were found. With one representation of the NPS for each noise source, it is possible to accurately model the total NPS at any dose level within the range of doses that NPS_t were acquired at. The assumption would begin to break down beyond this range.

7.1.1 Methodology

To validate this noise model, flat-field and CDMAM phantom images were synthesized as described in Chapters 4, 5 and 6 for the Hologic Selenia system.

The synthetic flat-field images, $I_U(x, y)$, were created by generating a blank image with a pixel value representing a specific dose level for the Hologic Selenia system. Three Gaussian noise images, $I_G(x, y)$, equal in size (2048x2048 pixels) to the synthetic flat-field image, $I_U(x, y)$, were created. Each Gaussian noise image was Fourier Transformed and each were applied to one of the NPS representations of the electronic, quantum and structural noise.

Correlated noise images were created by multiplying the Gaussian noise images with the NTF filters in Fourier space as defined in Equation 4.25 for each noise source.

$$NTF_e(x, y) = \sqrt{\frac{NPS_e(u, v)}{max(NPS_e(u, v))}} \tag{7.3}$$

$$NTF_q(x, y) = \sqrt{\frac{NPS_q(u, v).K}{max(NPS_q(u, v)).K}} \tag{7.4}$$

$$NTF_s(x, y) = \sqrt{\frac{NPS_s(u, v).K^2}{max(NPS_s(u, v)).K^2}} \tag{7.5}$$

The resultant filtered noise images were then inverse Fourier Transformed (IFFT):

$$I_{N,corr,e}(x, y) = IFFT\left[FT(I_G(x, y)).NTF_e(u, v)\right] \tag{7.6}$$

$$I_{N,corr,q}(x, y) = IFFT\left[FT(I_G(x, y)).NTF_q(u, v)\right] \tag{7.7}$$

$$I_{N,corr,s}(x, y) = IFFT\left[FT(I_G(x, y)).NTF_s(u, v)\right] \tag{7.8}$$

These correlated noise images were each applied to the flat field image, $I_U(x, y)$, based on the mean-variance model as described in Equation 4.35 for each noise source:

$$\sigma_t^2(K) = k_e^2.I_{N,corr,e} + k_q^2.I_{N,corr,q}.K + k_s^2.I_{N,corr,s}.K^2 \tag{7.9}$$

where K is the air kerma measured at the detector surface. The noise array is scaled on a pixel-by-pixel basis with respect to the flat-field image and added to the flat-field image to give the final simulated image.

$$I_{sim}(x, y) = I_U(x, y).\left(\sqrt{\sigma_t^2(K)}.I_U(x, y)\right) \tag{7.10}$$

This method was also applied to sixteen synthetic CDMAM phantom images for each of the five doses using non-uniformity considerations discussed in Chapter 6. The settings of the CDMAM phantom images are shown in Table 7.1

Table 7.1: Settings used for acquiring CDMAM phantom images, beam quality was maintained at 31kVp Mo/Rh. Tube current time product and mean glandular dose (for an equivalent 50:50 fatty:glandular 6cm thick breast) are shown for each set of images.

Set	Tube Current time product (mAs)	Mean Glandular Dose (mGy)	Number of Images
1	240	5.91	16
2	120	2.95	16
3	61	1.48	16
4	32	0.80	16
5	14	0.34	16

7.2 Validation

Figure 7.1 is the NNPS of five synthetic flat field images compared with their experimental counterparts for the Hologic Selenia system

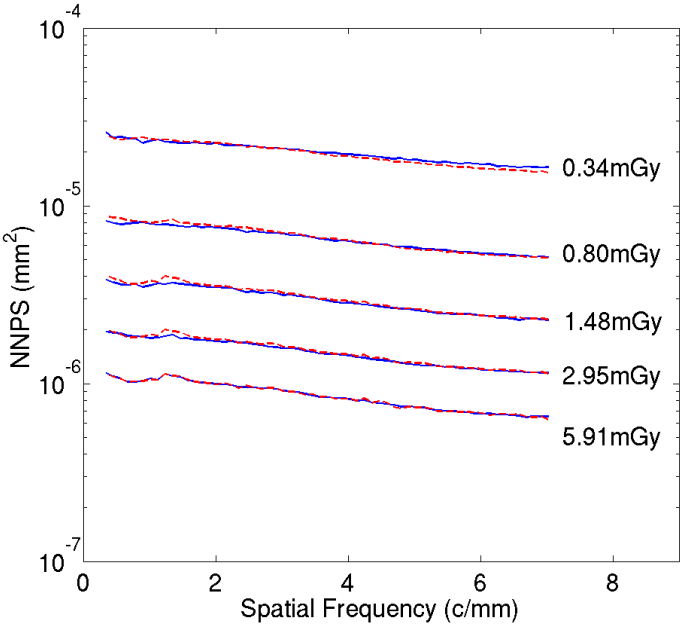


Figure 7.1: Radial NNPS of experimentally acquired flat-field images (blue) overlaid on synthetically derived flat-field images (red).

Relative difference between experimental and synthetic images for the radial NNPS

profiles in Figure 7.1 was found to be between 2.8 - 5.6% for the five doses.

Next, sixteen CDMAM images were synthesized for each of the five doses using the methodology described in Chapter 6 and the noise model described in the previous section. The contrast-detail curves are shown in Figure 7.2a for experimentally acquired and synthetically generated images. The ratio of the contrast-detail curves for experimentally acquired CDMAM images to synthetic CDMAM images are also presented in Figure 7.2b.

Results of the synthetic CDMAM images with the multiple noise source model applied show that the model provides average ratios (of experimental to synthetic contrast detail curves, $R_{d_{all}}$) of 0.98±0.06. This indicates a slightly lower detection rate (but insignificant) in the synthetic CDMAM phantom images than the experimental CDMAM phantom images. As can be seen, the results of the synthetic images were within the error bars (2 standard error means) of their experimentally acquired counterparts.

7.3 Modifying Experimental Images

To reduce the dose of an image would reduce the energy of the photons absorbed in the detector and thus increase the noise present in the image. Therefore, to halve the dose of an image, it would not be sufficient to only halve the pixel value intensity of the image. The noise present would need to be altered. As has been demonstrated by Båth et al[94], the image pixel intensity value will need to be scaled in line with the dose and the noise to be added will be equivalent to the difference in the noise between the high and low dose images.

7.3.1 Reducing the dose

Båth et al's methodology[94], which had been previously applied to chest X-ray images, has now been implemented for the first time to degrade the following experimentally acquired mammography images: CDMAM and mastectomy images.

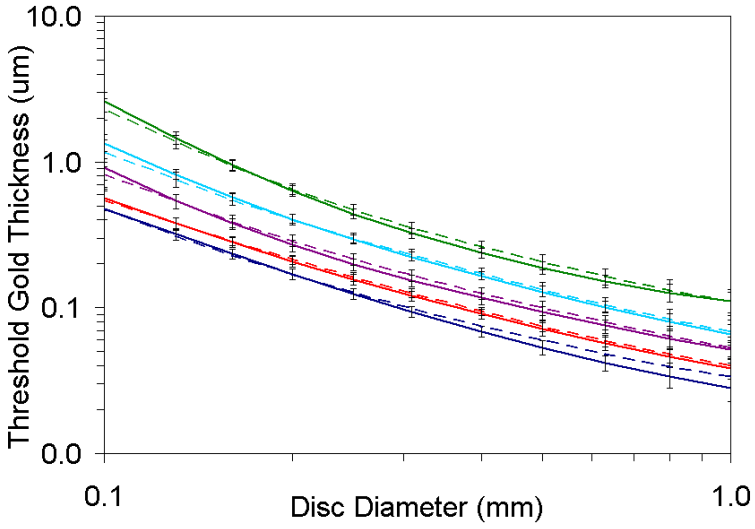
The linearised pixel intensity values of the original image, $I_o(x, y)$, were scaled by a ratio of the dose to be simulated, D_{sim}, to the original dose of the image, D_o, to give the original scaled image, $I_{o,sc}$.

$$I_{o,sc}(x, y) = I_o(x, y).SF \tag{7.11}$$

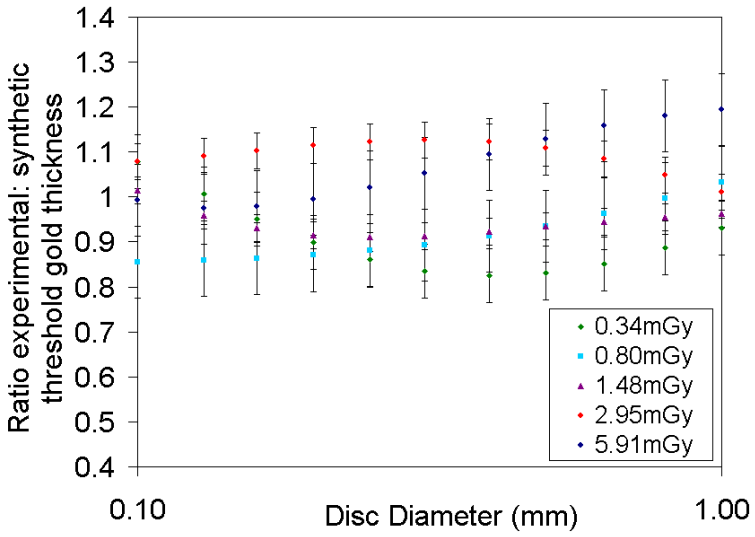
where

$$SF = \left(\frac{D_{sim}}{D_o}\right) \tag{7.12}$$

A noise image was created to account for the difference in noise level and frequency content between the $I_{o,sc}$ and that expected for a lower dose image, I_{sim}. This was undertaken through the use of a frequency-based noise filter equal to the difference of the NPS between the two images, I_{sim} and $I_{o,sc}$, and applied to a Gaussian noise image as described in Chapter 4. The main difference is that the NPS filter was modelled on three noise sources as described previously.



(a)



(b)

Figure 7.2: (a)Contrast-detail curves for the Holgic system. Dashed lines denote the contrast detail curves for the synthetic images whilst the solid lines denote the experimentally acquired counterparts. Error bars represent two standard error means.(b) Ratio of experimental to synthetic contrast-detail curves shown in (a) .

In the previous section, we established the NPS of the three noise components. These are used again in this section to model the total NPS needed to add the noise to the clinical image to be dose reduced. There is noise present in $I_{o,sc}(x,y)$, therefore we only need to model the difference in the noise between the target dose to be simulated and that found in $I_{o,sc}(x,y)$. The required noise filter was derived from the difference between the $NPS_{I_{o,sc}}$ and NPS_{sim}. As the structural noise scales correctly in $I_{o,sc}(x,y)$, there was no need to model the structural noise image. This NPS was normalised with the maximum value of the NPS and used to filter the Gaussian noise image to create a correlated noise image:

$$I_{N\Delta,corr,e}(x,y) = IFFT\left[FT(I_G(x,y)).(\sqrt{NPS_e(u,v)}).(1-SF^2)\right] \quad (7.13)$$

$$I_{N\Delta,corr,q}(x,y) = IFFT\left[FT(I_G(x,y)).(\sqrt{NPS_q(u,v).K_{sim}^2 - NPS_q(u,v).K.SF^2}\right] \quad (7.14)$$

where K is the dose of the $I_o(x,y)$. Each correlated noise image was scaled to the $I_{o,sc}$ on a pixel-by-pixel basis to create the noise image.As can be seen, the structure noise scales correctly with the dose.

Each noise image was added to $I_{o,sc}$ to create the simulated lower dose image.

$$I_{sim}(x,y) = I_o(x,y).SF + [k_Q.I_{N,q}(x,y).(I_o(x,y).(1-SF))^n] + (k_e.I_{N,e}(x,y).(1-SF)^2) \quad (7.15)$$

where k_Q and n are coefficients to be fitted. n was found to be 0.5 ± 0.03 for both systems and settings implemented in this chapter. This supports the validity of the assumption that the quantum noise is the dominant noise source, given that the model includes three noise sources with particular dose dependence each.

7.3.2 Flat-field validations

To validate the above methodology, flat field images of 5cm PMMA slabs were acquired on a Hologic Selenia system at five exposures as shown in Table 7.1. NPS measurements were made in a 1088x1088 pixel central portion of each of the images using a 128x128 pixel ROI as described in Section 4.6.1. The two dimensional NPS measurements were stored for use in the dose reduction process. The dose reduction methodology described above was applied to the highest dose image, 240mAs, to simulate images for the four subsequent lower doses. NNPS were measured for these synthetically dose reduced images and compared to the NNPS of experimentally acquired images.

Figure 7.3 show the NNPS of the experimentally acquired low dose images compared with the counterpart synthetically dose reduced images. The largest relative difference found between the synthetic and experimental low dose images was 4.7%. Svalkvist and Båth[97] report relative differences between experimental and synthetic NNPS data of less than 4%, close to the difference found in this work.

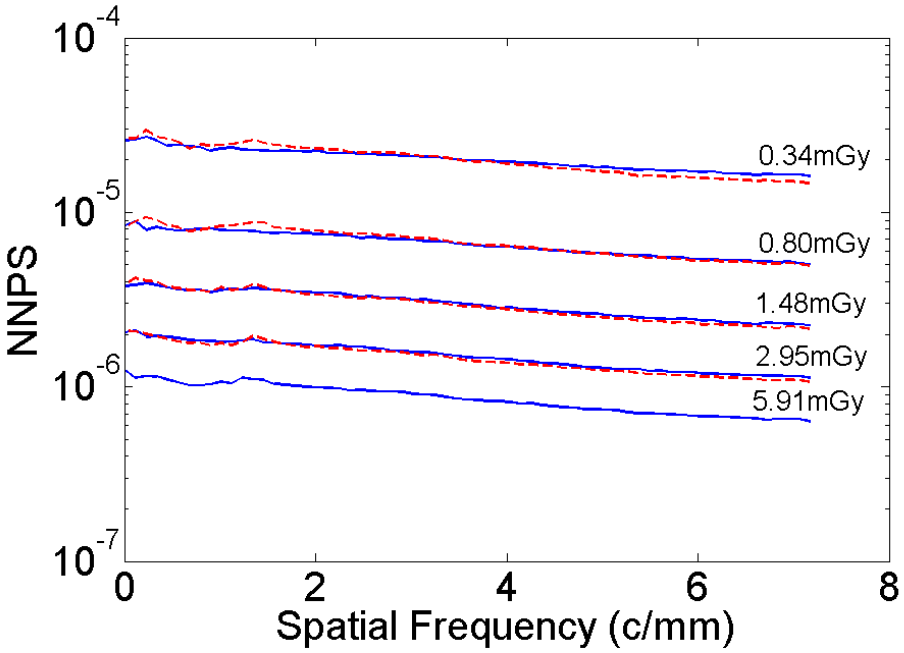


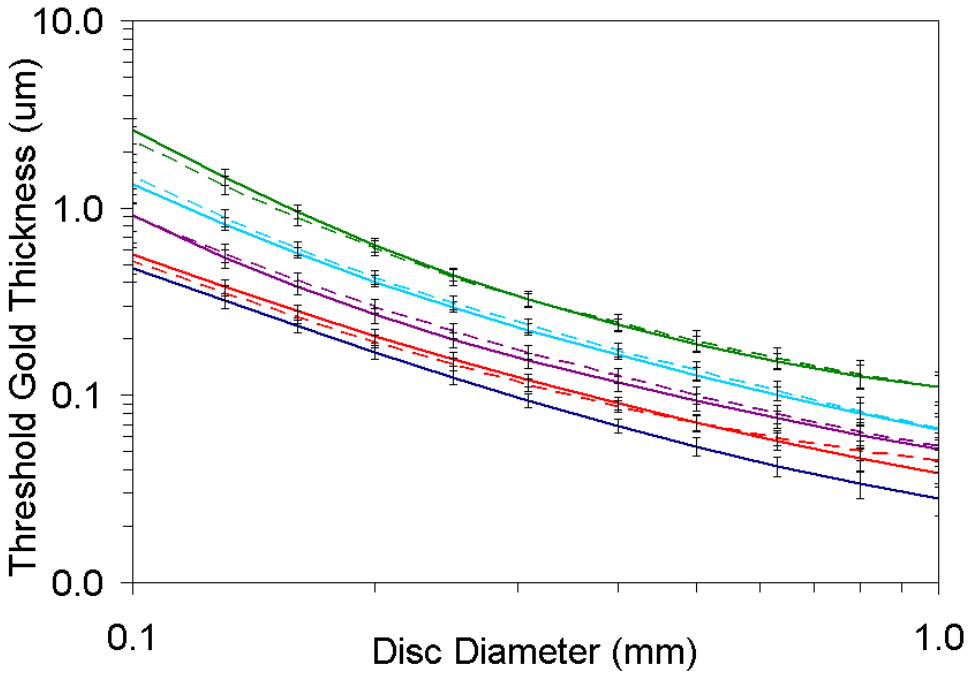
Figure 7.3: Radial profiles of the NNPS of experimentally acquired flat images at five doses are shown in solid blue lines. The highest dose was used to simulate the synthetic lower dose images. The NNPS for the synthetic images are shown in dashed red lines.

7.3.3 Contrast-detail Measurements of dose reduced images

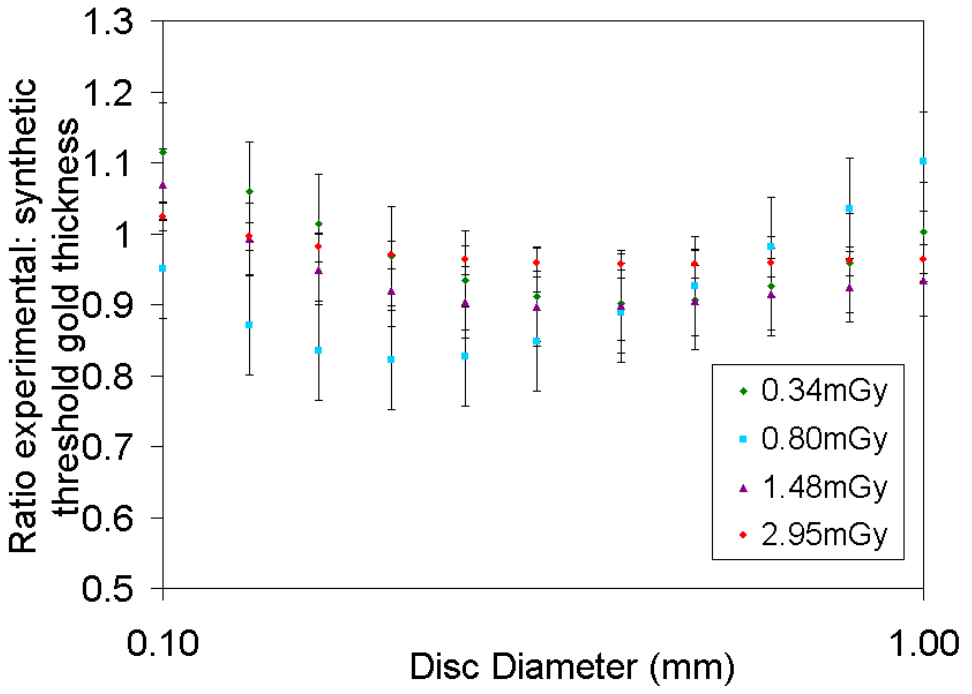
For degrading CDMAM images the highest dose (5.91mGy MGD) CDMAM image was used as the reference image from which low dose images (0.34, 0.80, 1.48, 2.95mGy MGD) were subsequently obtained. All experimentally acquired CDMAM images were scored with an automated scoring tool (CDCOM[38]) and contrast-detail curves derived for each dose as outlined in [16]. The same procedure was repeated for the synthesized dose reduced CDMAM images and compared with the experimentally acquired counterparts.

Figure 7.4 show the contrast detail curves obtained from the experimentally acquired and synthetically dose reduced CDMAM images. All the synthetically dose reduced images resulted in contrast detail curves within the error bars of the experimentally acquired images. The ratio of the contrast detail curves for experimental to synthetic CDMAM images is given in Figure 7.4. The average ratio $R_{d_{all}}$ found was 0.97±0.06 for all doses, suggesting an excellent agreement in the contrast-detail curves.

The dose reduction process has been validated with the use of flat field images as well as the CDMAM phantom. The next step is to apply the same methodology to clinical mastectomy images. Mastectomy images have been used as they provide the realistic anatomical background expected of mammograms. In addition, it is possible to expose the mastectomy samples to multiple settings with different beam qualities or dose levels without fear of overexposing patients to radiation.



(a)



(b)

Figure 7.4: (a)Contrast detail curves obtained from experimentally acquired CDMAM images at different doses (solid curves) and the simulated reduced dose CDMAM images (dashed curves) for the Hologic Selenia system. Four doses (0.34, 0.80, 1.48, 2.95mGy MGD, from top down) were simulated from the highest dose of 5.91mGy. Error bars denote two standard error means.(b) Ratio of contrast-detail curves shown in (a)(experimental to synthetic CDMAM images).

7.4 Clinical Mastectomy Images

7.4.1 Materials

Four sets of mastectomy images were acquired on the Siemens Novation system. Each mastectomy sample was placed on the breast support and compressed. The mastectomy sample was exposed with the tube voltage held constant whilst the tube current time product was varied. Care was taken not to move the mastectomy sample after each exposure. The highest dose mastectomy image was used as the reference image for synthesizing subsequent lowered dose images. Table 7.2 shows the doses used for each mastectomy set as well as their compressed thicknesses.

Table 7.2: Beam quality, Tube current time product and mean glandular dose settings for each mastectomy sample set. Doses in brackets denote the highest dose image from which the other low dose images were derived.

Set	Beam Quality (kVp target/filter)	Tube Current time product (mAs)	Mean Glandular Dose (mGy)	Compressed Breast Thickness (mm)
1	29 W/Rh	28, 57, 110 (220)	0.3, 0.7, 1.4 (2.7)	50
2	29 W/Rh	10, 20, 50, (68)	0.1, 0.2, 0.4 (0.6)	50
3	25 Mo/Rh	10 (61)	0.2 (1.3)	30
4	25 Mo/Rh	20, 34, 45 (199)	0.4, 0.7, 1.0 (4.3)	30

Flat field images using three and five centimetres of PMMA were used in the same setup as the mastectomy samples for detector response and NPS measurements to be used with the dose reduction methodology.

7.4.2 Flat-field Validations

Figure 7.5 shows the NNPS for the Siemens Novation system to validate the dose reduction process for this system for both set ups. For the 25kVp Mo/Rh set up, the relative difference in the synthetic to experimental NNPS profiles was 2.7%. For the 29kVp W/Rh set up, the relative difference was found to be 3.4%.

7.4.3 Analysis of modified clinical images

The dose reduced mastectomy images were compared, quantitatively and visually, with their experimentally acquired counterparts. In addition, noise power spectra[120, 121] were measured in the same region of interest for each dose for the simulated and experimental mastectomy images and the profiles compared. To ensure the same region was analysed in each image and that results were not affected by any slight movement of the mastectomy sample, the mastectomy images were checked for alignment. In addition, NPS analysis was undertaken within the central portion of the mastectomy samples to ensure uniform thickness was maintained in the region of interest.

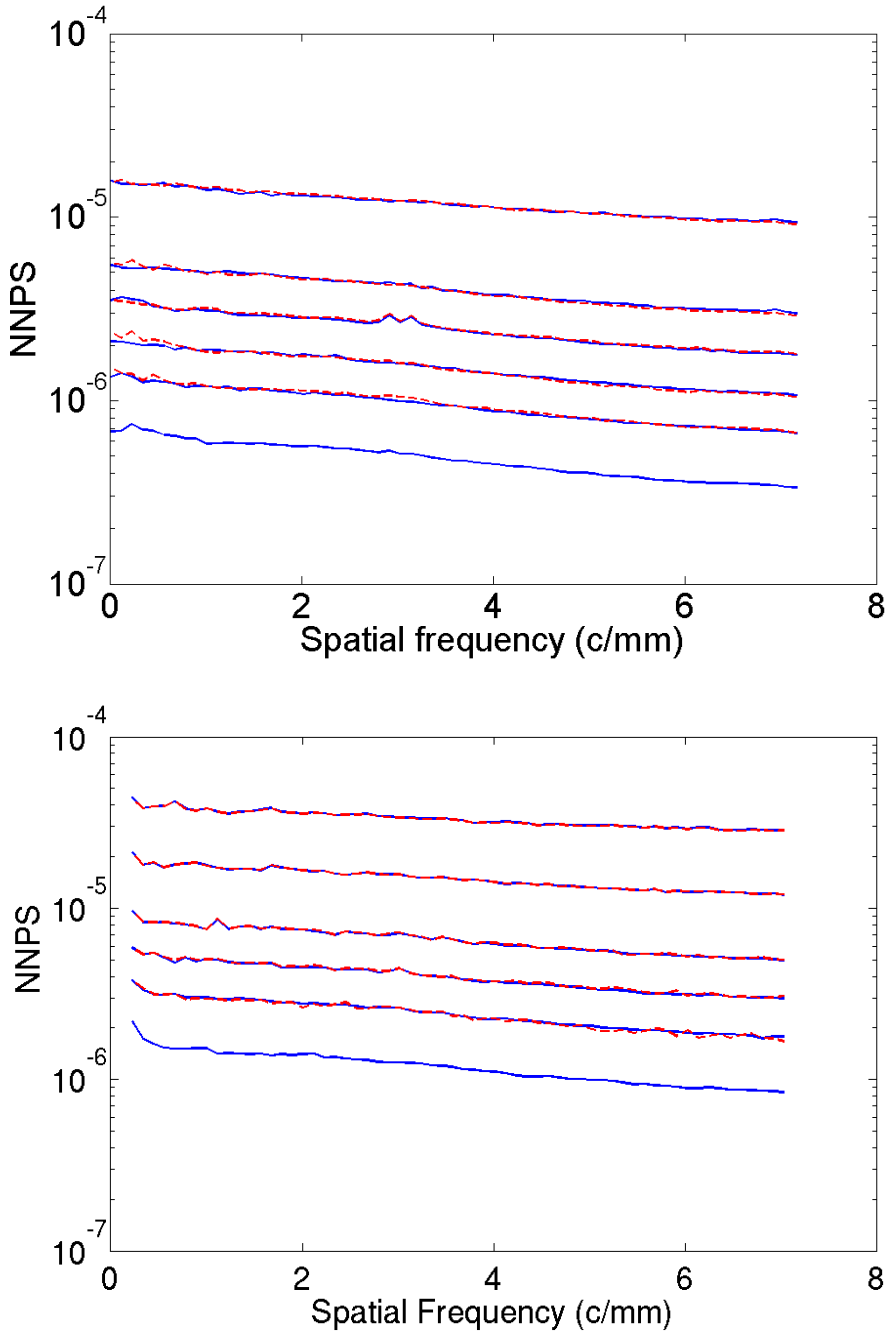
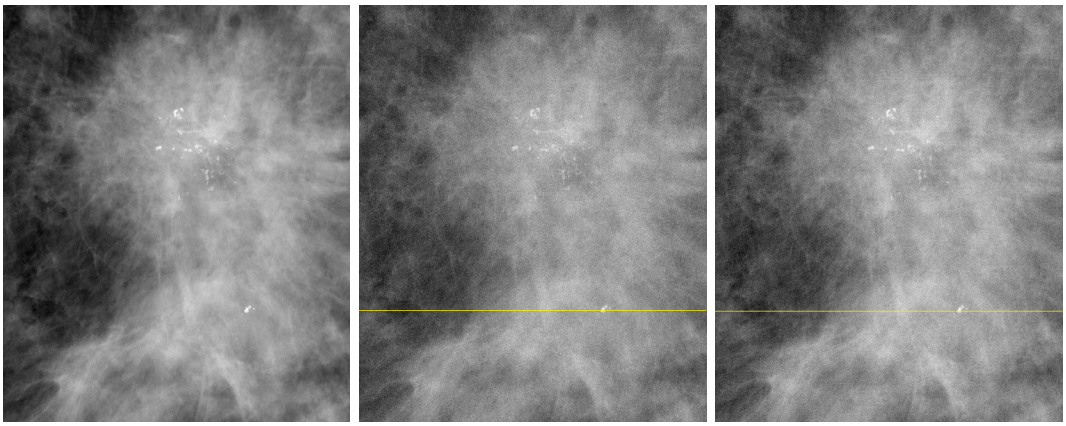


Figure 7.5: NNPS profiles for the Siemens Novation. (a) NNPS curves are given for (from top down) 0.2, 0.4, 0.7, 1.0, 1.3 and 4.3mGy MGD for the system setup with 3cm PMMA 25kVp Mo/Rh. (b) NNPS curves for (from top down) 0.1, 0.2, 0.4, 0.8, 1.3, 2.5mGy MGD for the system setup with 5cm PMMA 29kVp W/Rh. Blue solid curves show the NNPS profiles for experimentally acquired images and the red dashed curves show the NNPS profiles for the synthetic images.

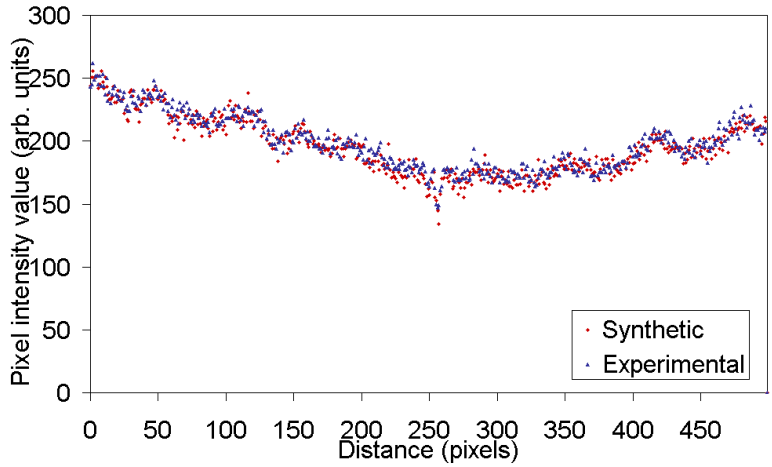
7.4.4 Qualitative Comparisons

Figure 7.6a and 7.6b shows a region of one set of mastectomy images at 4.3 and 1.0mGy MGD for the experimental, respectively. Figure 7.6c shows the mastectomy image manipulated to appear acquired at 1.0mGy. The appearance of the lesion in the region shown degraded dramatically as the dose was reduced down to one quarter of that for the high dose image. A profile of the experimental and synthetic images is also shown in Figure 7.6d, an average difference of 1% was found between the profiles.

Figure 7.7 shows cropped regions from image set 1, comparing experimentally acquired images with synthetically dose reduced images. When compared like for like, the synthetic images showed great similarity to the experimental images. The cropped region was selected to show the effect of noise upon the mass in this mastectomy sample.

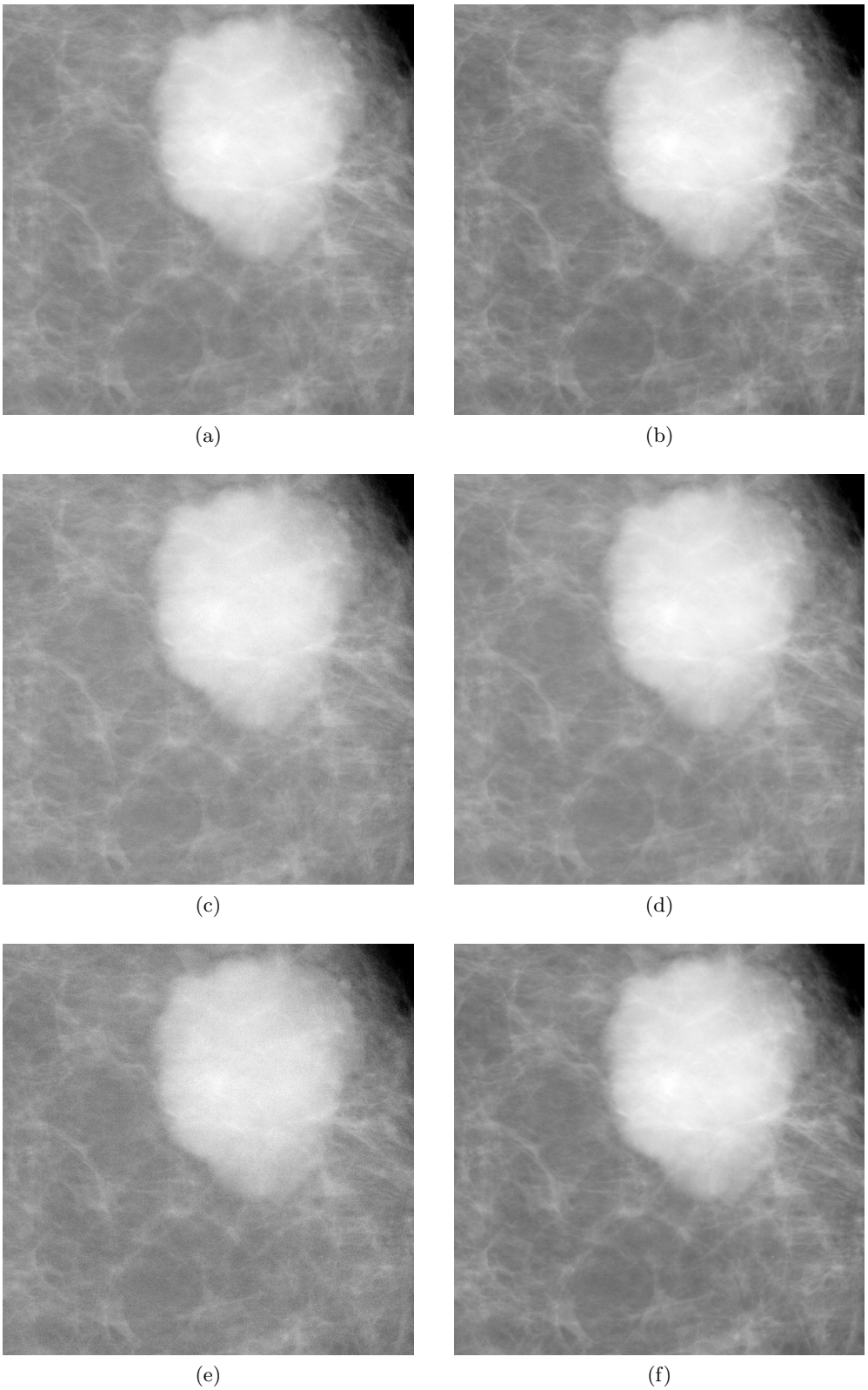


(a) (b) (c)



(d)

Figure 7.6: (a) and (b) show the same cropped region of a mastectomy acquired at 4.3 and 1.0mGy (MGD), respectively. (c) shows the mastectomy sample synthetically dose reduced from 4.3 to 1.0mGy. (d) shows the profiles taken across (b) and (c) to compare the experimentally acquired low dose image with the simulated low dose image.

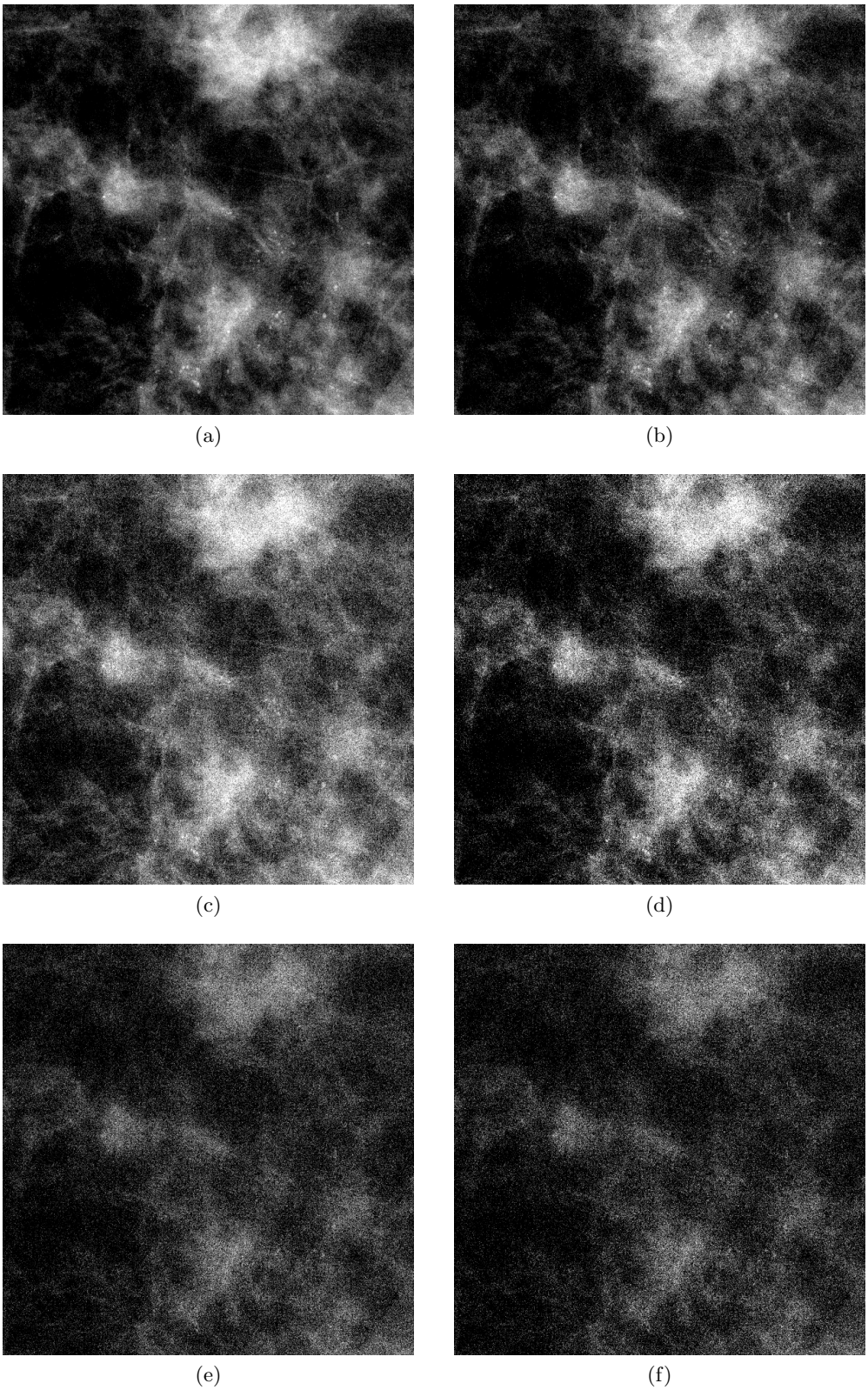


(a) (b)

(c) (d)

(e) (f)

Figure 7.7: (Left)Cropped region of mastectomy image set 1 acquired at 1.4, 0.7 and 0.4mGy MGD. (right) Cropped region of mastectomy image acquired at 2.7mGy synthetically dose reduced to the same dose level as shown on the left.



(a) (b)

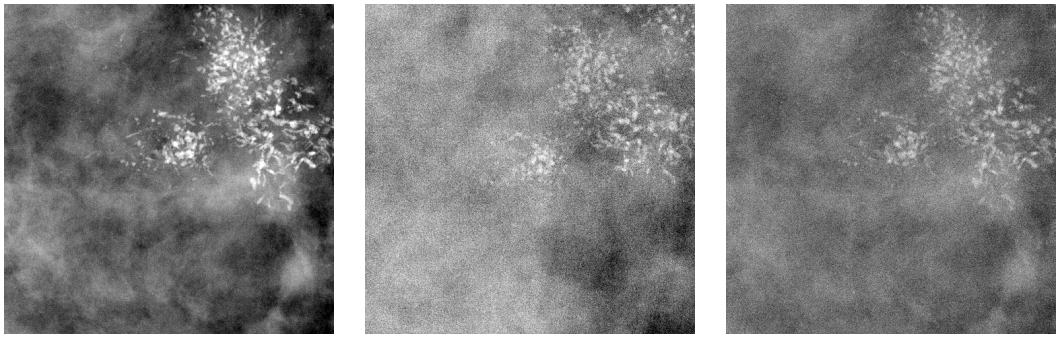
(c) (d)

(e) (f)

Figure 7.8: (Left)Cropped region of mastectomy image set 2 acquired at 0.4, 0.2 and 0.1mGy MGD. (right) Cropped region of mastectomy image acquired at 0.6mGy synthetically dose reduced to the same dose level as shown on the left.

Figure 7.8 shows cropped regions from image set 2, comparing experimentally acquired images with synthetically dose reduced images. When compared like for like, the synthetic images were very similar to experimental images. For the lowest dose presented, 0.1mGy MGD, visibility of the microcalcifications present in the high dose image had been degraded dramatically in the dose reduction process.

Figure 7.9 shows cropped regions from image set 3, comparing experimentally acquired image with the synthetically dose reduce counterpart. When compared like for like, the synthetic images were very similar to experimental images. However, it may be noted that there were some slight displacement of the calcifications present in the cropped region. This specific region was not used for NPS analysis.



(a) (b) (c)

Figure 7.9: (a) and (b) Cropped region of mastectomy image set 3 acquired at 1.3 and 0.2mGy MGD, respectively. (c) Cropped region of mastectomy image acquired at 1.3mGy synthetically dose reduced to 0.2mGy. Some calcifications have been displaced in this image between the two exposures.

7.4.5 Quantitative Comparisons

Noise power spectra were measured with 1088x1088 ROI within central portions of the mastectomy samples to ensure that uniform thickness was maintained where possible. Figure 7.10 shows the radially averaged noise power spectra for each set of mastectomy images listed in Table 7.2.

As the dose increased, the system noise increased as expected. Both NPS of the lower doses, 0.4 and 0.7mGy, have overestimated noise at higher spatial frequency components for set 1. The greatest differences were found in sample set 1, ratios of experimental image to synthetic image NPS were as large as 2.42 for 0.7mGy. For sample sets 2 – 4, the ratio of the NPS for experimental to synthetic images for between 0.98 – 1.27. Further investigation into the original experimental images for set 1 showed that the mastectomy sample in the low dose experimental image had moved slightly. This was verified by scaling the high dose mastectomy image to the lower dose and subtracting this from the experimental low dose mastectomy image. The result was a noise image with some small structure in the noise. Thus showing that the NPS measurement is very sensitive to the information in the ROI selected.

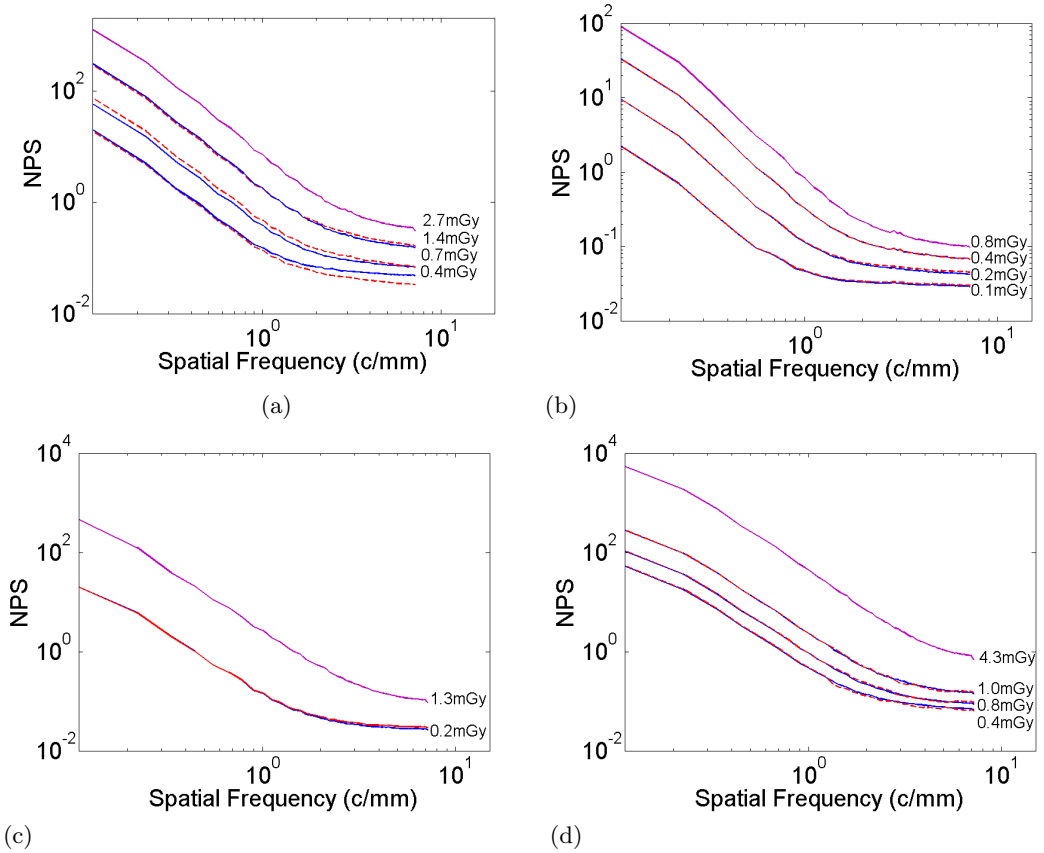


Figure 7.10: (a – d) Radially averaged noise power spectra of a region in sets 1 – 4, respectively, of mastectomy images acquired at different doses and their synthetic counterparts. The dark purple curve represents the highest dose image from which the other low dose images were degraded. Red dashed curves illustrate the NPS of synthetically degraded images whilst the blue solid curves show the NPS of their experimentally acquired counterparts.

Work by Bochud et al[120] and Heine[121] have shown that anatomical noise is the dominant source of noise. However, it can be see that if the mammographic image is only scaled and no noise is added; the noise at high spatial frequencies do not match up as shown in Figure 7.11.

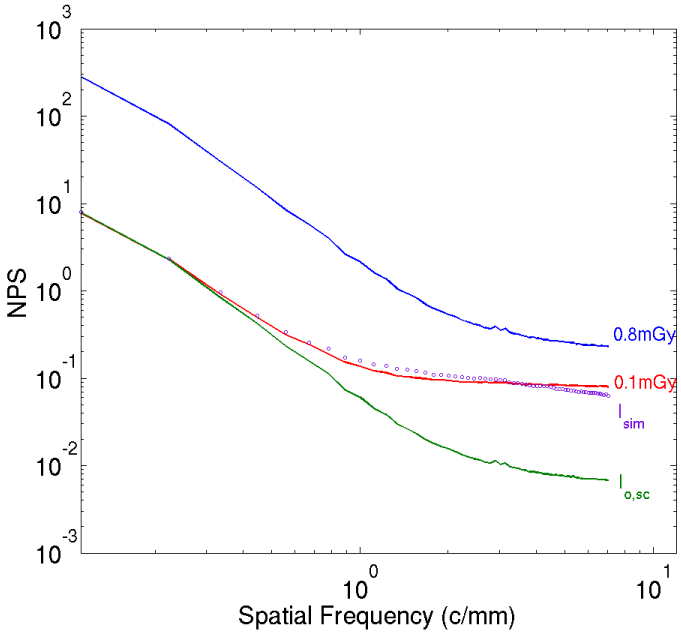


Figure 7.11: An example of the NPS for mastectomy set 2. NPS for the experimentally acquired mastectomy images is shown in red and blue (0.1 and 0.6mGy, respectively). As the high dose image is scaled to $I_{o,sc}$, the resultant NPS (shown in green) overlaps with the experimentally acquired low dose NPS for the low frequencies. However there is insufficient noise in $I_{o,sc}$ to match the low dose image. When the noise is added, the NPS measured for I_{sim} overlaps the experimental NPS for the higher spatial frequencies also. The ratio across all spatial frequencies for this set up was measured to be 1.04.

Work by Svalkvist and Båth[97] measured the NNPS in a region of an experimentally acquired low dose image (of an anthropomorphic chest phantom) and that for a synthetically dose reduced image. The error in the integrated NNPS was found to be less than 4% for the method described in the paper, compared to over 20% for the method described by Båth et al[94].

Figure 7.12 shows the NNPS of mastectomy set 4 for the doses simulated. As can be seen, below 1c/mm the NNPS overlap for all doses, both from experimental and synthetic images. The error was found to be up to 14% for mastectomy sets 2-4. This is larger than that described for Svalkvist and Båth's method which was validated with images of an anthropomorphic chest phantom, a rigid object. The error in this study may be attributed to changes in the anatomical information in the images as the mastectomy sample may have moved slightly between exposures.

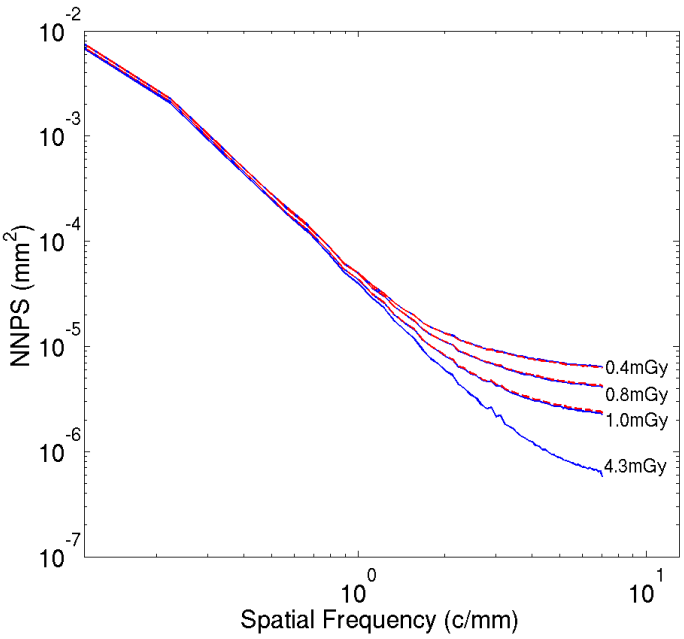


Figure 7.12: An example of the NNPS for mastectomy set 4. NNPS profiles from the experimental images are shown in solid blue and the synthetically dose reduced images are shown in dashed red.

7.5 Discussion and Conclusions

This chapter has introduced the multiple noise source model and validated this with the use of flat-field and CDMAM images. The multiple noise source model was further applied to degrade clinical images of CDMAM and mastectomy samples to appear as if acquired at a lower dose. This is the first time quantitative analysis has been made on such a dose reduction methodology.

The multiple noise source model was validated with flat-field and CDMAM phantom images as carried out with the previous chapters. Results for the synthetic images were in excellent agreement with the experimental images. NNPS measured from synthetic flat-field images deviated up to 5.6% from experimental images. The ratio of threshold contrasts for all disc diameters, $R_{d_{all}}$, was found to be 0.98±0.06 averaged for all five doses.

The dose reduction process was further applied to the same experimentally acquired flat-field and CDMAM phantom images. The synthetic dose reduced flat-field images gave NNPS that deviated up to 4.7% from the experimental counterpart low dose flat-field images. In comparison, Svalkvist and Båth published NNPS errors in their dose simulations of less than 4%. Excellent results were found for the dose reduced CDMAM phantom images: $R_{d_{all}}$ were calculated to be 0.97±0.06 between the experimental and synthetic contrast-detail curves for all doses. Such results are not dissimilar to the CDMAM phantom image simulations from idealised image set up.

Flat-field images from the Siemens system was also dose reduced to validation in preparation for the mastectomy images. Average relative differences in the NNPS, averaged across all doses, was found to be 2.7%. When the dose reduction process was applied to the mastectomy samples, visually the images had degraded as expected. Direct comparisons of the pixel intensity values showed only 1% difference showing the scaling process had been performed correctly. Further investigation into the NPS of the mastectomy samples showed excellent agreement for most of the samples except for one set. Examination of the images within this set showed that there was a slight offset to the mastectomy sample. Such slight movements in the sample led to large errors in the NPS demonstrating the sensitivity of the NPS measurement to positioning.

Endeavours were made to ensure that the central region was used for NPS measurements, on the assumption that this region presented the most uniform thickness in the mastectomy sample. Attempts had been made to acquire flat field images using PMMA thicknesses equivalent in attenuation to a composition of 50:50 glandular:adipose. Based on work by Dance et al[70], for the thickness of mastectomy samples used (assuming 50:50 adipose to glandular tissues composition), the equivalent thickness of PMMA would be 2.8cm and 4.3cm. Three and five centimetres of PMMA were used for detector response and NPS measurements. If the integral of the NPS is the variance in the image, and the variance is equal to the number of photons that reach the receptor (as shown in Chapter 3), some inferrences can be made.

For the sets 1 and 2, where 29kVp W/Rh beam quality was used, the number of photons reaching the receptor when 3cm of PMMA is used was found to be $4.24\text{x}10^6$, compared with 2.8cm of PMMA, N_p was found to be $4.89\text{x}10^6$. This is a relative difference of -13.2%. The same was calculated for sets 3 and 4, the relative difference between the two set ups with 5cm and 4.3cm of PMMA was seen to be 33.1%. A potential weakness of the above analysis is that intrinsic NPS was assessed with 3 and 5cm instead of 2.8 and 4.3cm, respectively. Therefore contributions of the NPS to measured experimental NPS represents an overestimate of the NPS. It is remarkable to see the degree of agreement despite this fact, suggesting that this error is insignificant when in the presence of anatomical noise in the image.

This chapter marks the first study to have used CDMAM test objects and mastectomy samples to validate the dose reduction process. Implementation of the image simulation framework to degrade clinical images presents one of the possibilities in creating larger image data sets for observer performance studies in comparing digital mammography system settings such as exposure settings.

Chapter 8

Conclusions and Further Work

Objective image quality assessment is well understood and typically takes the form of MTF and NPS measurements or other derived quantities. However, the link between objective and subjective image quality cannot be established easily. This provided a motivation to develop a framework by which objective image quality metrics can be used as an input to derive synthetic images. From these, observer performance can be measured in a meaningful way with respect to lesion detection studies. This thesis aimed to develop and validate an image simulation framework to simulate DM images that are clinically realistic and physically accurate. Validation of the image simulation framework took the form of image quality measures such as MTF, NPS and contrast-detail measurements.

The number of studies to simulate radiographic images with the use of image quality metrics has grown rapidly over the recent years[10, 82, 61, 103, 33, 32, 87, 94, 95, 97]. It was clear realistic DM images could be generated quickly and accurately for specific studies. The image simulation framework developed here provided a robust method to synthesize DM images of flat-field and straight edge images at arbitrary exposures for different DM systems. The image simulation framework was validated by comparing the images with their experimental counterparts. We modelled three of the most popular DM technologies: Hologic Selenia, GE Essential and Agfa CR. A new theoretical framework addressing the MTF blurring and resampling processes was developed and validated. Well-known artefacts caused by resampling were investigated and understood. Methods to address the causes of such artifacts have been presented. Excellent results were obtained, with 2% relative difference found between synthetic and experimental MTFs. Synthetic flat-field images similarly showed good agreement with relative error ranging between 1.2 - 6.8%for different doses.

Chapter 5 sought to validate the image simulation framework with a typical performance assessment tool, the CDMAM phantom. CDMAM phantom images (synthetic and experimentally acquired) were assessed with two software packages: the widely used CDCOM and one developed in-house, QAS. Early investigations only considered a uniform model with image quality metrics applied. This yielded visually poor-quality images, and demonstrated the need for greater levels of sophistication if truly realistic images were to be generated.

QAS was developed to score CDMAM phantom images and provide valuable data about the contrast, signal and noise of discs. This is information that the commercially available CDCOM cannot provide. With the data from QAS about the correctly detected discs, it was clear how the synthetic CDMAM phantom images lacked non-uniformity effects to match the experimentally acquired CDMAM phantom images.

The four principal non-uniformity degraded processes that affect the CDMAM phantom images' performance metrics were addressed: spatial intensity variation, local detector variance, geometric blurring and scatter. Accounting for the combined non-uniformity effects marks the first time such models have been used in image simulation. This enhanced visual similarity with experimentally acquired counterpart of the synthetic images. Monte Carlo was implemented to investigate the initial assumption of uniform scatter across the CDMAM simulation setup. Results were found to differ from previous simulations by a maximum absolute difference in the ratio of 0.10. It was seen that in refining the S/P model, the previous gross assumption of this model had in effect been obfuscating errors in the calculation of the disc contrast due to primary photons. It was acknowledged that there were further refinements needed in the disc contrast calculations to include other factors attenuating the photons in the CDMAM set up. Despite this, the Monte Carlo proved the assumption of a uniform scatter model was valid for this CDMAM phantom set up.

After non-uniformity effects were applied, the ratio of the contrast-detail curves derived from experimental and synthetic CDMAM phantom images were found to be unity for all the systems. Absolute difference in this ratio, before and after non-uniformity effects were considered, was 0.02, 0.04 and 0.15 for the Hologic Selenia, GE Essential and Agfa CR systems, respectively. In conclusion, this study provides a method in which CDMAM phantom images can be created that are physically accurate to experimentally acquired images. Considerations to non-uniformity effects is necessary to create truly realistic images, especially for DM systems susceptible to such effects such as CR technology.

Chapter 7 presented a multiple noise source model which was validated with synthetic flat-field and CDMAM phantom images as described in the previous chapters. This was further applied to experimental images of CDMAM phantom and mastectomy samples to create synthetic images as if acquired at lower doses. Simulation of low dose images were compared directly with their experimentally acquired counterparts with the use of contrast-detail curves and noise power spectra for images of mastectomy samples. Excellent agreement was seen between the contrast-detail curves for experimental and synthesized images, with ratio of experimental to synthetic contrast-detail curves found to be 0.98. The noise power spectra of the mastectomy images gave similarly excellent results. The ratio of the NPS for experimentally acquired to synthetically dose-reduced mastectomy images ranged between 0.98-1.27. When the NPS were normalised, the relative difference was measured to be approximately 14%. Sources of error were identified to be two-fold: (i) overestimation in the system NPS due to thicker PMMA slabs being used for NPS reference; (ii) the mastectomy sample may have moved slightly between exposures. In conclusion, the multiple noise source assumption provided an accurate model to predict the NPS in DM images for a wider range of doses (upto one order of magnitude). Mastectomy images provided an effective method to directly compare the

synthetically dose reduced images with the experimentally acquired counterparts.

This study has developed an image simulation framework which provides the link to compare and optimise DM systems. Physical performances metrics can be used as parameters for the image simulation framework to produce realistic DM images for observer based studies. This provides a potentially powerful tool to investigate the relationship between physical performance of DM systems and its clinical impact on lesion detection tasks.

8.1 Further Work

This image simulation framework could be combined with computer simulation models of the breast as developed by Bliznakova et al[35]. The computer model of the breast phantom would provide a valuable representative ground truth for which to assess the diagnostic performance of different technology platforms. With this, studies could be set up to assess the lesion detection performance of DM systems for different types of breasts, types of lesions such as masses (malignant or benign) or microcalcifications (such as cluster characteristics and sizes). Several breast phantoms could be derived and photon transport software could be applied to provide an image as an idealised synthetic breast image. This idealised synthetic breast image could be degraded with the image simulation framework to created a realistic synthetic mammogram.

This 3D model of the breast would also provide a method of extending the work to modelling breast tomosynthesis technology, where several projections of breast images are required. The signal and noise transfer models developed in this study are still valid as physical principles of the image acquisition process remains the same. Accurate measurement of the MTF at different angles is under debate[122, 123] as the detector remains stationary with respect to the X-ray tube during image acquisition. Badano et al[123] report that resolution properties of a tomosynthesis system varies greatly with the angle of X-ray incidence. Furthermore, Svalkvist and Båth[95] has shown that DQE needs to be taken account of when modelling the dose reduction process in breast tomosynthesis technology as the dose absorbed in the detector varies with different projections.

If the dose-reduction methodology applied to the mastectomy images were extended on a larger scale for mammograms, a range of NPS data would be needed from flat-field images with different beam qualities and PMMA thicknesses. As a result of studying the NPS, it was recognised that as the NPS_{tot} could be separated into different noise sources dependent on their relationship to dose, then such theory could be further extended to model the NPS for when different thicknesses of PMMA is imaged. It may be possible to accurately model how the NPS changes with not only the dose but also the thickness of PMMA slabs which is used to model attenuation properties of different breast thicknesses.

The image simulation frame work could also be applied to clinical images. The work presented here shows the potential of degrading images to appear as if acquired at lower doses. This could be extended to degrade images as if acquired with different

image receptors by altering the blurring, pixel sampling and noise properties of the image. This would be very useful for assessing the clinical impact of using different DM systems for cancer detection.

Appendix A

Anatomy and Pathology of the breast

A.1 The Breast

The female breast extends from under the collarbone to approximately the level of the sixth or seventh rib. The breast has six to nine overlapping lobes which divide further into lobules. These lobules end in tiny bulbs that produce milk. Ducts connect all these structures which end at the nipple. The lobes and ducts form what is known as glandular tissue which is denser than the adipose tissue that surrounds it as shown in Figure A.1. Glandular tissue form the so-called 'clutter' in mammograms, making any abnormalities hard to discern. The breast is attached to the chest wall by fibrous strands called Cooper's ligaments. The lymphatic vessels in the breast drain into a network of lymph nodes located in the underarm and near the collarbone. Blood vessels infiltrate the breast to deliver nutrients and oxygen as well as removing any waste products. It is via lymphatic and blood vessels that metastasis of breast cancer can occur.

A.2 Breast Cancer

Breast cancer is one of the most common form of cancer for women in the developed world. There are no known causes of breast cancer. However, there are major influences on breast cancer risk: reproductive factors such as low parity and late age at first pregnancy; obesity; alcohol consumption; exogenous hormones (contraceptive pill); heredity and possibly diet[124]. Magnitudes of these risk factors are hard to quantify, however it has been demonstrated that hereditary factors are minimal in comparison. Migrants from countries where risk of breast cancer is low living in countries with higher average risk of brease cancer increase their own chance of developing cancer. This would suggest tha genetic predisposition is far outweighed by the environmental exposures mentioned above. Change in the lifestyle of women has led to incidence rates in women below the age of 50 to increase. For this reason, NHSBSP will be increasing the age range at which screening is offered to women between the ages of 47 - 73[125].

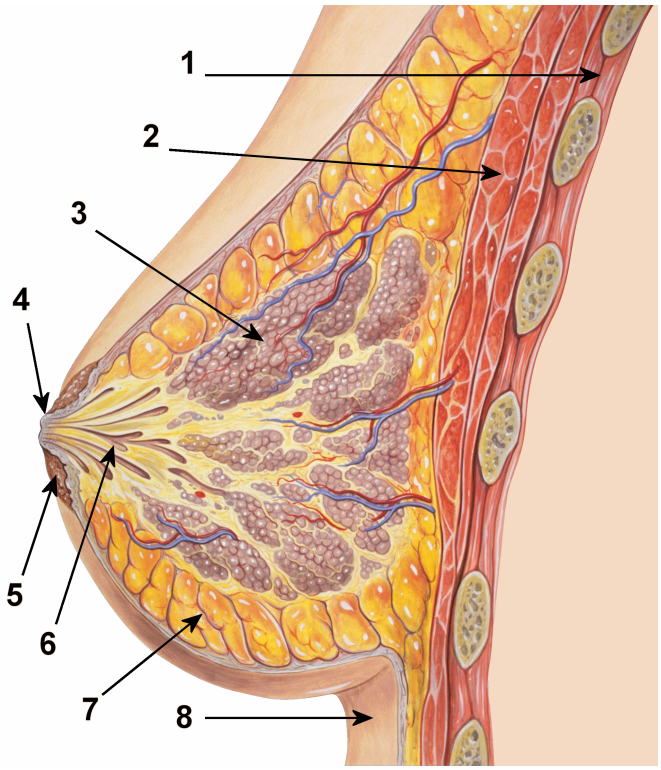


Figure A.1: Anatomy of the breast (1) Chest wall, (2) Pectoralis muscles, (3) Lobules (containing milk glands), (4) Nipple surface, (5) Areola, (6) Lactiferous duct, (7) Adipose (fatty) tissue, (8) Skin.[21]

There are several classifications of breast cancer. The majority of cases are classified as either *in situ* or *invasive*.

A.2.1 Lobular Carcinoma in situ (LCIS)

LCIS describes breast cancer confined to the milk producing glands (lobules) of the breast. This condition is often considered the precursor to the development of a more invasive cancer. LCIS does not generally produce a lump[126].

A.2.2 Ductal Carcinoma in situ (DCIS)

This form of breast cancer is confined to the milk ducts in the breast. As DCIS is confined to the breast, this renders the cancer cell unable to penetrate into the lymphatic and vascular system[126] and therefore develop into metastasis. Cancer cells accumulate in the milk ducts. This causes calcium to collect in the ducts and becomes visible in mammograms as clusters of microcalcifications. DCIS may also present as a palpable mass, bloody nipple discharge, detection of a mass with or without calcifications in a mammogram[126]. This accounts for 20-30% of breast cancers diagnosed in screening[127].

A.2.3 Invasive Lobular Carcinoma (ILC)

ILC develops in the lobules of the breast. The difference is that ILC has the ability to develop into metastasis. This is less likely to present in a mammogram as it presents as a 'thickening' of the breast consistency, not a mass as in DCIS.

A.2.4 Invasive Ductal Carcinoma (IDC)

IDC develops in the milk ducts and can invade the surrounding tissue and has the potential to metastasise to other parts of the body. This is the most common form of invasive breast cancer, approximately 85% of cases are diagnosed as IDC[128]. IDC presents as a hard lump with irregular borders that appear as an indistinct and spiculated mass as shown in Figure A.2.



Figure A.2: An invasive ductal carcinoma (denoted by the *) in the breast image on the right. There is also associated thickening of the skin (white arrows) shown in this digital mammogram.[22]

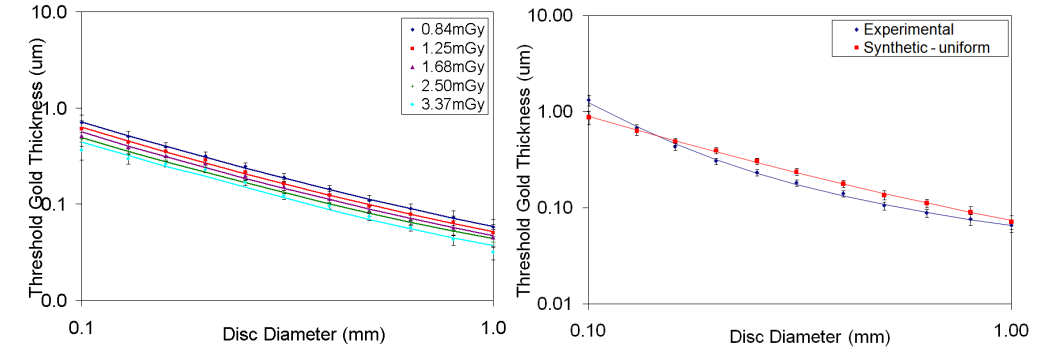
Pathology of breast cancer described above makes detection of breast cancer more complex for radiologists. Radiologists do not necessarily have difficulty in detecting lesions. It is more important to classify the lesion correctly as the different types may be more agressive than others. Image quality therefore is critical for characterising the lesions that may be present in the mammgrams. This thesis aims to offer a solution to elucidate this matter.

Appendix B

Individual contrast-detail curves

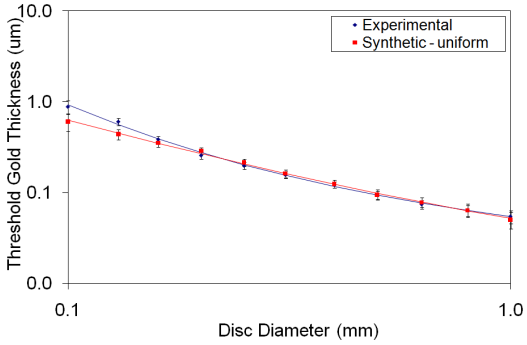
B.1 Hologic Selenia system - amorphous selenium technology

B.1.1 Uniform images

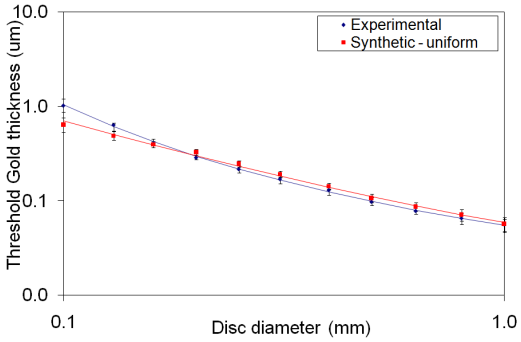


(a) All doses

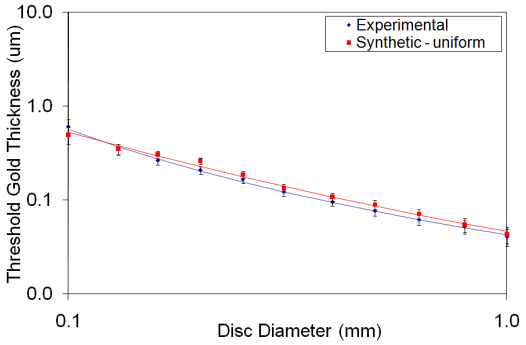
(b) 0.84mGy MGD



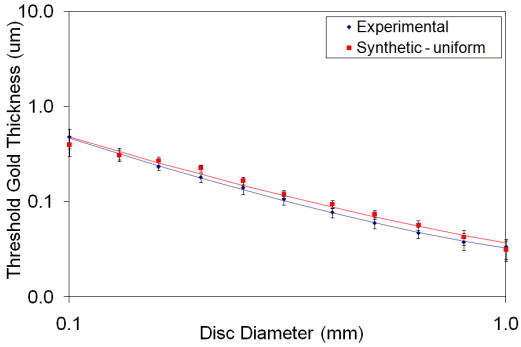
(c) 1.25mGy MGD



(d) 1.68mGy MGD



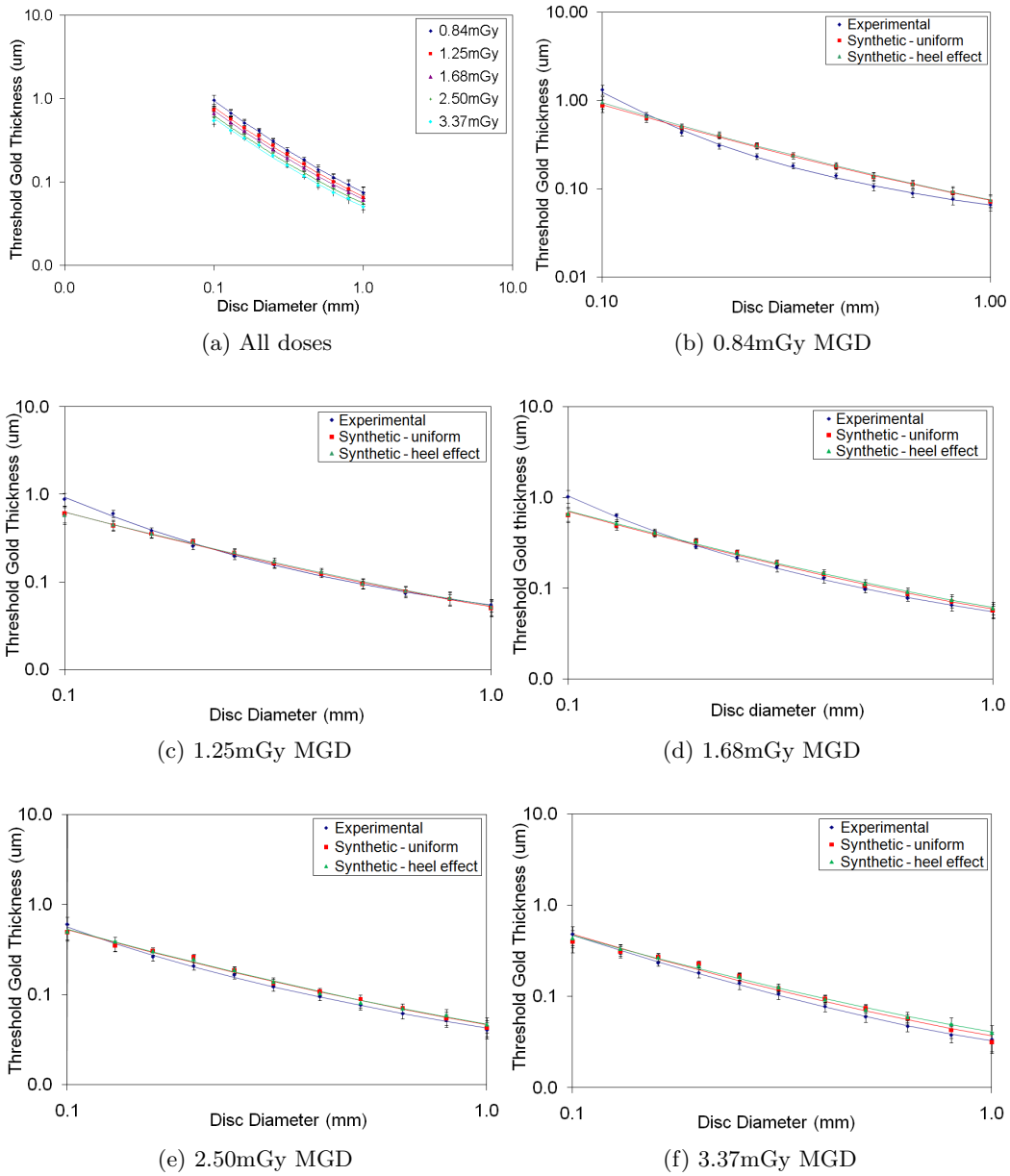
(e) 2.50mGy MGD



(f) 3.37mGy MGD

Figure B.1: Direct comparison of the contrast-detail curves for experimental and synthetic images for the Hologic Selenia system at each dose. Results are from Chapter 5.

B.1.2 Heel effect mask



(a) All doses

(b) 0.84mGy MGD

(c) 1.25mGy MGD

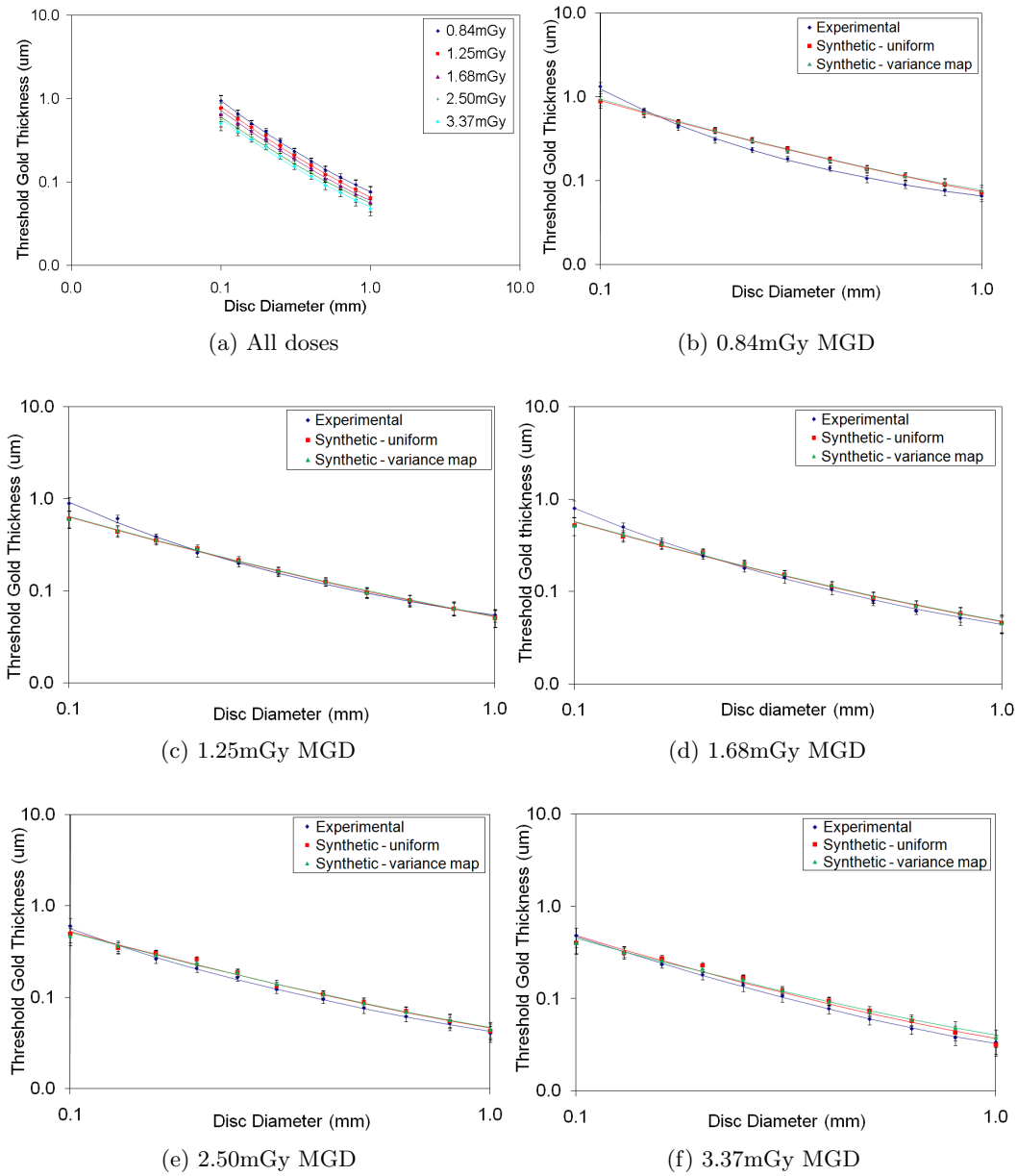
(d) 1.68mGy MGD

(e) 2.50mGy MGD

(f) 3.37mGy MGD

Figure B.2: (a)Contrast detail curves for all simulated doses with the heel effect mask applied for the Hologic Selenia system. Contrast detail curves for the simulated CDMAM images with the heel effect mask applied are presented overlapping the results for experimental and simulated CDMAM images from chapter 5 (b) - (f).

B.1.3 Variance Map



(a) All doses

(b) 0.84mGy MGD

(c) 1.25mGy MGD

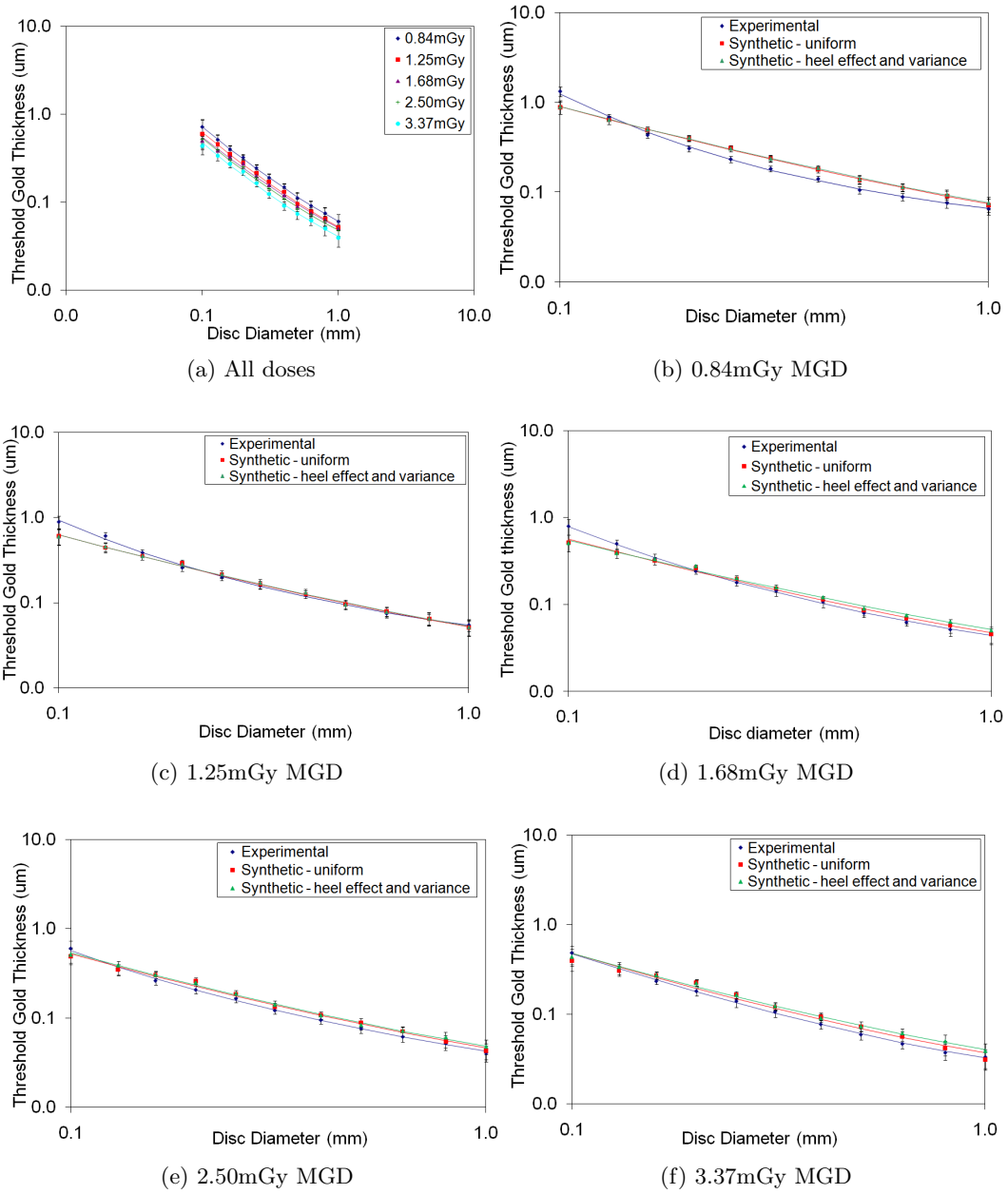
(d) 1.68mGy MGD

(e) 2.50mGy MGD

(f) 3.37mGy MGD

Figure B.3: (a)Contrast detail curves for all simulated doses with the variance map applied for the Hologic Selenia system. Contrast detail curves for the simulated CDMAM images with the variance map applied are presented overlapping the results for experimental and simulated CDMAM images from chapter 5 (b) - (f).

B.1.4 Heel effect and Variance Map



(a) All doses

(b) 0.84mGy MGD

(c) 1.25mGy MGD

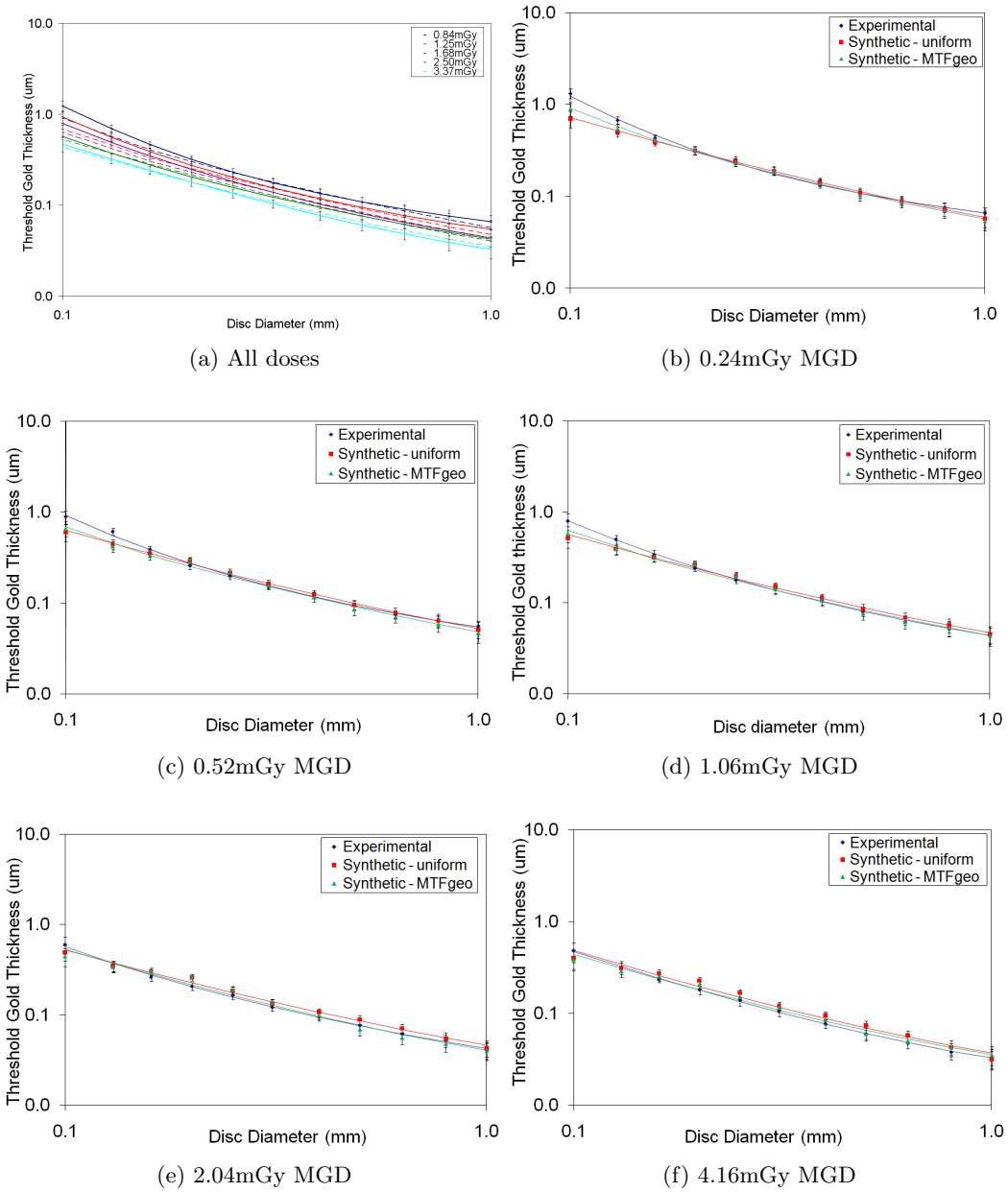
(d) 1.68mGy MGD

(e) 2.50mGy MGD

(f) 3.37mGy MGD

Figure B.4: (a)Contrast detail curves for all simulated doses with the variance map and heel effect mask applied for the Hologic Selenia system. Contrast detail curves for the simulated CDMAM images with the variance map applied are presented overlapping the results for experimental and simulated CDMAM images from chapter 5 (b) - (f).

B.1.5 Geometric blurring



(a) All doses

(b) 0.24mGy MGD

(c) 0.52mGy MGD

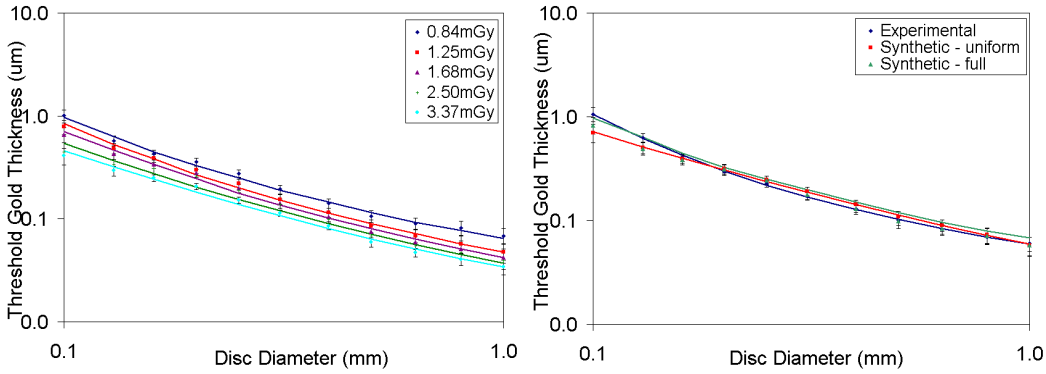
(d) 1.06mGy MGD

(e) 2.04mGy MGD

(f) 4.16mGy MGD

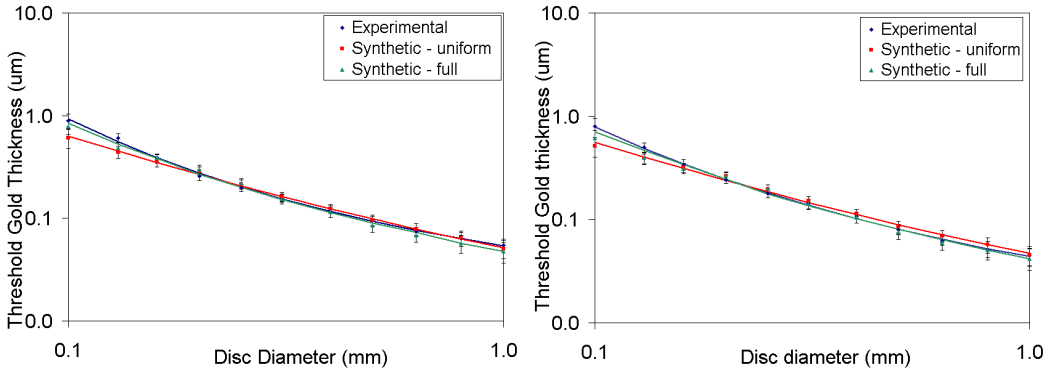
Figure B.5: a)Contrast detail curves for all simulated doses with the geometric MTF applied for the Hologic Selenia system. (b) - (f) Contrast-detail curves for the simulated CDMAM images with the non-uniformity effects applied are presented overlapping the results for experimental and simulated CDMAM images (with uniform model from the chapter 5.

B.1.6 Non-uniformity effects



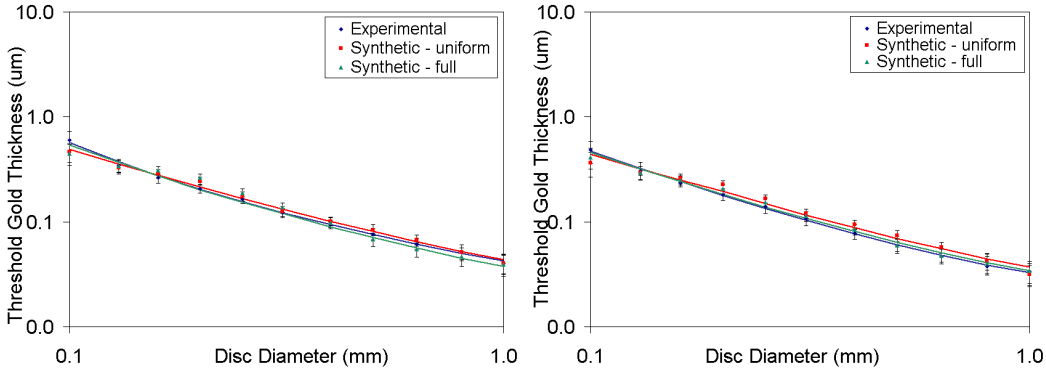
(a) All doses

(b) 0.24mGy MGD



(c) 0.52mGy MGD

(d) 1.06mGy MGD

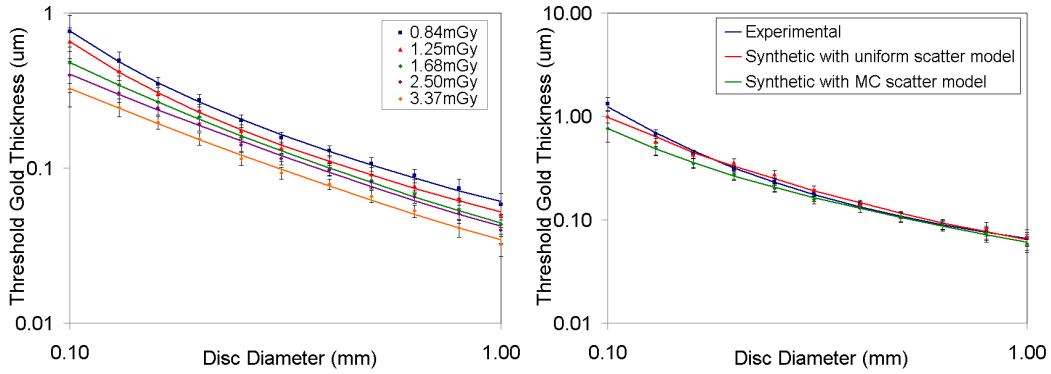


(e) 2.04mGy MGD

(f) 4.16mGy MGD

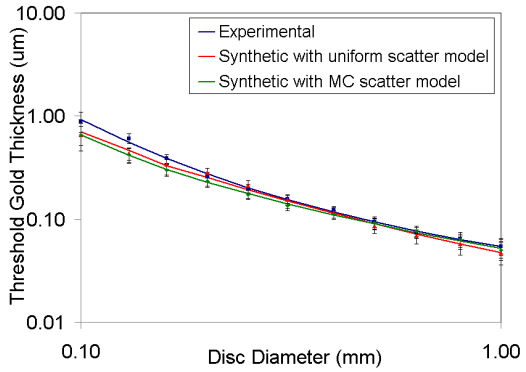
Figure B.6: a)Contrast detail curves for all simulated doses with the heel-effect mask, variance map and geometric MTF applied for the Hologic Selenia system. (b) - (f) Contrast-detail curves for the simulated CDMAM images with the non-uniformity effects applied are presented overlapping the results for experimental and simulated CDMAM images (with uniform model from the chapter 5.

B.1.7 Comparison of scatter models

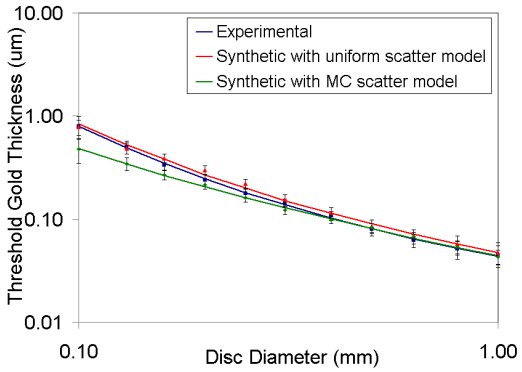


(a) All doses

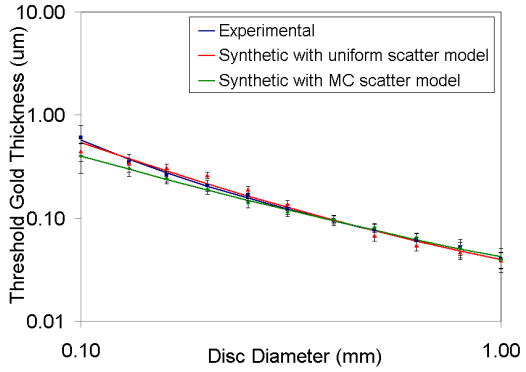
(b) 0.24mGy MGD



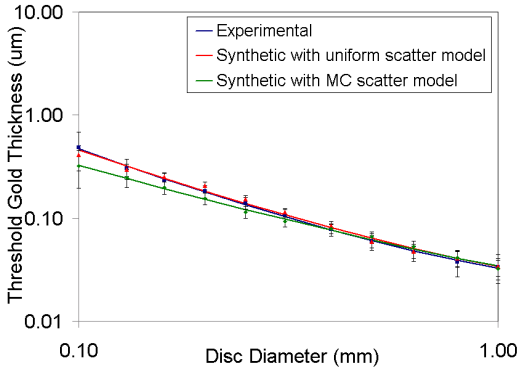
(c) 0.52mGy MGD



(d) 1.06mGy MGD



(e) 2.04mGy MGD

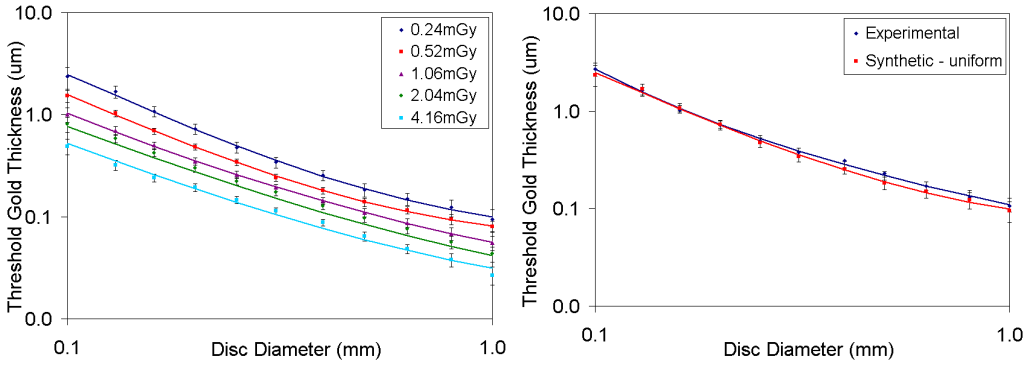


(f) 4.16mGy MGD

Figure B.7: a)Contrast detail curves for all simulated doses with the heel-effect mask, variance map and geometric MTF applied for the Hologic Selenia system. (b) - (f) Contrast-detail curves for the simulated CDMAM images with the non-uniformity effects applied are presented overlapping the results for experimental and simulated CDMAM images (with the all non-uniformity effects shown in Figure B.6).

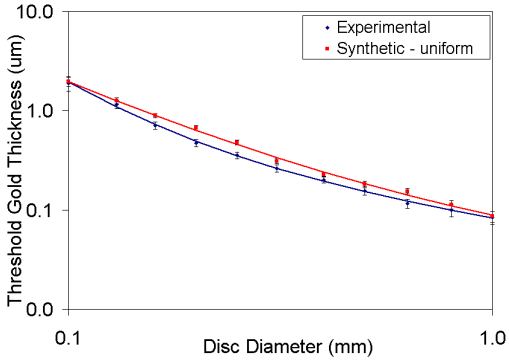
B.2 GE Essential system - Caesium Iodide - amorphous silicon flat panel technology

B.2.1 Uniform images

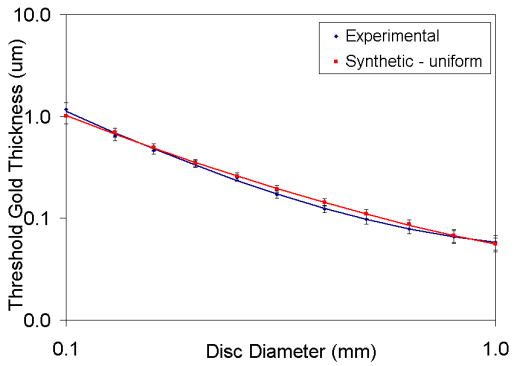


(a) 0.24mGy MGD

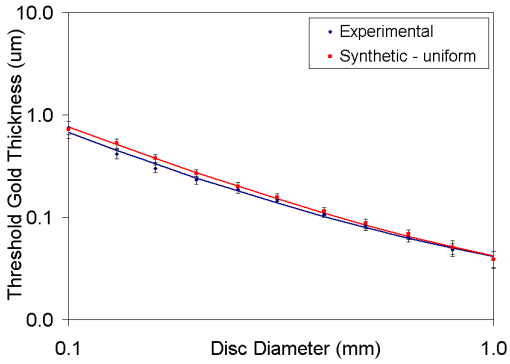
(b) 0.24mGy MGD



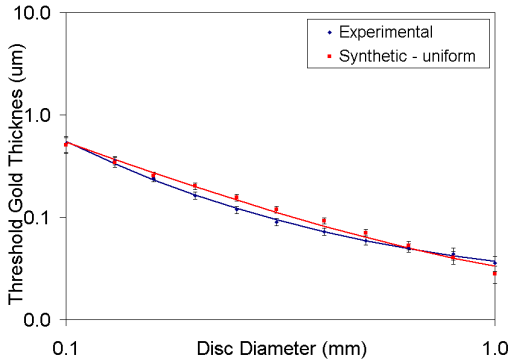
(c) 0.52mGy MGD



(d) 1.06mGy MGD



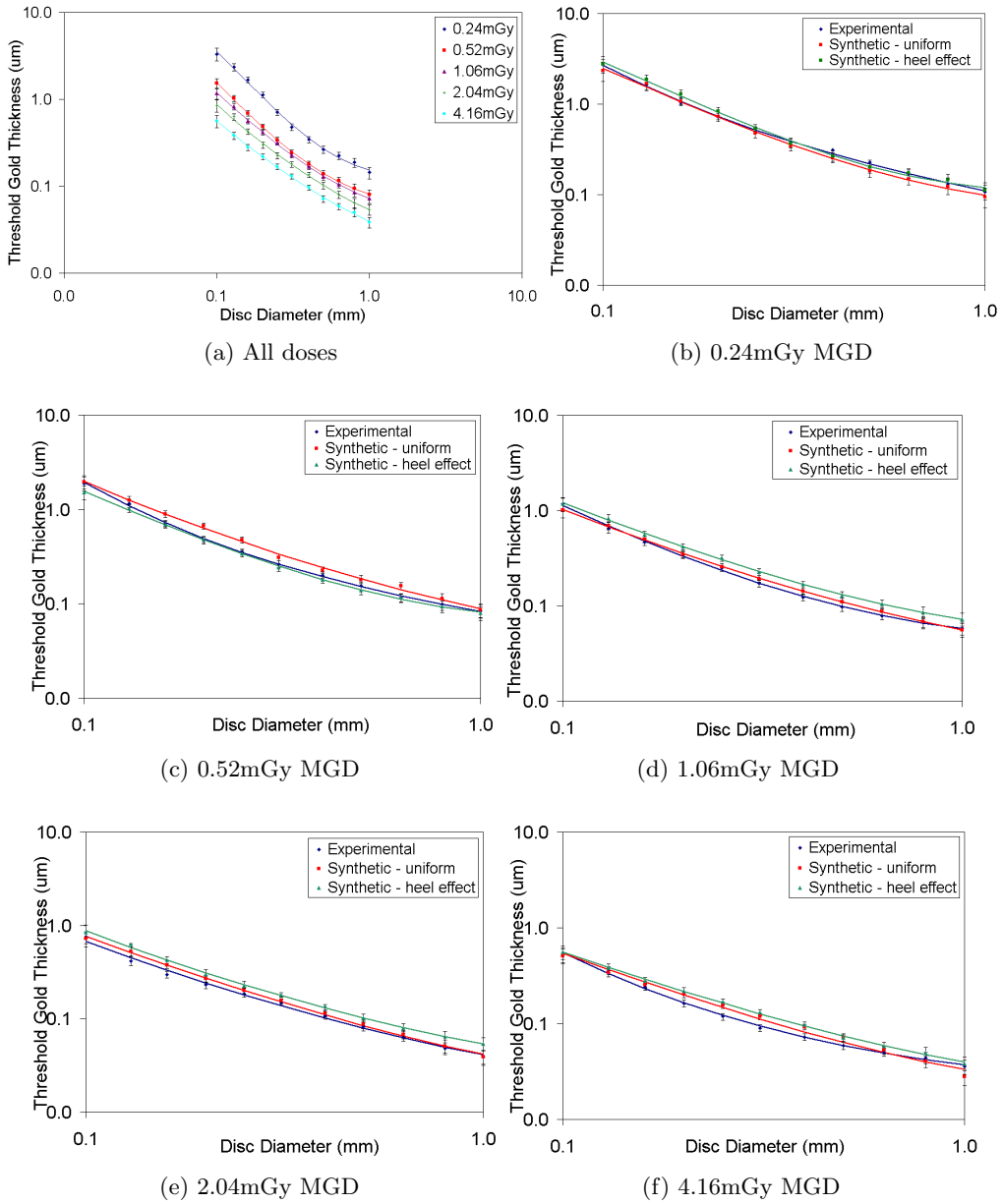
(e) 2.04mGy MGD



(f) 4.16mGy MGD

Figure B.8: Direct comparison of the contrast-detail curves for experimental and synthetic images for the GE Essential system at each dose.

B.2.2 Heel effect mask



(a) All doses

(b) 0.24mGy MGD

(c) 0.52mGy MGD

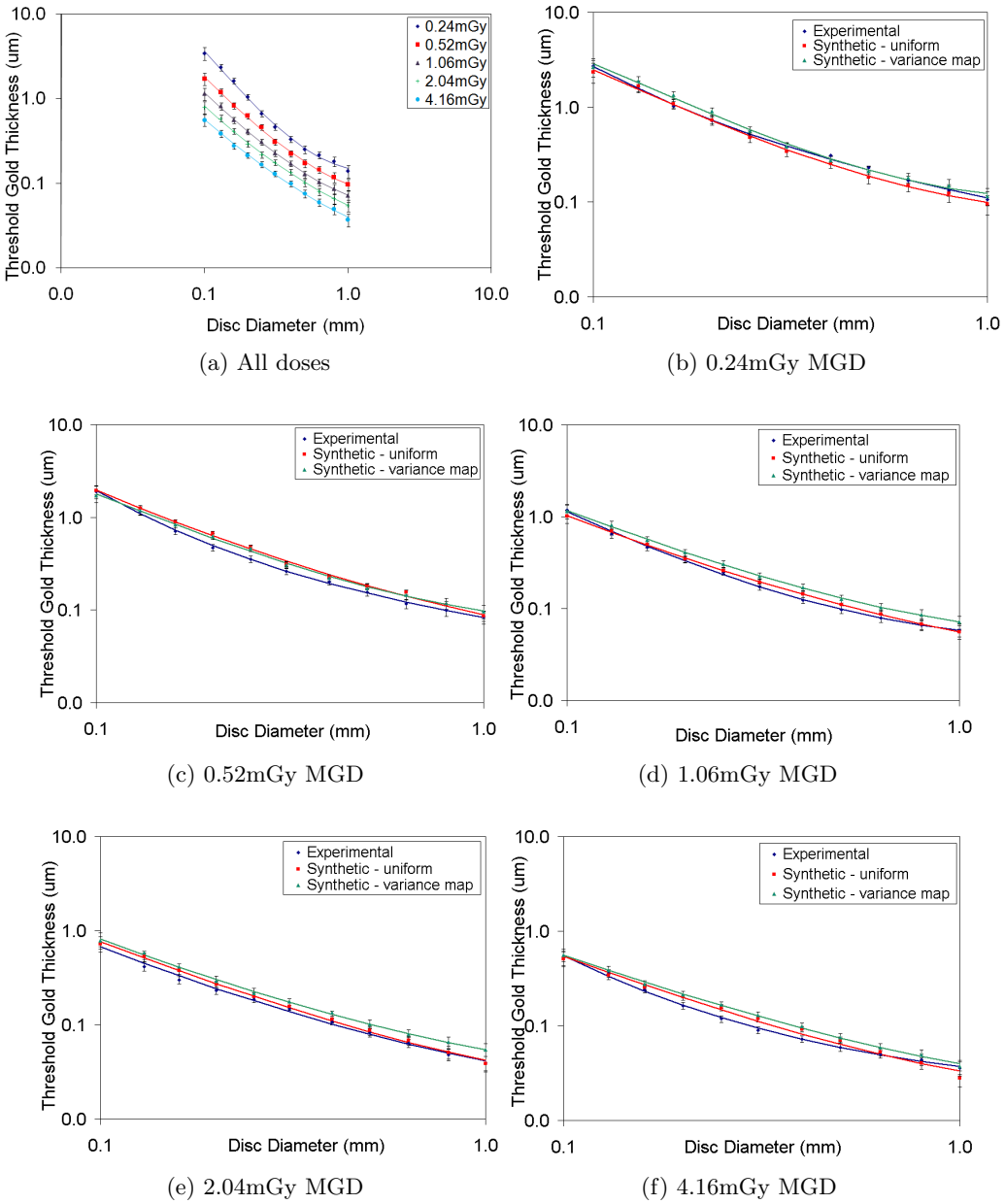
(d) 1.06mGy MGD

(e) 2.04mGy MGD

(f) 4.16mGy MGD

Figure B.9: (a)Contrast detail curves for all simulated doses with the heel effect mask applied for the GE Essential system. Contrast detail curves for the simulated CDMAM images with the heel effect mask applied are presented overlapping the results for experimental and simulated CDMAM images from chapter 5 (b) - (f).

B.2.3 Variance Map



(a) All doses

(b) 0.24mGy MGD

(c) 0.52mGy MGD

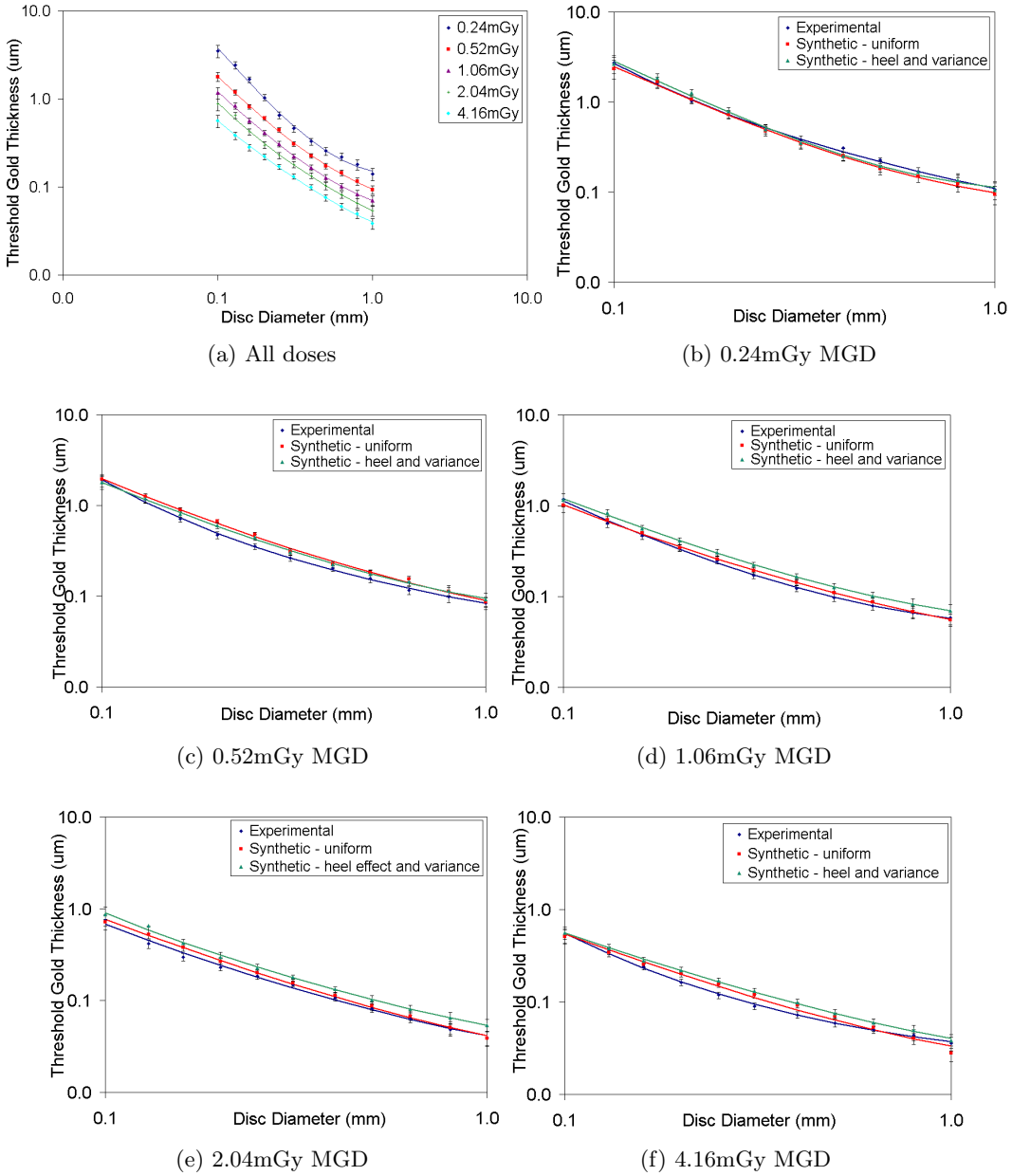
(d) 1.06mGy MGD

(e) 2.04mGy MGD

(f) 4.16mGy MGD

Figure B.10: (a)Contrast detail curves for all simulated doses with the variance map applied for the GE Essential system. Contrast detail curves for the simulated CDMAM images with the heel effect mask applied are presented overlapping the results for experimental and simulated CDMAM images from chapter 5 (b) - (f).

B.2.4 Heel effect and Variance Map



(a) All doses

(b) 0.24mGy MGD

(c) 0.52mGy MGD

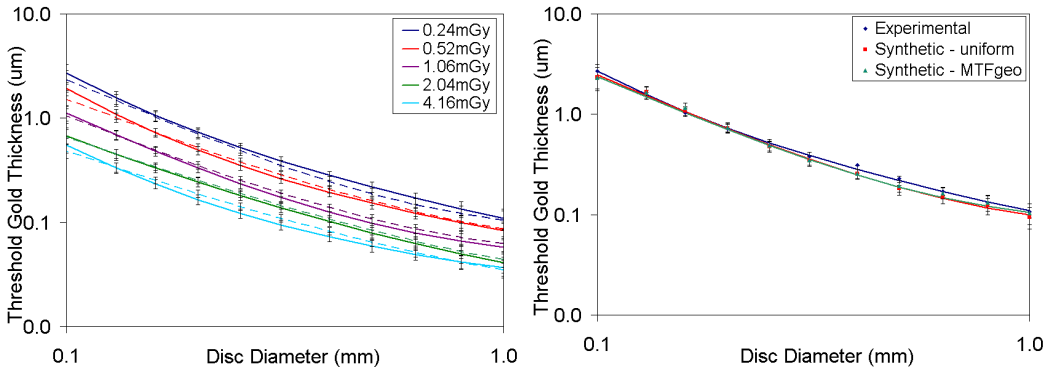
(d) 1.06mGy MGD

(e) 2.04mGy MGD

(f) 4.16mGy MGD

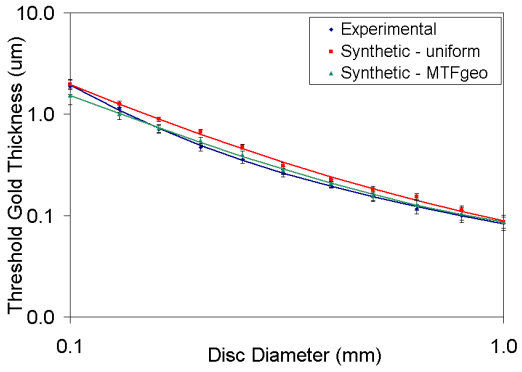
Figure B.11: (a)Contrast detail curves for all simulated doses with the heel effect mask and variance map applied for the GE Essential system. Contrast detail curves for the simulated CDMAM images with the heel effect mask applied are presented overlapping the results for experimental and simulated CDMAM images from chapter 5 (b) - (f).

B.2.5 Geometric blurring

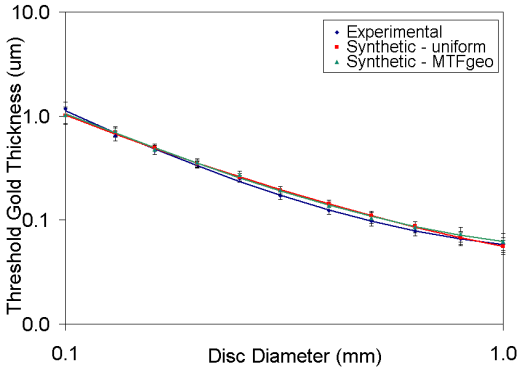


(a) All doses

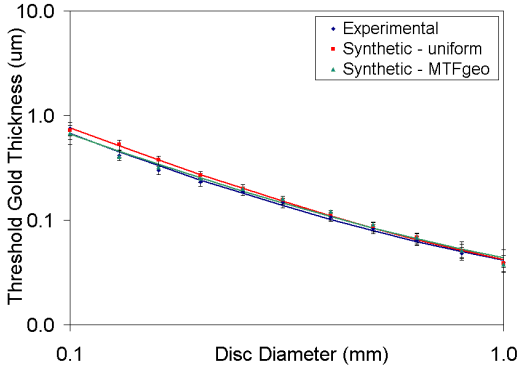
(b) 0.24mGy MGD



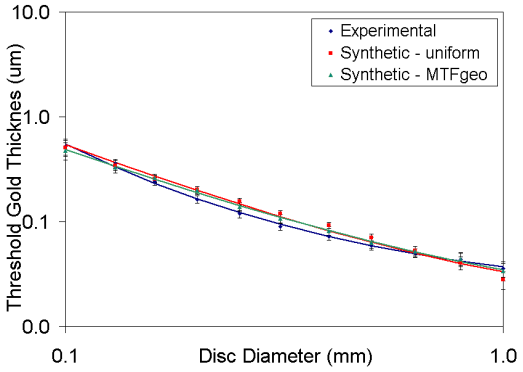
(c) 0.52mGy MGD



(d) 1.06mGy MGD



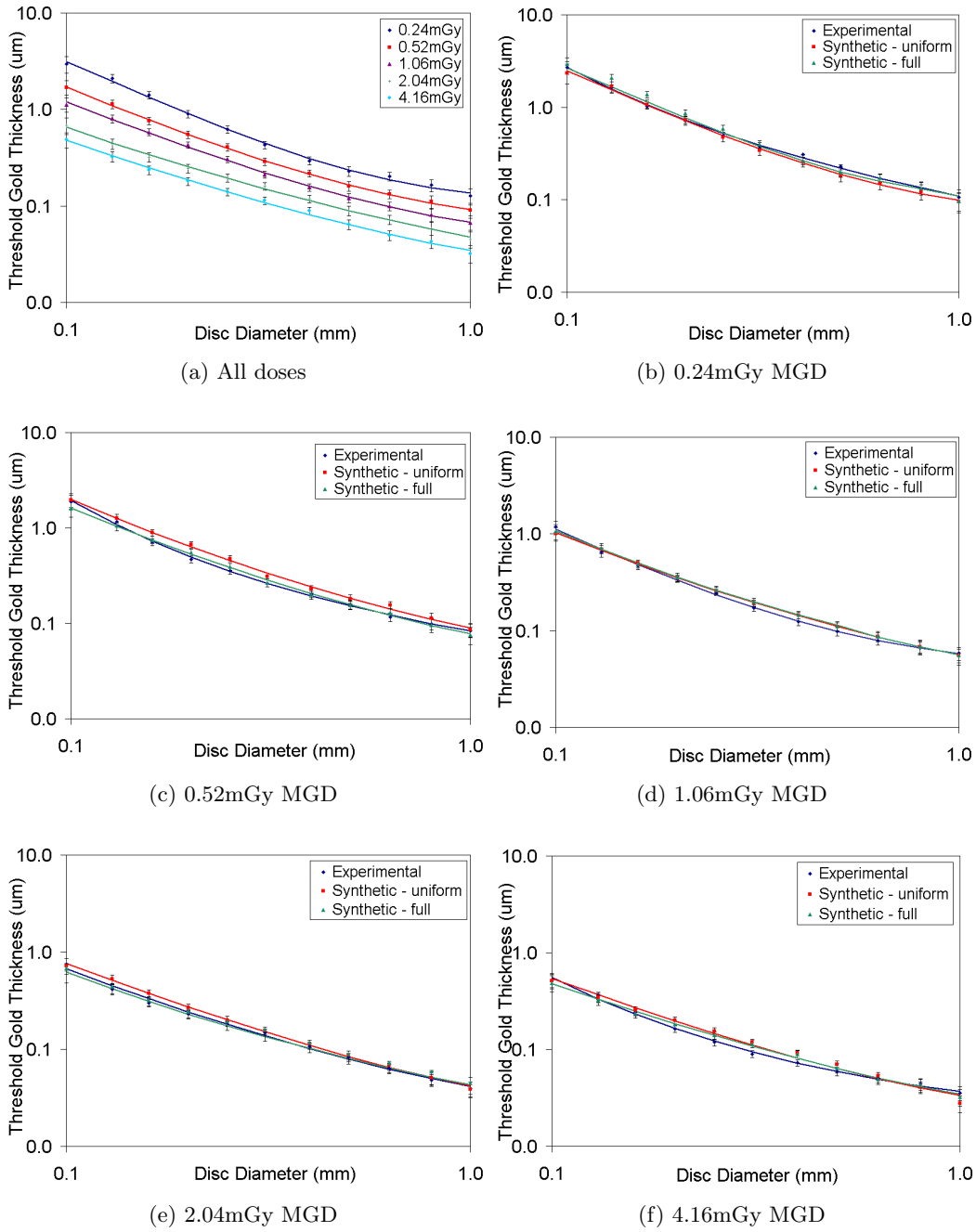
(e) 2.04mGy MGD



(f) 4.16mGy MGD

Figure B.12: (a)Contrast detail curves for all simulated doses with the geometric MTF applied for the GE Essential system. (b) - (f) Contrast-detail curves for the simulated CDMAM images with non-uniformity effects applied are presented overlapping the results for experimental and simulated CDMAM images(with the uniform model from Chapter 5.

B.2.6 Non-uniformity effects



(a) All doses

(b) 0.24mGy MGD

(c) 0.52mGy MGD

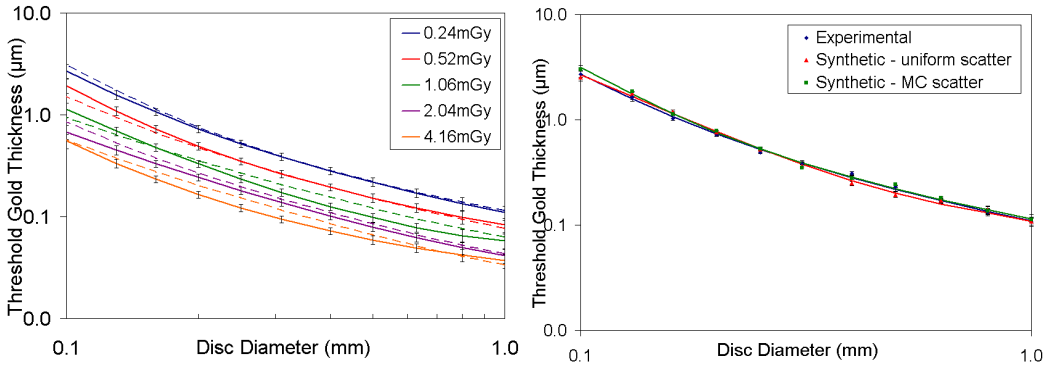
(d) 1.06mGy MGD

(e) 2.04mGy MGD

(f) 4.16mGy MGD

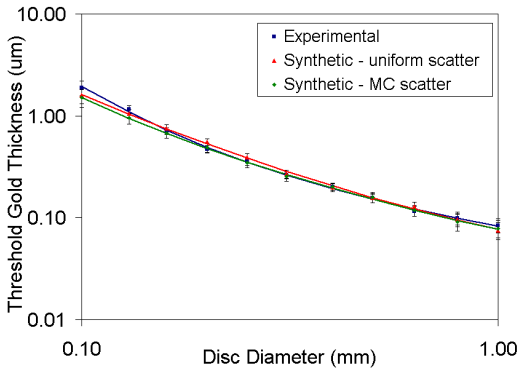
Figure B.13: (a)Contrast detail curves for all simulated doses with the heel effect mask, variance map and geometric MTF applied for the GE Essential system. (b) - (f) Contrast-detail curves for the simulated CDMAM images with non-uniformity effects applied are presented overlapping the results for experimental and simulated CDMAM images(with the uniform model from Chapter 5.

B.2.7 Comparison of scatter models

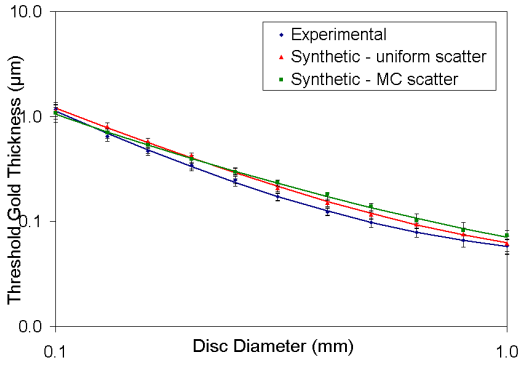


(a) All doses

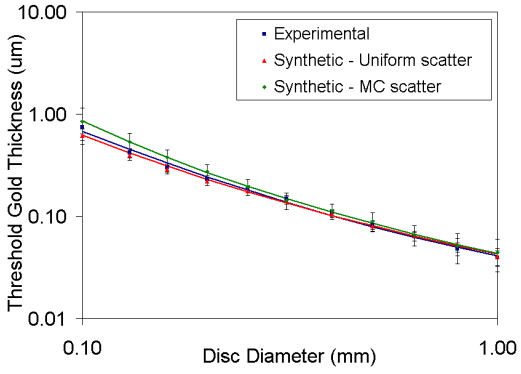
(b) 0.24mGy MGD



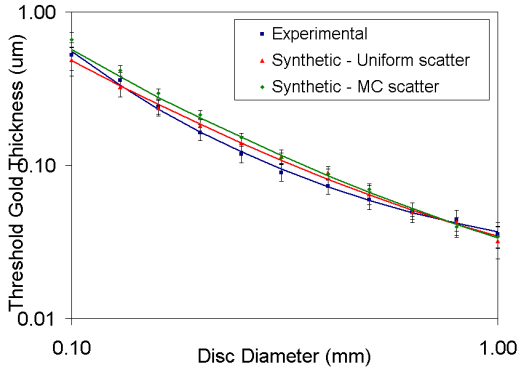
(c) 0.52mGy MGD



(d) 1.06mGy MGD



(e) 2.04mGy MGD

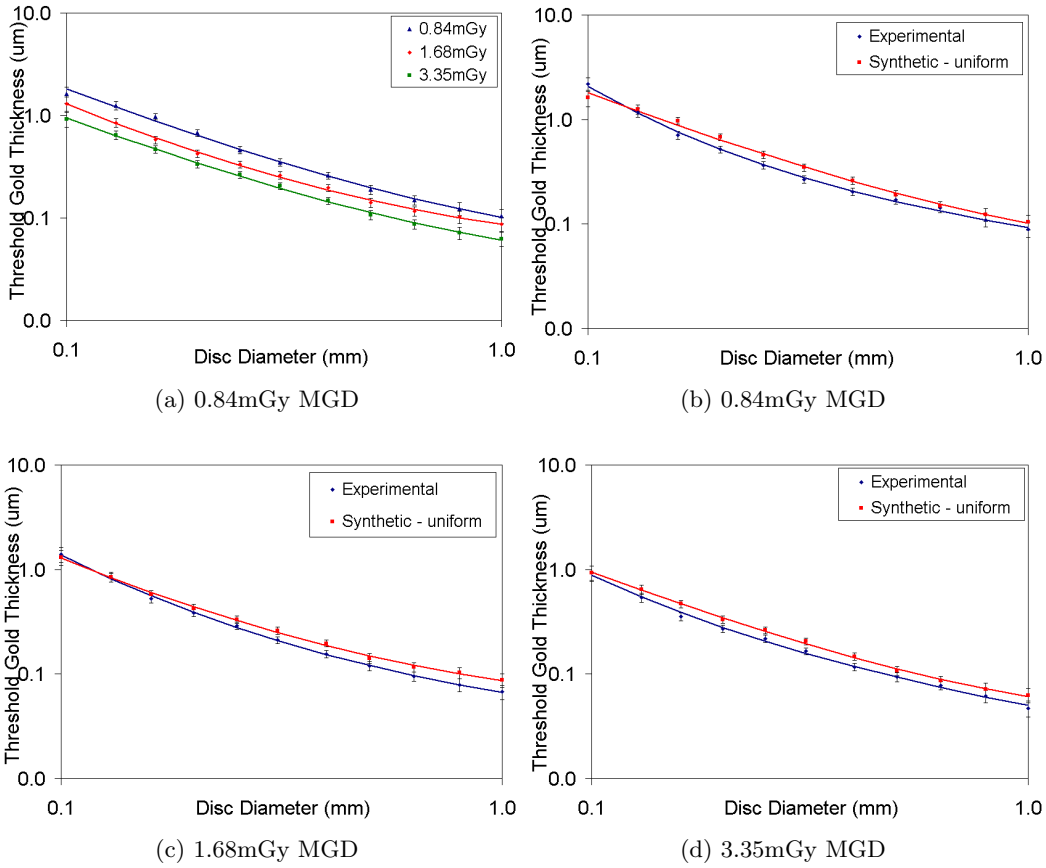


(f) 4.16mGy MGD

Figure B.14: (a)Contrast detail curves for all simulated doses with the heel effect mask, variance map and geometric MTF applied for the GE Essential system. (b) - (f) Contrast-detail curves for the simulated CDMAM images with non-uniformity effects applied are presented overlapping the results for experimental and simulated CDMAM images(with the all non-uniformity effects shown in Figure B.13) .

B.3 Agfa CR system - caesium bromide needle crystal imaging plate technology

B.3.1 Uniform images



(a) 0.84mGy MGD

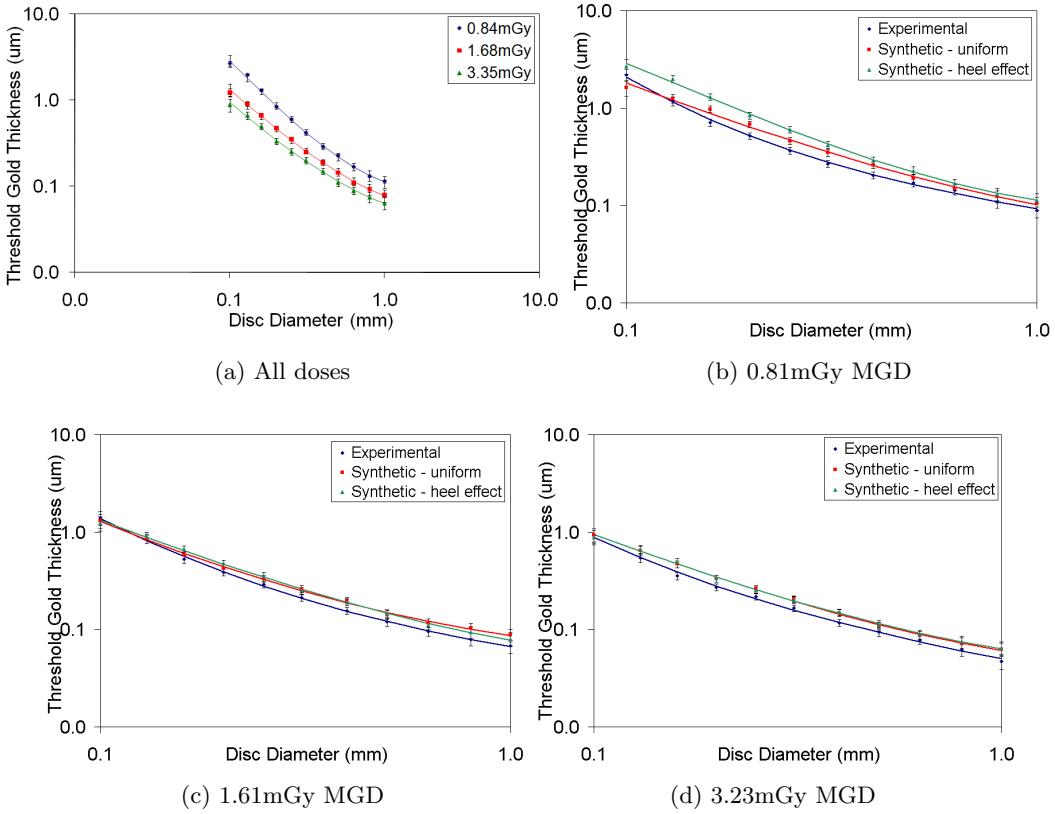
(b) 0.84mGy MGD

(c) 1.68mGy MGD

(d) 3.35mGy MGD

Figure B.15: Direct comparison of the contrast-detail curves for experimental and synthetic images for the Agfa Needle-IP system at each dose.

B.3.2 Heel effect mask



(a) All doses

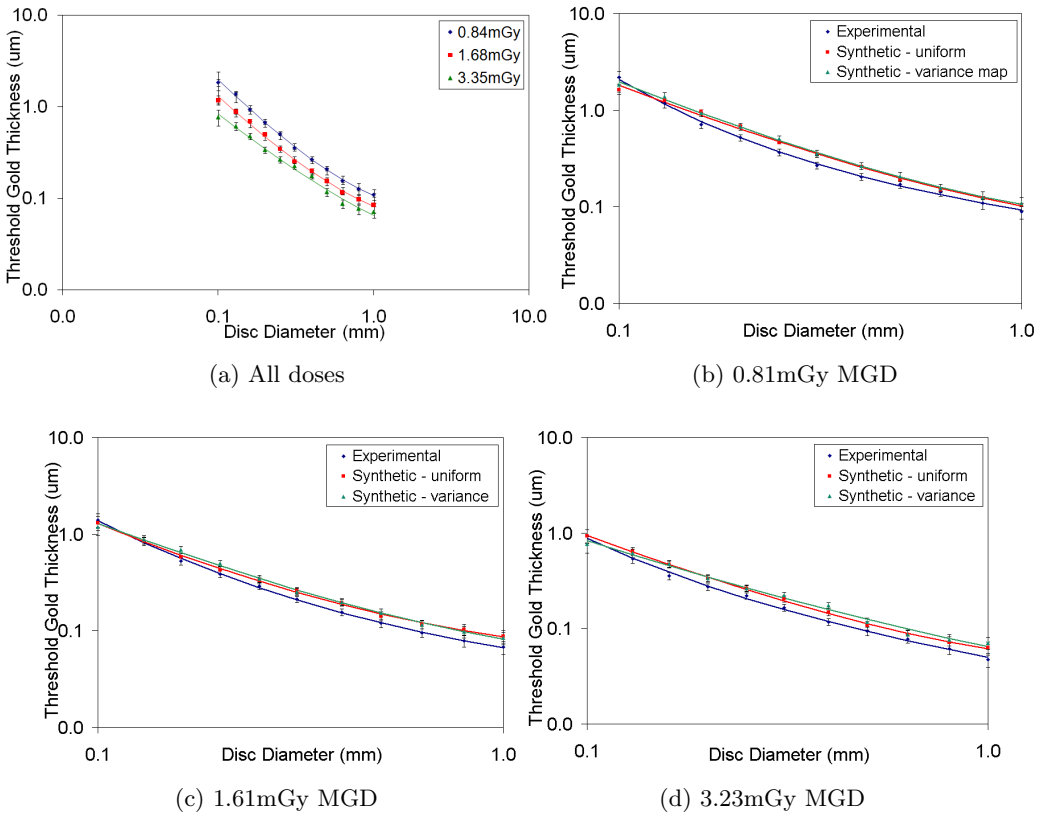
(b) 0.81mGy MGD

(c) 1.61mGy MGD

(d) 3.23mGy MGD

Figure B.16: a)Contrast detail curves for all simulated doses with the heel effect mask applied for the Agfa CR system. Contrast detail curves for the simulated CDMAM images with the heel effect mask applied are presented overlapping the results for experimental and simulated CDMAM images from chapter 5 (b) - (d).

B.3.3 Variance Map



(a) All doses

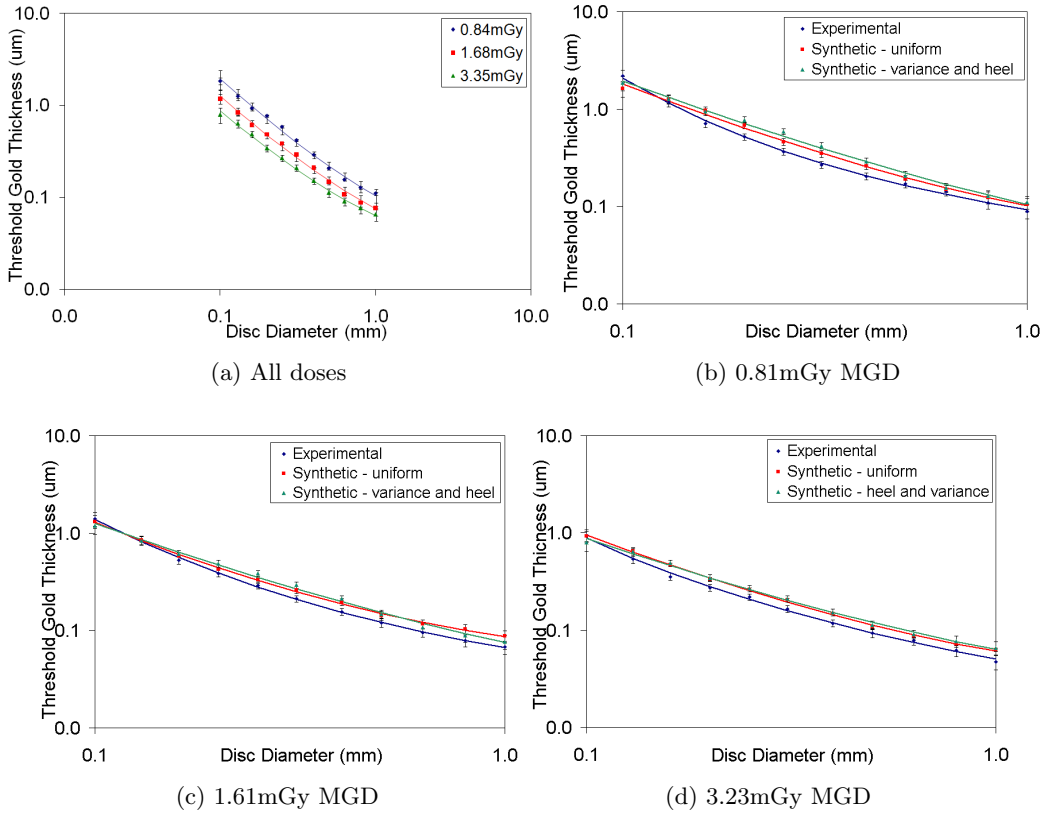
(b) 0.81mGy MGD

(c) 1.61mGy MGD

(d) 3.23mGy MGD

Figure B.17: (a)Contrast detail curves for all simulated doses with the variance map applied for the Agfa CR system. Contrast detail curves for the simulated CDMAM images with the heel effect mask applied are presented overlapping the results for experimental and simulated CDMAM images from chapter 5 (b) - (d).

B.3.4 Heel effect and Variance Map



(a) All doses

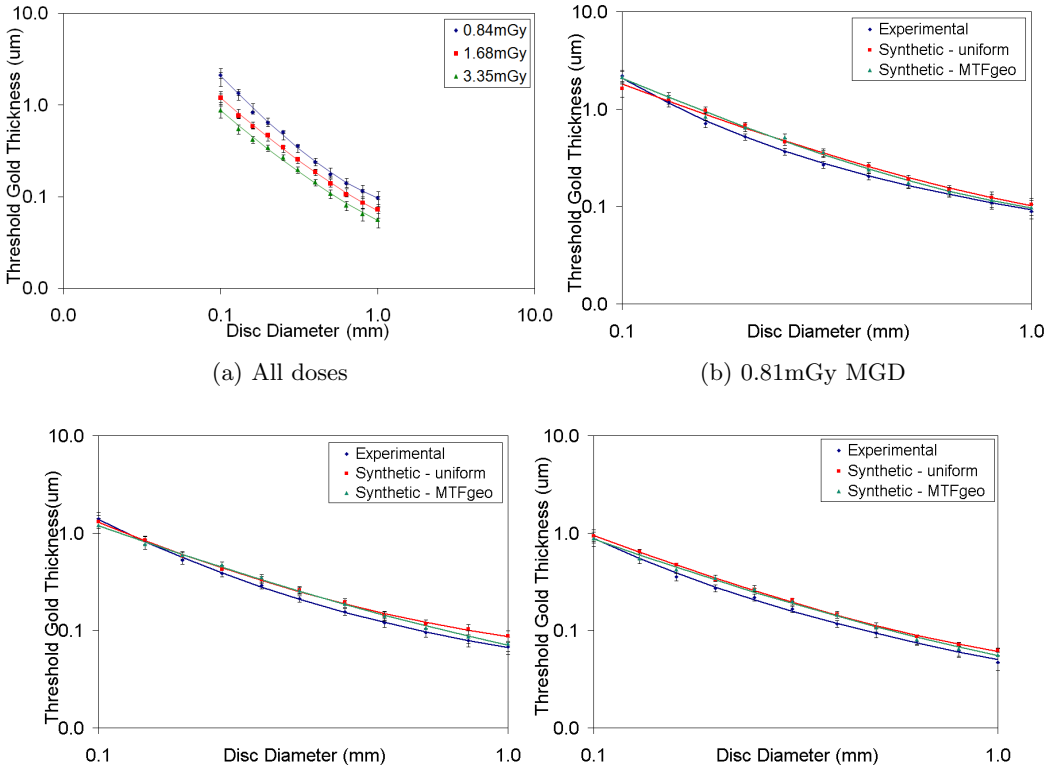
(b) 0.81mGy MGD

(c) 1.61mGy MGD

(d) 3.23mGy MGD

Figure B.18: (a)Contrast detail curves for all simulated doses with the heel effect and variance map applied for the Agfa CR system. Contrast detail curves for the simulated CDMAM images with the heel effect mask and variance map applied are presented overlapping the results for experimental and simulated CDMAM images from chapter 5 (b) - (d).

B.3.5 Geometric Blurring



(a) All doses

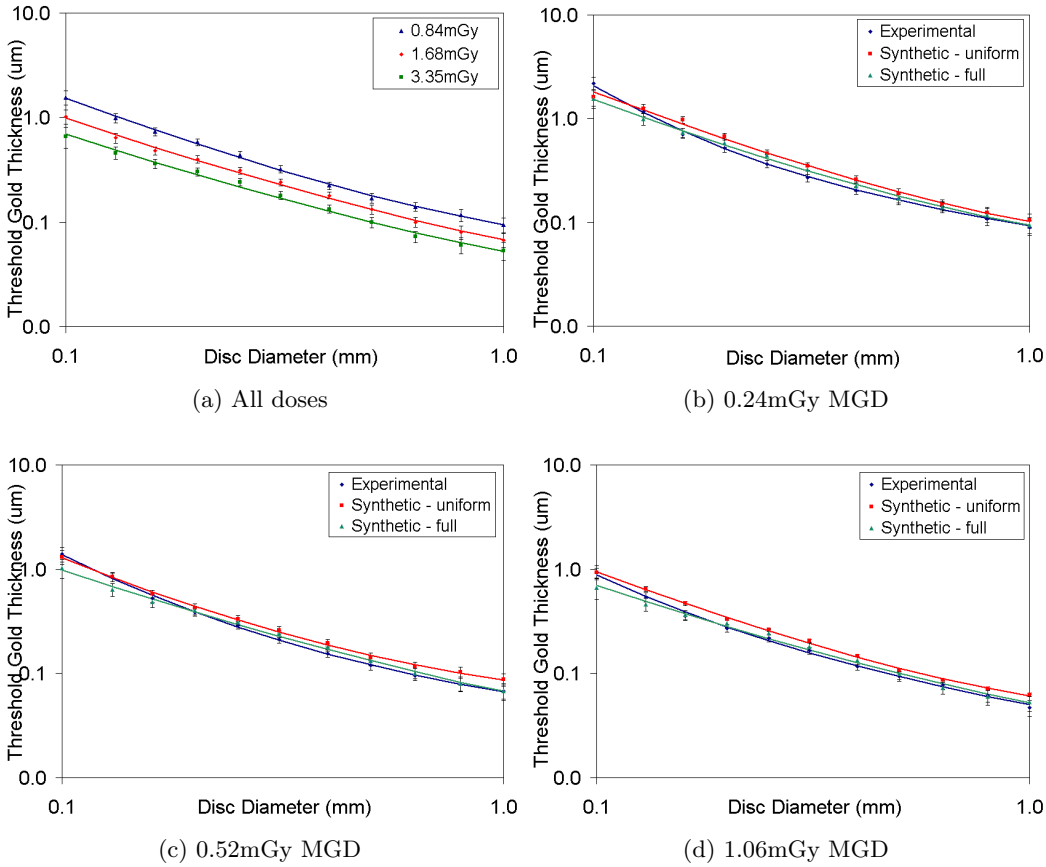
(b) 0.81mGy MGD

(c) 1.61mGy MGD

(d) 3.23mGy MGD

Figure B.19: (a)Contrast detail curves for all simulated doses with the geometric blurring applied for the Agfa CR system. Contrast detail curves for the simulated CDMAM images with the heel effect mask and variance map applied are presented overlapping the results for experimental and simulated CDMAM images from chapter 5 (b) - (d).

B.3.6 Non-uniformity effects



(a) All doses

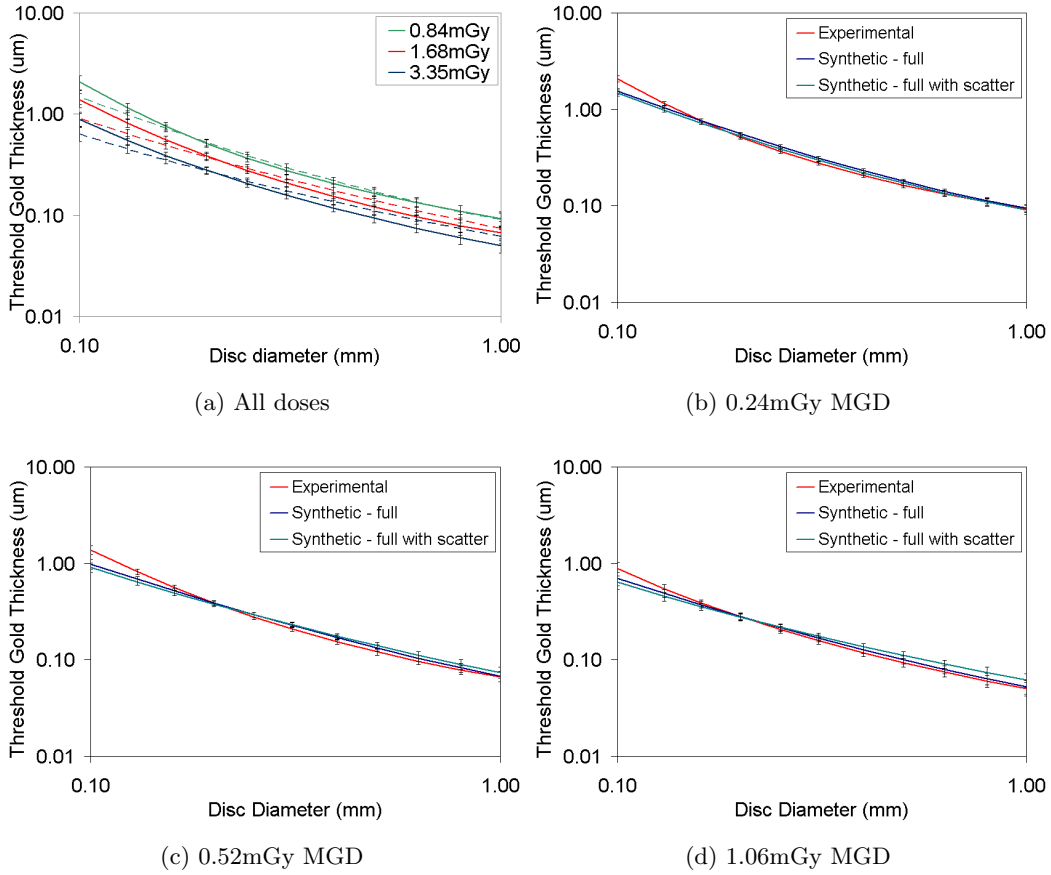
(b) 0.24mGy MGD

(c) 0.52mGy MGD

(d) 1.06mGy MGD

Figure B.20: (a)Contrast-detail curves for all simulated doses with the heel-effect mask, variance map and geometric MTF applied for the Agfa CR system. (b) - (d) Contrast-detail curves for the simulated CDMAM images with the non-uniformity effects applied are presented overlapping the results for experimental and simulated CDMAM phantom images (with the uniform model from the chapter 5 .

B.3.7 Comparison of scatter models



(a) All doses

(b) 0.24mGy MGD

(c) 0.52mGy MGD

(d) 1.06mGy MGD

Figure B.21: (a)Contrast-detail curves for all simulated doses with the heel-effect mask, variance map and geometric MTF and Monte Carlo derived S/P map applied for the Agfa CR system. (b) - (d) Contrast-detail curves for the simulated CDMAM images with the non-uniformity effects applied are presented overlapping the results for experimental and simulated CDMAM phantom images (with the all non-uniformity effects shown in Figure B.20) .

Appendix C

Sensitivity of Disc Contrast calculations

Chapter 6 introduced the use of a sophisticated S/P model which exposed factors missing in the original disc contrast calculations due to primary photons. In this section, the different factors that would affect the calculations are investigated. In the current model of the primary disc contrasts, receptor efficiency is assumed to be 100%. The energy absorption efficiency ε for CsI technology was calculated using the following equation:

$$\varepsilon = (1 - e^{-\mu_{tot}.t}).\frac{\mu_{en}}{\mu_{tot}} \tag{C.1}$$

where μ_{tot} is the total linear attenuation coefficient of the detector (CsI), μ_{en} is the linear energy-absorption coefficient[1] and t is the thickness of the detector. The first component gives the fraction of photons attentuated in the detector. Whereas, the amount of energy absorbed by the detector per attenuated X-ray photon is given by the second component[129]. This calculation has been further verified with Monte Carlo measurements.

The compression paddle had not been included in the original calculations of the primary disc contrasts. Inclusion of this will reduce the contrast as the compression paddle would attenuate the photons slightly.

Finally, the HVL is a measure of the quality of the spectrum. This is individual to each X-ray tube. Matching the X-ray spectra to the HVL of X-ray spectra used in the systems could provide a better estimation of the contrasts. Table C.1 shows the ratio of the disc contrasts calculated before and after each factor is included. The compression paddle has been modeled with a polycarbonate composition and 2.4mm thickness, for each detector. Receptor efficiency has been calculated for a CsI receptor of $200\mu m$ thickness to model the GE Essential as an example of the sensitivity of such factors.

For the Hologic Selenia system used in this study, it would be expected that the receptor effeciency would be higher than the GE essential technology, thus the assumption of 100% efficiency may be valid. As for the Agfa CR technology, it is expected that the

[1] From the NIST database http://www.nist.gov/physlab/data/xraycoef/index.cfm

Disc thickness (μm)	ε	Compression paddle	HVL matching	Combined effects
0.03	1.030	0.992	0.990	1.029
0.16	1.030	0.992	0.990	1.028
0.71	1.029	0.992	0.990	1.027
1.42	1.028	0.993	0.991	1.026
2.00	1.027	0.993	0.991	1.025

Table C.1: Ratios of a selection of disc contrasts for 29kVp Rh/Rh GE Essential system before and after different factors such as the receptor efficiency, ε; compression paddle; HVL matching were modeled. Effects of combining all factors have been shown in the last column.

receptor efficiency is poorer. Therefore the contrast calculations may be affected more by than the GE Essential technology.

This difference of $\pm 2\%$ in the contrast from the original calculations is very small. The overall sensitivity of the contrast as a result of these improved calculations is comparatively weak compared with the other factors in the image simulation framework.

Bibliography

[1] Parkin DM, Bray F, Ferlay J, Pisani P. Global Cancer statistics, 2002. A cancer journal for clinicians. 2005;55:74–108.

[2] Breast Cancer: Incidence continues to rise; 2008. Accessed on June 2009. http://www.statistics.gov.uk/cci/nugget.asp?id=575.

[3] Palpable Breast Lesion As Initial Manifestation Of Disseminated Renal Cell Carcinoma; 2009. Accessed on the March 2010. http://www.ispub.com/journal/the_internet_journal_of_surgery/volume_8_number_2/article/palpable_breast_lesion_as_initial_manifestation_of_disseminated_renal_cell_carcinoma.html.

[4] Johns PC, Yaffe MJ. X-ray characterization of normal and neoplastic breast tissues. Physics of Medicine and Biology. 1987;32:675–695.

[5] Cranley K, Gilmore BJ, Fogarty GWA, Desponds L. Report 78: Catalogue of Diagnostic X-Ray Spectra and Other Data. IPEM;.

[6] DSR (Dual-Side Reading) Technology; accessed 2010. http://www.fujifilm.com/products/medical/technologies/dsr/index.html.

[7] Samei E, Buhr E, Granfors P, Vandenbroucke D, Wang X. Comparison of edge analysis techniques for the determination of hte MTF of digital radiographic systems. Physics of Medicine and Biology. 2005;50:3613–3525.

[8] Rivetti S, Lanconelli N, Campanini R, Bertolini M, Borasi G, Nitrosi A, et al. Comparison of different commercial FFDM units by means of physical characterization and contrast-detail analysis. Medical Physics. 2006;33(11):4198–4209.

[9] Young KC, Oduko JM, Asad M. Technical Evaluation of Agfa DX-M Mammography CR Reader with HM5.0 Needle Image Plate; 2009.

[10] Carton AK, Vandenbroucke D, Struye L, Maidment ADA, Kao YH, Albert M, et al. Validation of MTF measurement for digital mammography quality control. Medical Physics. 2005;32(6):1684–1695.

[11] Williams MB, Mangiafico PA, Simoni PU. Noise Power Spectra of Images of Digital Mammography Detectors. Medical Physics. 1999;26(7):1279–1293.

[12] Marshall NW. Early experience in the used of quantitative image quality measurements for the quality assurance of full field digital mammography x-ray systems. Physics in Medicine and Biology. 2007;52:5545–5568.

[13] Yip M, Chukwu W, Kottis E, Lewis E, Young KC, Oduko J, et al. Automated scoring method for the CDMAM phantom. In: Proceedings of the SPIE: Medical Imaging; 2009. p. 409–416.

[14] Young KC, Oduko JM, Gundogdu O, Alsager A. Technical Evaluation of the GE Essential Full Field Digital Mammography System; 2009.

[15] Young KC, Oduko JM, Gundogdu O, Alsager A. Evaluation and clinical assessment of the Hologic Selenia Full Field Digital Mammography System; 2009.

[16] Young KC, Cook JJH, Oduko JM. Automated and human determination of threshold contrast for digital mammography systems. In: S M Astley ea, editor. International Workshop of Digital Mammography, 2006. vol. 4046. Springer; 2006. p. 266–272.

[17] Young KC, Cook JH, Oduko JM, Bosmans H. Comparison of software and human observers in reading images of the CDMAM test object to assess digital mammography systems. vol. 6142. SPIE; 2006. p. 614206. Available from: `http://link.aip.org/link/?PSI/6142/614206/1`.

[18] Pawluczyk O, Yaffe MJ. Field nonuniformity correction for quantitative analysis of digitized mammograms. Medical Physics. 2001;28(4):438–444.

[19] do Nascimento MZ, Frre AF, Germano F. An Automatic Correction Method for the Heel Effect in Digitized Mammography Images. Journal of Digital Imaging. 2008;21(2):177–187.

[20] Behiels G, Maes F, Vandermeulen D, Suetens P. Retrospective correction of the heel effect in hand radiographs. Medical Image Analysis. 2002;6(3):183–190.

[21] Lynch PJ, Jaffe CC. Breast anatomy; 2007. `http://patricklynch.net/portfolios/medical-illustration/content/breast_anatomy_normal_Copyright_Lynch_2007_large.html`.

[22] Faridah Y. Digital versus screen film mammography: a clinical comparison. Biomedical Imaging Intervention Journal. 2008;4(4):e31.

[23] Dobbins JT. Intercomparison of methods for image quality characterization. II. Noise power spectrum. Medical Physics. 2006;33(5):1466–1475.

[24] van Engen R, Young K, Bosmans H, Thijssen M. The European protocol for the quality control of the physical and technical aspects of mammography screening; 2005.

[25] Ferlay J BFFDMC Shin HR, DM P. GLOBOCAN 2008, Cancer Incidence and Mortality Worldwide: IARC CancerBase No. 10 . Lyon, France: International Agency for Research on Cancer; 2008. Accessed on January 2010. `http://globocan.iarc.fr`.

[26] Forrest P. Breast cancer screening : report to the Health Ministers of England, Wales, Scotland and Northern Ireland / by a working group chaired by Sir Patrick Forrest. London : H.M.S.O.; 1986.

[27] Woodman CB, Threlfall AG, Boggis CR, Prior P. Is the three year breast screening interval too long? Occurence of interval cancers in NHS Breast Screening Programme's north western region. British Medical Journal. 1995;310:224–226.

[28] on Breast Cancer Screening AC. Screening for Breast Cancer in England: Past and Future; 2006.

[29] Oduko JM, Young KC, Burch A. A survey of patient doses from digital mammography systems in the UK in 2007 to 2009. In: et al JM, editor. International Workshop on Digital Mammography LNCS. Heidelberg: Springer; 2010. .

[30] Pisano ED, Gatsonis C, Hendrick E, Yaffe M, Baurn JK, Acharrya S, et al. Diagnostic Performance of Digital versus Film Mammography for Breast Cancer Screening. The New England Journal of Medicine. 2005;353(17):1773–1783.

[31] Duffy SW, Tabar L, Olsen AH, Vitak B, Allgood PC, Chen THH, et al. Absolute numbers of lives saved and overdiagnosis in breast cancer screening, from a randomized trial and from the Breast Screening Programme in England. Journal of Medical Screening. 2010;17:25–30.

[32] Samei E, Saunders RS, Baker JA, Delong DM. Digital Mammography: Effects of Reduced Radiation Dose on Diagnostic Performance. Radiology. 2007;243(2):396–404.

[33] Ruschin M, Timberg P, Båth M, Hemdal B, Svahn T, Saunders RS, et al. Dose dependence of mass and microcalcification detection in digital mammography: Free response human observer studies. Medical Physics. 2007;34(2):400–407.

[34] Saunders RS, Baker JA, Delong DM, Johnson JP, Samei E. Does image quality matter? Impact of resolution and noise on mammographic task performance. Medical Physics. 2007;34(10):3971–3981.

[35] Bliznakova K, Bliznakov Z, Bravou V, Kolitsi Z, Pallikarakis N. A three-dimensional breast software phantom for mammography simulation. Physics in Medicine and Biology. 2003;48(22):3699–3719. Available from: `http://stacks.iop.org/0031-9155/48/3699`.

[36] Bakic PR, Albert M, Brzakovic D, Maidment ADA. Mammogram synthesis using a 3D simulation. II. Evaluation of synthetic mammogram texture. Medical Physics. 2002;29(9):2140–2151. Available from: `http://link.aip.org/link/?MPH/29/2140/1`.

[37] Tischenko O, Hoeschen C, Dance DR, Hunt RA, Maidment ADA, Bakic PR. Evaluation of a novel method of noise reduction using computer-simulated mammograms. Radiation Protection Dosimetry. 2005;114(1-3):81–84.

[38] Visser R, Karssemeijer N. Manual CDCOM version 1.5: software for automated readout of CDMAM 3.4 images; 2007.

[39] Yip M, Lewis E, Young KC, Wells K. Validation of a digital mammography image simulation chain with automated scoring of CDMAM images . In: Proceedings of the International Workshop on Digital Mammography. Springer; 2008. p. 409–416.

[40] Yip M, Zanca F, Mackenzie A, Workman A, Young KC, Dance DR, et al. Validation of a simulated dose reduction methodology using digital mammography CDMAM images and mastectomy images. In: Proceedings of the International Workshop on Digital Mammography, To be published;. .

[41] Hermann G, Janus C, Schwartz IS, Papatestas A, Hermann DG, Rabinowitz JG. Occult Malignant breast lesions in 114 patients:relationship to age and the presence of microcalcifications. Radiology. 1988;169:321–324.

[42] Barnes S. Contrast and Scatter in X-ray Imaging. Radiographics. 1991;11:307–323.

[43] Yaffe MJ, Mainprize JG. Detectors for Digital Mammography. Technology in Cancer Research and Treatment. 2004;3(4):309–324.

[44] Chowdhury L, Tousignant O, DeCrescenzo G, Guathier P, Leboeuf J, Rowlands JA. Effect of ghosting on the modulation transfer function of amorphous selenium based flat panel detectors. In: Flynn MJ, Hsieh J, editors. SPIE: Medical Imaging: Physics of Medical Imaging. vol. 4046. Springer; 2006. p. 61421S.

[45] Lundqvist M, Danielsson M, Cederström B, Chmill V, Chuntonov A, Åslund M. Measurements on a full-field digital mammography system with a photon counting crystalline silicon detector. vol. 5030. SPIE. SPIE; 2003. Medical Imaging 2003: Physics of Medical Imaging.

[46] Monnin P, Gutierrez D, Bulling S, Guntern D, Verdun FR. A comparison of the performance of digital mammography systems. Medical Physics. 2007;34.

[47] Bosmans H, Carton AK, Rogge F, Zanca F, Jacobs J, Van Ongeval C, et al. Image quality measurements and metrics in full field digital mammography: an overview. Radiation Protection Dosimetry. 2005;117(1-3):120–130.

[48] Commission IE. Medical electrical equipment - Characteristics of digital X-ray imaging devices - Part 1: Determination of the detective quantum efficiency. Geneva, Switzerland; 2003.

[49] Determination of the detective quantum efficiency Detectors used in mammography.;.

[50] Marshall NW. Retrospective analysis of detector fault for a full field digital mammography system. Phys Med Biol. 2006;51:5655–5673.

[51] Evans DS, Workman A, Payne M. A comparison of the imaging properties of CCD-based devices used for small field digital mammography. Physics in Medicine Biology. 2002;47:117–135.

[52] Ravaglia V, Bouwman R, Young K, van Engen R, Lazzari B. Noise analysis of full field digital mammography systems. In: Samei E, Hsieh J, editors. SPIE Medical Imaging 2009: Physics of Medical Imaging. vol. 7258; 2009. p. 72581B.

[53] Marshall NW. A comparison between objective and subjective image quality measurements for a full field digital mammography system. Phys Med Biol. 2006;51:2441–2463.

[54] Samei E, Ranger NT, Dobbins JT, Chen Y. Intercomparison of methods for image quality characterization. I. Modulation Transfer Function. Medics Physics. 2006;33(5):1454–1465.

[55] Buhr E, Günther-Kohfahl S, Neitzel U. Accuracy of a Simple Method for Deriving the Presampled Modulation Transfer Function of a Digital Radiographic System from an Edge Image. Medical Physics. 2003;30(9):2323–2331.

[56] Rogge F, Bosmans H, Willems P, Marchal G. The use of MTF calculation in global and local resolution assessmenet in digital mammography. In: Medical Imaging 2003: Physics of Medical Imaging;. .

[57] Fujita H, Tsai DY, Itoh T, Doi K, Morishita J, Ueda K, et al. A Simple Method for Determining the Modulation Transfer Function in Digital Radiography. IEEE Transactions on Medical Imaging. 1992 March;11(1):34–39.

[58] Dobbins JT. Image Quality Metrics for Digital Systems. In: Beutel J, Kundel HL, Van Metter RL, editors. Handbook of medical imaging: physics and psychophysics;. .

[59] Granfors PR, Aufrichtig R. Performance of a 41 x 41 cm^2 amorphous silicon flat panel x-ray detector for radiographic imaging applications. Medical Physics. 2000;27:1324–1331.

[60] Samei E, Flynn M. Experimental comparison of detector performance for direct and indirect digital radiography systems. Medical Physics. 2003;30(4):608–622.

[61] Saunders RS, Samei E. A method for modifying the image quality parameters of digital radiographic images. Medical Physics. 2003;30(11):3006–3017.

[62] Reichenbach SE, Park SK, Narayanswamy R. Characterizing digital image acquisition devices. Opt Eng. 1991;30:170–177.

[63] Dobbins JT. Effects of undersampling on the proper interpretation of modulation transfer function, noise power spectra, and noise equivalent quanta of digital imaging systems. Am Assoc Phys Med. 1995;22(2):171–181.

[64] Carton AK. Development and application of methods for the assessment of image quality and detector performance in digital mammography. Katholieke Universiteit Leuven; 2004.

[65] Monnin P, Gutierrez D, Bulling S, Lepori D, Valley JF, Verdun FR. A comparison of the performance of modern screen-film and digital mammography systems. Physics in Medicine Biology. 2005;50:2617–2631.

[66] Jiang H, Chen WR, Liu H. Techniques to improve the accuracy and to reduce the variance in noise power spectrum measurement. IEEE Transactions on Biomedical Engineering. 2002;49(11):1270–1278.

[67] Giger ML, Doi K, Metz CE. Investigation of basic imaging properties in digital radiography. 2. Noise Wiener Spectrum. Medical Physics. 1984;11(6):797–805.

[68] Mackenzie A, Honey IA. Characterization of noise sources for two generations of computed radiography systems using powder and crystalline photostimulable phosphors. Medical Physics. 2007;34.

[69] Young KC, Oduko JM, Gundogdu O, Alsagar AA. Comparing the performance of digital mammography systems. In: E A Krupinski ea, editor. International Workshop of Digital Mammography, 2008. vol. 5116. Springer; 2008. p. 732–739.

[70] Dance DR, Skinner CL, Young KC, Beckett JR, Kotre CJ. Additional factors for the estimation of mean glandular breast dose using the UK mammography dosimetry protocol. Physics in Medicine and Biology. 2000;45:3225.

[71] Karssemeijer N, Thijssen MAO. Determination of contrast-detail curves of mammography systems by automated analysis. In: Doi GMLNRM K, Scmidt RA, editors. International Workshop of Digital Mammography. Elsevier; 1996. p. 155–160.

[72] Prieto G, Chevalier M, Guibelalde E. A CDMAM image phantom software improvement for human observer assessment. In: Proceedings of the International Workshop on Digital Mammography, LCNS 5116;. .

[73] Young KC, Oduko JM, Bosmans H. Optimal beam quality selection in digital mammography. In: 7th International Workshop on Digital Mammography; 2004. .

[74] Huda W, Sajewicz AM, Ogden KM, Dance DR. Experimental investigation of the dose and image quality characteristics of a digital mammography imaging system. Medical Physics. 2003;30(3):442–448. Available from: `http://link.aip.org/link/?MPH/30/442/1`.

[75] Signal detection theory and psychophysics. New York: Wiley; 1966.

[76] Aufrichtig R. Comparison of low contrast detectability between a digital amorphous silicon and a screen-film based imaging system for thoracic radiography. Medical Physics. 1999;26(7):1349–1358.

[77] Kelly DH. Motion and Vision II stabilized spatio-temporal threshold surface. J Opt Soc Am. 1979;69:1340–1349.

[78] Young KC, Alsager AA, Dance DR, Oduko JM, Gundogdu O, Spyrou NM. Predicting contrast detail performance from objective measurements in digital mammography. In: Samei E, Hsieh J, editors. SPIE Medical Imaging: Physics of Medical Imaging. vol. 7258. SPIE; 2009. p. 72581C.

[79] Metz CE. ROC analysis in medical imaging: a tutorial review of the literature. Radiological Physics and Technology. 2008;1(1):2–12.

[80] Swaving M, Van Houwelingen H, Ottes FP, Steerneman T. Statistical comparison of ROC curves from multiple readers. Medical Decision Making. 1996;16:143–52.

[81] Chakraborty DP. Maximum likelihood analysis of free-response receiver operating characteristic (FROC) data. Medical Physics. 1989;16(4):561–568. Available from: `http://link.aip.org/link/?MPH/16/561/1`.

[82] Zanca F, Chakraborty DP, Van Ongeval C, Jacobs J, Claus F, Marchal G, et al. An improved method for simulating microcalcifications in digital mammograms. Medical Physics. 2008;35(9):4012–4018.

[83] Zheng B, Chakraborty DP, Rockette HE, Maitz GS, Gur D. A comparison of two data analyses from two observer performance studies using Jackknife ROC and JAFROC. Medical Physics. 2005;32(4):1031–1034. Available from: `http://link.aip.org/link/?MPH/32/1031/1`.

[84] Timberg P, Ruschin M, Bath M, Hemdal B, Andersson I, Mattsson S, et al. Potential for lower absorbed dose in digital mammography: A JAFROC experiment usng clinical hybrid images with simulated dose reduction. In: Proceedings of SPIE Medical Imaging 2006: Image Perception, Observer Performance, and Technology Assessment;. .

[85] Gonzalez RC, Woods RE. Digital Image Processing. Pearson Prentice Hall; 2008.

[86] Grosjean B, Muller S, Souchay H, Rico R, Bouchevreau X. Automated scoring for CDMAM phantom from simulated images. In: IWDM 2004, LNCS 4046. LNCS. Springer-Verlag Berlin Heidelberg; 2004. .

[87] Gong X, Glick SJ, Liu B, Vedula AA, Thacker S. A computer simulation study comparing lesion detection accuracy with digital mammography, breast tomosynthesis, and cone-beam CT breast imaging. Medical Physics. 2006 april;33(4):1041–1052.

[88] Workman A. Simulation of Digital Mammography. vol. 5745. Bellingham, WA: SPIE; 2005. p. 933–942.

[89] Grahn A, Hemdal B, Andersson I, Ruschin M, Thilander-Klang A, Börjesson S, et al. Clinical evaluation of a new set of image quality criteria for mammography. Radiation Protection Dosimetry. 2005;114(1-3):389–394.

[90] Zanca F, Van Ongeval C, Jacobs J, Marchal G, Bosmans H. A quantitative method for evaluating the detectability of lesions in digital mammography. Radiation Protection Dosimetry. 2008;129(1-3):214–218.

[91] Zanca F, Van Ongeval C, Jacobs J, Pauwels H, Marchal G, Bosmans H. Performance evaluation of image processing algorithms in digital mammography. In: SPIE Medical Imaging: Image Perception, Observer Performance, and Technology Assessment. vol. 6917; 2008. p. 691709.

[92] Carton AK, Bosmans H, Vandenbroucke D, Souverijns G, Ongeval CV, Marchal G. Quantification of Al-equivalent thickness of just visible microcalcifications in full field digital mammograms. Medical Physics. 2004;31(7):2165–2176.

[93] Highnam RP, Brady JM, English RE. Simulating disease in mammography. In: International Workshop of Digital Mammography, 2000;. p. 727–731.

[94] Båth M, Håkansson M, Tingberg A, Månsson LG. Method of Simulating Dose Reduction for Digital Radiographic Systems. Radiation Protection Dosimetry. 2005;114(1-3):253–259.

[95] Svalkvist A, Båth M. Simulation of dose reduction in tomosynthesis. Medical Physics. 2010;37(1):258–269.

[96] Veldkamp WJH, Kroft LJM, van Delft JPA, Geleijns J. A Technique for Simulating the Effect of Dose Reduction on Image Quality in Digital Chest Radiography. Journal of Digital Imaging. 2009;22(2):114–125.

[97] Svalkvist A, Bäth M. The benefit of accounting for "DQE" variations in simulated dose reduction of digital radiographic systems. Radiation Protection Dosimetry. 2010;22:1–5.

[98] Abramoff MD, Magelhaes PJ, Ram SJ. Image Processing with ImageJ. Biophotonics International. 2004;11:36–42.

[99] MATLAB; 2007.

[100] Parker JA, Kenyon RV, Troxel DE. Comparison of Interpolating Methods for Image Resampling. IEEE Transactions on Medical Imaging. 1983;MI-2.

[101] Press WH, Teukolsky SA, Vetterling WT, Flannery BP. Numerical Recipes in C. Cambridge University Press; 2002.

[102] Zhou J, Zhao B, Zhao W. A computer simulation platform for the optimization of a breast tomosynthesis system. Medical Physics. 2007 april;34(3):1098–1109.

[103] Mackenzie A, Workman A, Dance DR, Yip M, Wells K, C YK. Adapting Clinical Images to Appear with Different Noise and Sharpness to Model a Different Detector. In: et al JM, editor. International Workshop of Digital Mammography, 2010. vol. 6136. Springer; 2010. p. 319–326.

[104] Duvauchelle P, Freud N, Kaftandjian V, Babot D. A computer code to simulate X-ray imaging techniques. Nuclear Instruments and Methods in Physics Research B. 2000;170:245–258.

[105] Marshall NW. Detective quantum efficiency measured as a function of energy for two full-field digital mammography systems. Physics in Medicine and Biology. 2009;54:2845–2861.

[106] Cranley K, Gilmore BJ, Fogarty GWA, L D. Report 78: Catalogue of Diagnostic X-Ray Spectra and Other Data; 1997.

[107] Alm Carlsson G, Carlsson CA, Nielsen B, Persliden J. Generalised use of contrast degradation anc contrast improvement factors in diagnostic radiology. Application to vanishing contrast. Physics in Medicine and Biology. 1986;31(7):737–749.

[108] Dance DR, Day GJ. The computation of scatter in mammography by Monte Carlo methods. Physics in Medicine and Biology. 1994;29:237–247.

[109] Sechopoulos I, Suryanarayanan S, Vedantham S, D'Orsi C, Karellas A. Scatter radiation in digital tomosynthesis of the breast. Medical Physics. 2007;34(2):564–576.

[110] Young KC; 2010. Private communication.

[111] Boone JM, Cooper VN. Scatter/primary in mammography: Monte carlo validation. Medical Physics. 2000;27(8):1818–1831.

[112] Boone JM, Lindfors KK, Cooper VN, Seibert JA. Scatter/primary in mammography: Comprehensive results. Medical Physics. 2000;27(10):2408–2416.

[113] Alsager A, Young KC, Oduko JM. Impact of heel effect and ROI size on the determination of contrast-to-noise ratio for digital mammography systems. vol. 6913; 2008. p. 69134I.

[114] Terry JA, Wagner RG, Blough MA. Half Value and Intensity variations as a function of position in a the radiation field for film-screen mammography. Medical Physics. 1999;26:259–266.

[115] Burgess A. On the noise variance of a digital mammography system. Medical Physics. 2004;31(7):1987–1995.

[116] Sandborg M, Dance DR, Alm Carlsson G. Implementation of unsharpness and noise into the model of the imaging system: Applications to chest and lumbar spine screen-film radiography. Department of Radiation Physics, Linkoping University; 1999.

[117] Sandborg M, Dance DR, Alm Carlsson G. Calculation of contrast and signal-to-noise degradation factors for digital detectors in chest and breast imaging. Department of Radiation Physics, Linkoping University; 2003.

[118] Nykänen K, Siltanen S. X-ray scattering in full-field digital mammography. Medical Physics. 2003;30(7):1864–1873.

[119] Seibert JA, Boone JM. X-ray scatter removal by deconvolution. Medical Physics. 1988;15(4).

[120] Bochud FO, Valley JF, Verdun FR. Estimation of the noisy component of anatomical backgrounds. Medical Physics. 1999;26(7):1365–1370.

[121] Heine JJ. On the statistical nature of mammograms. Medical Physics. 1999;26(11):2254–2265.

[122] Mainprize JG, Bloomquist AK, Kempston MP, Yaffe MJ. Resolution at oblique incidence angles of a flat panel imager for breast tomosynthesis. Medical Physics. 2006;33(9):3159–3164.

[123] Badano A, Kyprianou IS, Jennings RJ, Sempau J. Anisotropic imaging performance in breast tomosynthesis. Medical Physics. 2007;34(11):4076–4091.

[124] Parkin DM, Fernandez LMG. Use of statistics to assess the global burden of breast cancer. The Breast Journal. 2006;12(1):70–80.

[125] NHS Breast Screening Programme; 2010. Accessed June 2009. `http://www.cancerscreening.nhs.uk/breastscreen/`.

[126] Torosian M. Breast cancer: a guide to detection and multidisciplinary therapy. 3rd ed. Humana Press; 2002.

[127] Intelligent patient guide to breast cancer. 4th ed. Intelligent Patient Guide Ltd; 2006.

[128] UK Breast Cancer incidence statistics; 2009. Accessed on December 2009. `http://info.cancerresearchuk.org/cancerstats/types/breast/incidence/`.

[129] Beutel J, Kundel HL, Van Metter RL, editors. Handbook of Medical Imaging:. SPIE; 2000.